Precision Spectroscopy of Neutral Radium: Towards Searches for Permanent Electric Dipole Moments

Santra, Bodhaditya

Precision Spectroscopy of Neutral Radium: Towards Searches for Permanent Electric Dipole Moments

To My Parents and Family

COVER: Cartoon of a particle with finite spin on a Möbius strip. When the time axis is assumed along the side of the strip and a detector is placed in front of the strip, the direction of spin appears to the detector as opposite for two different section of the strip. This is an example of time reversal symmetry violation of the particle observed by the detector in its reference frame.

This work has been performed as part of the research program of the "Stichting voor Fundamenteel Onderzoek der Materie" (FOM) through programme 114 (TRIμP), which is financially supported by the "Nederlandse Organisatie voor Wetenschappelijk Onderzoek" (NWO). Additional funding was provided by the European Comission under contract HPRI-CT-2001-50034 (NIPNET) and HPRI-CT-2001-50022 (Ion Catcher).

Printed by: Ipskamp Drukkers, Enschede, December 2012

RIJKSUNIVERSITEIT GRONINGEN

Precision Spectroscopy of Neutral Radium: Towards Searches for Permanent Electric Dipole Moments

Proefschrift

ter verkrijging van het doctoraat in de
Wiskunde en Natuurwetenschappen
aan de Rijksuniversiteit Groningen
op gezag van de
Rector Magnificus, dr. E. Sterken,
in het openbaar te verdedigen op
vrijdag 18 januari 2013
om 11.00 uur

door

Bodhaditya Santra

geboren op 18 januari 1985
te Burdwan, India

Promotor:	Prof. dr. K. Jungmann
Copromotor:	Dr. L. Willmann
Beoordelingscommissie:	Prof. dr. W. Heil
	Prof. dr. Y. Blumenfeld
	Prof. dr. P. Butler

ISBN: 978-90-367-5915-1 (printed version)
ISBN: 978-90-367-5914-4 (electronic version)

Abstract

Searches for non-zero *permanent Electric Dipole Moments* (EDM) of fundamental particles provide one promising approach for testing the range of validity of fundamental symmetries. An EDM can arise from the known CP-violation within the Standard Model (SM). However it is lower by several order of magnitude compared to the sensitivity of current and proposed EDM searches. In order to push the EDM limit towards the SM prediction and beyond we have to explore the sensitivity of experiments which depends on various issues. The present most stringent experimental upper bound on dipole moment in an atomic system is observed in ^{199}Hg vapor, yielding a limit of $|d(^{199}\mathrm{Hg})| < 3.1 \times 10^{-29}$ e cm [1]. This thesis describes a new experimental approach to search for an EDM in radium which provides the highest possible sensitivity in such systems. The sensitivity depend on the particular isotope and the atomic state considered. Production of rare isotopes of radium with 1/2 nuclear spin and study the atomic physics properties such as, absolute frequency measurement of the strongest laser cooling transition and most suitable transition for trapping the radium atoms are the main challenges of this thesis work. The challenge is accomplished by successful operation of effusive atomic beam of the isotope ^{225}Ra, production of thermal ^{213}Ra atoms and absolute frequency measurement of the main cooling transition $7s^2\ {}^1S_0 - 7s7p\ {}^1P_1$ and trapping transition $7s^2\ {}^1S_0 - 7s7p\ {}^3P_1$ with an accuracy better than 5 MHz. The hyperfine structure interval of the $7s7p\ {}^1P_1$ level is also determined with an accuracy better than 4 MHz which is in good agreement with previous measurement at the ISOLDE facility at CERN. Further, a strategy based on two-photon Raman transition is demonstrated with barium atoms for sensitive probing of the metastable D stated in radium. These measurements provide indespensible input to investigate SM predictions and beyond by means of observing an EDM in optically trapped radium atoms.

Contents

Chapter 1

Introduction

In particle physics elementry particles and their interactions are studied. Theories and discoveries till date have provided ever deeper insights into the structure and behavior of the most fundamental building blocks of nature. The Standard Model (SM) summarizes the present understanding of particle physics [2–5] in one coherent physical theory.

According to the SM there are 12 elementary fermions and 12 force-carrier bosons. The elementary fermions are the three generations of leptons, i.e. electron, muon, tau and their respective neutrinos and the three generations of quarks, i.e. (up, down), (charm, strange) and (top, bottom), which are the building blocks of matter. The force-carrier bosons include the photon for electromagnetic interactions, $W^{\pm}$ and Z^0 bosons for the weak interactions, and 8 independent gluons for the strong interactions. An overview of the elementary particles −fermions and bosons− described by the SM is shown in Fig. 1.1. In the framework of the SM the strong, weak, and electromagnetic interactions arise from local symmetry principles [6].

Recent progress has been reported by the two collaborations CMS [7] and ATLAS [8] at the Large Hadron Collider (LHC), CERN at Geneva, Switzerland. Both experiments provided clear evidence for a new boson at a mass of about 126 GeV/c^2 [7, 8]. This particle could very well be the long sought Higgs boson, which completes the fundamental particles included in the SM (see Fig. 1.1). In the near future the properties of this newly observed particle will be studied in detail in order to identify it unanimously as the Higgs boson or recognize it as a not yet foreseen new particle −which is still a possibility at present.

The SM provides at present the best and most complete description of all

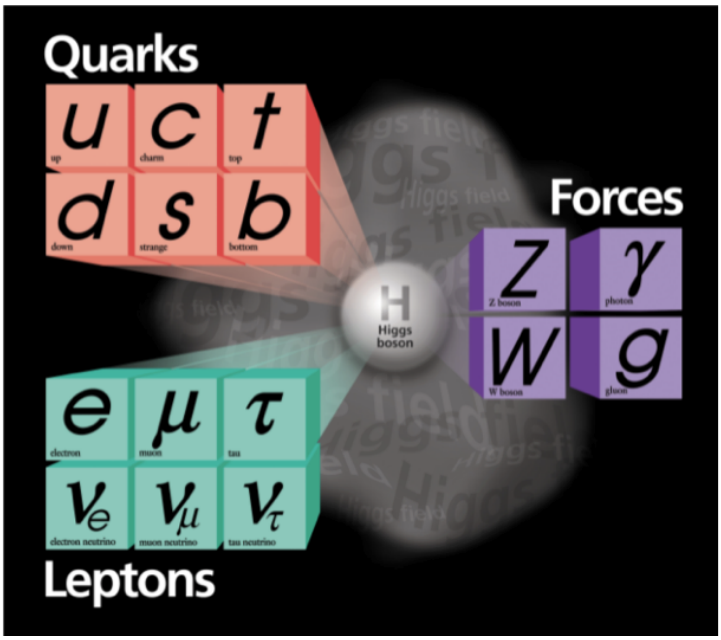

FIG. 1.1: The Standard Model of elementary particle physics with the elementary fermions in first three columns representing particle generations, four types of gauge bosons at two right most column and the Higgs boson at the center [9].

observed subatomic processes, whereas it still does not provide answers to many yet open questions in particle physics. For example, the dominance of matter over antimatter in the universe, the spectrum of fundamental particle masses and the number of the three fundamental fermion generations are not yet explained. The search for answers to such questions provides the driving force to performing experiments at highest available energies at, e.g. LEP [10] or LHC [11], searching for new particles, precision experiments such as the muon magnetic anomaly [12], and experiments with highest possible sensitivity at low energies such as the determination of experimental limits on flavor violation in rare decays [13] and searches for symmetry violations in fundamental processes [14, 15]. The latter type of experiments has revealed insights into nature where the SM can not provide a prediction, in particular at energy scales which are by far not reachable with present accelerator facilities. High mass yet undiscovered particles can show up in vacuum polarization loops and can therefore be studied indirectly in precision experiments. Examples of experiments where this road has lead to a significant increase of our understanding about the elementary particles are the observation of parity violation in weak interactions [16] in ^{60}Co decay [17] and the observation of CP-violation in the $K^0 - \overline{K^0}$ oscillation [18]. These facts are

incorporated in the SM, however neither explained nor motivated.

Searches for non-zero *permanent Electric Dipole Moments* (EDM) of fundamental particles provide one promising approach for testing the range of validity of fundamental symmetries. An EDM can arise from the known CP-violation within the SM. The EDM of a fundamental particle is lower than 10^{-32} e cm according to the SM [19]. The present most stringent experimental upper bound on an EDM is $|d(^{199}Hg)| < 3.1 \times 10^{-29}$ e cm [1]. This limit was established by an EDM measurement which used a dense vapor sample of ^{199}Hg. In order to push the EDM limit towards the SM prediction and beyond we have to explore the sensitivity of experiments which depends on various issues.

Structure of This Thesis

This thesis describes a new experimental approach to search for an EDM in an atom which provides the highest possible sensitivity in such systems, i.e. the radium (Ra) atom (see Fig. 3.2). In this chapter 1 we provide a general introduction to the subject of Permanent Electric Dipole Moments and the framework of the Standard Model in which the present research is carried out.

In Chapter 2 we introduce the EDM of a particle and its connection to fundamental interaction and symmetries. In this context we describe fundamental forces and discrete symmetries. The principle of measurement of an EDM is discussed in general. Various mechanisms contributing to enhancement factors for the EDM of composite particles, such as atoms and molecules, are described. We also estimate an achievable sensitivity for several different types of EDM experiments. The higher sensitivity arises in radium from intrinsic enhancement mechanisms for fundamental particle EDMs (Section 2.4.1) due to the particular level scheme. Another relevant aspect of experimental searches is the achievable signal-to-noise ratio of an EDM measurement which is compared for different experimental approaches (Section 2.4.2).

In Chapter 3 we report the properties of radium as a physical and chemical element, its atomic structure. Particularly we describe the atomic enhancement of an intrinsic fundamental EDM.

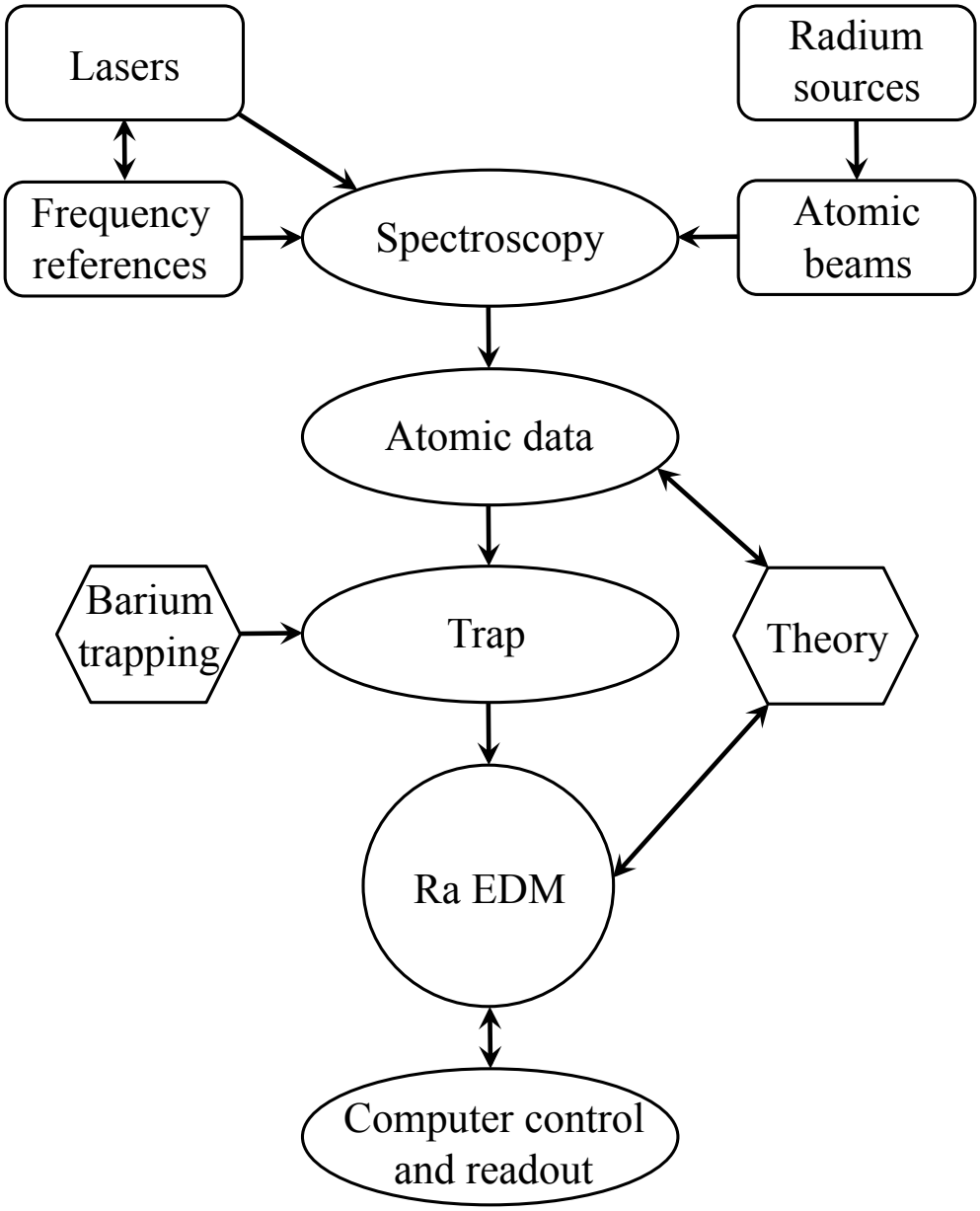

FIG. 1.2: Block diagram of the principal components of the radium EDM experiment. Obtaining spectroscopic data on the atomic and the nuclear data of radium is a crucial step. This requires a radium atomic beam, several lasers operating at the relevant optical frequencies and corresponding frequency references. The experimental data together with the parameters of the experimental setup are recorded and stored using a data acquisition system. It provides in particular for remote control of the experiment.

Chapter 4 to 6 contain the main body of the experimental work carried out in the framework of this thesis. In Chapter 4 we describe potential sources of radium isotopes. All radium nuclei are subject to radioactive decay. The characteristics of an effusive atomic beam are discussed and the development of two different effusive beam apparatuses is reported. Chapter 5 explains the optical setup for precision spectroscopy of radium. In particular several necessary laser systems and experimental tools are described. The frequency references are based on molecular transitions in molecular tellurium and iodine. An absolute calibration of the optical frequencies is performed with an optical frequency comb.

Chapter 6 exploits the achievements which are described in the previous two chapters. Precision spectroscopy of the main transitions in atomic radium is carried out in a radioactive atomic beam described in Chapter 4 using the calibrated laser systemdeveloped in Chapter 5. Optical transition frequencies are determined with an accuracy better than the natural linewidth of the transitions. This is required for a stable operation of optical trapping of radium isotopes. Furthermore, a strategy for a sensitive detection scheme of metastable D-states in radium atoms is demonstrated with the chemical homologue barium.

In Chapter 7 we conclude this work with a discussion of the prospects of an EDM experiment in radium.

Chapter 2

Permanent Electric Dipole Moments

2.1 Fundamental Interactions and Symmetries

The Standard Model of particle physics contains three generations of fundamental fermions, i.e. quarks and leptons, force carrying bosons and the new paradigm Higgs boson. In this chapter we describe the fundamental forces and discrete symmetries. A discussion of possible *Permanent Electric Dipole Moment*s in fundamental and in composite particles is presented.

2.1.1 Fundamental Forces

There are four fundamental forces which are mediated by the exchange of gauge bosons between fermioninc particles. Electromagnetic interactions are mediated by photons and affects charged leptons and quarks. Weak interactions are mediated by $W^{\pm}$ and Z^0 bosons. In the electroweak theory electromagnetic and weak forces are recognized as two different aspects of one force. Strong interactions are mediated by gluons which carry a color charge. The strong force is independent of electric charge and acts only on the quarks, nucleons. Gravity, which is not included in the SM, is mediated by the graviton, which has not been observed yet. An overview of the four fundamental forces is given in Table. 2.1 where also their relative strengths and ranges are given. For massless force carriers the range is infinite, while for massive ones the range is limited by the finite lifetime of these particles.

Force	Carrier	Strength proportionality with distance	range [m]	Relative strength
Strong	gluons	1	10^{-15}	10^{38}
Electromagnetic	photon	$\frac{1}{r^2}$	∞	10^{36}
Weak	$W^{\pm}$, Z^0 bosons	$\frac{1}{r}\exp\{-km_B \cdot r\}$	10^{-18}	10^{25}
Gravitation	graviton	$\frac{1}{r^2}$	∞	1

TABLE 2.1: An overview of four fundamental forces. The force carriers, strength of the forces as a function of distance r, range and relative strength for the corresponding interactions are given.

2.1.2 Discrete Symmetries C, P and T

Symmetries and invariances play an important role in physics. According to Emmy Noether's theorem every symmetry is connected to a conservation law [20]. There are two different types of symmetries. Continuous symmetries which are characterized by continuous mathematical functions and discrete symmetries.

Examples of continuous symmetries contain translation and rotation. Invariance under translational and rotational symmetry leads to the conservation of linear and angular momentum respectively.

The SM knows the three discrete symmetries, the charge conjugation (C), the parity (P) and the time reversal (T).

Charge conjugation means the exchange of all particles with their antiparticles mathematically described by the charge conjugation operator $\hat{C}$. This operator $\hat{C}$ has the properties

$$\hat{C}\hat{C}|\psi\rangle = C^2|\psi\rangle \ , \tag{2.1}$$

where $|\psi\rangle$ is an eigenstate of the operator and the eigenvalue C can be $+1$ or -1.

A Parity operation means the inversion of the spatial coordinates $\vec{r} \rightarrow -\vec{r}$ through the origin. This operation is identical to a mirror image and a rotation. Parity symmetry is represented by the parity operator $\hat{P}$ through

$$\hat{P}\hat{P}|\psi\rangle = P^2|\psi\rangle \ , \tag{2.2}$$

where the eigenvalue P can be $+1$ or -1.

The Time reversal symmetry is the invariance of a particle or an interaction under the transformation $t \rightarrow t' = -t$. There is no quantum number associated with the time reversal symmetry. For this symmetry we have

$$|\psi(r,t)^2| \xrightarrow{\hat{T}} |\psi'(r,t)^2| = |\psi(r,-t)^2| \ . \tag{2.3}$$

Reaction rates and detailed balances in all chemical reactions are conserved because of time reversal invariance.

The role of a violation of the combined charge conjugation and parity operation, $\hat{C}\hat{P}$, is of particular importance because of possible relation to the observed matter-antimatter asymmetry in the universe. A. Sakharov [21] has suggested that the asymmetry in matter-antimatter may be explained via CP-violation in the early universe in a state of thermal non-equilibrium together with baryon number violating processes. The known sources of CP-violation in the SM are insufficient to satisfy the needs of this elegant model. In particular the known strength of CP violating processes is too small. EDMs, which also violate $\hat{C}\hat{P}$, offer excellent oppertunities to find and identify new sources of CP-violation beyond the present theory [22].

2.2 Electric Dipole Moment

The electric dipole moment $\vec{d}$ of a system is a vectorial quantity. For a system composed of two charges $+e$ and $-e$ separated by distance $\vec{r}$ it is defined as

$$\vec{d} = e \cdot \vec{r} \ . \tag{2.4}$$

The vector $\vec{d}$ is parallel to the direction of the spin $\vec{I}$ of a quantum mechanical object since all components perpendicular to $\vec{I}$ are averaged to zero over time [23]. Thus we can write

$$\vec{d} = d\frac{\vec{I}}{|\vec{I}|} \ , \tag{2.5}$$

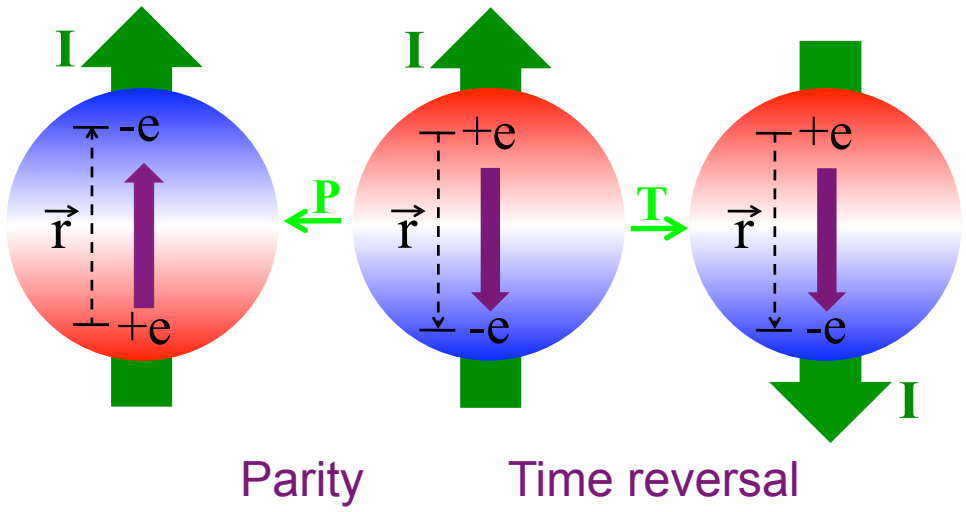

FIG. 2.1: Electric dipole moment of a particle violates parity (P) and time reversal (T) symmetries at the same time.

where d can be seen as the electrical counterpart to the magnetic moment μ. The Hamiltonian of a neutral non-relativistic particle in a magnetic field $\vec{B}$ and an electric field $\vec{E}$ is

$$H = -(\mu\vec{B} + d\vec{E}) \cdot \frac{\vec{I}}{|\vec{I}|} \ , \tag{2.6}$$

where $\vec{\mu}$ is the magnetic moment and $\vec{d}$ is the electric dipole moment of the particle.

Under a parity operation we have $\hat{P}(\vec{B}\cdot\vec{I}\,) = \vec{B}\cdot\vec{I}$ for the magnetic interaction, whereas $\hat{P}(\vec{E}\cdot\vec{I}\,) = -\vec{E}\cdot\vec{I}$ for the electric interaction. Therefore the existance of a non-zero value of $\vec{d}$ will mean a violation of parity. Under the time reversal operation we have $\hat{T}(\vec{B}\cdot\vec{I}\,) = \vec{B}\cdot\vec{I}$, whereas $\hat{T}(\vec{E}\cdot\vec{I}\,) = -\vec{E}\cdot\vec{I}$. Therefore, there will be a violation of time reversal symmetry if a non-zero value of $\vec{d}$ is found. Hence, a non-zero $\vec{d}$ can only exist if and only if parity and time resersal symmetry are violated [24].

A *Permanent Electric Dipole Moment* of any fundamental particle violates both parity (P) symmetry and time reversal (T) symmetry. With the assumption of CPT invariance an Electric Dipole Moment also violates CP symmetry. EDMs for all particles which are due to known sources of CP violation are at least 4 orders of magnitude below the present experimentally established limit [22]. A large number of theoretical models foresees *Permanent Electric Dipole Moments* which could be as large as the present experimental limits just allow [22]. His-

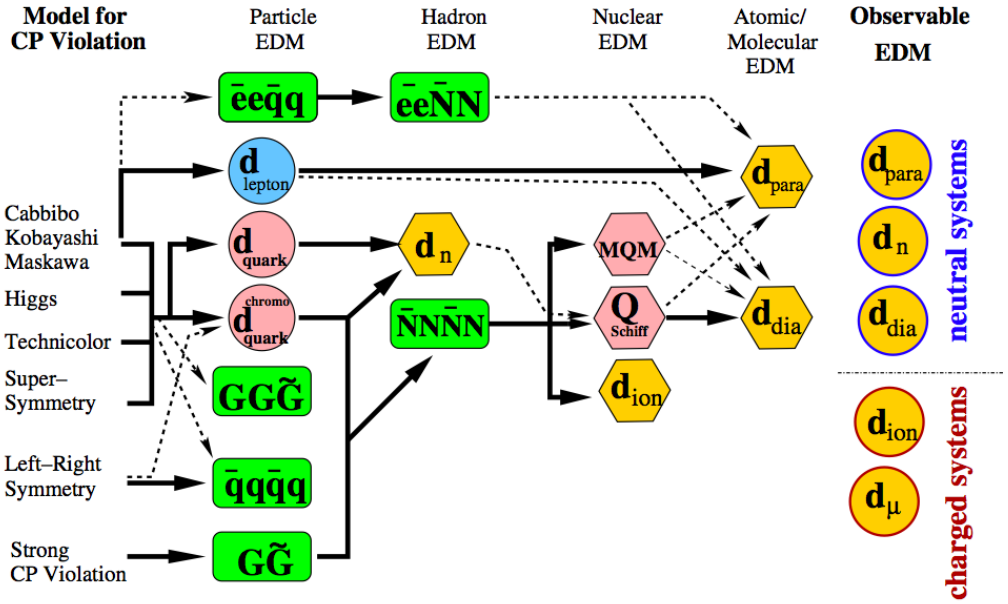

Fig. 2.2: A variety of underlying mechanism responsible for an induced EDM of a composite particle by EDM of fundamental particle [25].

torically the non-observation of *Permanent Electric Dipole Moments* has ruled out more speculative models than any other single experimental approach in all of particle physics [26]. The discovery of a non-zero EDM will also limit the $\bar{\theta}$ term in the QCD Lagrangian. The $\bar{\theta}$ term is one of the fundamental SM parameters and, at this point, cannot be calculated from first principles [27]. There is no prediction for this parameter within the SM. A limit on this term provides information on the "Strong CP-problem" [28, 29]. *Permanent Electric Dipole Moments* have been searched for several systems with different sensitivities (see Table 2.2).

Any new limit on an EDM which is larger than the SM predicted values can provide steering to model building. This could provide clues and hints towards answering questions such as the asymmetry in the baryogenesis which led to the large asymmetry of matter and antimatter in the universe [21].

EDM of a fundamental particle may be enhanced in composed systems such as the atoms or molecules. Fig. 2.2 give an overview of mechanisms that explain how an EDM of a fundamental particle can induce an EDM into a composite system. A compilation of recent experimental limits on a possible Electric Dipole Moment is given in Table. 2.2.

Particle	EDM Limit [e·cm]	SM prediction [e·cm]
μ	1.8×10^{-19} (95% C.L.) [30]	$< 10^{-36}$ [31]
n	2.9×10^{-26} (90% C.L.) [32]	$< 10^{-32}$ [33]
^{199}Hg	3.1×10^{-29} (95% C.L.) [1]	$\sim 10^{-33}$ [24]
YbF	10.5×10^{-28} (90% C.L.) [34]	$< 10^{-38}$ [35]
^{129}Xe	3.4×10^{-27} (90% C.L.) [36]	$\sim 10^{-34}$ [37]
^{205}Tl	1.6×10^{-27} (90% C.L.) [38]	

TABLE 2.2: Limits on electric dipole moments of different systems as of 2012. Here we have muon (μ), neutron (n), Mercury (^{199}Hg), Ytterbium fluoride (YbF), Xenon (^{129}Xe) and Thallium (^{205}Tl).

2.3 Measurement Principle for Permanent Electric Dipole Moment

A search for the existence of a non-zero *permanent Electric Dipole Moment* (EDM) of a fundamental particle is an exclusively experimental assignment [14]. An EDM of a fundamental particle can induces an EDM into composite particles like nuclei, atoms and molecules. The radium atom is one of such composite systems which has excellent properties for searching non-zero EDMs [39]. In order to develop an EDM experiment using atomic radium, the atomic and nuclear properties of radium atom has to be known with high precision, i.e. all relevent atomic properties need to be known at the 10^{-3} level for a state of the art experiment capable of steering theory development.

For a particle with nuclear spin $\vec{I}$, the Larmor precession frequency for parallel and anti-parallel magnetic ($\vec{B}$) and electric ($\vec{E}$) fields are

$$|\overrightarrow{\omega_1}| = \frac{\vec{\mu} \cdot \vec{B} + \vec{d} \cdot \vec{E}}{\hbar |\vec{I}|} \text{ and} \tag{2.7}$$

$$|\overrightarrow{\omega_2}| = \frac{\vec{\mu} \cdot \vec{B} - \vec{d} \cdot \vec{E}}{\hbar |\vec{I}|} \ . \tag{2.8}$$

The difference between the frequencies $\vec{\omega_1}$ and $\vec{\omega_2}$ is proportional to the contribution from the electric dipole moment $\vec{d}$ (Eq. 2.9) and the electric field $\vec{E}$. A measurement of $\vec{d}$ is a measure of linear Stark shift of the energy level of the

particle under consideration

$$\vec{d} = \frac{\hbar|\vec{I}|(\overrightarrow{\omega_1} - \overrightarrow{\omega_2})}{2|\vec{E}|} \quad . \tag{2.9}$$

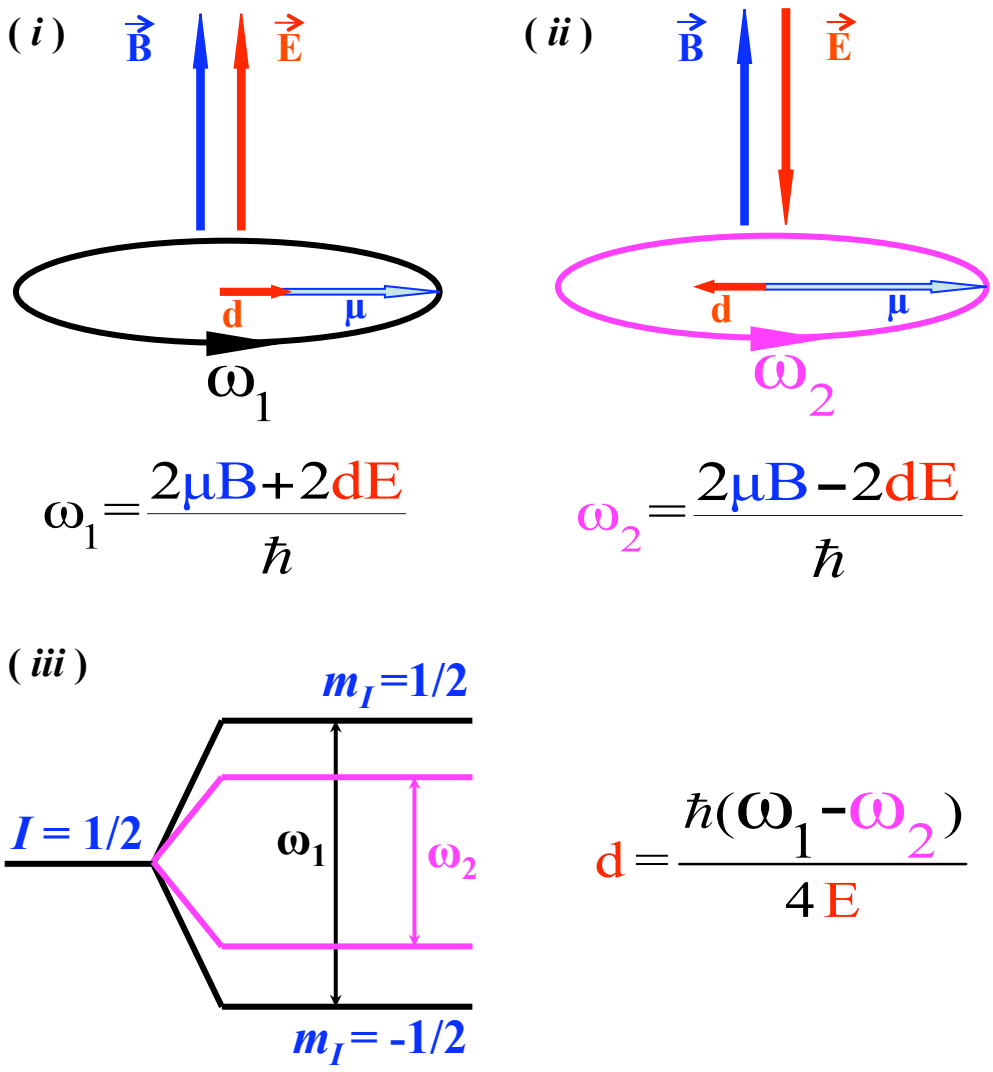

Fig. 2.3: Principle of an EDM measurement, where a spin I = 1/2 particle is alternatively subjected to parallel and antiparallel external magnetic and electric fields orthogonal to its spin. An EDM manifests itself as a difference in the spin precision frequencies ω_1 and ω_2 for both cases.

2.4 Sensitivity of an Experiment for Measuring a Permanent Electric Dipole Moment

At present the most sensitive limit on an Electric Dipole Moment of a particle comes from an experiment in a composite particle, the ^{199}Hg atom. Particularly in composite systems large internal fields can exist, which increase the sensitivity of an EDM experiment. The present limits obtained for an Electric Dipole Moment in different systems arise not only from the statistical sensitivity of the EDM experiments but also they are due to the limited control over experimental parameters in such experiments. In this section we discuss the aspects of gaining sensitivity in an EDM experiment through the choice of a particular system and control over systematic uncertainties.

2.4.1 Enhancement Factors

The predicted value of an EDM of a fundamental particle in the Standard Model of particle physics is too small to be detect at the currently possible experimental sensitivity. However, many extensions of the SM predict values, which could well be detected with the achievable sensitivity of many experiments.

Heavy Nuclei

The EDM of a fundamental particle can induce an EDM into a composite system like atoms or molecules. Paramagnetic atoms and molecules are sensitive to the EDM which arises from an unpaired electron. In heavy paramagnetic atoms a possible EDM of the electron is enhanced by a factor R$\equiv d_{atom}/d_e$. R is given by Eq. 2.10 [24].

$$R \sim 10\frac{Z^3\alpha^2}{J(J+1/2)(J+1)^2} \ . \tag{2.10}$$

For a large Z this factor can provide for a few orders of magnitude enhancement of the electric field inside the atom or molecule [24]. Enhancement factors for electron EDMs for several atoms and molecules are given in Table. 2.3 and Table. 2.4.

Atom	Cs	Au	Tl	Fr	Ra ($^3D_1$)
$R \equiv d_{atom}/d_e$	133	260	585	1150	5400

Table 2.3: Enhancement factors R of electron EDMs for several atomic systems.

Molecule	YbF	WC	HfF^+
$\lvert E_{eff}\rvert/10^{10}$ [V/cm]	2.5	6	2.4

Table 2.4: Enhancement factors of electron EDMs for several molecular systems. In presence of external electric field the effective internal electric field E_{eff} in the molecules is enhanced by large factors.

Schiff Moment

In an external electric field there is an enhancement of the effective electric field in an atom. If the atom is placed in an external electric field the original charge distribution of the atom is polarized in such a way that the positive charges are accumulated in one direction while the negative charges are accumulated in the opposite direction to cancel the external electric field (Fig. 2.4). The

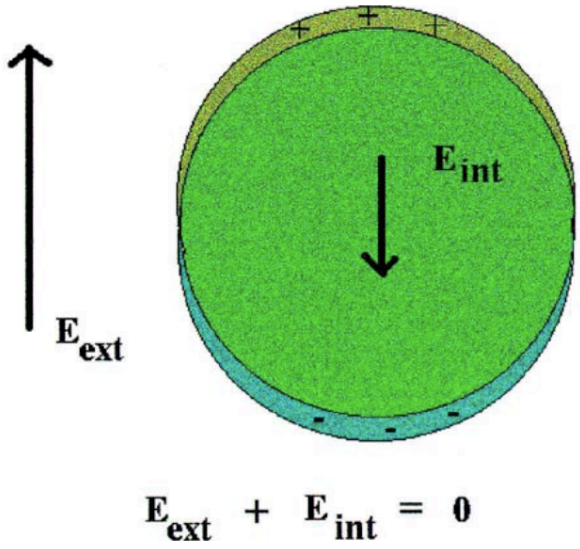

Fig. 2.4: Redistribution of the charge distribution of the electron cloud in an atom while placed in an external electric field [40, 41].

redistribution of charges produce a net zero field at the center of the charge distribution which effectively works in atoms as a shielding of the nucleus [40,41]. This argument does not include the fact that the size and structure of the particle is finite, the direction of spin of the particle is correlated with the direction of electric field, the corrections due to relativistic effects are incorporated in the interaction Hamiltonian of the particle, and the spin dependent forces are connected to the dynamics of the particle [40, 41].

Atomic Structure

In an external electric field the states of opposite parity in a composite system are mixed. The electric field due to a fundamental EDM may polarize the composite system and the resultant EDM is then modified. As a consequence an EDM of its constituents is enhanced in an atom. The polarizability of the atom is inversely proportional to the difference in energy between the degenerate states of opposite parity. The enhancement of the EDM increases as the energy difference between the closely laying states decreases [42].

2.4.2 Achievable Sensitivity for an EDM

The achievable sensitivity for an EDM depends on the statistical and the systematic uncertainties. The statistical sensitivity arises from the number of particles (N_{total}) in the experiment and the efficiency of the detection of the dipole moment. Systematic uncertainties arise from the overall control over the parameters which effect the spin precession measurement. This includes the electric field (E), the polarization (P), the coherence time (τ) and the efficiency of the experiment (ε). The generic sensitivity of an electric dipole moment $|\vec{d}|$ is

$$\delta d = \frac{\hbar|\vec{I}|}{EP\varepsilon\tau\sqrt{N_{total}}} \ . \tag{2.11}$$

The estimate of the total number of particles N_{total} depends on the type of the EDM experiment. This is analyzed for experimental strategies employing beams, cells or magnetic bottles, or neutral atom traps.

For a beam of flux F and total measurement time T_{total}, N_{total} can be written as

$$N_{total}^{beam} = F \cdot T_{total} \ . \tag{2.12}$$

In a beam experiment atoms or molecules can not be reused for more than one measurement. In a cell experiment particles can be reused for more than one

measurement. For a cell of volume V filled with particles of density n, N_{total} is

$$N_{total}^{cell} = n \cdot V \cdot N_{measurements} \ . \tag{2.13}$$

An estimate of N_{total} for an EDM experiment in a trapped sample is similar to that in a cell. For a number of trapped atoms N_{trap} for a single measurement, the total number of atoms in the EDM experiment is

$$N_{total}^{trap} = N_{trap} \cdot N_{measurements} \tag{2.14}$$

For such an EDM experiment in a trap, $N_{measurements}$ can be decomposed as

$$N_{measurements}^{trap} = \zeta \frac{T}{\tau} \tag{2.15}$$

where ζ is a proportionality constant. Depending on experimental stability ζ can have a value in the range of $0.1 < \zeta < 1$. T is the time how long the atoms are available for the measurement. For short-lived atoms T is defined by the mean life time of the atomic nucleus and the trap lifetime. For an EDM experiment with trapped atoms the sensitivity of the measurement can be redefined as

$$[\delta d]_{trap} = \frac{\hbar |\vec{I}|}{EP\varepsilon\tau \sqrt{N_{trap} \cdot \zeta \frac{T}{\tau}}} \ . \tag{2.16}$$

From Eq. 2.16 one can see that the technique of trapping atoms renders the possibility to reuse the atoms and thereby to perform more than one measurement on each of them. This provides an advantage in particular for an EDM measurement in scarce atomic isotopes. Reusing the atoms leads to a lower requirement on the incoming flux of atoms. This increases the feasibility of a higher sensitivity experiment for an EDM with rare atoms.

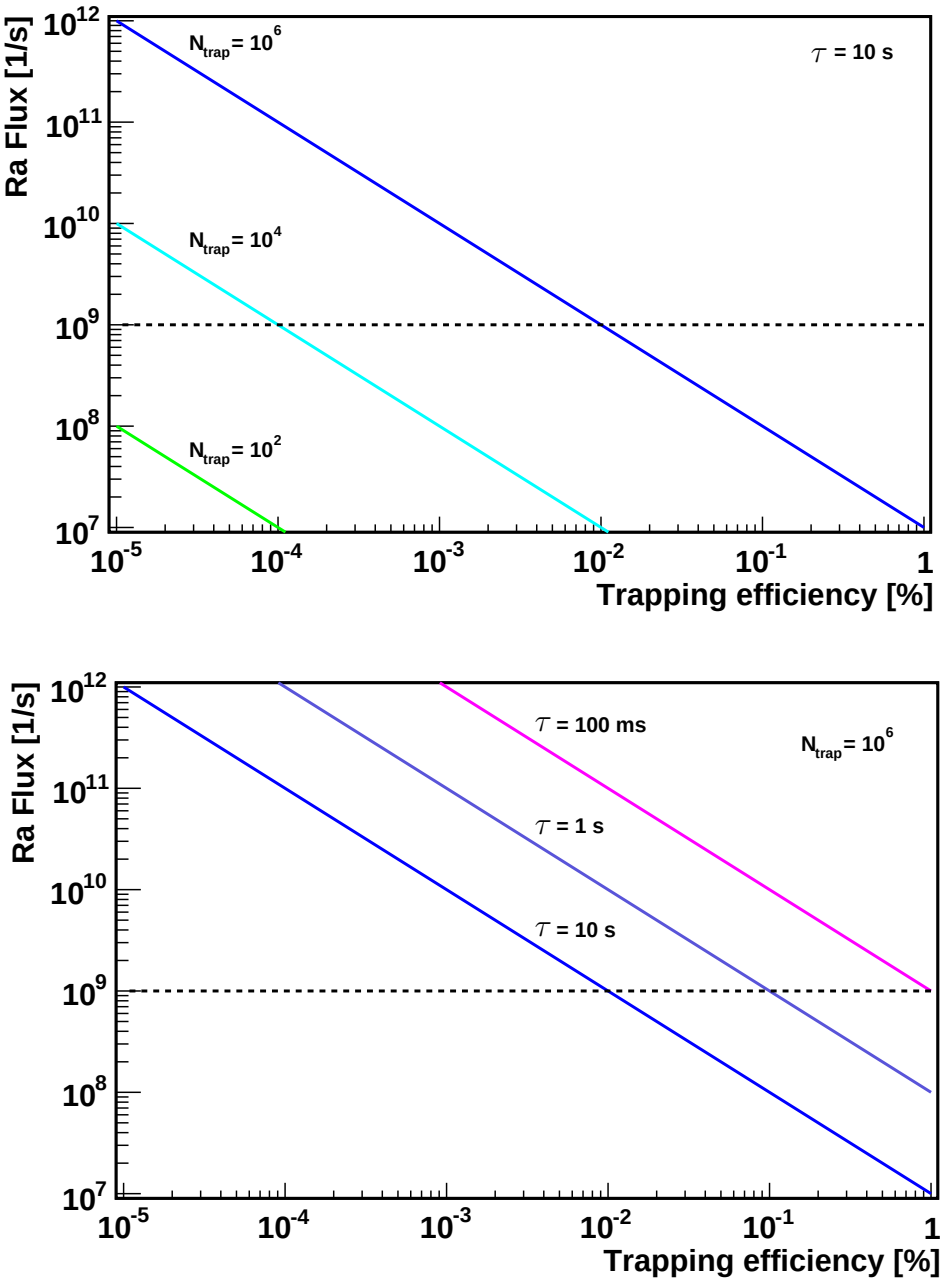

FIG. 2.5: (Top): Required flux of radium atoms for an EDM experiment as a function of trapping efficiency (ϵ_{trap}) and for a spin coherence time τ = 10 s. Three different solid lines in the plot represents three different particle numbers (N_{trap}) in the trap. (Bottom): Required flux of radium atoms for an EDM experiment as a function of trapping efficiency for $N_{trap} = 10^6$. Three different solid lines correspond to three different spin coherence times (τ). The dotted line in both the plots shows the yield of ^{225}Ra at the ISOLDE facility at CERN as an example of present possibilities.

Flux of atoms required for a trapping efficiency ϵ_{trap} is given by,

$$F = \frac{N_{trap}}{\epsilon_{trap}} \cdot \frac{1}{\tau} \ , \tag{2.17}$$

where τ is the spin coherence time and N_{trap} is the number of particles in the trap. A plot of required flux as a function of trapping efficiency is shown in Fig. 2.5. The top plot shows required flux of radium atoms required for a trap experiment as a function of trapping efficiency for a spin coherence time of 10 s. Three different lines in the plot represent three different particle numbers (N_{trap}) in the trap. The bottom plot shows the required flux of radium atoms as a function of trapping efficiency for $N_{trap} = 10^6$ particles in the trap. Three different lines correspond to three different spin coherence times (τ). This analysis shows that a larger trapping efficiency enables the feasibility of an EDM experiment even with a low particle flux and with shorter spin coherence time.

The parameters affecting the sensitivity of an EDM measurement for several completed EDM experiments are summarized in Table. 2.5. For each experiment the sensitivity of the EDM of the particle in the experiment is extracted for one day of measurement time. This extraction is performed by considering the overall sensitivity of the EDM experiment and the total measurement time. Atomic enhancement factors are taken into account in order to find the sensitivity to the EDM of the atom or molecule in the experiment.

EDM experiments on the deuteron and the atomic radium are presently under development. The key parameters for the efficiency of the EDM experiments with deuteron and radium atoms are summarized in Table. 2.6. The experimental sensitivity of the radium EDM is analyzed for three possible EDM measurements in three different states of the radium atom.

Fig. 2.6 represents a graphical comparison of the experimental efficiency for several EDM experiments. The efficiency of the experiments are displayed as a function of the total number of particles required per day for an EDM measurement. Blue markers correspond to already completed EDM experiments. Green markers represent the deuteron and Radium EDM experiments. The lines in the plot represent the efficiency of an EDM experiment as a function of the total number of particles per day in that particular experiment. Three lines are plotted for three different EDM sensitivities (δd). This graphical analysis (Fig. 2.6) is a compilation of the parameters given in Table. 2.5 and Table. 2.6 for several EDM experiments. This analysis provides a guideline for choosing a direction for a further increase of the experimental sensitivity of one of the EDM experiments shown in Fig. 2.6.

Particle	State	Enhancement over e EDM $[d_A/d_e]$	Number of particle N_{total}/day $[day^{-1}]$	Coherence time τ [s]	Electric field $\lvert\vec{E}\rvert$ [kV]	Measurement time [day]	Measured EDM d [e· cm]	Efficiency ε
^{199}Hg	$^1S_0$	-0.014 [43]	10^{17}	$2 \cdot 10^2$	10	~ 100	$(0.49 \pm 1.29_{stat} \pm 0.76_{syst}) \times 10^{-29}$ [1, 44]	$8 \cdot 10^{-3}$
^{129}Xe	$^3P_2$	130 [45]	10^{21}	$2 \cdot 10^3$	3.6	~ 100	$(0.7 \pm 3.3_{stat} \pm 0.1_{syst}) \times 10^{-27}$ [36, 46, 47]	$6 \cdot 10^{-8}$
^{205}Tl	$6\ ^2P_{1/2}$	-585 [48]	10^{22}	$2.4 \cdot 10^{-3}$	123	6	$(6.9 \pm 7.4) \times 10^{-28}$ [38, 49]	$2 \cdot 10^{-5}$
YbF	$X^2\Sigma^+$	$2 \cdot 10^6$ [34, 50]	10^{11}	$1.5 \cdot 10^{-3}$	10	26	$(-2.4 \pm 5.7_{stat} \pm 1.5_{syst}) \times 10^{-28}$ [34, 51]	$3 \cdot 10^{-2}$
n	-	-	$6 \cdot 10^6$	$\sim 2 \cdot 10^2$	10	~ 600	$(0.2 \pm 1.5_{stat} \pm 0.7_{syst}) \times 10^{-26}$ [32, 52, 53]	$4 \cdot 10^{-1}$
μ	-	-	10^{16}	$4.365 \cdot 10^{-6}$	2.7	200	$(0.0 \pm 0.9) \times 10^{-19}$ [30, 54]	$4 \cdot 10^{-4}$

Table 2.5: Key parameters affecting the experimental efficiency for several yet completed EDM experiments. For each experiment an efficiency ε is given based on the sensitivity to an EDM for a particular particle for one day ($\sim 10^5$ s) of measurement time. The atomic or molecular enhancement factor is excluded for this estimate of experimental efficiency.

Particle	State	Enhancement over e EDM $[d_A/d_e]$	Enhancement over ^{199}Hg EDM $[d_A/d_{Hg}]$	Number of particle N_{total}/day $[day^{-1}]$	Coherence time τ [s]	Electric field $\lvert\vec{E}\rvert$ [kV]	Measurement time [day]	EDM limit d [e· cm]	Efficiency ε
deuteron	-	-	10^3 [1, 55]	10^{13}	10^3	120	~ 100	$< 10^{-29}$ [56]	$1 \cdot 10^{-2}$
^{225}Ra	$^1S_0$	-	$10^2 - 10^3$ [57, 58]	10^9	10^2	100	100	3×10^{-28} [59]	$7 \cdot 10^{-1}$
^{225}Ra	$^3D_2$	-	10^5 [39, 42]	10^{15}	$3 \cdot 10^{-5}$ [42]	10	1	$< 10^{-22}$	$4 \cdot 10^{-1}$
^{225}Ra	$^3D_1$	$5 \cdot 10^3$ [39, 42]	-	10^{14}	$5 \cdot 10^{-4}$ [42]	10	1	$< 10^{-23}$	$9 \cdot 10^{-1}$

Table 2.6: The parameters affecting the efficiency of the EDM experiments using deuteron and radium atoms. The radium atom is analyzed for three possible EDM experiments and for three different atomic states. These experiments are presently at a development stage. The experimental efficiency ε is estimated for one day measurement time.

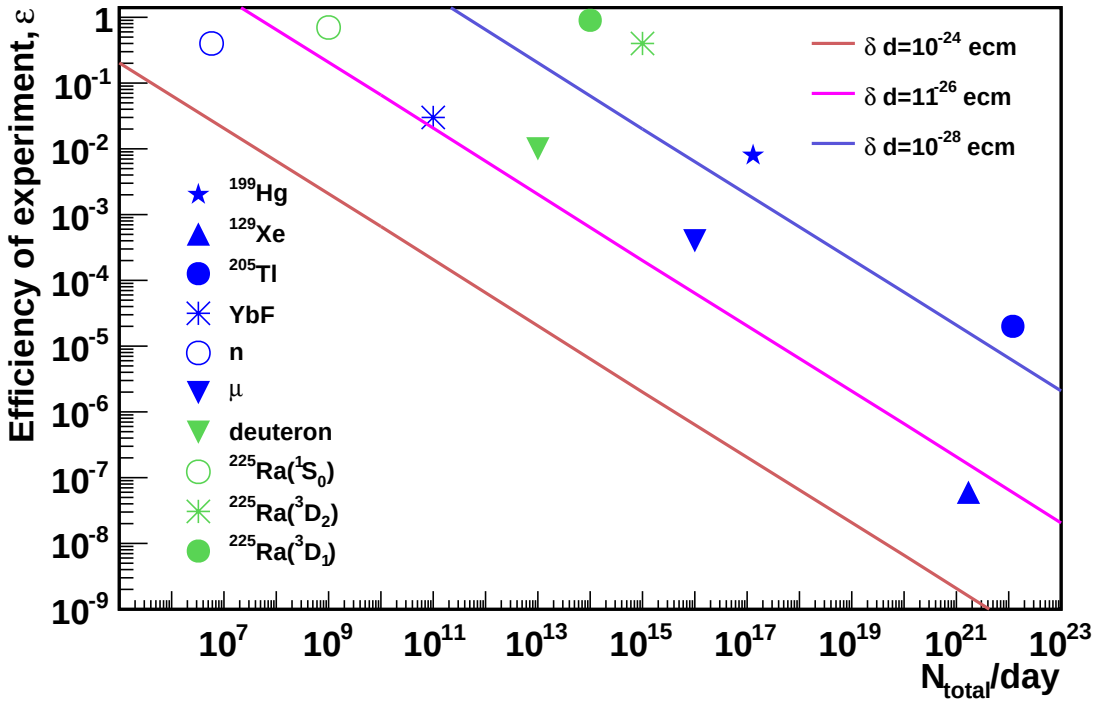

FIG. 2.6: The efficiency of EDM experiments as a function of the total number of particles N_{total} per day for several EDM experiments. Blue markers represent the completed EDM measurements. Green markers represent EDM experiments under development. The lines in this graph represent the efficiency (ε) of the respective EDM experiments as a function of N_{total} per day. Three lines are plotted for three different EDM sensitivities (δd). The uncertainty reported with the data are smaller than the symbol sizes. The data were compiled in Table 2.5 and 2.6 where references are given.

Chapter 3

Properties of Radium

A *permanent Electric Dipole Moment* (EDM) is proportional to the angular momentum in a fundamental system. Therefore the system needs to have a finite angular momentum in order to exploit for an EDM search. Isotopes of radium with non-zero nuclear spin, i.e. the isotopes with an odd number of nucleons, have been identified as excellent candidates for such experiments [39]. In particular the isotopes with nuclear spin 1/2, i.e. ^{225}Ra and ^{213}Ra, are well suited candidates because they offer a less complicated atomic level structure. The peculiarities in the nuclear and atomic energy level structures of radium offers large enhancement factors of a potential nuclear and electron EDM. This results in an induced atomic EDM which is several order of magnitude larger than in other atomic systems. This amplification gives access to a range of values for EDMs which is not accessible otherwise. In order to develop an EDM experiment with radium its nuclear and atomic properties need to be determined preciously.

This chapter provides an overview of radium, which is the heaviest element in the second group of elements in the periodic table, the alkaline earth metals. Group-2 elements have two valance electrons in the outer shell. All isotopes of radium are radioactive with half lifetimes varying from 182 ns for ^{216}Ra to 1600 years for ^{226}Ra. The concentration of the naturally occurring isotope ^{226}Ra in nature is about one part in a trillion or 1 pCi g^{-1} [60]. It originates from the ^{234}U decay chain.

The physical properties of metallic radium, such as the vapor pressure, the radioactive half lifetime and the nuclear spin are relevant for the design of an atomic beam of radium. The knowledge of the atomic energy level structure of radium is indispensable since not only the enhancement factors for a possible EDM, but also the state preparation and manipulation depends on it. Informa-

tion on atomic transition frequencies, hyperfine structures, lifetimes of excited states and metastable states is necessary for the design and operation of an EDM experiment.

3.1 Physical Properties

In 1896 Henry Becquerel discovered the natural occurrence of phosphorescence in pitchblende, an ore that contain uranium oxide. Shortly after that in 1898 Marie Curie and Pierre Curie investigated this new property of pitchblende and extracted by chemical means a substance which was found to be much more active than the original pitchblende. This new substance was named radium derived from the Latin word *radiare* meaning *radiating*. There is about 1 g of radium in 7000 kg of pitchblende. The term radioactivity was also coined by Marie Curie. The activity of 1 g ^{226}Ra was defined later used to the unit of radioactivity, Curie (Ci). In 1911 radium was extracted as a pure metal, which is brilliant white and solid. A list of various atomic properties of radium is given below (Table. 3.1).

Property	Radium
Symbol	Ra
Atomic number	88
Atomic mass	226.03 gm/mol
Phase	solid
Density	5 gm/cm^3
Melting point	973 K
Boiling point	2010 K
1st ionization energy	509.3 kJ/ mol
2nd ionization energy	979.0 kJ/ mol
Most abundant isotope	^{226}Ra (>90%)
Electron configuration	[Rn] 7s^2
Ground state	7s^2 ^{1}S$_0$

TABLE 3.1: Properties of the heavy alkaline earth element radium [61, 62].

Figure. 3.1 shows the vapor pressure dependence on temperature for the alkali metal element sodium and the alkaline earth metal elements strontium, radium,

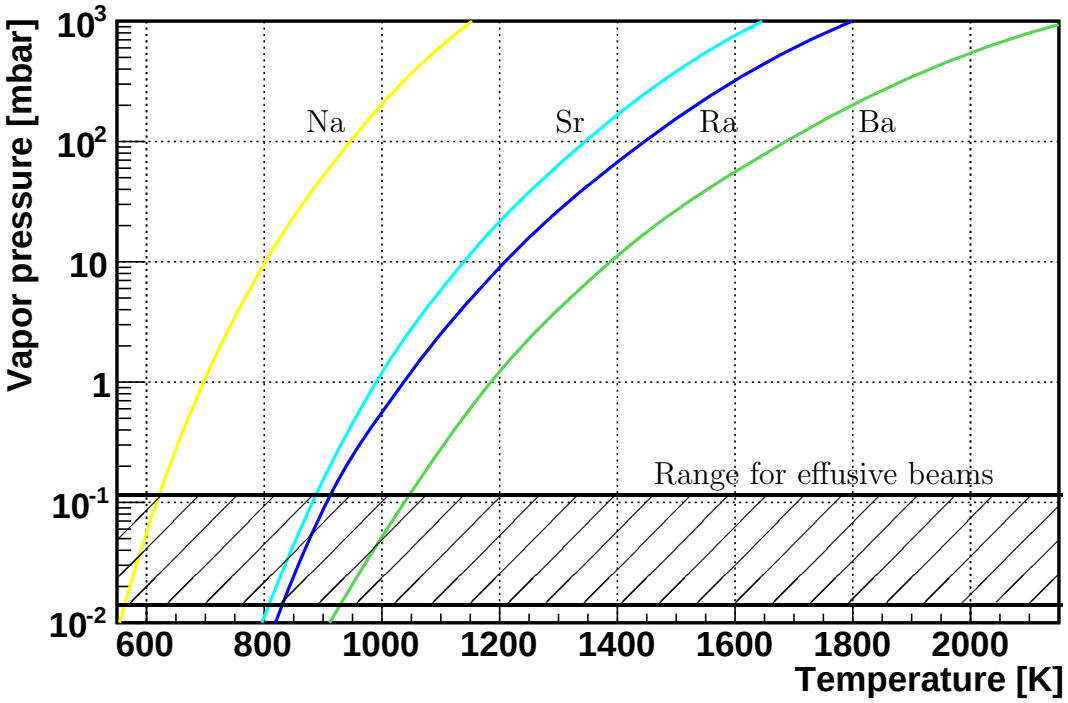

Fig. 3.1: Vapor pressure curves for the alkali metal sodium (Na) and alkaline earth metals strontium (Sr), radium (Ra), and barium (Ba). The temperature range achievable with the oven in the experiment is indicated as well as the vapor pressure range where atomic beams can be operated.

and barium. The typical saturated vapor pressure for an effusive beam oven is in the range of $10^{-2} - 10^{-1}$ mbar which is reached in a temperature range well below 1000 K. These curves provide the information for the design of an oven in particular on the oven temperature for an atomic beam apparatus. Since the vapor pressure curves are similar for the different alkaline and alkaline earth elements we can learn the design of effusive beam ovens which are described for example in [63, 64].

Atomic mass (A)	Nuclear spin (I)	Nuclear magnetic moment (μ_I) [μ_N]	Half-life ($T_{1/2}$)
207	(3/2, 5/2)	-	1.3 s
208	0	0	1.3 s
209	5/2	0.865(13)	4.6 s
210	0	0	3.7 s
211	5/2	0.8780(38)	13 s
212	0	0	13 s
213	1/2	0.6133(18)	2.73 m
214	0	0	2.46 s
221	5/2	-0.1799(17)	28 s
223	3/2	0.2705(19)	11.43 d
224	0	0	3.66 d
225	1/2	-0.7338(15)	14.9 d
226	0	0	1600 y
227	3/2	-0.4038(24)	42.2 m
228	0	0	5.75 y
229	5/2	0.5025(27)	4 m
230	0	0	93 m
231	(5/2)	-	103 s
232	0	0	4.2 m
233	-	-	30 s
234	0	0	30 s

TABLE 3.2: Radium isotopes with nuclear half-life $T_{1/2} > 1$ s. The atomic mass (A), the nuclear spin (I), the half-life and the nuclear magnetic moment (μ_I) are presented. μ_I is given in units of nuclear magneton $\mu_N = 3.1524512605(22)\times10^{-14}$ MeV T^{-1} [65].

3.2 Isotopes of Radium

A crucial aspect relating to the development of an EDM experiment on radium is the availability of suitable radium isotopes. All isotopes of radium are scarce because of the rather short lifetimes of these radioactive isotopes. Radium has 25 different known isotopes [66]. Isotopes with a nuclear half-life larger than 1 s are listed in Table 3.2. The isotope with the largest abundance and the longest lifetime is ^{226}Ra. Its nuclear spin is I = 0 and thus it is not suitable for EDM searches. Some of the radium isotopes are daughter product of the decay chain of uranium or thorium isotopes. All other radium isotopes can be produced at the nuclear reactors.

The argument of spin 1/2 isotope of radium for the interpretation of a possible EDM singles out the isotopes ^{213}Ra and ^{225}Ra. While ^{225}Ra is available from a ^{229}Th source (Section 4.1.1) the short lived ^{213}Ra is only available at radioactive isotope production facilities, e.g. TRIμP, KVI, Groningen, The Netherlands or ISOLDE, CERN, Geneva, Switzerland or TRIUMF, Vancouver, Canada.

3.3 Atomic Structure

Data on optical spectroscopy of the rare element radium are scare. Here we present the spectroscopic work and the results from atomic structure calculations that has been performed on atomic radium to date.

The first optical spectroscopy of radium was performed in 1933 by E. Rasmussen on atomic [67] and ionic [68] ensembles. The spectrum with a total of 96 transitions was recorded on photographic plates after a grating spectrometer. The uncertainty of this measurement was estimated to 10^{-2} cm^{-1} or a relative accuracy of 10^{-6} [67]. These measurements gave the first atomic energy level structure of radium which confirmed identified radium as an alkaline earth element. In 1934 a reanalysis by H. N. Russel yielded corrections to several term energies of the triplet D states [69]. The new assignment resulted in a shift of a few levels of 612 cm^{-1} with respect to their earlier classification by Rasmussen [67]. The analysis also yielded the first ionization potential of atomic radium to be 5.252 eV [69]. In 1967 and 1980 the Rydberg series in radium atom was measured by absorption spectroscopy in a radium cell [70, 71].

The first time laser spectroscopy of radium was performed in 1983 at the ISOLDE isotope production and separation facility of CERN in Geneva, Switzerland [72]. The hyperfine structures and isotope shifts of a series of radium iso-

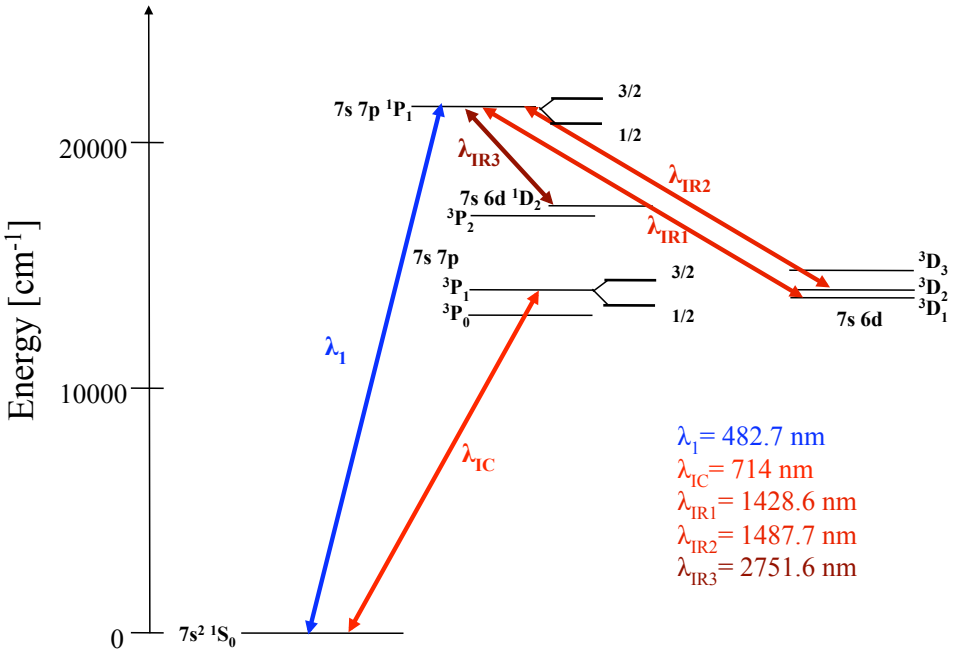

FIG. 3.2: Simplified energy level structure of atomic radium. The hyperfine states are shown only for $^1P_1$ and $^3P_1$ states. Wavelengths are taken from [67].

topes with half-lives between 23 ms and 1600 year were investigated using online collinear fast beam laser spectroscopy [72]. The measuremens were carried out on 18 radium isotopes in the range A = 208 − 232 with intensities of up to 10^8 radium atoms/s in a beam of 60 keV of energy. The $7s^2\ ^1S_0$− $7s7p\ ^1P_1$ transition in the radium atom and the $7s\ ^2S_{1/2}$−$7p\ ^2P_{1/2}$ transition in the Ra^+ ion were observed. The hyperfine splittings and the isotope shifts were evaluated with an experimental error of <10 MHz. Later the isotope shift of the $7s^2\ ^1S_0$− $7s7p\ ^3P_1$ and the $7s^2\ ^3P_2$− $7s7p\ ^3D_3$ transitions were measured by the same technique [73]. The nuclear magnetic moments (μ_I) of ^{213}Ra and ^{225}Ra were measured by observing the Larmor precession of optically pumped atoms in a fast beam at the ISOLDE facility [74]. A list of the nuclear magnetic moments, (μ_I) in units of nuclear magneton (μ_N) is compiled, in Table. 3.2.

Recently the $7s^2\ ^1S_0$− $7s7p\ ^1P_1$, $7s^2\ ^1S_0$− $7s7p\ ^3P_1$ and $7s^2\ ^1P_1$− $7s7p\ ^3D_1$ transition frequencies were measured at the Argonne National Laboratory, Chicago, IL, USA with uncertainties of 180 MHz [78], 30 MHz [79] and 600 MHz [80] respectively. The lifetimes of the $7s7p\ ^3P_1$ [79], $7s6d\ ^3D_1$ [80] and $7s6d\ ^1D_2$ [78]

Upper level	Lower level	Wavelength [nm]	Transition probability (A_{ik}) [s^{-1}]	
		Ref. [67, 69]	Ref. [75]	Ref. [76]
7s8p $^1P_1$	7s^2 $^1S_0$	304.3	-	$2.9{\cdot}10^7$
	7s6d $^1D_2$	633.9	-	-
6d7p $^3D_1$	7s^2 $^1S_0$	310.3	-	-
	7s6d $^1D_2$	660.1	-	-
	7s6d $^3D_2$	548.4	-	-
	7s6d $^3D_1$	540.1	-	-
7s8s $^1S_0$	7s7p $^1P_1$	1417.9	-	$1.2{\cdot}10^7$
7s8s $^3S_1$	7s7p $^1P_1$	1656.1	-	$3.2{\cdot}10^5$
	7s7p $^3P_1$	748.8	-	$2.4{\cdot}10^7$
7s7p $^1P_1$	7s^2 $^1S_0$	482.7	$1.8{\cdot}10^8$	$1.8{\cdot}10^8$
	7s6d $^1D_2$	2751.6	$3.2{\cdot}10^5$	$2{\cdot}10^5$
	7s6d $^3D_2$	1487.7	$1{\cdot}10^5$	$8{\cdot}10^4$
	7s6d $^3D_1$	1428.6	$3.3{\cdot}10^4$	$4.4{\cdot}10^4$
7s6d $^1D_2$	7s7p $^3P_2$	25451.1	$5.9{\cdot}10^0$	$6.4{\cdot}10^0$
	7s7p $^3P_1$	3244.6	$6.7{\cdot}10^2$	$1.4{\cdot}10^3$
7s7p $^3P_1$	7s^2 $^1S_0$	714.3	$2.4{\cdot}10^6$	$2.7{\cdot}10^6$
	7s6d $^3D_2$	1848428.8	$1.8{\cdot}10^{-3}$	$2{\cdot}10^{-3}$
	7s6d $^3D_1$	35269.6	$8.8{\cdot}10^1$	$1{\cdot}10^2$

Table 3.3: Wavelengths and decay rates of relevant transitions between low energy states in radium.

states were also measured in the same setup. Within the framework of this thesis, the 7s^2 $^1S_0$– 7s7p $^1P_1$ and the 7s^2 $^1S_0$– 7s7p $^3P_1$ transition frequencies have been determined by Doppler free fluorescence spectroscopy with uncertainties of less than 5 MHz. The laser frequency in these measurements was stabilized with an optical frequency comb (see also Section 5.3.2).

The unique nuclear and atomic properties are the core reason for the large enhancement factors in radium isotopes which make precision experiments to investigate fundamental characteristics of nature feasible [39]. This provides a strong motivation for performing high precision calculations of wave functions for different atomic states in radium [25, 81]. Knowledge of the wave function close to and in some distance from the nucleus are important for the hyperfine

Lifetimes of the excited states in radium					
States	Theory				Experiment
	Ref. [42]	Ref. [77]	Ref. [76]	Ref. [75]	Ref. [78–80]
7s7p $^1P_1$	5.5 ns	5.53 ns	5.5 ns	5.56 ns	
7s7p $^3P_2$	74.6 ns	5.55 μs	5.4 μs	6.46 μs	
7s7p $^3P_1$	505 ns	362 ns	360 ns	421 ns	422(20) ns
7s7p $^3P_0$	-	-	-	34(15) s	
7s6d $^1D_2$	38 ms	129 ms	710 μs	1.37 ms	385(45) μs
7s6d $^3D_3$	-	-	-	157 s	
7s6d $^3D_2$	15 s	3.3 s	-	3.95 s	
7s6d $^3D_1$	617 μs	654 μs	640 μs	719 μs	510(60) μs

TABLE 3.4: Lifetimes of low lying states in atomic radium.

interactions and the transition probabilities. Calculations on the radium atom are challenging because high precision calculations need to be carried out relativistically. Precision measurements of transition frequencies, hyperfine structure intervals, lifetime of excited states and isotope shifts provide indispensable input for such calculations. Different theoretical approaches such as relativistic Hartree-Fock (RHF), many-body perturbation theory (MBPT), multiconfiguration Dirac-Hartree-Fock (MCDHF) models were followed by different groups [75–77, 82, 83] for these calculations. The term energies and lifetimes calculated with different models have shown large discrepancies for some cases such as lifetime of metastable D-states. The present knowledge about the transition wavelengths and transition probabilities of different states of atomic radium are represented in Table. 3.3. Theoretical and experimental values of lifetimes of several lower laying atomic states of radium are listed in Table. 3.4. The large variation of the results from the atomic structure calculations underlines the need for experimental data which provides anchor points for such calculations.

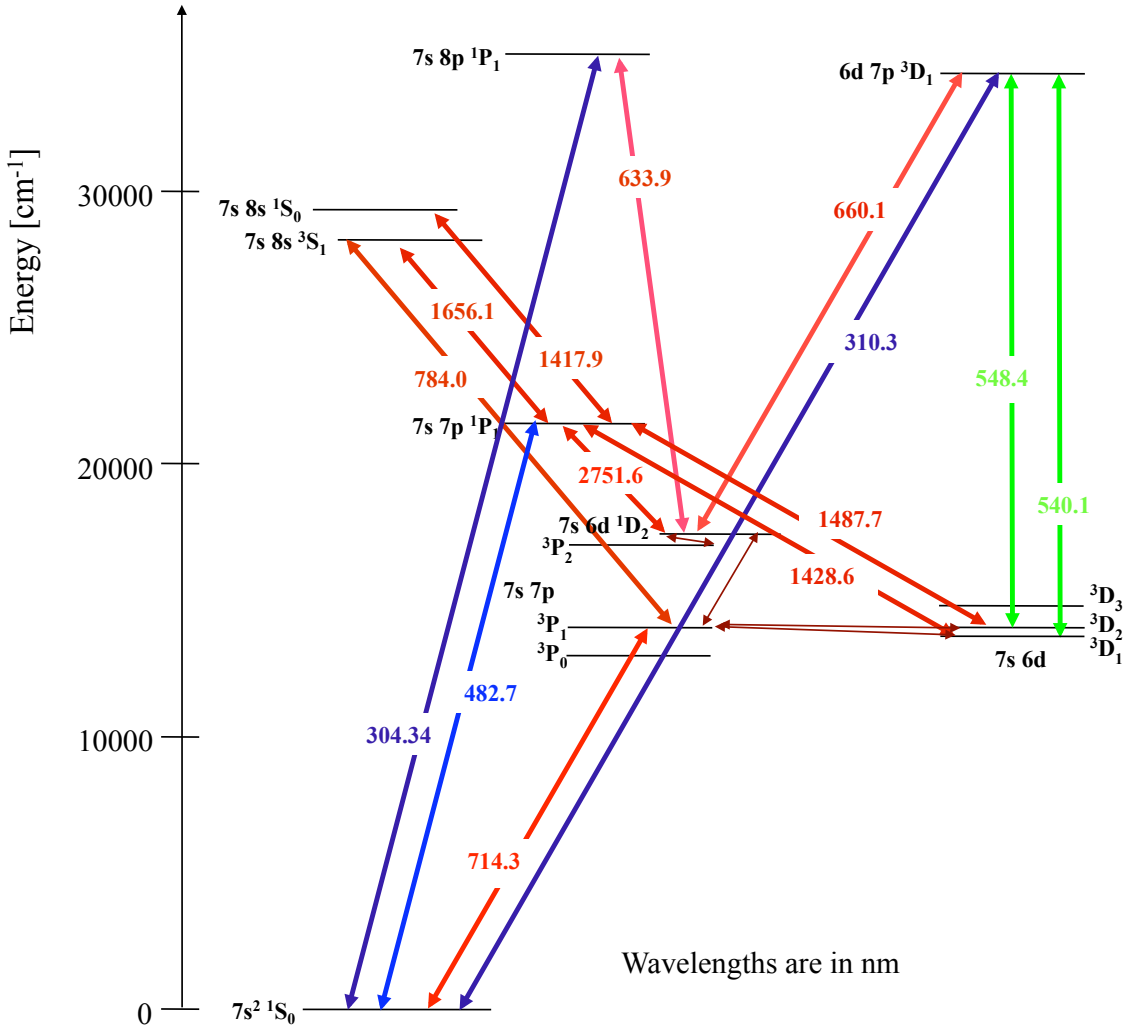

Fig. 3.3: Energy level structure of atomic radium showing the wavelengths of all relevant transitions for efficient laser cooling of radium atoms. The data is taken from atomic structure calculations [76, 77], grating spectrometer data [67], and laser spectroscopy ([78–80] and this thesis). The near degeneracy of the ^3P_i and the ^3D_j - states are the cause for the large atomic enhancement factors of intrinsic EDMs in atomic radium.

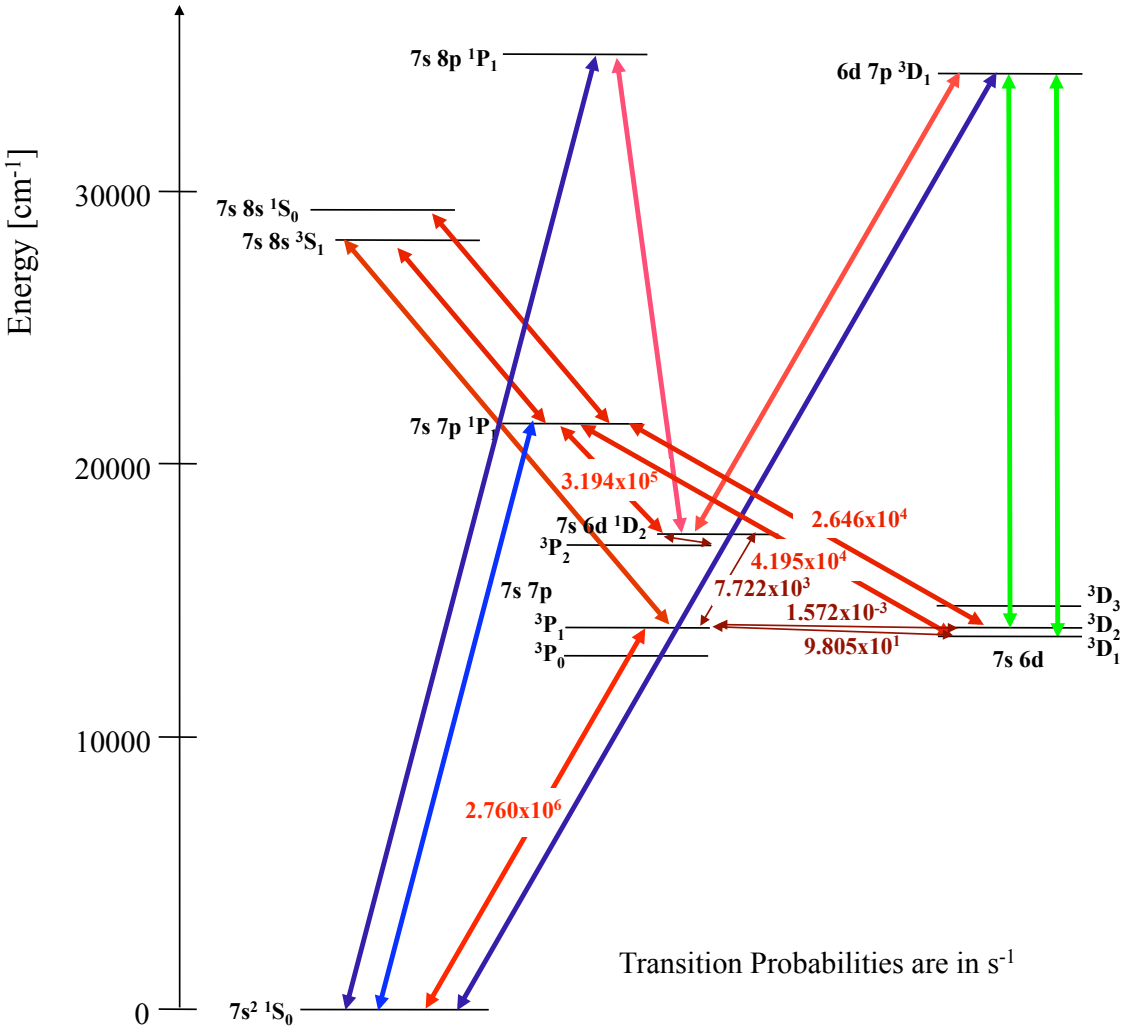

FIG. 3.4: Energy level structure of atomic radium showing the transition probabilities from the excited states to the ground state and to metastable states of relevant transitions. They are relevant for an efficient laser cooling scheme for radium atoms. The data is taken from atomic structure calculations [76, 77], and laser spectroscopy ([78–80] and this thesis).

3.4 Permanent Electric Dipole Moments in Radium

In atomic radium there are several different effects present which cause strong enhancements leading to potentially large atomic electric dipole moments. The enhancements depend on the particular isotope and the atomic state considered. It further depends on the actual source of the EDM. The different contributions to the enhancement factor are described below.

Heaviest Alkaline Earth Atom

The enhancement of a nuclear EDM in heavy nuclei grows faster than the third power of the atomic number Z (Section 2.4.1). Radium is the heaviest alkaline earth element with atomic number Z = 88. Therefore an EDM in radium is enhanced by a factor of 3 over an EDM in mercury [58].

Electron EDM in the 7s6d ^{3}D$_1$ state

The EDM of an electron interacts with the internal electric field of an atom. The interaction results in a mixture of the states with the same total orbital angular momentum but with opposite parity. As a consequence the EDM of an electron d_e induces an EDM d_A into the atom. The Hamiltonian of the interaction of d_e with the internal electric field $\vec{E}$ of the atom can be written as

$$H_{EDM} = -d_e \beta (\vec{\Sigma} \cdot \vec{E}) \ , \tag{3.1}$$

where, β is the Dirac matrix (Eq. 3.2) and $\vec{\Sigma}$ is the relativistic spin operator (Eq. 3.3).

$$\beta = \begin{pmatrix} 1 & 0 \\ 0 & -1 \end{pmatrix} \tag{3.2}$$

$$\vec{\Sigma} = \begin{pmatrix} \vec{\sigma} & 0 \\ 0 & \vec{\sigma} \end{pmatrix} \tag{3.3}$$

The atomic EDM in the 7s6d ^{3}D$_1$ state of radium is enhanced by the presence of opposite parity state 7s7p ^{3}P$_1$ at very close energy separation [39, 42]. Under the approximation that only the closest states are involved in the interaction of the electronic EDM of radium in the 7s6d ^{3}D$_1$ state can be written as

$$d_{^3D_1} = 2 \frac{\langle 7s6d\ ^3D_1 | -er | 7s7p\ ^3P_1 \rangle \langle 7s7p\ ^3P_1 | H_{EDM} | 7s6d\ ^3D_1 \rangle}{E(7s6d\ ^3D_1) - E(7s7p\ ^3P_1)} \ . \tag{3.4}$$

The enhancement of the atomic EDM arising from an electron EDM in the 7s6d $^3D_1$ state of radium is about a factor of 5000 [42].

Nuclear EDM in the 7s6d $^3D_2$ state

An atomic EDM may also arise from the interaction of an electron with the nuclear Schiff moment. The Hamiltonian of interaction between the electron and the Schiff moment is

$$H_{Schiff} = 4\pi \vec{S} \cdot \vec{\nabla}\rho(r) \ , \tag{3.5}$$

where $\vec{S}$ represents the nuclear Schiff moment and $4\pi\vec{\nabla}\rho(r)$ represents the electron part in the Hamiltonian caused by the Coulomb interactions. In the 7s6d $^3D_2$ state the Schiff moment contribution to an EDM is strongly enhanced due to the presence of closely lying 7s7p $^3P_1$ state of opposite parity. The effective EDM in the 7s6d $^3D_2$ state can be approximated by

$$d_{^3D_2} = 2\frac{\langle 7s6d\ ^3D_2| - er|7s7p\ ^3P_1\rangle\langle 7s7p\ ^3P_1|H_{Schiff}|7s6d\ ^3D_2\rangle}{E(7s6d\ ^3D_2) - E(7s7p\ ^3P_1)} \ . \tag{3.6}$$

This results in a large enhancement of an EDM in the 7s6d $^3D_2$ state of radium [39, 42, 83] by a factor of about 10^5 compared to the enhancement in the EDM of ^{199}Hg. The enhancement does not mean that the EDM in radium is 10^5 times larger than the EDM in mercury, but rather that, radium EDM experiment requires a fraction of the sensitivity of the ^{199}Hg EDM experiment [84] in order to achieve comparable limits on sources of CP violation.

Nuclear EDM in the ground state

An atomic EDM can occur because of the collective T-odd and P-odd moments as a consequence of the asymmetric shape of an atomic nucleus. An enhancement on an EDM may arise from the collectiveness of the intrinsic Schiff moment, classically represented as [85]

$$\vec{S} = \frac{1}{10}\int \rho_{ch}(\vec{r})\left(r^2 - \frac{5}{3}\overline{r_{ch}^2}\right)\vec{r}\cdot d^3r \ \ , \tag{3.7}$$

where ρ_{ch} is the charge density of an atomic nucleus and $\overline{r_{ch}^2}$ is the mean square charge radius. Because of octupole deformation of the charge distribution (Fig. 3.5) of several radium nuclei near the valley of stability the Shiff moment causes a large enhancement factor on radium EDM [57, 58, 85, 86]. The enhanced Shiff moment and parity doubling induces an enhancement in the radium EDM of

10^2-10^3 compared to the EDM in ^{199}Hg. The octupole deformation in the region of radium is experimentally studied by measuring the collectivity of nuclear excitations in Coulomb excitation experiments with the Miniball detector array and post accelerated radioactive beams from ISOLDE, CERN [87].

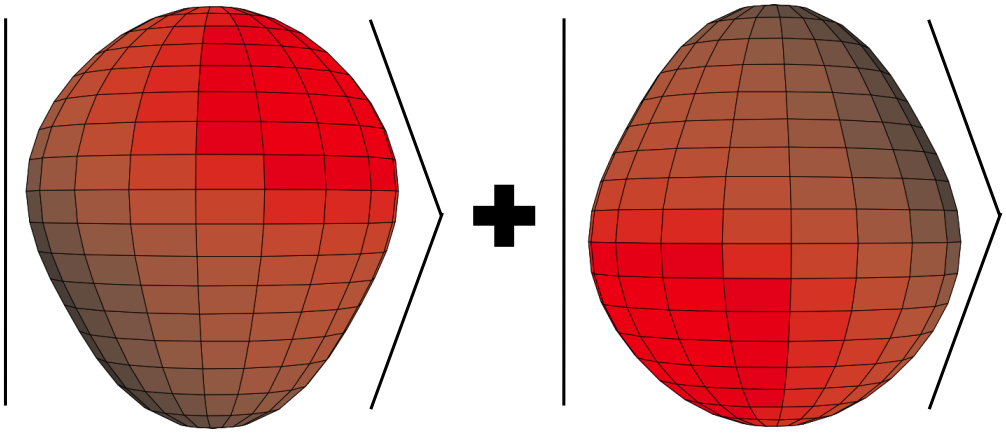

Fig. 3.5: Shape of the nuclear charge distribution of ^{225}Ra [58]. An octupole deformation is associated with a peer like shape of the charge distribution in the nucleus. Since the shape is not an eigenstate of energy the nuclear state is a superposition or identical of two intrinsic shapes [88].

3.5 Conclusion

The atomic and nuclear properties of the alkaline earth element radium makes it a sensitive experimental system for studying fundamental symmetry violating properties like EDM. The largest known atomic enhancement factor and the design of an atomic physics measurement of the EDM depends strongly on the precise knowledge of the atomic structure. The study of this and the creation of thermal atomic beam of rare isotopes of radium is the main challange of this thesis work and will be discussed in the subsequent chapters.

Chapter 4

Radium Atomic Beam Development

A sensitive search for an EDM in the radium atom requires particular equipment which is essential and necessary to reach the highest possible accuracy. To this extent several key elements have been developed and optimized. We focus here on the isotopes ^{213}Ra and ^{225}Ra, where sources to obtain these isotopes have been developed. For ^{213}Ra a beam of ^{206}Pb from the AGOR cyclotron is utilized which is directed on a ^{12}C target and for ^{225}Ra the α-decay of a radioactive ^{229}Th source is exploited. For both isotopes low energy atomic beams have been developed.

4.1 Sources of Radium Atoms

Atoms with nuclei of spin I = 1/2 have particular advantages for EDM experiments because in such nuclei there is no quadrupole moment and also the number of hyperfine components in their optical spectra is minimal. Therefore the isotopes ^{213}Ra and ^{225}Ra, with nuclear spin I = 1/2, are of special interest. Although, other isotopes are of particular future interest, e.g. in connection with atomic parity violation experiments, some of them may also be exploited in future EDM experiments, because of nuclear enhancement mechanisms such as octupole deformation [87]. Most of the isotopes are available from nuclear reactions. The full set of radium isotopes can be obtained from fusion and evaporation reactions, from radioactive decay, or spallation of a uranium target with a proton beam. In Table 4.1 we give summary of the possible radium isotope production mechanisms.

Atomic mass (A)	Decay series	Source	Available at KVI
208	-	^{204}Pb + ^{12}C → ^{208}Ra + 8n	√
209	-	^{204}Pb + ^{12}C → ^{209}Ra + 7n	√
210	-	^{204}Pb + ^{12}C → ^{2010}Ra + 6n	√
211	-	^{204}Pb + ^{12}C → ^{211}Ra + 5n	√
212	-	^{206}Pb + ^{12}C → ^{212}Ra + 6n	√
213	-	^{206}Pb + ^{12}C → ^{213}Ra + 5n	√
214	-	^{206}Pb + ^{12}C → ^{214}Ra + 4n	√
221	-	spallation	
223	^{235}U	^{227}Ac (21.8 y)	√
224	^{232}Th	^{228}Th (1.9 y)	
225	^{233}U	^{229}Th (7340 y)	√
226	^{238}U	^{226}Ra, ^{230}Th (1.9 y)	
228	^{232}Th	^{228}Ra	
230	-	spallation	
231	-	spallation	
232	-	spallation	

TABLE 4.1: Possible production mechanisms for a series of radium isotopes. The isotopes with A= 208 - 214, 223 and 225 are available at KVI. Isotopes with A = 208 -214 are produced at TRIμP facility. Isotopes with A = 225 and 223 are produced from a radioactive parent sources.

Radium isotopes with non-zero nuclear spin I are typically short lived (see Table 3.2). Here we focus particularly on the spin I = 1/2 isotopes, i.e. ^{213}Ra and ^{225}Ra. This requires online production of the isotope ^{213}Ra which has $T_{1/2}$ = 2.73 min lifetime, while the isotope ^{225}Ra which has a halflife of $T_{1/2}$ = 14.9 day can be obtained from a radioactive source.

For the envisioned EDM experiment in radium at KVI a radium atomic beam has been developed with low average kinetic energy. Atoms at such temperatures can be conveniently cooled by laser cooling. Effusive beams have been well studied before for alkaline and alkaline earth elements [63, 89]. The achievable beam parameters can be best estimated using the information accumulated from the performance of a barium atomic beam.

Fig. 4.1: $^{225}_{88}$Ra is the daughter product of the $^{229}_{90}$Th α-decay. $^{225}_{88}$Ra decays to $^{225}_{89}$Ac, which decay to $^{221}_{87}$Fr. The decay chain further continues until the stable isotope $^{209}_{83}$Bi is reached [66].

4.1.1 Radium from Radioactive Sources

Some long lived radium isotopes can be obtained from the radioactive decay of suitable parent nuclei. Such sources are ^{227}Ac with a halflife of 21.8 years or ^{229}Th with $T_{1/2}$ of 7340 year. We exploit the latter possibility. The production of an effusive atomic beam as it has been employed in this work, is shown in Fig. 4.6 (details of its design are discussed in Section 4.2). The typical temperatures of such ovens for producing atomic beams of alkaline earth elements are of order melting temperatures of the respective alkaline earth elements. At these temperatures the vapor pressure is $\sim 10^{-2}$ mbar (Fig. 3.1). This oven design is for practical purposes only suited for long lived isotopes ($T_{1/2} > 1$ day), because the radioactive material needs to be reloaded into the crucible and vacuum needs to be achieved also. Nevertheless since the lifetime of the isotopes with nuclear spin $I \neq 0$ is of order 15 days or less, frequent refilling of the oven is required. Such a strategy is followed in the experiment at the Argonne National Laboratory [90]. There the isotope ^{225}Ra is used which is chemically extracted from ^{229}Th at the Oak Ridge National Laboratory. Samples of 10^6 s^{-1} radium atoms (250 μCi activity) [79] are then transferred to a crucible in a radiation safety guarded lab-

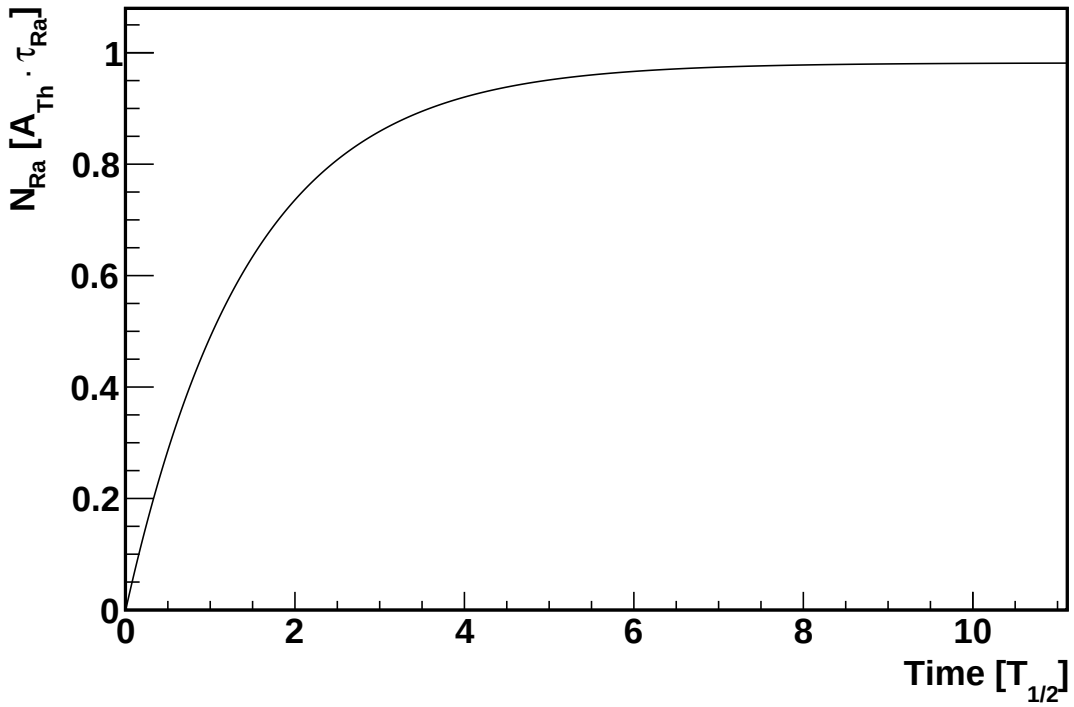

FIG. 4.2: Buildup of the amount of ^{225}Ra inside the cavity containing ^{229}Th of activity A_{Th}. The ^{225}Ra reaches 92(2) % of the saturation value after 4 half lifetimes of the ^{225}Ra nuclei.

oratory. In this experiment at KVI, however, ^{229}Th is transferred only once to the crucible and breading of ^{225}Ra occurs inside the oven cavity (Section 4.2).

Radium is extracted from the decay chain of ^{229}Th (Fig. 4.1). The long-lived isotope ^{229}Th ($T_{1/2}$ = 7340 years) [66] decays via α-decay into ^{225}Ra

$$^{229}Th\ (T_{1/2} = 7340\ years) \rightarrow \alpha +\ ^{225}Ra\ (T_{1/2} = 14.9\ days)\ \ . \tag{4.1}$$

Therefore a ^{225}Ra atomic beam can be obtained from an oven which contains ^{229}Th in a cavity with a small opening. The very long lifetime of the parent isotope ^{229}Th provides for a constant production rate of ^{225}Ra inside this cavity. The ^{225}Ra atoms from ^{229}Th decay can be accumulated in such an oven. The number of radium atoms built up inside the cavity is

$$N_{(t)} = N_{Ra}\left\{1 - exp\left(-\frac{t}{\tau}\right)\right\}\ , \tag{4.2}$$

where t is the buildup time and τ (= $T_{1/2}$/ln2) is the mean lifetime of ^{225}Ra. N_{Ra} is the number of radium atoms in equilibrium inside the oven which is reached

after a time t>> $T_{1/2}(^{225}Ra)$. This number is given by the product of the activity A_{Th} of ^{229}Th and the mean lifetime $\tau_{(^{225}Ra)}$.

$$N_{Ra} = A_{Th} \cdot \tau_{(^{225}Ra)} \quad . \tag{4.3}$$

After 4 half lifetimes the number of radium atoms inside the cavity has reached more than 92(2) % of the saturation value.

4.1.2 $^{209-214}$Ra at the TRIμP Facility

The other available source for isotopes of radium is the TRIμP facility at KVI. The superconducting cyclotron AGOR (Accelerator Groningen ORsay) [91] provides primary beams of light and heavy ions. They are exploited for the production of radioactive particles in inverse kinematics.

In our experiments a lead beam of 8 MeV/u from the AGOR cyclotron bombarded a diamond-like-carbon (DLC) target of thickness 4 mg/cm^2. Short lived $^{209-214}$Ra isotopes have been produced at the TRIμP facility in inverse kinematics with fusion-evaporation reactions, ^{204,206}Pb+^{12}C [94,95]. The radium isotopes were separated from the primary beam and the fission fragments by using the TRIμP magnetic separator [96]. The energetic radium isotopes were converted into low energy ions at the thermal ionizer(TI).

The energy of the secondary beam is too high (a few MeV/u) for performing precision experiments, in particular laser spectroscopy, because the transit time through the experiments would be too short ($\cong$ 1m/μs at 1 MeV) and the Doppler shift would be large. For 1 MeV beam of radium the Doppler shift is about 2 THz for the strongest transition at 483 nm. The secondary beam is decelerated to a low energy beam by stopping and extraction from hot metal surface of a thermal ionizer. The principle of operation of the thermal ionizer can be explained in five consecutive steps: (*i*) stopping of the nuclei in the foils, (*ii*) diffusion of atoms in the foils, (*iii*) effusion of atoms from the foils, (*iv*) ionization of atoms on hot tungsten, and (*v*) extraction of ions from the cavity [92,93,97].

The TRIμP thermal ionizer (TI) consists of a stack of 0.75 μm thick tungsten foils placed in a cavity made of Tungsten. A schematic drawing of the TRIμP thermal ionizer is shown in Fig. 4.3. The design of the TI at the TRIμP facility is optimized for alkali and alkaline earth elements.

The production rate for ^{213}Ra and ^{214}Ra at the exit of the TI was 650 and 200 s^{-1} per particle nA. At a maximum particle current of $\sim$ 70 nA the yield of ^{213}Ra is 5$\times$10^4 s^{-1} [94].

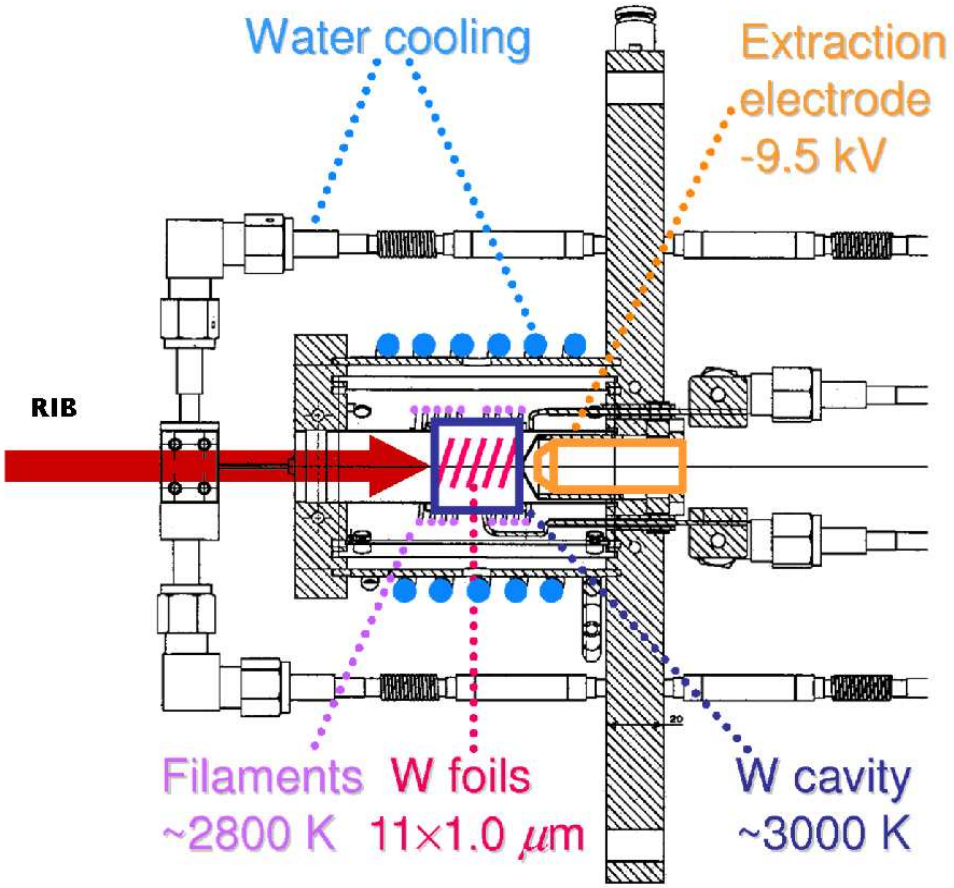

FIG. 4.3: Schematic diagram of the thermal ionizer (not to scale). It thermalizes the radioactive ion beams (RIB) for TRIμP experiments [92, 93] and provides singly charged ions at thermal energies.

The secondary particles at the exit of radioactive isotope separator are completely stopped by the stack of tungsten foils inside the TI cavity. The maximal thickness of the foils is chosen such that the full energy distribution of secondary particles at the exit of the separator can be stopped in them. For the experiments reported here, a stack of 3×0.75 μm foils has been used. The stopped particles diffuse to the surface of the foils. Since the diffusion time to the surface depends quadratically on thickness, thin foils are needed. The thickness of the foils is as small as the rolling manufacturing process allows. The diffusion process is enhanced by heating the foils of the cavity at about 2500 K. The TI cavity is heated by electron bombardment from tungsten filament surroundings. At the surface of the foils the particles escape by effusion. They are thermally ionized by collisions with the surface of the stopping foils and with the tungsten cavity

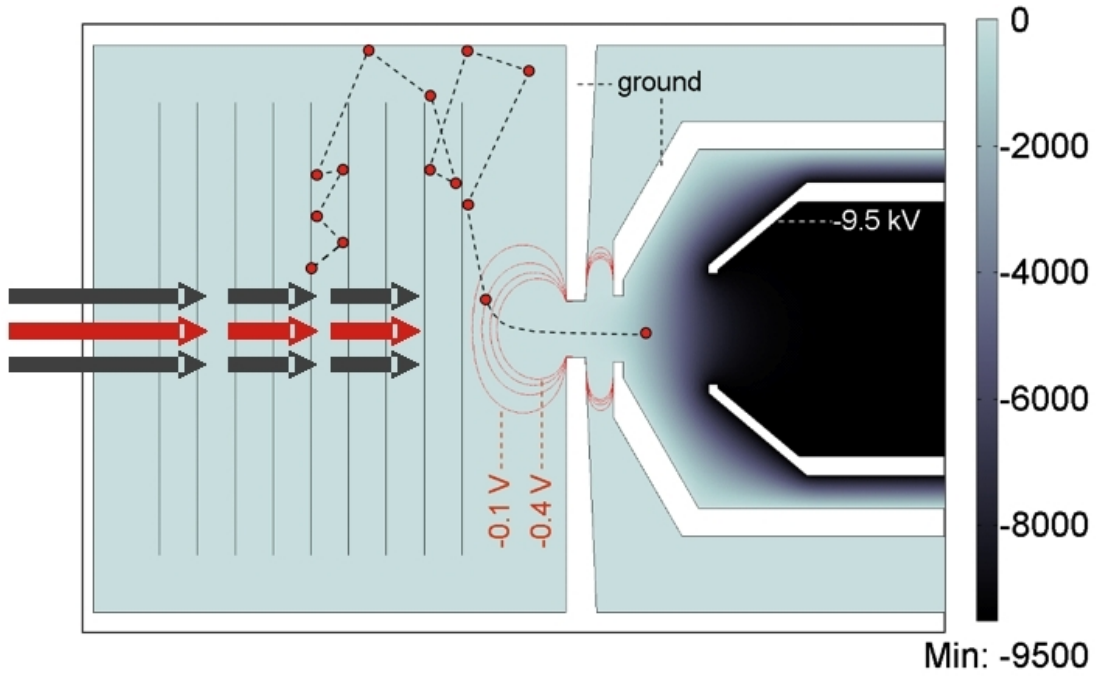

Fig. 4.4: Calculation of electric potentials inside the thermal ionizer cavity created by an extraction electrode potential of -9.5 kV. Equipotential lines are shown for -0.1, -0.2, -0.3, and -0.4 V. A schematic of the trajectory of an ion is shown in the figure [92, 93].

wall of the thermal ionizer. During the multiple collisions of atoms its charge state changes many times. A fraction of the particles is always neutral. The charged particles can be extracted out of the Tungsten cavity of the thermal ionizer by electrostatic extraction, using an electric field formed by a DC potential on an extraction electrode (see Fig. 4.3). The extraction process is schematically depicted in Fig. 4.4.

The extracted particles are singly charged radium ions. Neutral radium atoms inside the thermal ionizer remain there. They will diffuse out at a relatively lower rate. The fraction of radium ions with charge states higher than +1 are negligible, because of the difference in the work function of tungsten and the necessary ionization energy to create higher charge states. Typical extraction efficiencies are about 9 % for radium (Fig. 4.5), about 70 % for sodium and about 40 % for rubidium [97].

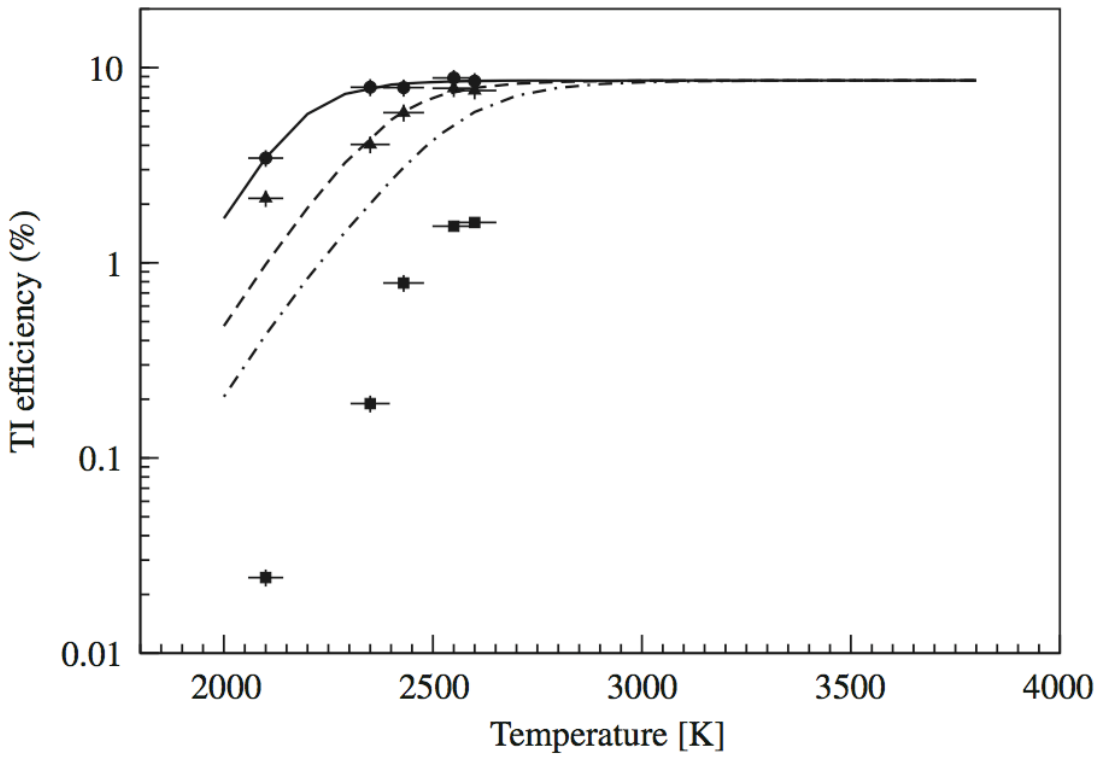

FIG. 4.5: Experimental extraction efficiencies of the TI as a function of temperature for ^{212}Ra(triangle), ^{213}Ra (circle) and ^{214}Ra (square). The predictions according to the diffusion model described in [97] are ^{212}Ra (dashed line), ^{213}Ra (solid line), and ^{214}Ra (dot-dashed line)).

4.2 Offline Atomic Beam of Radium

A source of 10 μCi ^{229}Th has been installed in a titanium crucible for producing a ^{225}Ra atomic beam at KVI. Because of the rather low vapor pressure of thorium the accumulated radium can be heated out of the crucible at temperatures of about 850 K without loosing ^{229}Th mother nuclei. In order to achieve a vapor pressure of 10^{-2} mbar for thorium a temperature of 2700 K is needed, whereas for radium 850 K is sufficient. The vapor pressure of thorium is about 15 order of magnitude smaller at the lower temperatures. The vapor pressure of thorium at 1400 K is $\sim 10^{-13}$ mbar [98] which would lead to an escape rate of less than 1 Bq/ day of thorium from the oven at that temperature.

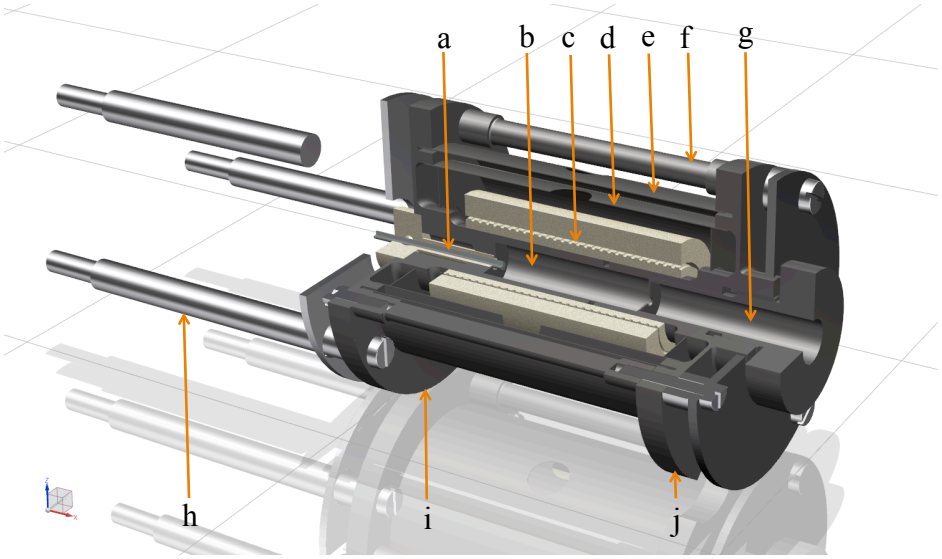

Fig. 4.6: Schematic view of the ^{225}Ra oven: (a) thermocouple; (b) titanium crucible; (c) heater element; (d) inner heat shield; (e) outer heat shield; (f) holding rod; (g) end cap; (h) mounting bars to CF40 feedthrough; (i) back holding flange; (j) front holding flange. The full assembly can be mounted to a CF40 port to a vacuum chamber (see also Fig. 4.7).

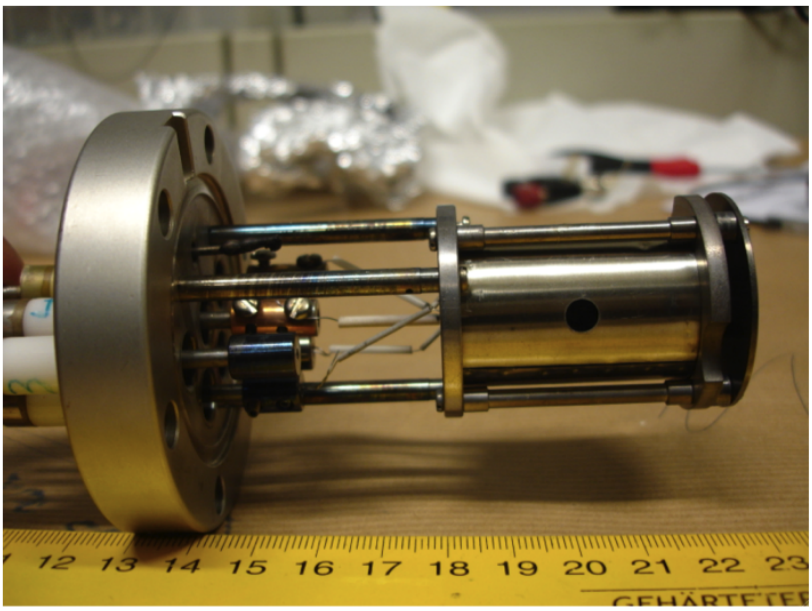

Fig. 4.7: The ^{225}Ra oven is mounted on a CF40 vacuum electric feedthrough. The oven is loaded with ^{229}Th. At temperature 900 K a thermal atomic beam of ^{225}Ra emerges from the oven cavity.

The oven was built at KVI. A schematic view and a picture are shown in Fig. 4.6 and 4.7. The geometry of the crucible is of 6 mm diameter and 20 mm length. The exit aperture of the crucible consists of six holes of 0.5 mm diameter in a 5 mm thick end cap. The crucible is surrounded by 0.25 mm thick tantalum wires which provide a resistive heater element. The tantalum wire is held in alumina ceramic pieces in order to protect it from short circuit. The temperature of the oven is measured with a N-type thermocouple. The operating temperature of around 900 K is achieved at a heater power of about 50 W and is reached within a few 100 sec after the heating commences. The design was developed for experiments on spectroscopy and laser cooling and trapping od barium at KVI [63, 89]. The oven is mounted on a standard CF40 flange to a vacuum chamber with a residual gas pressure of about 10^{-10} mbar inside it. When the oven is heated to its operating temperature of $\sim$ 900 K the gas pressure in the vacuum chamber increases to about 10^{-8} mbar.

The ^{229}Th activity was transferred to the crucible at NRG (Nuclear Research and consultancy Group) in Petten, NL. The activity of ^{229}Th as a solution in nitric acid was dried inside the titanium crucible. A small amount of $BaCO_3$ ($\sim$ 50 mg) together with fine grain zirconium powder was added inside the crucible. Barium serves as a reducing agent for radium. Further it provides an atomic barium beam which has the same characteristics as the radium beam and overlaps with it. This can be exploited for alignment of the optical layout and light collection elements. Radium is accumulated in the cold oven for timescales of the order of the ^{225}Ra lifetime. The saturated population N_{Ra} inside the oven is the 2×10^{11} atoms.

The α-decay of ^{229}Th results in a rather large recoil energy of $\sim$ 100 keV to the ^{225}Ra atoms. Because of this the ^{225}Ra atoms are implanted into the walls of the crucible. The ^{229}Th atoms (10 μCi correspond to 5×10^{-5} g) are distributed inside the crucible. An even distribution corresponds to a layer of thickness 10 nm. The range distributions of 100 keV ^{225}Ra in titanium and thorium have been calculated with SRIM [99]. They are shown in Fig. 4.8. 100 keV radium has a range of $\sim$ 20 nm in thorium. The depth reached by radium in titanium is of order 30 nm. Thus, the ^{225}Ra will gets trapped inside the oven wall material. Depending on the direction of recoil the ^{225}Ra may either stay in the thorium layer or enter the bulk of titanium crucible material. The implantation depth is such that only a small fraction of a few percent can be desorbed from the walls of the crucible at the operation temperature. In order to leave the surface ^{225}Ra has to first diffuse out of the titanium wall and it then diffuses out of the thorium

layer.

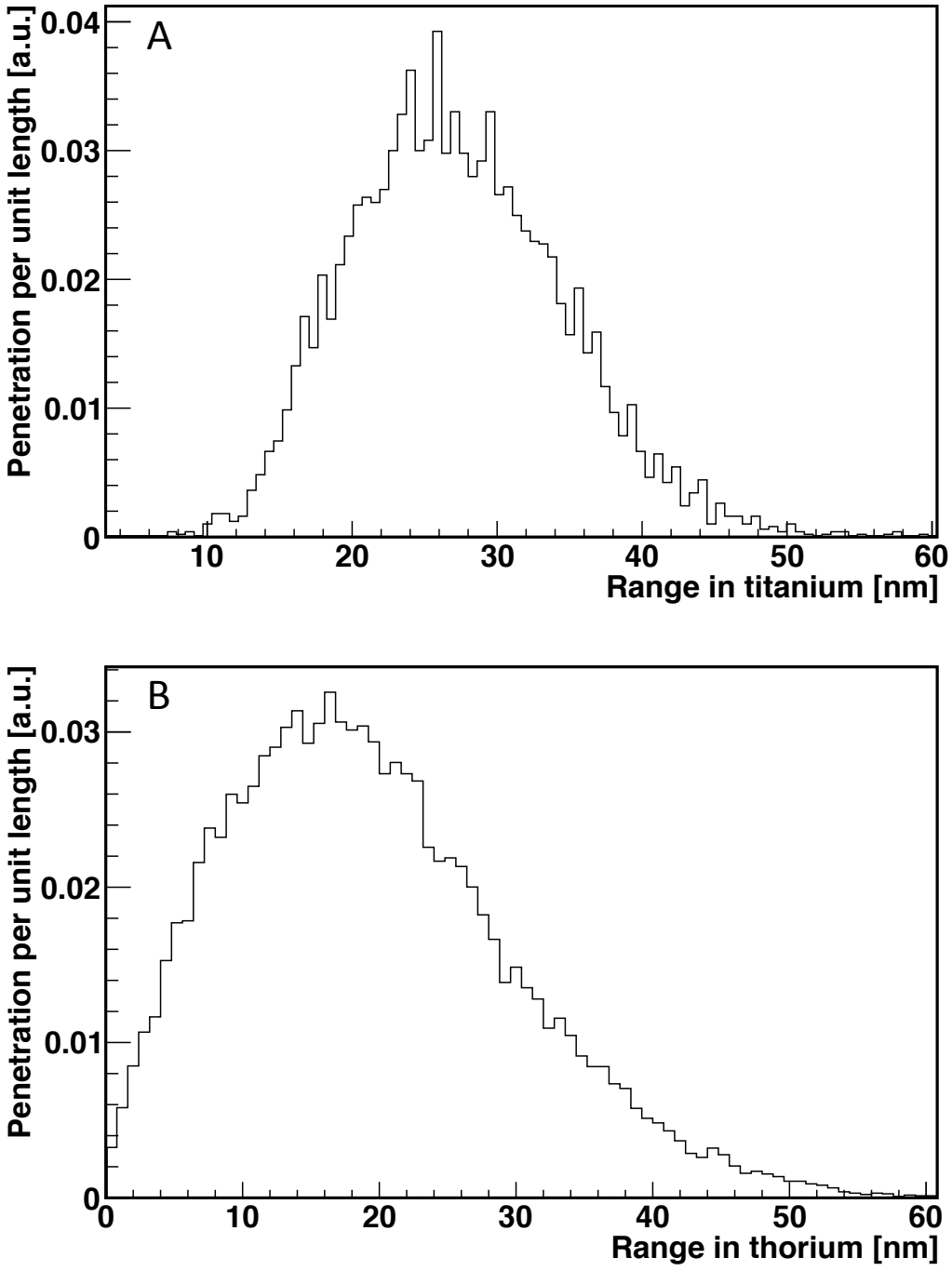

Fig. 4.8: Penetration range distribution of 100 keV ^{225}Ra from the decay $^{229}Th \rightarrow \alpha +^{225} Ra$, where the recoil particles have the kinetic energies $E_\alpha = 5168.1$ keV and $E_{^{225}Ra} = 100$ keV in (A) titanium and (B) thorium calculated with SRIM [99].

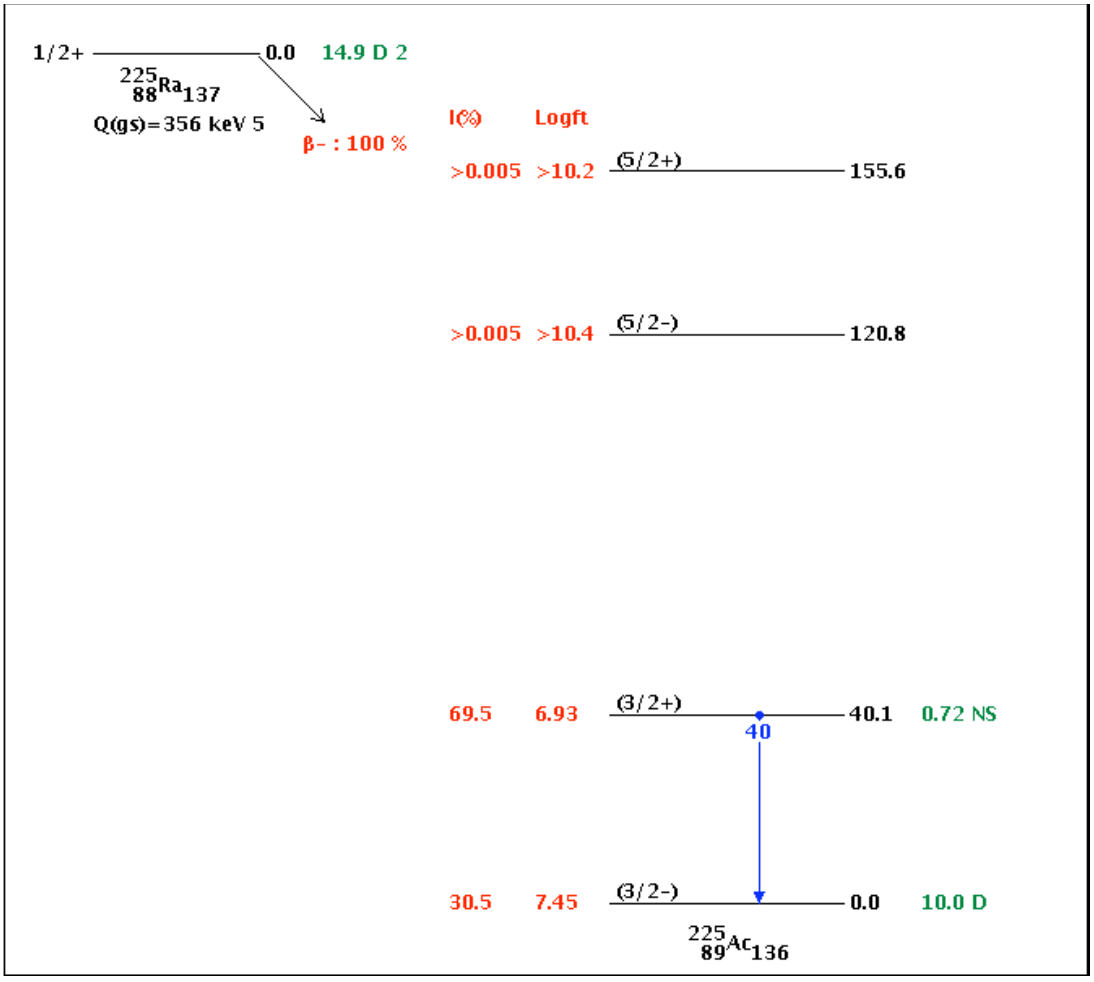

FIG. 4.9: Decay scheme of $^{225}_{88}$Ra. It β^--decay to 100 % into $^{225}_{89}$Ac. The intensity of the characteristic γ-rays at 40 keV following this decay is 30 % [66].

Next we consider how much of the radium can diffuse out of the oven when the source is heated. The fraction of particles implanted at depth a and which leave the material is

$$\frac{N_{out}}{N_{in}} = exp\left(-\frac{a}{\sqrt{D\tau}}\right), \tag{4.4}$$

where N_{in} is the number of atoms entering, N_{out} is the number of atoms diffusing out, D is the diffusion coefficient, and τ is lifetime of the particle. For particles evenly distributed in a foil of thickness a we have [97]

$$\frac{N_{out}}{N_{in}} = \frac{\sqrt{D\tau}}{a} tanh\left(\frac{a}{\sqrt{D\tau}}\right). \tag{4.5}$$

The time Δt for the diffusion process to take place is of the order

$$\Delta t = a\sqrt{\frac{\tau}{D}} \quad . \tag{4.6}$$

The diffusion coefficient D depends on temperature and target material. There are no data for D available for radium in titanium and thorium for temperature around 1000 K. For an order of magnitude estimate we take known values for radium in titanium and thorium targets, where D is $D_{Ti} = 10^{-13}$ cm^2 s^{-1} and $D_{Th} = 10^{-20}$ cm^2 s^{-1}. This estimate is based on the diffusion of the alkaline earth atom calcium in titanium [100] and the alkaline earth atom radium in tungsten around 1000 K [94]. We assume the fraction of radium that diffuses out of the titanium bulk material is given by Eq. 4.4. The fraction of radium diffusing out of the thin thorium layer is governed by Eq. 4.5. The diffusion time for radium in titanium is about 4×10^3 s and that for radium in thorium is about 1×10^7 s. This is in agreement with the observation that a few percent of the produced radium atoms are released in the effusive beam.

The flux of radium was measured by the deposition of ^{225}Ra on a glass window 70 cm downstream of the oven. For this the characteristic γ-ray spectrum emitted from there has been recorded with a Germanium detector. A spectrum is shown in Fig. 4.11. ^{225}Ra is identified by characteristic emission of a 40.0(1) keV γ-ray photon after its β^--decay (Fig. 4.9). Other characteristic gamma energies of products in the decay chain of ^{225}Ra were also observed.

At temperature 900 K of the crucible the accumulated ^{225}Ra atoms leave the oven in about 1000 s and provide a beam of 10^6 atoms per second in an angular divergence of 100 mrad. This beam is sufficient for spectroscopy and optical detection of the 7s^2 ^{1}S$_0$ - 7s7p ^{1}P$_1$ and the 7s^2 ^{1}S$_0$ - 7s7p ^{3}P$_1$ transitions in atomic ^{225}Ra (see Chapter 6).

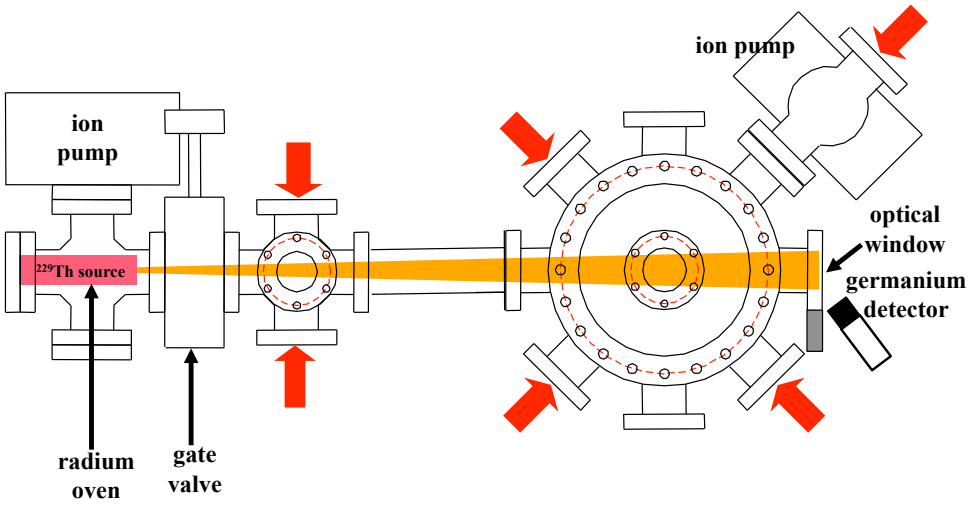

FIG. 4.10: Vacuum chamber for laser cooling and trapping of ^{225}Ra. The germanium detector is situated in order to only detect γ-rays which originate from the surface of the optical window. The measurement of the rate of 40 keV γ is used to determine the flux of ^{225}Ra atoms from the oven.

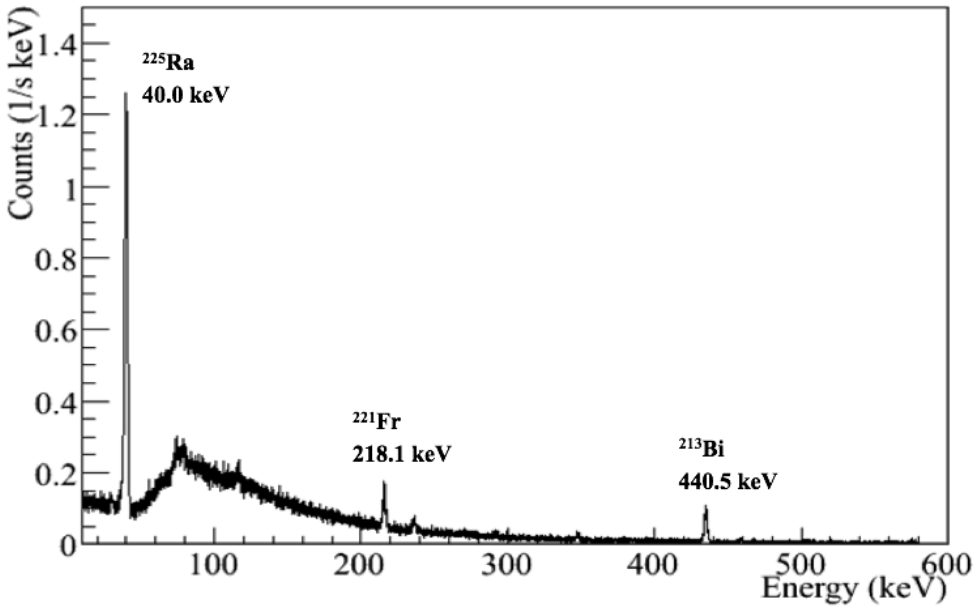

FIG. 4.11: Energy spectrum of γ-rays originating from atoms in the beam emerging from the radium oven. The spectrum is measured by a high resolution Germanium detector. ^{225}Ra is identified by the characteristic γ-ray peak at 40 keV. The peak at 218.1 keV arises from the decay of ^{221}Fr. The halflife of ^{221}Fr is 286 s and the vapor pressure is $\sim 10^3$ mbar at the oven temperature 900 K. The peak at 440.5 keV arises from the decay of ^{213}Bi.

4.3 Conversion of Ion to Atom

Short-lived isotopes of radioactive elements are typically produced as ion beams at the online isotope production facilities. In order to produce atomic beams these ions need to be neutralized. In the following a model and the experimental realization of an ion-to-atom converter is presented. This device was tested at KVI but it can be implemented in any radioactive ion beam facility. Furthermore it is a general setup which can be applied to many different isotopes. The concept exploits the advantages of ion beam manipulation and the well proven design of effusive atomic beams.

The time scale for neutralization and effusion from such a device is of crucial importance for short lived radioactive isotopes. Thus we will discuss the relevant parameters in the following. We have used the radioactive beams provided at KVI for the determination of efficiencies.

4.3.1 Characteristics of Effusive Beam

At a gas pressure of 10^{-4} atm at room temperature, the mean free path of an atom is of order 1 mm. The pressure region where the mean free path of atoms is much larger than the dimension of the apparatus is called the Knudsen region [101]. We estimated the beam characteristics for a container with a small tube as an exit pass (Fig. 4.12). The parameters used for this estimate are introduced below.

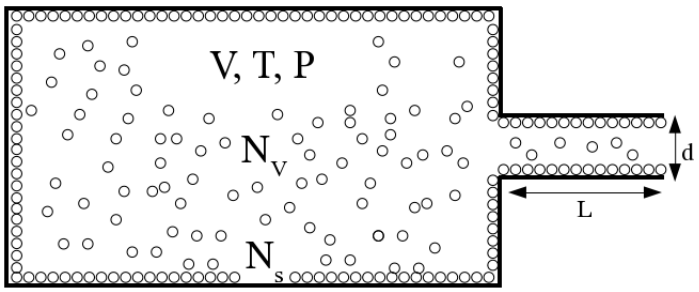

Fig. 4.12: Conceptual model of an effusive atomic beam. Vapor pressure of the element is a crucial parameter for designing such an oven.

The number of density n at a gas pressure P and at a temperature T is

$$n = \frac{P}{k_B T} = \frac{N_V}{V} \ , \tag{4.7}$$

where k_B is the Boltzmann constant and N_V is the number of atoms in a container of volume V. With the number of atoms on the inner surface of the container N_s,

the total number of atoms inside the container is

$$N = N_V + N_s. \tag{4.8}$$

The characteristic time scale for the atoms inside the container before effusing out through the exit tube can then be written as

$$\tau_{res} = \frac{N}{\Phi}. \tag{4.9}$$

For a density n of atoms inside such a container the flux of atoms through a tube of conductance S is

$$\Phi = nS \ . \tag{4.10}$$

The conductance for a hole of area A is

$$S_{hole} = \frac{1}{4} A v_{ave} \ , \tag{4.11}$$

whereas for a tube of length L and diameter d the conductance is

$$S_{tube} = \frac{2k_B T d^3}{3 M v_{ave} L} \ . \tag{4.12}$$

Here, M is the mass and v_{ave} is the average velocity.

The number of atoms N_V in the volume of the container is proportional to the time τ_V during which the atoms are in gas phase. The number of atoms N_s at the surface of the container is proportional to the sticking time (τ_s) of the atoms to the surface of the container. The atoms get stuck to the surface of the container by the physisorption or chemisorption interactions. At high temperatures (T>1000 K) the physisorption or chemisorption bonding of atoms to the surface breaks.

Physisorption interactions arise from the intermolecular forces between the particle and the metal surface, which is similar to van der Waals forces. An atom is physisorbed to the metal surface mainly because of its geometrical alignment with the metal surface. This process does not produce significant changes in the electronic structure of the interacting species. Physisorption plays an important role as a precursor of the chemisorption interactions.

Chemisorption interactions arise essentially from the chemical reactions of the atom with the metal surface. These reactions cause the formation of a chemical compound. As a consequence atoms are bonded to that chemical potential barrier. The strength of this potential barrier is determined by the interaction energy of the species and the relative distance between them at equilibrium.

The Hamiltonian for the interaction of an atom with a metal surface is

$$H_{atom-metal} = H_A + H_M + H_{em} + H_{SR} + H_{VW} \ , \tag{4.13}$$

where H_A and H_M are the Hamiltonians of the isolated atom and the metal. H_{em} is the Hamiltonian of the vacuum quantized electromagnetic field, H_{SR} represents the Hamiltonian which arises from the short-range interaction between the atom and metal and H_{VW} is the Hamiltonian of the interactions between all the particles involved in the atom-metal interaction phenomena and quantized by the long-wave-length electromagnetic field i.e., the Van der Walls interaction [102].

The sticking time τ_s for an atom adsorbed on a surface at temperature T is given by

$$\tau_s = \tau_0 \exp\left(\frac{H_{at}}{RT}\right) \ , \tag{4.14}$$

where H_{at} is the enthalpy of atomization, R is the universal gas constant and τ_0 is the period of vibration of the bond between the adsorbed atom and the surface material [103]. There are no experimental data on sticking time and for τ_0 available for radium on titanium or tungsten surfaces. For an order of magnitude estimate we take $\tau_0 \sim 10^{-9}$ s based on the known values for barium atom on tungsten surfaces [104, 105]. H_{at} is estimated to 159 kJ/mol for radium and 182 kJ/mol for barium [106].

The characteristics time scale for effusion, τ_{res} is defined as the sum of the time spend in the volume τ_V between two successive collisions with walls and the sticking time τ_s of the atom at the wall surface [92]

$$\tau_{res} = \chi(\tau_V + \tau_s) \ . \tag{4.15}$$

Here χ is the mean number of collisions before leaving the exit aperture of the oven.

^{225}Ra Crucible at KVI

A measurement of the time the atomic beam needs to leave the existing ^{225}Ra oven is used to estimate the sticking time τ_s of radium on a mixed surface of titanium, thorium and other elements, e.g. barium, zirconium. Total number of ^{225}Ra atoms N inside the crucible is 10^{11} and the operating temperature is around 900 K. The mean number of collisions of the radium atoms inside the crucible before leaving the exit aperture is estimated to $\chi \approx 500$. An estimate for the residence time τ_{res} for a set of parameters is given in Table. 4.2.

Geometry of the container	Fraction of atoms in the volume (N_V/N)	Volume of container (V) [m^3]	Density of atoms (n) [atoms/m^3]	Conductance (S) [m^3/s]	Residence time of the atoms in the container (τ_{res}) [s]	Time spend in the volume (τ_V) [s]	Sticking time at surface (τ_s) [s]
^{225}Ra crucible	10^{-5}	10^{-7}	10^{13}	10^{-5}	10^{3}	10^{-5}	2
TI cavity	0.96	10^{-5}	10^{10}	10^{-4}	0.04	10^{-5}	10^{-5}

Table 4.2: Parameters for estimating τ_{res} for the ^{225}Ra crucible and the thermal ionizer (TI) cavity at KVI.

Diameter of entrance hole (d_{hole}) [mm]	diameter of exit hole (d_{tube}) [mm]	Length of tube (L) [mm]	Temperature (T) [K]	Conductance entrance hole (S_{hole}) [m^3/s]	Conductance of exit hole (S_{tube}) [m^3/s]	Probability of exit of atoms through exit hole [%]	Divergence of atomic beam (θ) [degree]
1.6	4	10	900-2000	10^{-4}	5×10^{-4}	77	±22
1.6	4	20	900-2000	10^{-4}	10^{-4}	63	±11
1.6	6	20	900-2000	10^{-4}	10^{-3}	85	±17
1.6	8	20	900-2000	10^{-4}	2×10^{-3}	93	±22

Table 4.3: Parameters for estimating τ_{res} for TI like cavity after the ion optics lens for ^{213}Ra. Performance characteristics for different aspect ratios of the geometry.

At the Thermal Ionizer Cavity

A measurement of the diffusion time out of the thermal ionizer provides further data for radium on sticking to and diffusion on W surfaces [97]. The length of the cavity is 25 mm and the diameter is 30 mm. The cavity has an entrance window of thickness 62 μm and an exit tube of 2 mm diameter and 2 mm length. For the estimate we assume that there are no stopping foils inside the TI. The total number of atoms N inside the TI is 10^5 and the operating temperature of the TI is about 2500 K. Mean number of collisions χ is estimated to 2000. An estimate of τ_{res} at the TI cavity is given in Table. 4.2.

Conclusion

The main temperature dependent parameter which determines the residence time of radium inside a thermal oven is the average sticking time τ_s of the radium atoms to the W cavity surface walls. The estimates extracted from the existing ^{225}Ra oven and thermal ionizer cavity at KVI indicate that this time is 2 s at 900 K and 10^{-5} s at 2500 K. Thus an ion-to-atom converter should operate at temperatures around 900 - 1200 K for ^{213}Ra ($T_{1/2}$ = 2.73 min).

4.3.2 Release of Radium from a Zirconium Foil

The adsorption of gas molecules and atoms on metal surfaces is one of the most relevant phenomena in the interaction of gas particles with metal surfaces. The understanding of the physical and chemical reactions between the particles and the metal surfaces play an important role in the control of parameters governing such interactions. We use the short lived radium isotopes from the TRIμP facility to study the capture and release of radium from hot metal foils. We have chosen zirconium because of the low work function (4.05 eV), the mechanical properties and the high melting point of 2100 K. This material was also used for neutralization and release os sodium. In these studies release fraction of $\simeq$ 40 % at temperature of 1080 K and release times shorter than 0.1 s have been observed [107]. Further release studies have been published for alkali atoms from several different materials (V, Fe, Ni, Y, Zr, Nb, Mo, Hf, Ta, W, Re, C, and Pt) [108]. No information on alkaline earth elements can be found in literature.

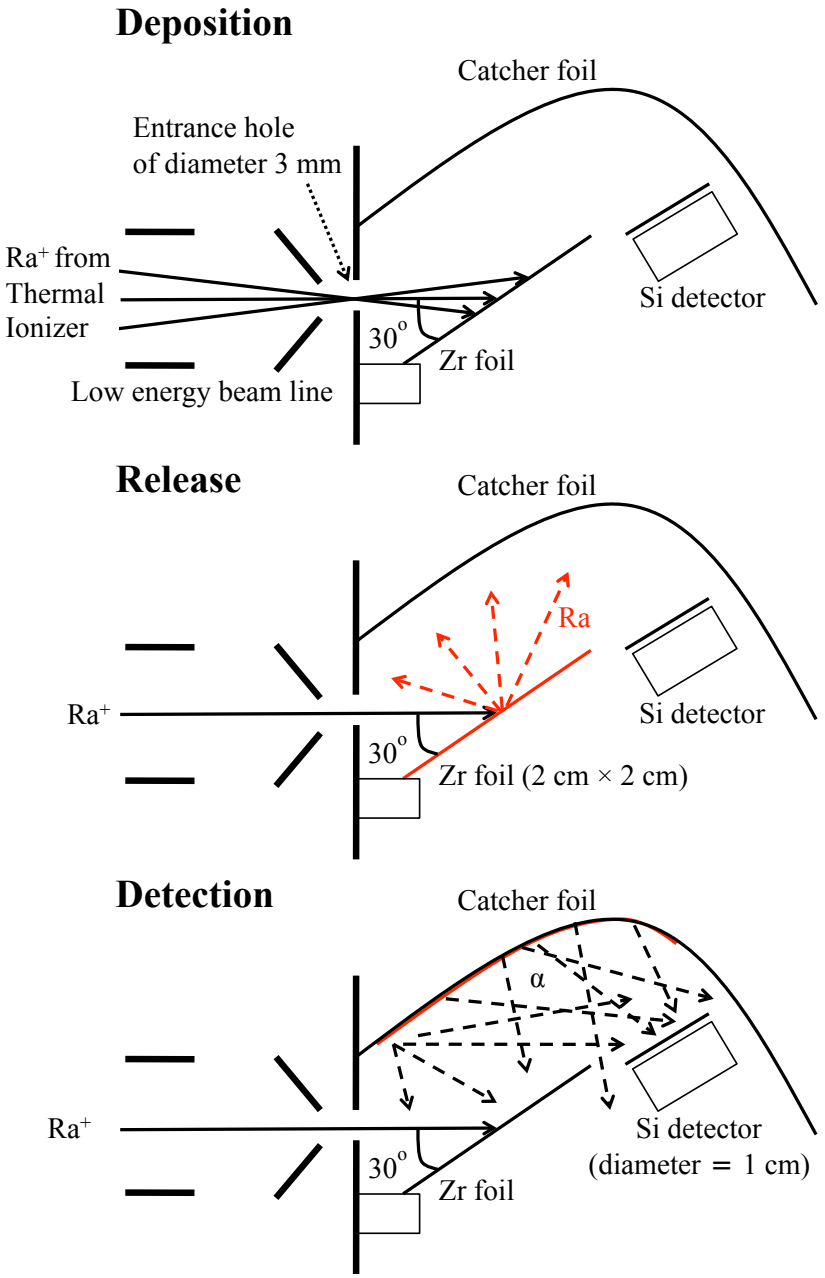

Fig. 4.13: Schematic view of the sequence for measuring the capture and release of radium from a zirconium foil as a function of temperature. Deposition: radium is accumulated from the thermal ionizer on the cold zirconium foil for an interval t_a. Release: Immediately after accumulation the zirconium foil is heated for a short time interval δt_h. During δt_h a fraction of the accumulated Ra atoms emerges from the zirconium foil and spreads over 2π solid angle. A fraction of the atoms end up at the surface of the catcher foil. Detection: The radium atoms which reside on the catcher foil emit α particles in their nuclear decay. The α-particles which are emitted into the detection solid angle of the Si detector are detected.

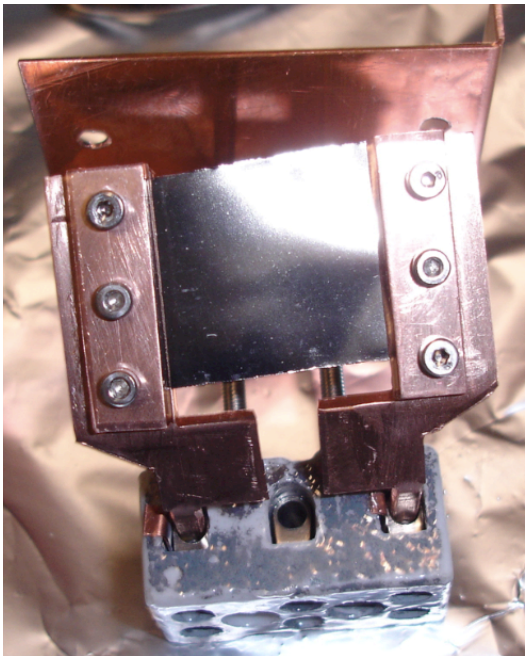

FIG. 4.14: Zr foil mounted on a copper support frame. The size of the foil is ~ 2 cm $\times$ 2 cm. The radium ion-beam is projected on this foil. The release of radium is measured by heating the foil for a short time interval. A fraction of the released radium resides on the surface of a catcher foil (not shown here). A fraction of the α-particles emitted from the radium atoms are detected by a Si detector. The foil can be electrically biased to prevent the escape of charged particles.

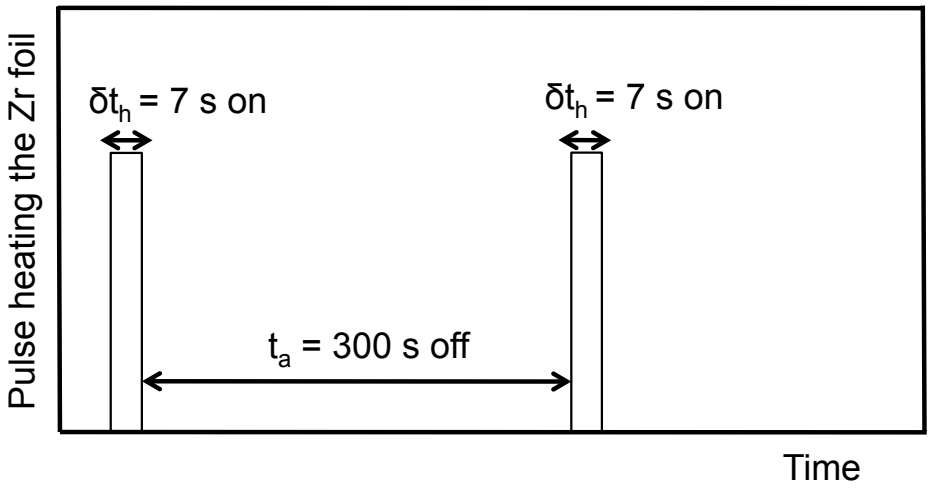

FIG. 4.15: Heating sequence of the Zr foil. radium is accumulated for $t_a = 300$ s. Then the foil is resistively heated for $\delta t_h = 7$ s.

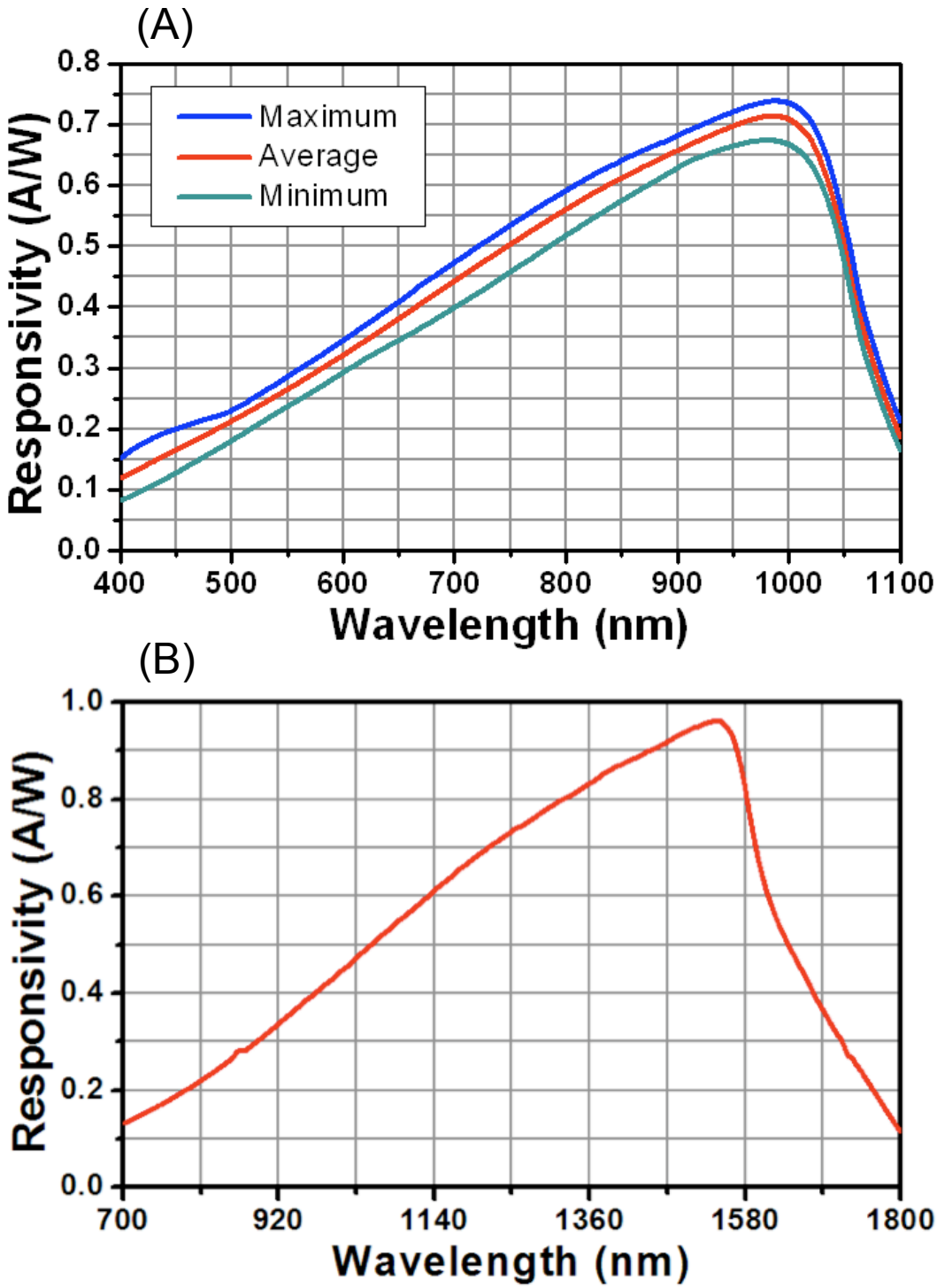

Fig. 4.16: Responsivity of (A) the FDS1010 Silicon photodiode and (B) the FDG Germanium photodiode (from [109]). The different wavelength dependence in the response to light permits the determination of the temperature of a blackbody radiator.

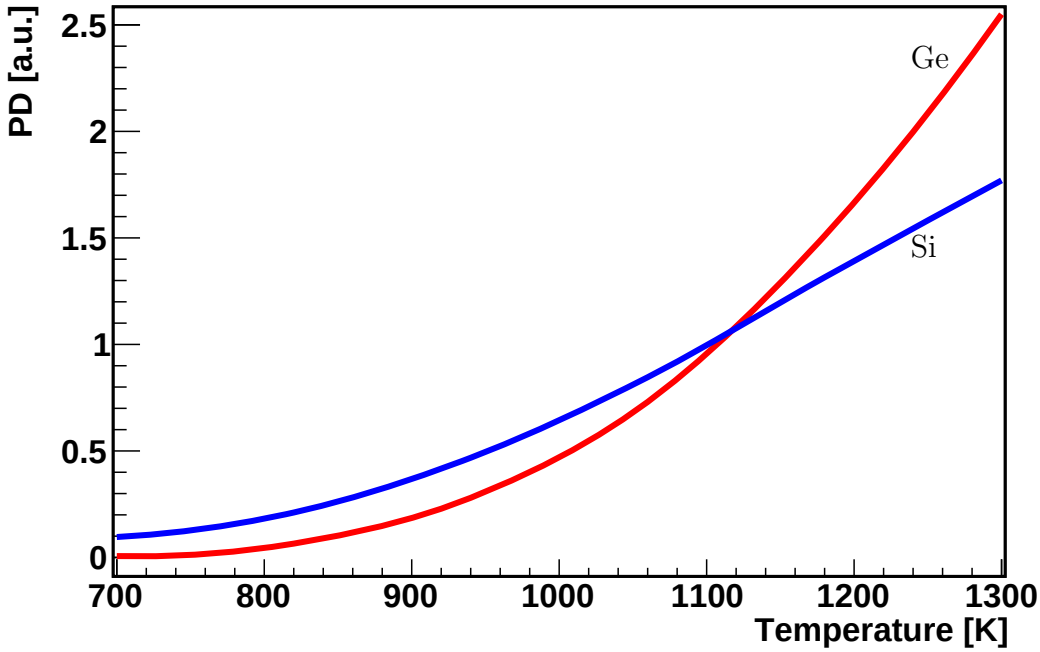

FIG. 4.17: Measurement of temperature of the zirconium foil by exploiting the difference in response of a germanium and a silicon photodiode to the blackbody radiation from the heated zirconium foil.

The singly charged Ra^+ are electrostatically extracted from the thermal ionizer. A transport system consisting out of an electrostatic lens, a Wien filter for mass selection and another lens for focussing permits an efficient capturing of the ions through a small aperture. The setup was designed for the injection of ions into a gas filled radio-frequency quadrupole which is used as a cooler and buncher in another experiment at the TRIμP facility [92,93] The geometry of the setup for measuring release of neutral radium from zirconium surface (Fig. 4.13) is designed such that all Ra^+ ions which are focussed through the entrance hole for ions end up on the zirconium foil. The size of the zirconium foil is $\sim$ 2 cm $\times$ 2 cm. It is placed at an angle of 30^o at 2 cm from the entrance hole for ions. The amount of radium is determined by the activity which is recorded on the silicon detector. It is very small when the foil is not heated. The silicon detector has an area of 150 mm^2 and was protected against the light from the heated zirconium foil by a 1.8 μm thin aluminum foil.

The Zirconuim foil is resistively heated by currents of up to 22 A which correspond to a temperature of 1300(50) K. The voltage across the foil is $\sim$ 3.5 V. The temperature is monitored by the emitted light from the hot foil. We employ two photodiodes, one Silicon and one Germanium diodes each of which cover dif-

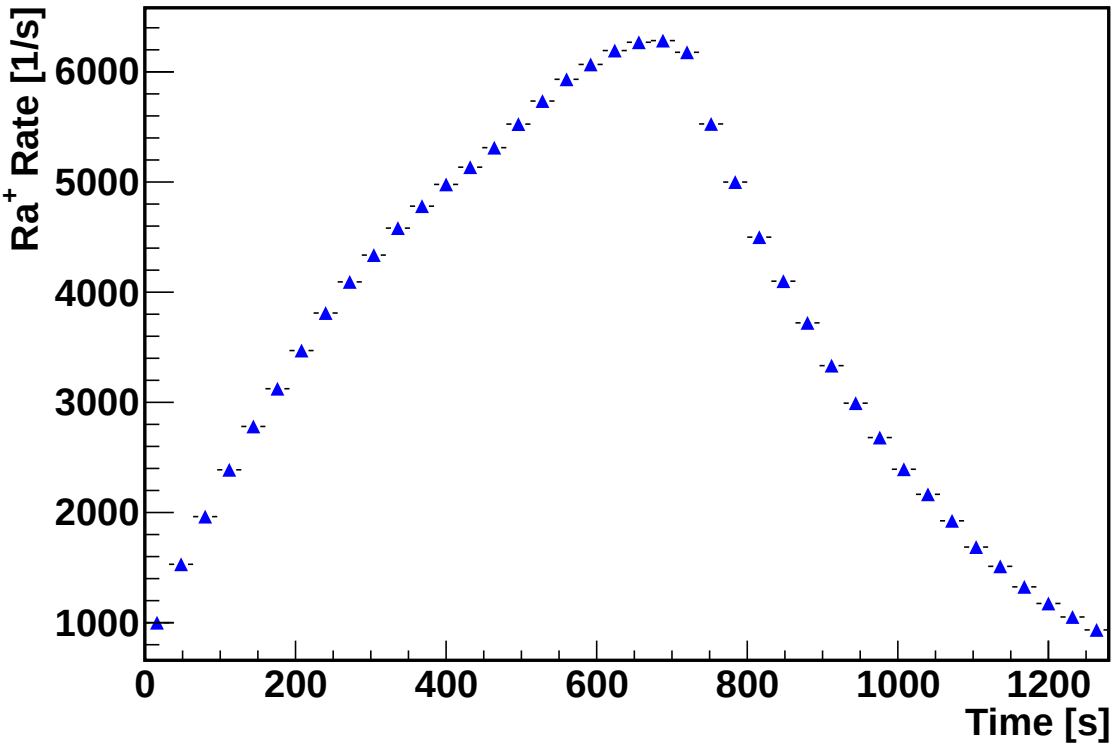

Fig. 4.18: Activity of $^{213}Ra^{+}$ measured on a Silicon detector in front of the entrance of the ion-to-atom converter. This measurement is used as the incoming flux for the determination of the efficiency of the conversion.

ferent wavelength ranges as shown in Fig. 4.16. The photodiodes integrate over a different part of the spectrum of black body radiation and their scaling with temperature is different. From these measurements we estimate the temperature of the foil with an uncertainty of $\simeq$ 100 K.

The release of radium from a zirconium foil is measured at different temperatures of the Zirconium foil (Fig. 4.21). The sequence of the different steps in the measurement is shown in Fig. 4.13. The low-energy Ra^{+} ion beam is projected to the Zirconium foil. The accumulation of radium is followed by an electric heating pulse to the Zirconium foil. Released fraction of neutral radium atoms from the zirconium foil is measured by detecting the α-particles from the radium seating on the surface of a catcher foil (Fig. 4.20). The released fraction of radium from the zirconium foil can be quantified as

$$R_{Si} = \Omega_{total} \cdot N_{Ra} \ , \tag{4.16}$$

where R_{Si} is the count rate seen by the silicon detector and Ω_{total} is the total

solid angle due to the geometry of the setup.

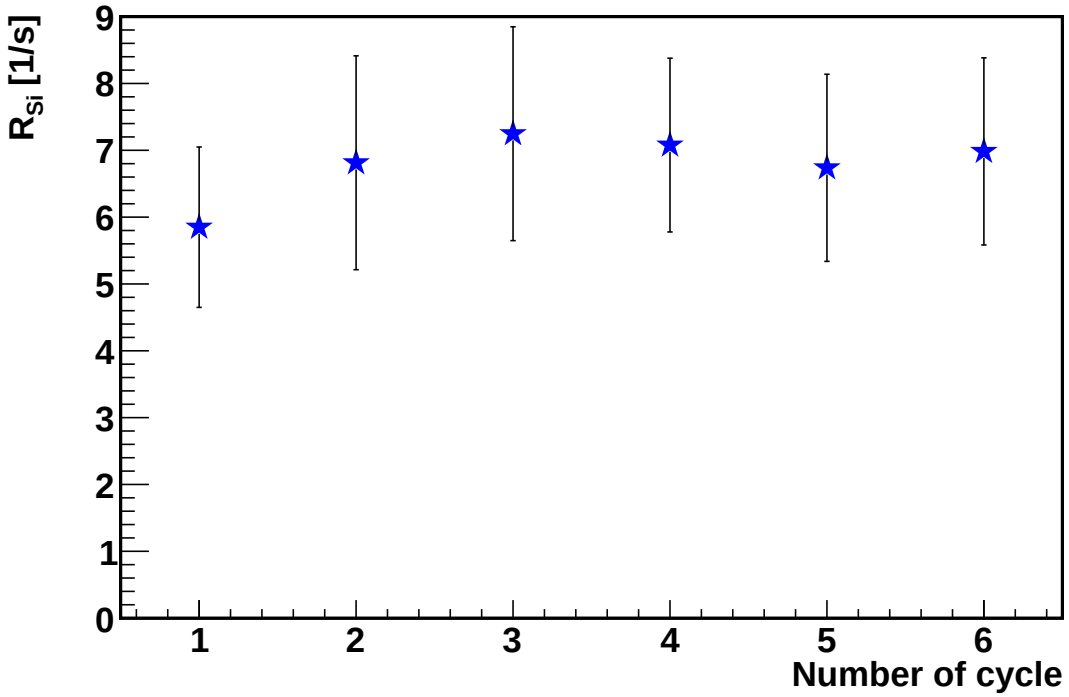

FIG. 4.19: Rate of neutral radium measured with a Silicon detector for six consecutive accumulation and release cycle. Each cycle consists of deposition of Ra^+ on the zirconium foil for 300 s followed by a 7 s heating pulse to the zirconium foil which desorbs out neutralized radium from the zirconium foil. The measurement started with an zirconium foil without radioactive material on it. The heating pulse causes the release of a fraction f_{rel} from the foil. This factor (1-f_{rel}) remaining on the foil contributes to the release in following cycle. The small increase of cycle 2 indicates that a large fraction has been released. As the number of events increases the residue of Ra on the Zr foil increases. At one point the amount of residual Ra reaches equilibrium. Therefore the Silicon detector reads a stable count rate after first few events.

The solid angle Ω_{total} can be split into two parts. First, the release of radium from the zirconium foil which distributes the atoms on the catcher foil. Second, the fraction of α-decays which are detected by the Silicon detector.

The probability for the released radium atoms to be detected is $\Omega_{total} = 2(1)\cdot 10^{-3}$. The highest yield of radium atom detected is $R_{Si} = 7(2)$ s^{-1}. Behind the thermal ionizer we had of 6000(80) s^{-1} ions. This yields a total neutralization

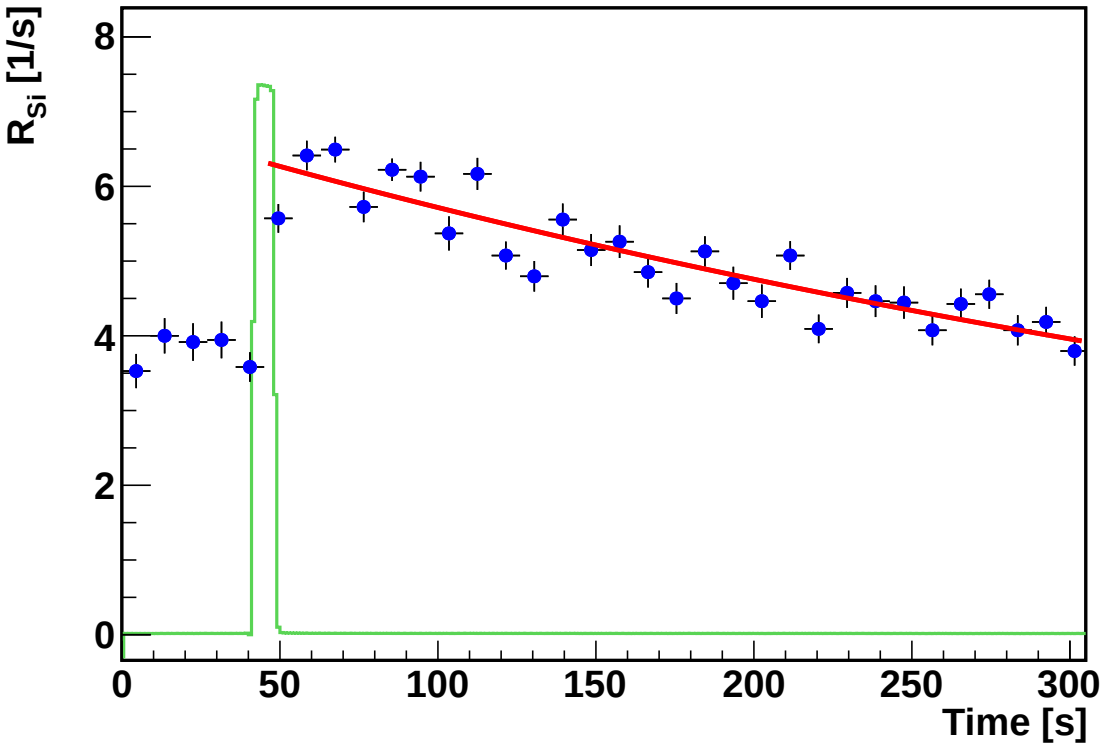

FIG. 4.20: Release of radium from the Zr foil measured by the Si detector. The green line represents the heating pulse for the Zr foil for a time interval δt_h of 7 s. Accumulation time t_a is 300 s. Six individual measurements have been averaged over the heating on/off cycle. The red line is a fit through the data points. The fit function $R_{Si}(t)=A+Be^{-t/\tau}$ is an exponential plus a polynomial of degree 0. The fit yields a halflifetime of 175 (70) s which confirms ^{213}Ra as the observed decaying isotope.

Conclusion

Radium isotopes are available at radioactive beam facilities typically in beams of several keV ions. The longer lived isotopes can also be extracted from radioactive sources. Radium EDM experiments require the availability of atomic radium at low enough energies for laser cooling and trapping. This can be provided by effusive atomic beams. Here the design of such devices for offline available radium from sources and online available short lived isotopes are described. A first offline radium atomic beam is operated successfully at KVI. The design can be scaled upto higher intensities if larger sources of ^{229}Th are used. Also we demonstrate the concept of an ion-to-atom converter which can be operated at radioactive ion beam facilities like ISOLDE at CERN, Geneva, CH.

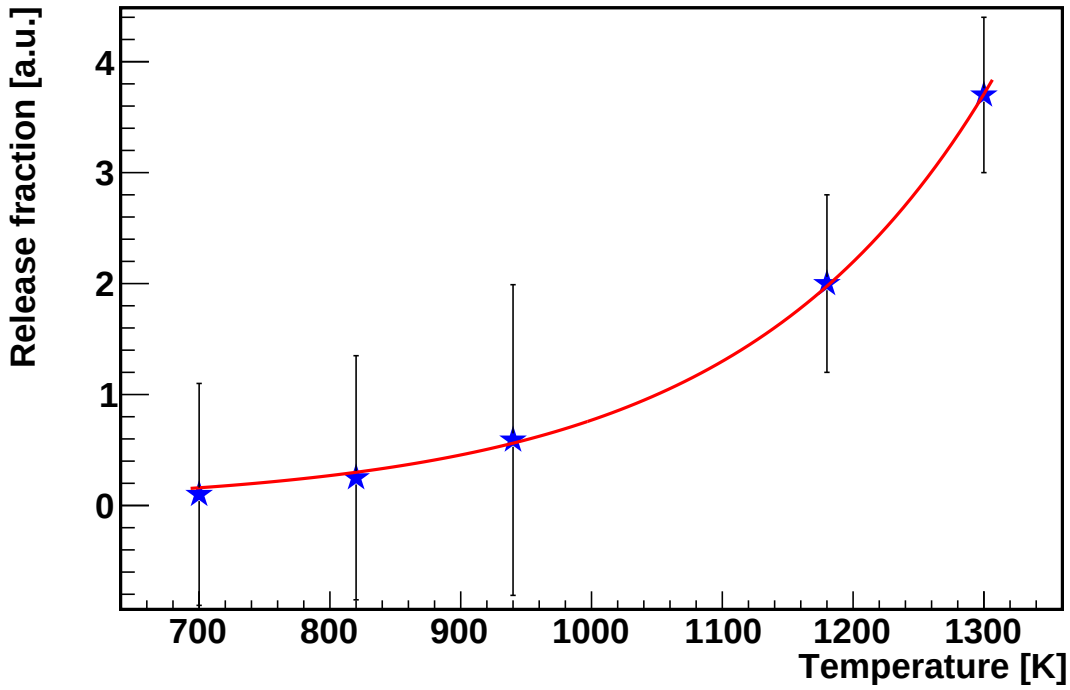

FIG. 4.21: The temperature dependence of the release of neutral radium from a zirconium foil. α-particles from the decay of radium atoms at the catcher foil are detected by a Silicon detector. The red line fitted through the measured data points shows exponential ($e^{-E/T}$) behavior of the release fraction of radium from the Zr foil as a function of temperature.

4.3.3 The Ion to Atom Converter

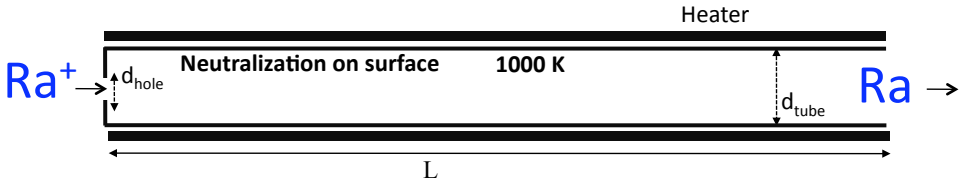

Fig. 4.22: Conceptual drawing of the ion-to-atom converter built at KVI. Ions are injected into the converter through a hole of diameter d_{hole}. After neutralization at the surface of the converter a large fraction of the atoms leaves through the exit hole of diameter d_{tube}.

The geometry of the device is an important aspect. The working principle of the ion-to-atom converter developed at KVI is shown in Fig. 4.22. The central part of the device is a zirconium tube of diameter d_{tube} = 4.55 mm and length L = 100 mm. One end of the tube is closed with a zirconium disc which has a hole of diameter d_{hole} = 1.6 mm at the centre. The low energy ion beam is injected into the converter through this hole. The zirconium tube is surrounded by tantalum wire for resistive heating of the tube. A detail geometric view of the ion-to-atom converter is shown in Fig. 4.24 and Fig. 4.25. The source of radium for the converter is a low energy ($\sim$ 150 eV) ion beam from TRIμP thermal ionizer. Fig 4.23 shows the direction of trajectory of the injected ions inside the ion-to-atom converter. For the geometry mentioned above, more than 90 % of the injected ions are deposited and neutralized at the inner surface of the zirconium tube. As the conductance of the atoms through d_{tube} is much larger than the conduction through d_{hole}, a large fraction of neutralized atoms effuse out through d_{tube}. This provides an atomic beam with thermal velocity distribution. An estimate of the probability of exit of atoms through d_{tube} for several set of geometry of the ion-to-atom converter is presented in Table. 4.3. An estimate of the residence time of the neutralized atoms inside the Zirconium tube for different temperatures is given in Table 4.4. The calibration of the temperature of the ion-to-atom converter is shown in Fig. 4.26.

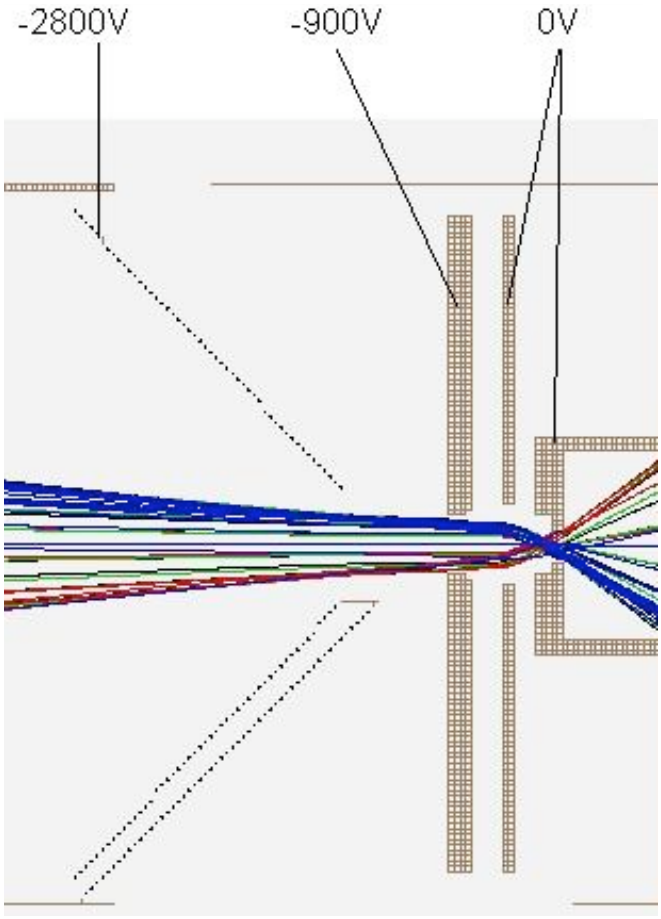

FIG. 4.23: A low energy ion beam from TRIμP thermal ionizer is injected into the ion-to-atom converter by a set of focussing electrodes. The direction of the trajectories of the injected ions inside the ion-to-atom converter is shown. These simulations were performed with SIMION code [110].

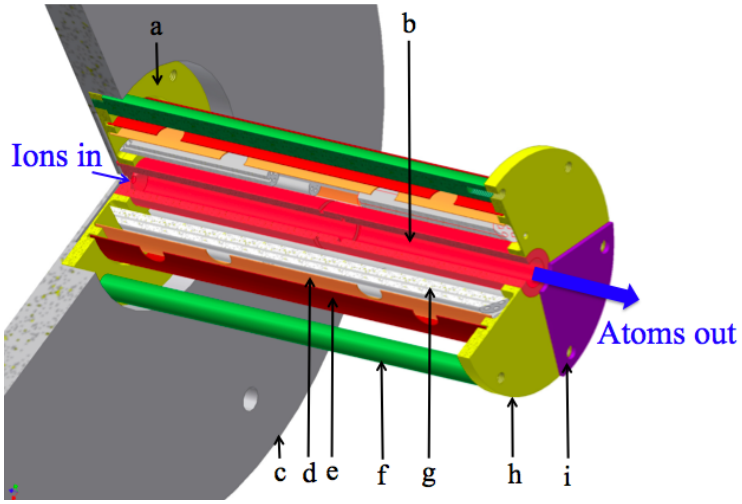

Fig. 4.24: Schematic view of the ion-to-atom converter: (a) holding flange; (b) converter tube of length 100 mm; (c) flange for mounting the device in beam-line; (d) inner heat shield; (e) outer heat shield; (f) holding rod; (g) heater element; (h) front holding flange; (i) spring load to keep the converter tube in place. The Ions are injected through an injection hole of diameter 1.6 mm. After neutralization at the inner surface of the converter the atoms leave the converter through an exit hole of diameter 6 mm with a thermal velocity distribution corresponding to the temperature of the converter.

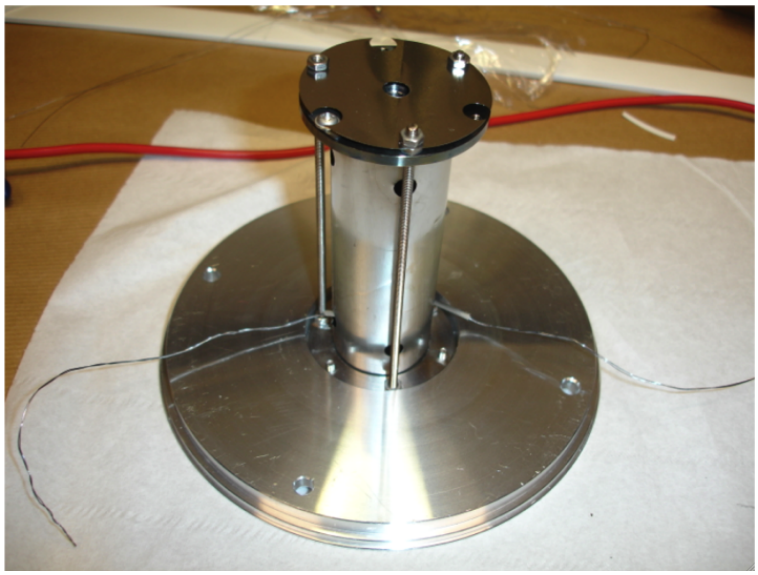

Fig. 4.25: Ion-to-atom converter. A vacuum flange serves for mounting the ion-to-atom converter to the beam-line as well as to the last electrode of the ion-optics, which serves for injecting the ions from the low energy beam-line into the converter.

Temperature (T) [K]	Average velocity of the atoms (V_{ave}) [m/s]	Time spend in the volume (τ_V) [s]	Sticking time at surface (τ_s) [s]	Fraction of atoms in the volume (N_V/N)	Residence time of the atoms in the container [τ_{res}] (s)
900	270	10^{-4}	2	10^{-4}	424
1200	310	9×10^{-5}	10^{-2}	10^{-2}	2
1500	350	8×10^{-5}	4×10^{-4}	10^{-1}	0.1
2000	400	7×10^{-5}	10^{-5}	10^{-1}	0.02

Table 4.4: Parameters for estimating τ_{res} for the TI like cavity with exit tube diameter of 6 mm after ion optics lens for ^{213}Ra. Volume (V) of the cavity is 10^{-5} m^3.

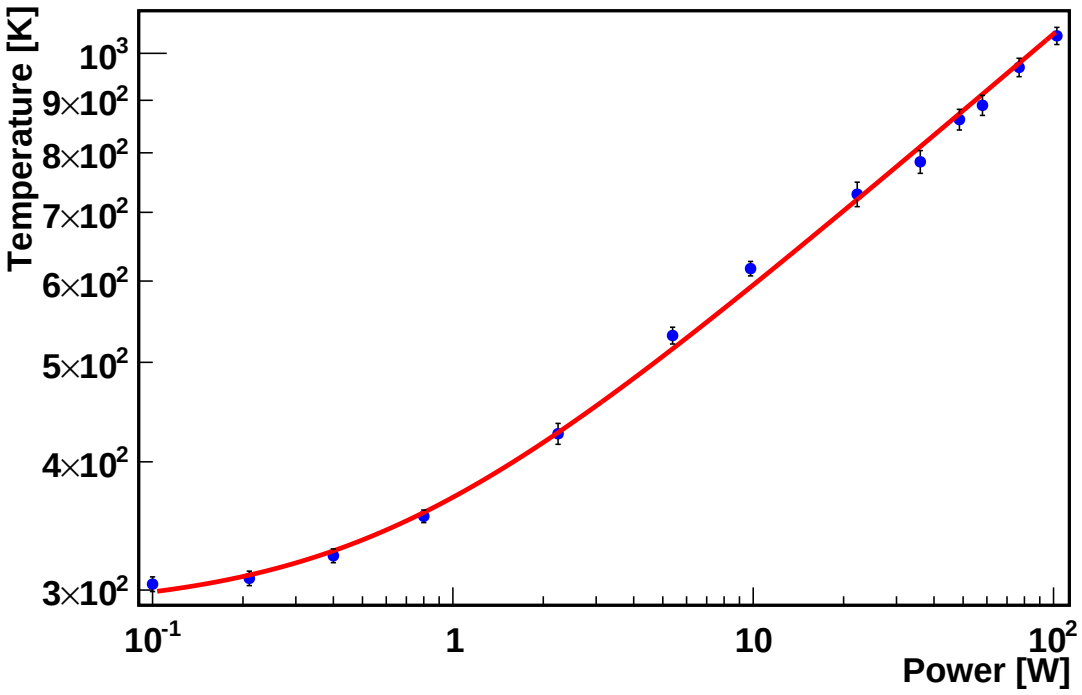

Fig. 4.26: The calibration of the temperature of the ion-to-atom converter was performed with a K-type thermocouple. The solid line is a fit to the data points. The fit line assumes a purely radiatively cooled converter. In this case the dissipated power $P = A \cdot (T^4 - T_0^4)$, where A is a proportionality constant and T_0 is the temperature of the environment.

4.4 Conclusion

We considered an effusive beam of atomic radium for the experimental search for EDMs. Radium is collected from a radioactive source of ^{229}Th inside of the crucible of the oven. The flux of the atomic beam is 10^6 s^{-1}cm^{-2} and is scalable to high fluxes with larger activity of the parent nuclei ^{229}Th. Short lived isotopes of radium require a different approach since they are only available as ion beam at radioactive beam facilities. We have observed the neutralization of radium ions on a zirconium surface and the subsequent release of neutral radium of more than 58(33)% when the zirconium foil is heated. This is exploited in the design of an ion-to-atom converter which can be employed at existing radioactive beam facilities to create intense atomic beams.

Chapter 5

Lasers and Spectroscopy Setup

For the optical spectroscopy of radium atoms a laser system consisting of several diode lasers have been set up. This system included establishing frequency references and also the calibration of optical secondary frequency standards. The reduction of background for the detection of the optical signal requires a precise optical imaging system. For recording of the measurements a data acquisition (DAQ) system was installed and integrated with the experiment and control system. The development of these crucial elements for the EDM experiment and their optimization is described in detail in this chapter.

Laser cooling of radium requires many lasers at different wavelengths. The absolute stability and reproducibility of transition wavelengths is important. Not for all wavelengths a secondary reference line like molecular iodine (I_2) or molecular tellurium (Te_2) can be found. There is a versatile option arises from an optical frequency comb which is available within the TRIμP facility. The frequency comb is shared with other experiments within the TRIμP group. We are in particular interested in the laser light for the main laser cooling transition of radium. Light at wavelength λ_1 is required for exciting the $^1S_0$ - $^1P_1$ transition which offers the strongest laser cooling force for radium atoms. Light at wavelength λ_{IC} is needed to excite the $^1S_0$ - $^3P_1$ transition which can serve as the transition for trapping the radium atoms. Furthermore the main repumping transitions are in the infrared wavelength region. Light at 1428 nm and 1488 nm is required to repump the atoms from the metastable D state to the laser cooling cycle.

5.1 Light at Wavelength λ_1 from a Frequency Doubled Ti:Sapphire Laser

Light at wavelength λ_1 excites the radium atoms from the ground state to the 7s7p $^1P_1$ state. The light is produced by second harmonic generation of infrared light from a Ti:Sapphire laser.

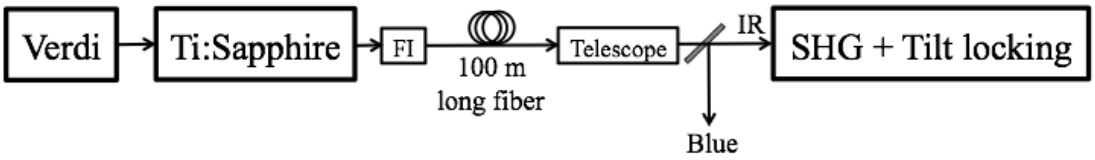

FIG. 5.1: Block diagram showing the steps involved in the production of blue light at wavelength λ_1.

A commercial Ti:Sapphire laser(Coherent MBR-110) provides the infrared light. The Ti:Sapphire crystal is pumped by a diode pumped solid-state laser (Coherent Verdi-V10, 10 W) at 532 nm. The laser is arranged in a bow-tie cavity. The linewidth is specified to be 500 kHz. It can be operated in the wavelength range of 700-1000 nm. For 6 W pump power it delivers 300 mW at 965 nm. The cavity of the laser is continuously flushed with dry nitrogen gas to reduce the water vapor in the beam path, which shows strong absorption lines in this wavelength range. The laser is tuned up to 40 GHz by adjusting the thickness of an etalon.

The laser laboratory where the Ti:Sapphire laser is located is separated by 100 m from the radiation area where the radium atomic beam is accessible. Light from the Ti:Sapphire laser is transported to the experimental hall by a single mode optical fiber. Coherent Brillouin backscattering limits the available power at the end of the optical transport fiber in the radiation area to about 120 mW.

Light at wavelength λ_1 is produced by frequency doubling the infra red light from the Ti:Sapphire laser [111]. Optical non-linear behavior of potassium niobate ($KNbO_3$) is utilized for obtaining the frequency doubling because of its nonlinear coefficients at this wavelength [112, 113]. The crystal is placed in a cavity (Fig. 5.2). Phase matching is critical for an efficient doubling process. Furthermore, the phase matching condition can be achieved not only by the angle of the fundamental light beam with the optical axis of the crystal, but also by temperature [114–116]. In particular efficient phase matching for $KNbO_3$ is achieved by temperature tuning.

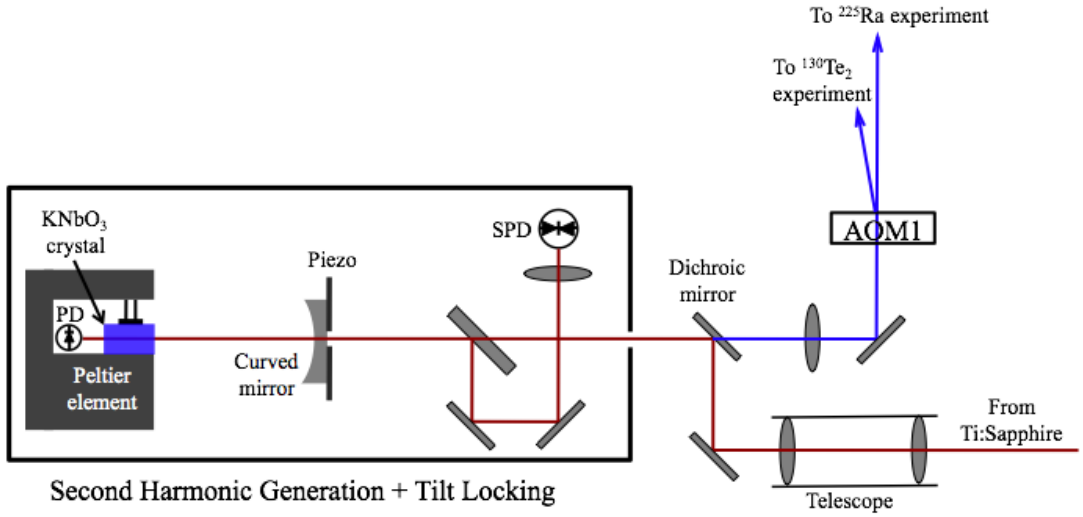

Fig. 5.2: Schematic of the second harmonic generation cavity and tilt locking set-up.

The strong correlation of the index of refractive index with crystal temperature leads to an acceptance of only few mK for the crystal temperature [112,117]. The crystal temperature is controlled by a thermal contact to a Peltier element. A stability of temperature is achieved by a servo loop to a level of a few mK.

The linear doubling cavity consists of a curved mirror and a flat mirror (Fig. 5.2). The flat mirror is realized by a reflective coating for both the fundamental and second harmonic wavelengths at the back end surface of the $KNbO_3$ crystal. The input coupler of the cavity is mounted on a piezo making the cavity length tunable.

The error signal for locking the cavity length corresponding to resonance condition is generated by tilt locking technique [118]. The fundamental laser beam is slightly tilted with respect to the cavity and this tilted beam produces a non-resonant spatial mode in the cavity. The interference between the two spacial modes TEM_{00} and TEM_{01} reflected from the cavity is analysed by splitting of a fraction of the beam and focussing the individual lobes of the TEM_{01} mode on different halves of a split-photodiode.

The difference of the signals from the two parts of the spilt photodiode shows a dispersive shape. The maximum value of the blue laser power corresponds to the zero crossing of the dispersive signal. A servo loop controls the length of the cavity by a piezo actuator and keeps the cavity on on resonance with the incoming light. The servo bandwidth of the system is 5 kHz which ensures stable

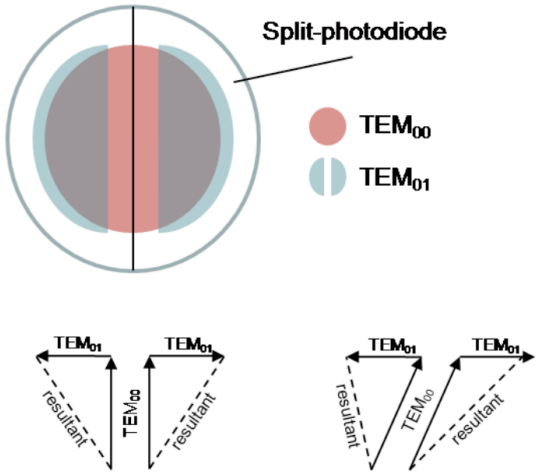

FIG. 5.3: The two spatial modes TEM00 and TEM01 are focussed on the split-photodiode. Individual lobes are falling onto different halves of the photodiode. The bottom part shows the TEM00 mode being tilted, resulting in different size on the separate halves of the photodiode [118].

operation in noisy environments.

The doubling efficiency of the crystal as a function of temperature is shown in Fig. 5.4. A dip in the middle of the efficient doubling range is observed. This is a property of the thickness of the double reflective coating at the end of the crystal. This property causes a mismatch of the IR and blue laser phases [119]. This phase mismatch yield a destructive interference between the second harmonic generation and the reflected blue light. A coating taking care of the phase can be designed in principle. In that case the maximum doubling efficiency can be a factor of two larger [119]. The crystal used in this work was manufactured with a cut at an angle $\theta = 19\ ^o$ by FEE [120]. The phase matching temperature for doubling light at 965 nm is calculated with the program SNLO [121] is 20 ^{o}C. The optimum temperature at the experiment for this crystal at wavelength λ_1 is 13.9 ^{o}C. The difference between these two temperatures could not be resolved.

Typically blue light of more than 20 mW power is produced using 125 mW of infrared light using this setup. We split this light using an AOM and use simultaneously for ^{225}Ra and $^{130}Te_2$ spectroscopy.

Conclusion

Laser light necessary to excite the $7s^2\ ^1S_0$ - $7s7p\ ^1P_1$ transition in the radium atom can be provided by second harmonic generation of a Ti:Sapphire laser beam. The

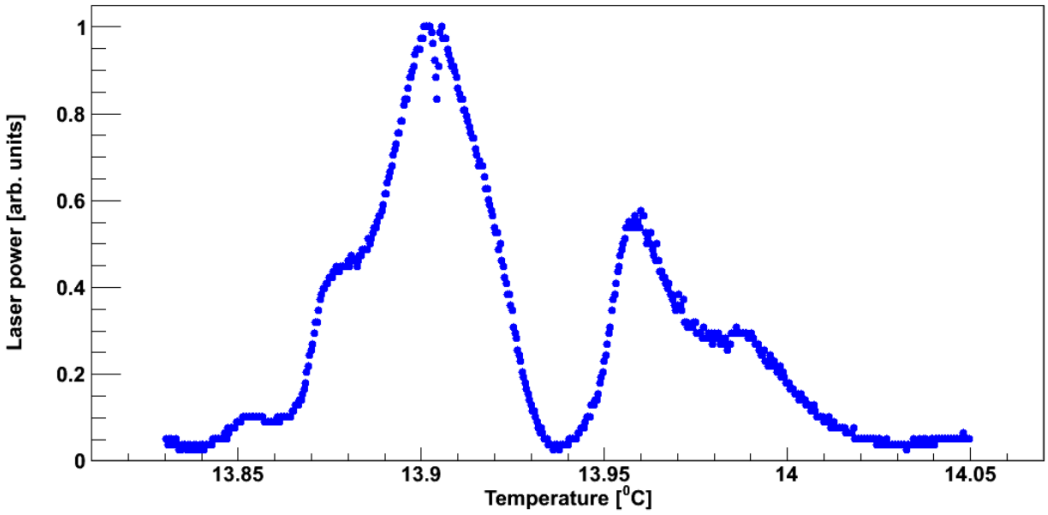

Fig. 5.4: Blue laser power as function of the temperature of the $KNbO_3$ crystal. A dip in the overall is observed at 13.94 ^{o}C. The maximum output power is achieved at 13.9 ^{o}C. This temperature is critical within a few mK. This measurement was obtained by varying slowly the temperature of crystal while monitoring the lock of the second harmonic cavity. The dip at around 13.9 ^{o}C was caused by a brief unlock of the cavity.

laser frequency can be locked to error signal generated by tilt locking technique, which provides a robust stability for the frequency and the power of the light. The achieved scan range covers the necessary full frequency range for all radium isotopes. Temperature tuning of the crystal allows the tuning of the SHG over a range of more than 20 nm for the fundamental wavelength. In particular wavelength of 987 nm can be doubled efficiently at a crystal temperature of 72 ^{o}C providing light for barium ion spectroscopy.

5.2 Diode Lasers

Lasers ranging from visible to infrared wavelengths are required to drive the transitions in atomic radium (Fig. 3.3). Many of the transitions can be accessed with commercially available semiconductor diode lasers. These lasers are convenient for using from economical and operational aspects [122, 123]. The home built diode laser systems with such laser diodes and their frequency stabilizations are described in this section.

The diode lasers for radium atom experiment are build and frequency stabilized in an external cavity diode laser (ECDL) in Littrow configuration by providing frequency selective optical feedback [122, 123]. Laser diodes are possible to operate in a single longitudinal and transverse mode. Within the gain profile the wavelengthnof the emitted light is highly sensitive to optical feedback. This feature is exploited in ECDL configuration where a grating provides frequency selective optical feedback. A schematic drawing of the mechanical set up of a ECDL in Littrow configuration is shown in Fig. 5.5.

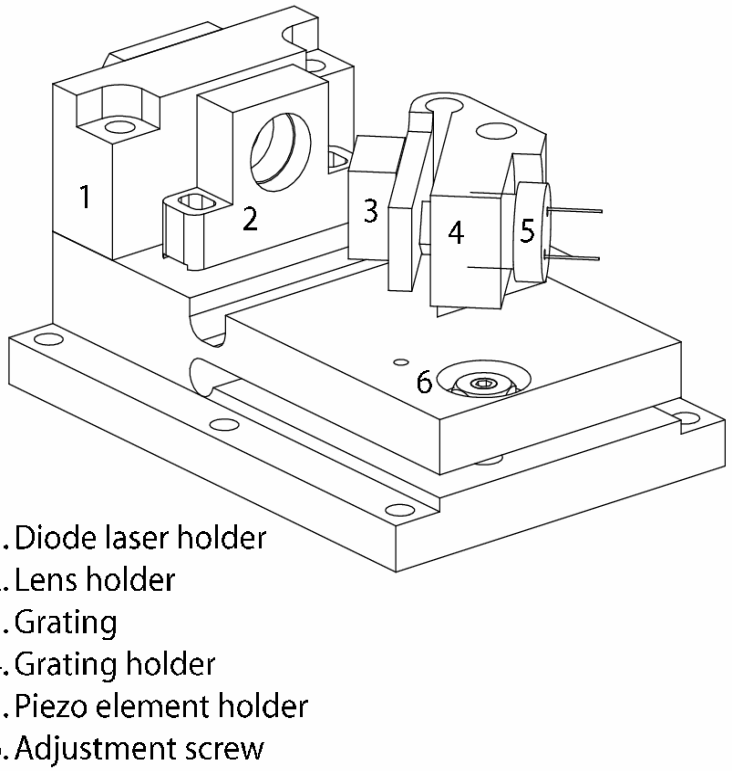

FIG. 5.5: Schematic drawing of the mechanical set up of the External Cavity Diode Laser in Littrow configuration. The design used in this thesis was developed at KVI [63].

The external cavity consists of a diffraction grating which reflects a fraction of the emitted light back into the diode. The grating angle is set in such a way that it can reflect light for a particular wavelength against the direction of the incoming light. This is the concept of frequency stabilization in the Littrow configuration. The angle of diffraction for the grating in the Littrow configuration fulfills the grating equation

$$2d \sin\theta = n\lambda \ , \tag{5.1}$$

where d is the groove spacing which is inversely proportional to the number of grooves per unit length, θ is the angle of incidence, n is the order of diffraction, and λ is the wavelength of the incident light. The 0^{th} order diffraction beam is coupled out of the external resonator cavity and the -1^{st} order diffraction beam is coupled into the laser diode. The fraction of light which is coupled back into the laser diode is around 20% of total emitted light. This defines the choice of the grating in the external cavity. The wavelength which fulfills Eq. 5.1 is reflected back into the diode. The frequency of the emitted light from the laser diode can be tuned By changing the angle θ.

The mechanical setup for the ECDL configuration for the lasers for the experiments in the TRIμP group is shown in Fig. 5.5. The setup consists of holders for the laser diode and the collimation optics and an adjustable mount for the grating. A temperature sensor (AD590) measures the temperature of the diode and a thermoelectric cooling (TEC) element placed under the laser diode acts as a heat sink. The laser diode is placed inside its mount in a way that the polarization axis is aligned vertically. The light beam from the diode is collimated by an aspheric lens.The narrow expansion of the beam is in the vertical direction and direction of the polarization is orientated parallel to the lines in the grating. Fine tuning of the grating angle is executed with the help of two screws, one changes the direction perpendicular to the vertical plane while the other changes the direction perpendicular to the horizontal plane. When the -1^{st} order diffraction beam is coupled back into the laser diode the brightness of the emitted light increases as a result of the initiation of the lasing action. The threshold current of the laser diode for lasing action is decreased due to the optical feedback typically by several mA. The whole mechanical setup is covered with a plastic or metal box which screen the acoustic wave to the diode laser setup. The box also provides an increased temperature stability of the diode laser.

The lasers operated in this configuration in our experiments are stable for several hours. The frequency of such lasers can be scanned continuously over 10

GHz by tuning the operating current together with the PZT voltage.

The diode laser at 714 nm for driving the intercombination line in radium (HL7001MG from Opnext [124]) is set up with a holographic grating (1800 lines/mm from Edmund Optics) with the angle of incidence θ. The diode can provide 50 mW of power at an operation current of 150 mA.

The diode lasers at 1428 nm and 1488 nm are build for performing spectroscopy of the 7s6d $^3D_2$ - 7s7p $^1P_1$ and the 7s6d $^3D_1$ - 7s7p $^1P_1$ transitions in atomic radium. Each of the lasers can provide more than 30 mW of power. We can lock them using a wave length meter.

5.3 Frequency References

The stabilization of the frequency of a number of lasers required for radium trapping demands absolute frequency stabilization over a large part of the optical spectrum. Optical frequency references were identified and implemented in the experimental setup. The state of the art technology of optical frequency combs opens access to optical reference lines over a spectrum ranging from extreme ultraviolet [125, 126] down to the mid infrared [127, 128]. The drawback of such a system is that one has to resolve the ambiguity in frequency measurement within multiples of the frequency comb line spacing or repetition rate (Section 4.4.2). This is in principle possible by performing two measurements where the comb repetition rate difference is larger than the uncertainty of one individual measurement. Another possibility to resolve this issue is the use of secondary frequency references like transitions in atoms or molecules or the use of calibrated wavelength meters. We have employed in this work all the different methods. Secondary references are used to calibrate the wavelength meter and for the unambiguous identification of the comb mode number.

5.3.1 Secondary Frequency References

Widely used secondary frequency references are molecular absorption lines, in particular transitions in iodine and tellurium. Application of saturated absorption spectroscopy techniques provide a reproducibility of the frequencies to a level better than MHz.

High resolution saturated absorption spectroscopy of molecular $^{127}I_2$ hyperfine transitions deliver a natural frequency grid in the 500 nm - 900 nm range. Particular properties like the absence of an intrinsic electric dipole moment lead

to extremely small perturbation by external electromagnetic fields. The many strong transitions with typical linewidth of a few MHz make it an ideal secondary frequency standard. There are more than 60000 iodine lines, which give about one hyperfine multiplet for every 5 GHz. Many of these lines have been calibrated with precisions of better than 1 MHz [129]. Tellurium absorption lines provide precise optical frequency standard for many atomic transition frequencies in the visible wavelength region, especially in the blue part of the spectrum. The absence of hyperfine structure results in a simpler Doppler-free spectrum. The absorption lines are cataloged in the tellurium atlas [130]. Several particular lines have been absolutely calibrated for particular experiments in the past. In particular for Hydrogen and Deuterium 1S - 2S transitions, Positronium and Muonium spectroscopy [131]. It has been reported that several tellurium lines show deviations from the values given in the tellurium atlas of the order of 0.003 cm^{-1} or 100 MHz [132], which makes a careful calibration necessary for relevant reference lines in such experiments. The optical transitions in both molecular references are between some excited rotational and vibrational states. This requires that the vapor of the molecules to be heated to up to 900 K depending on which part of the spectrum is of interest.

Reference for the $^1S_0$ - $^1P_1$ Transition in Atomic Radium

This transition is around 483 nm and was first identified by E. Rasmussen. Although isotope shifts and hyperfine structures were determined with MHz accuracy in online collinear spectroscopy at CERN ISOLDE [72, 73], the absolute frequency was only know to within 1GHz uncertainty. We have chosen to use molecular tellurium as a reference. We employ Doppler-free saturated absorption spectroscopy of molecular tellurium. There are several strong lines in the vicinity of the radium transition. The strongest reference line is at 20715.4777 cm^{-1} which has the label 2004 in the tellurium atlas [130].

The $^{130}Te_2$ is kept in a quartz cell in order to maintain a high temperature. The cell has a diameter of 25 mm and a length of 100 mm. It is placed in a heater element (Watlow, USA) of inner diameter of 50 mm and 150 mm length. A K-type thermocouple is inserted next to the cell to monitor the temperature. The oven is surrounded by glass wool as isolation. The cell can be heated to temperatures up to 900 K with about 100 W of electric heating power.

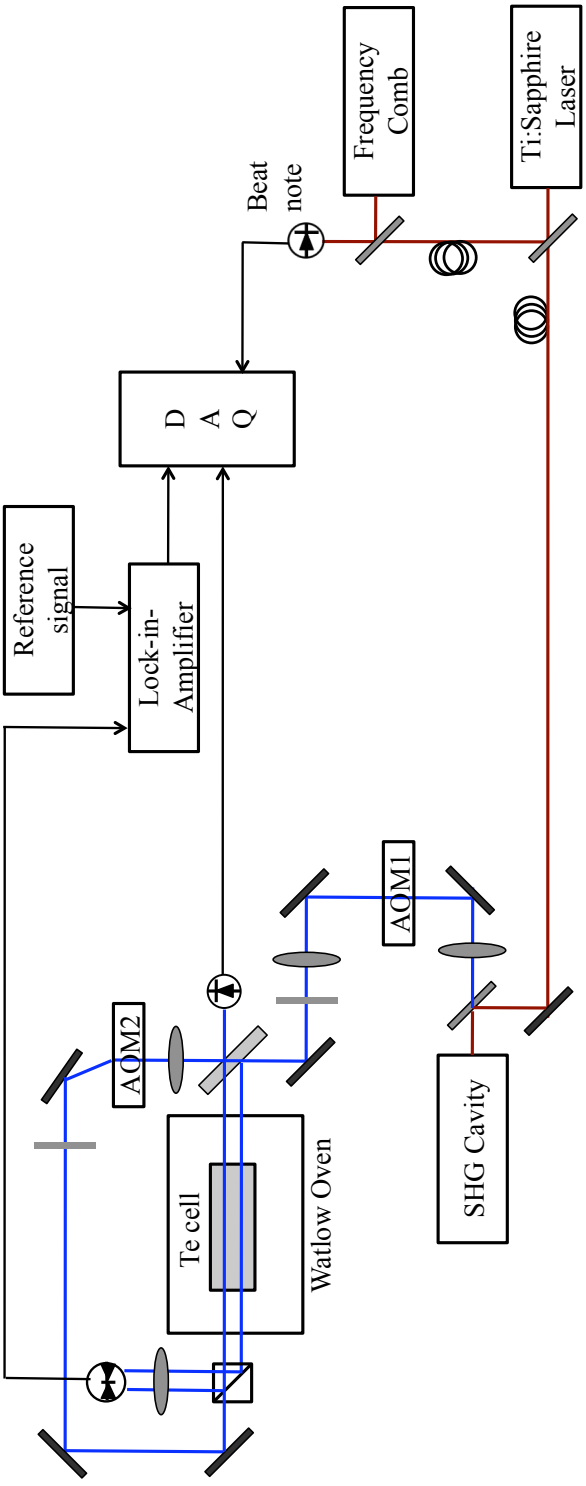

FIG. 5.6: Setup for amplitude modulation saturated absorption spectroscopy of tellurium. The pump beam is amplitude modulated with a modulation frequency around 13 kHz with the acousto-optic-modulator AOM2. The difference signal between transmission between the two probe beams passing through the tellurium cell is detected on a balanced split photodetector.

The amplitude modulated saturated absorption spectroscopy setup is shown schematically in Fig. 5.6. About 2 - 4 mW of light at wavelength λ_1 is taken from the output of the frequency doubling setup (Section 4.3.1). The light is split of by an AOM1 which allows for a flexible division of the light between the tellurium spectroscopy and the radium spectroscopy. Furthermore it provides also a frequency offset between the two parts. The AOM1 operates between 250 - 500 MHz [(MT350-AO, 12VIS) from AA Optoelectronics [133]]. We operated it mainly at 328.5 MHz to bridge the gap between the radium and tellurium line. After the AOM1 we pass the light through a thick glass plate in order to produce two weak probe beams of about 4 % of the main beam. The beams are directed through the heated Te-cell.

Overlap of the pump beam and the probe beam inside the tellurium cell is determined by looking at the overlap on a white card at a distance of 130 mm away from the centre of the cell. This was done on both ends of the cell. The counter-propagating beam alignment cancels the first-order Doppler shift, but the second-order Doppler shift $(v^2/2c^2)\mathrm{f}_{Te}$ is not. The shift could be obtained by substituting the root mean square velocity $v = \sqrt{3k_BT/M}$ into the expression of second-order Doppler shift. This gives shift of 0.001 MHz for the operating temperature of our cell. The shift estimated here is an upper bound for the second-order Doppler shift.

The intensities of the two probe beams are measured in a split photo diode which is operated as a balanced photo detector. The signal of the individual photodiodes is amplified and subtracted in a homebuild amplifier [63] and the difference is sent to a lockin amplifier. The transmitted beam is focused into a second AOM2 operated at 60 MHz. The -1^{st} order is overlapped on a polarizing beam splitter with one of the probe beams. The rf to this AOM2 is amplitude modulated (chopped) at around 13 kHz to provide the amplitude modulation of the pump beam. The transmitted power through the tellurium cell is measured on a photodiode in order to measure the linear absorption of tellurium. The output from the lockin-amplifer provides the saturated absorption spectrum of tellurium with a good signal-to-noise ratio. It is digitized by feeding the signal in a voltage-to-frequency converter and counting the frequency (Appendix B).

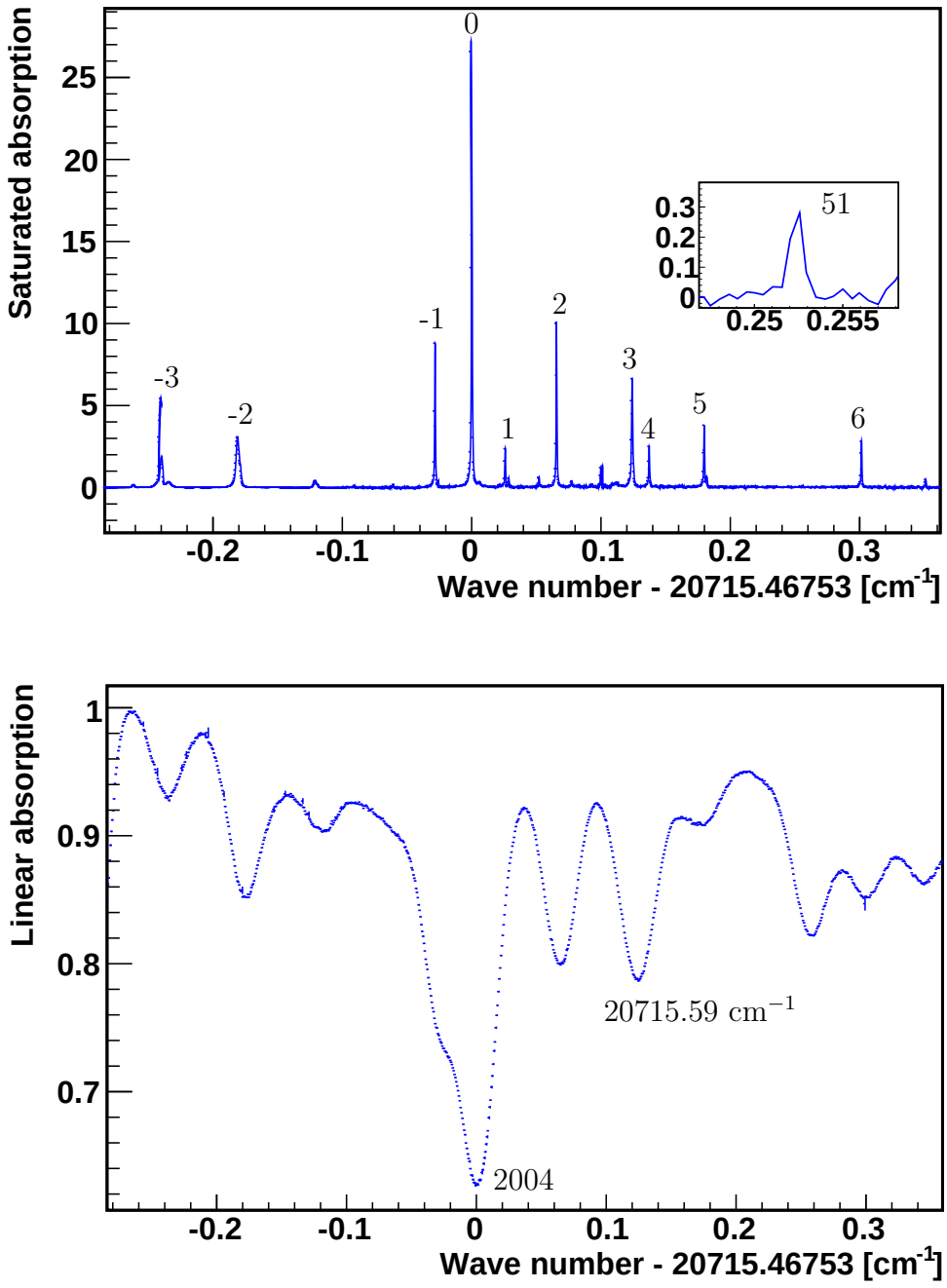

FIG. 5.7: Saturated absorption and linear absorption spectrum of $^{130}Te_2$ covering the 2004 line in Te atlas. Saturated absorption line corresponding to the 2004 absorption line is calibrated to 20715.46886(5) cm^{-1}. (Inset) The saturated absorption line at 20715.72148(5) cm^{-1} is closest to the $7s^2\ ^1S_0$(F=1/2) - $7s7p^1P_1$(F=3/2) transition in ^{225}Ra.

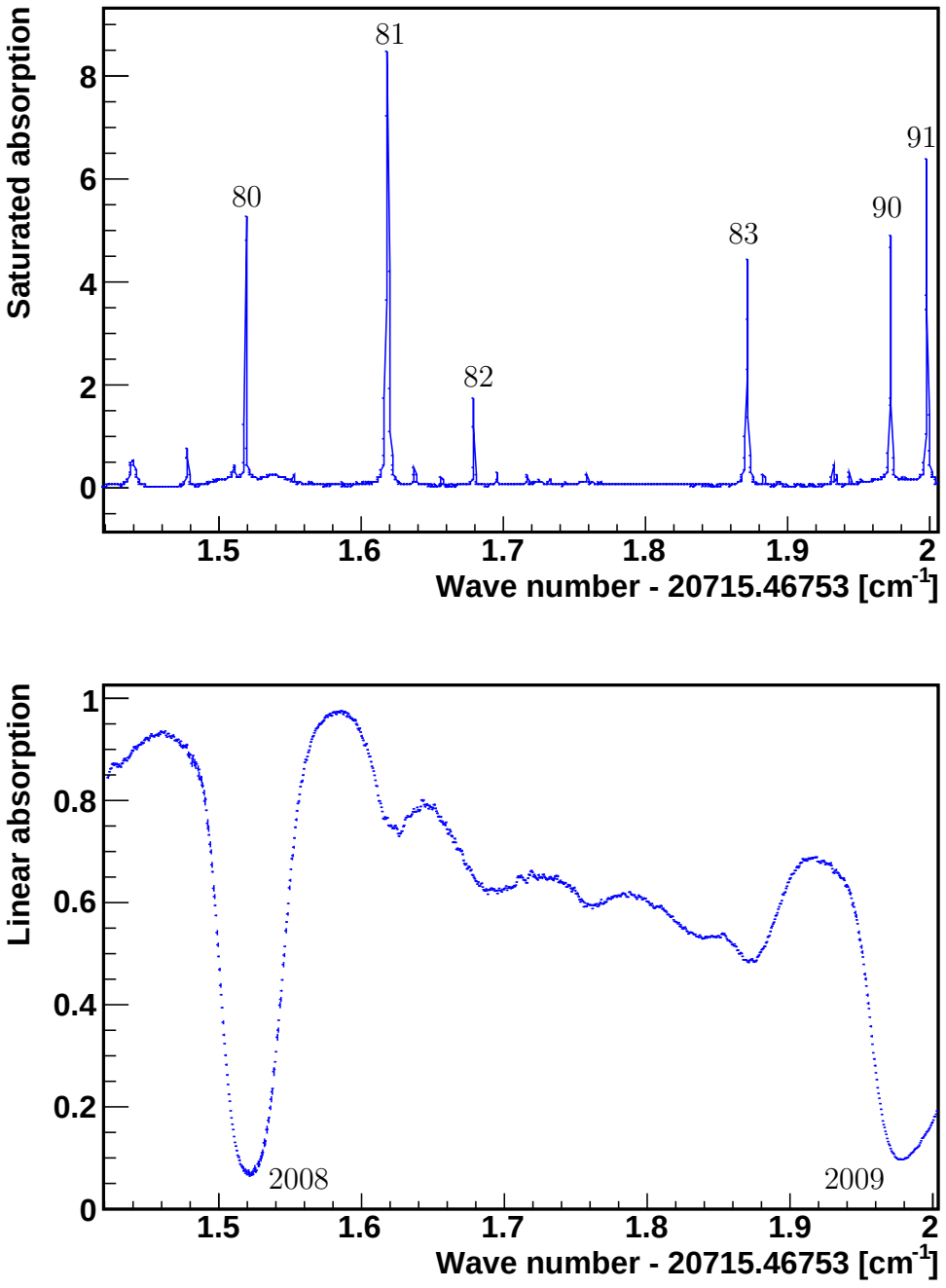

Fig. 5.8: Saturated absorption and linear absorption spectra of $^{130}Te_2$ covering the lines 2008 and 2009 in the tellurium atlas [130].

Reference for the $^1S_0$ - $^3P_1$ Transition in Atomic Radium

This intercombination transition is around 714 nm and has a narrow line width. To achieve a lower Doppler temperature for trapped radium atoms a second-stage laser cooling is required as there is no sub-Doppler cooling mechanism possible for alkaline earth atoms as in alkali atoms. The second stage cooling can be employed by the intercombination transition. We perform Doppler free saturated absorption spectroscopy of molecular iodine to determine the absolute frequency of the intercombination transition in radium.

To excite the molecules to these states the iodine is heated inside an oven at about 650 K. The temperature of the iodine vapor is measured with a K-NiCr type thermocouple in the middle of the oven. At these elevated temperatures the pressure of the iodine is so high that the individual transition lines become invisible because of collisional broadening. A cold finger made of copper and is kept at a temperature of about 340 K is employed to overcome this problem. The molecular iodine condenses on this cold finger which reduces the overall vapor pressure in the cell and make the transition visible.

The saturated absorption setup of iodine is quite similar to the setup used for tellurium. Two small fraction of laser beams, the probe and reference are split with an optical window, while the principle pump beam is guided around the oven to make it counter propagating with respect to the other probe and reference beams.

The frequency modulation is realized by double passing a laser beam through an AOM, which is modulated in frequency with the pump beam. The pump beam passes through a $\lambda/4$ plate and is then focussed in the AOM. A concave mirror reflects the beam at 180^o and only the 1^{st} order beam is used for double passing while the 0^{th} order is blocked by a diaphragm. The reflected beam passes through the AOM and $\lambda/4$ plate again which rotates the polarization of the beam by 90^o . The beam can pass then through the polarizing beam splitter (PBS).

The probe beam is saturated by the pump beam by overlapping both the probe and pump beams within the iodine cell. The probe and reference beams are monitored by a split-photodiode, giving the absolute difference between the two halves as an output signal. This signal is feed into the input of a lock-in amplier, which extracts the frequency modulated signal with a good signal-to-noise ratio.

Saturated Absorption Spectroscopy of $^{127}I_2$

Iodine is another well known secondary frequency reference for stabilizing the laser frequencies at visible wavelengths. The experimental setup for frequency modulated saturated absorption spectroscopy setup for providing secondary frequency reference for radium intercombination transition is same as described in reference [63].

The first diode laser at wavelength λ_{IC} is locked to the R(116) (2-9) a15 transition of $^{127}I_2$ at 13999.2459 cm^{-1}. This laser was referenced to an optical frequency comb for absolute frequency measurement of radium intercombination transition. A series of iodine transitions including the reference transition for radium is shown in Fig.5.10.

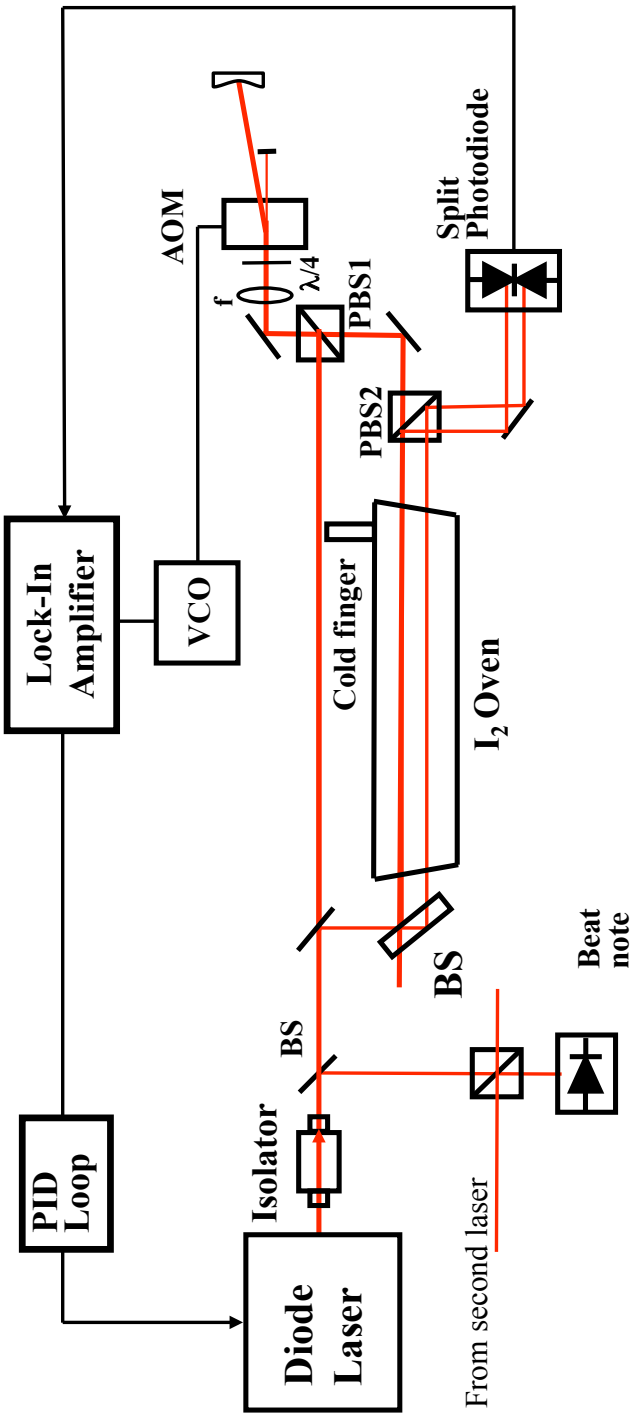

FIG. 5.9: Setup for frequency modulation saturated absorption spectroscopy of iodine $^{127}I_2$. Linear polarized laser light is employed both for the probe and the pump beam. The pump beam polarization is orthogonal to the polarization of the two probe beams. The pump beam light is frequency modulated with a double passed AOM. The difference signal between the two probe beams is detected on a balanced split photodetector [63, 134].

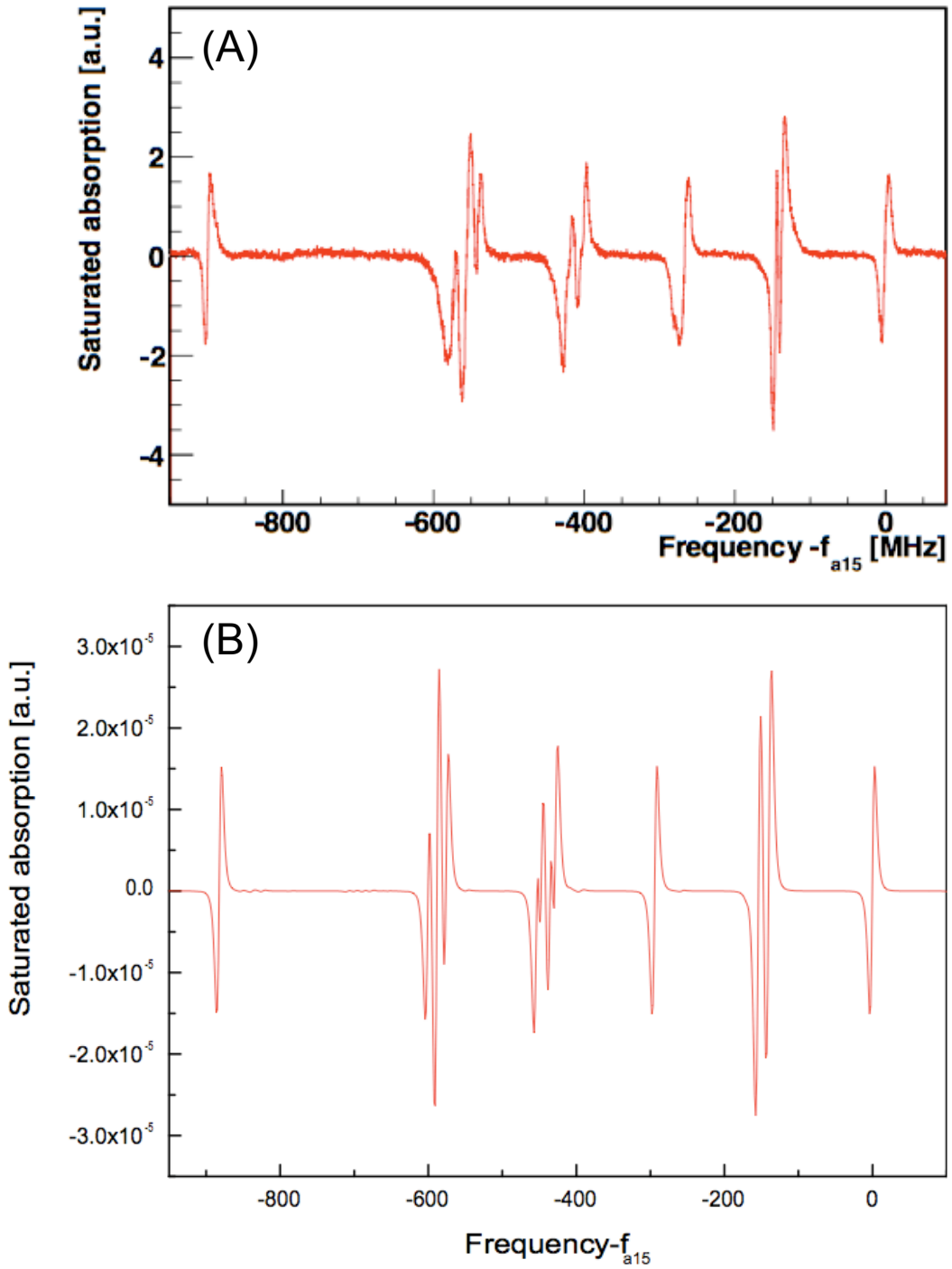

Fig. 5.10: (A) Recorded saturated absorption spectrum of molecular iodine, $^{127}I_2$ for the secondary frequency reference for the intercombination transition at wavelength λ_{IC} in atomic radium. (B) Calculated spectrum of the using the iodine software [135]. The parameters used are temperature T = 650 K and hyperfine linewidth = 0.0003 cm^{-1}.

5.3.2 Frequency Comb

An optical frequency comb is a very precise tool to measure frequencies of light with unprecedented accuracy. The accuracy of a reference frequency in the radio frequency domain is transferred to the optical regime by the exploitation of properties of a mode-locked laser. The output of a mode-locked laser in the time domain consists out of short pulses which are separated by a constant time Δt_{rep}. Furthermore, the phase between the envelope and the carrier has a deterministic evolution, i.e. the phase shift between to consecutive pulses is a constant (Fig. 5.11). Under these conditions the Fourier transformation of the electric field of the light field results in a comb like structure with lines separated by a frequency interval $f_{rep} = 1/t_{rep}$. Due to the phase shift $\Delta\Phi$ between two pulses in the time domain the frequencies of the lines can be written as

$$f_n = n \cdot f_{rep} + f_{CEO} \ , \tag{5.2}$$

where n is the mode number and $f_{CEO} = \Delta\phi/t_{rep}$ is the so called carrier envelop offset. The typical repetition rate of frequency comb is 50 MHz upto GHz. In order to exploit such a mode locked laser for optical frequency measurements the repetition rate and the phase shift $\Delta\phi$ have to be controlled to a high accuracy.

Offset Frequency Determination of an Optical Frequency Comb

The spectral width over which the optical power is distributed depends on the pulse width of the individual pulses in the domain. Coupling the light into a photonic crystal fiber causes an additional broadening of the optical spectrum [137] which can then span more than one octave. In this case the carrier envelope phase offset f_{CEO} can be measured. Light from the long wavelength part of the spectrum is frequency doubled in a nonlinear crystal. This light is overlapped with light from the short wavelength part of the spectrum. The two frequencies are then

$$f_{2n} = 2nf_{rep} + f_{CEO} \quad \text{and} \quad f' = 2f_{2n} = 2nf_{rep} + 2f_{CEO} \ . \tag{5.3}$$

The difference frequency of this two frequencies can be detected as a beat note on a fast photodiode. The repetition rate and the career envelope offset f_{CEO} can be electronically locked to a stable rf reference and transfer by this the stability to all comb lines. We employ a frequency comb from Menlo systems with a repetition rate between 248.8 - 251.2 MHz. The comb operates in infrared region between 1 - 2.1 μm. The visible part of the spectrum is covered by frequency doubling

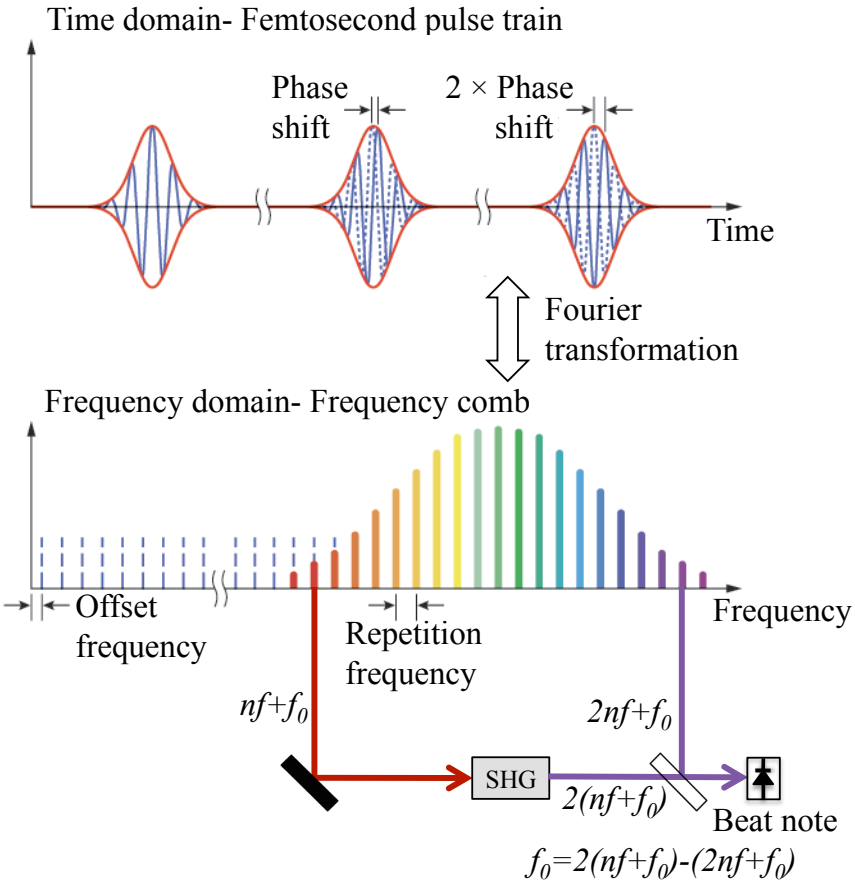

Fig. 5.11: (Top) Pulse train emitted from a mode locked laser. As the carrier wave (blue) moves with a phase velocity while the envelop (red) moves with a different group velocity the carrier wave experiences a phase shift with respect to the envelop after each round trip. (Bottom) Working principle of an optical frequency synthesizer [136].

of the amplified output of the comb which is centered around 1560 nm. The doubled light at 780 nm is then broadened in a crystal fiber to cover the optical spectrum from 480 nm - 1000 nm.

Determination of Unknown Optical Frequencies

Principle equation for determining the frequency of the light from a CW laser is

$$f_{CW} = n f_{rep} \pm f_{CEO} \pm f_{BN} \tag{5.4}$$

where, f_{BN} is the beat-note produced by the CW laser and the comb laser frequencies.

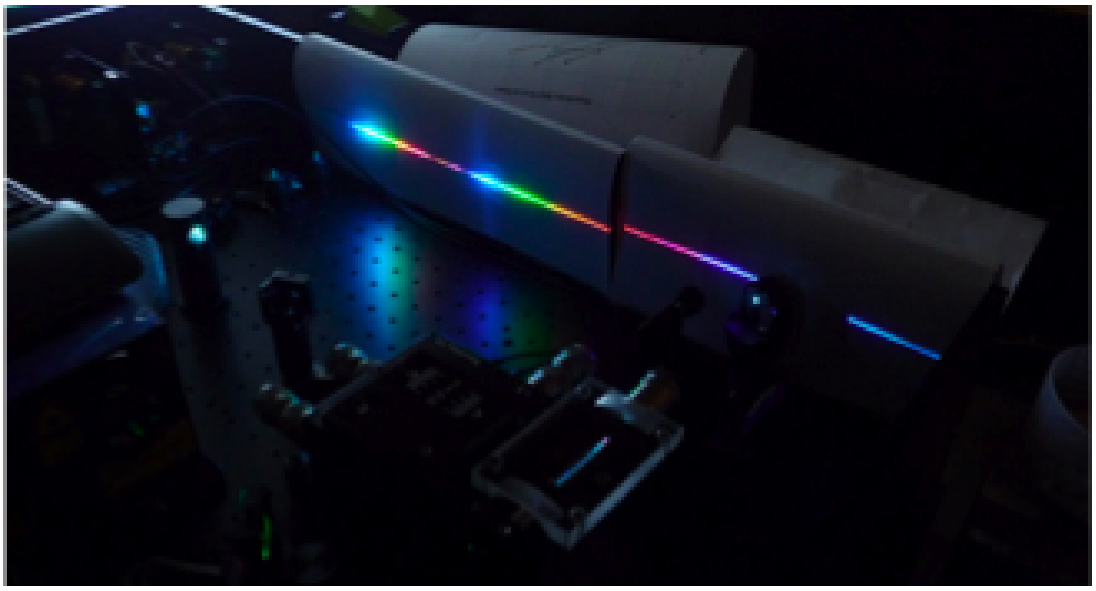

FIG. 5.12: Broad spectrum from a photonic crystal fiber frequency comb laser in the TRIμP optics laboratory at KVI.

The repetition rate of the comb laser is approximately 250 MHz. This rate can be calculated using the following equation

$$f_{rep} = \frac{f_{DDS}}{4} + 245 \quad MHz \tag{5.5}$$

where, f_{DDS} is the counter readout for the corresponding repetition rate.

The mode number n for a light at wave length λ can be obtained by taking the integer part of the following equation,

$$n = \frac{c}{\lambda f_{rep}} \quad . \tag{5.6}$$

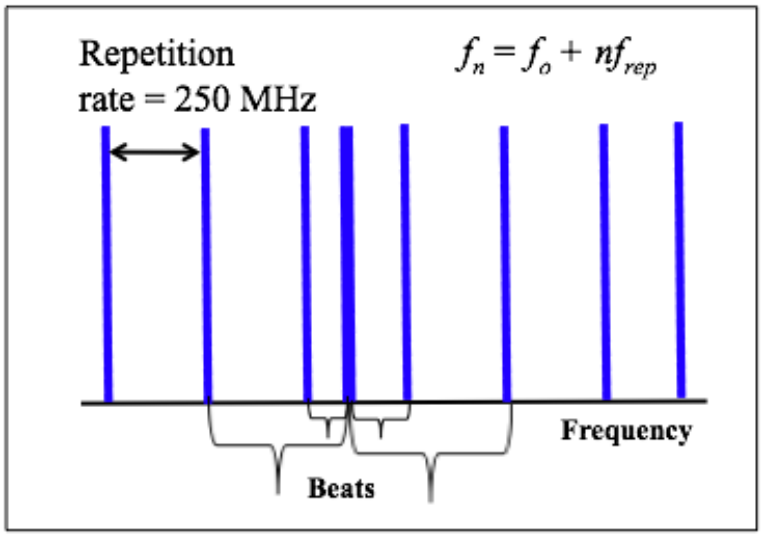

Fig. 5.13: The light from a CW laser produces beat-notes with more than one neighboring modes in the frequency spectrum of the frequency comb.

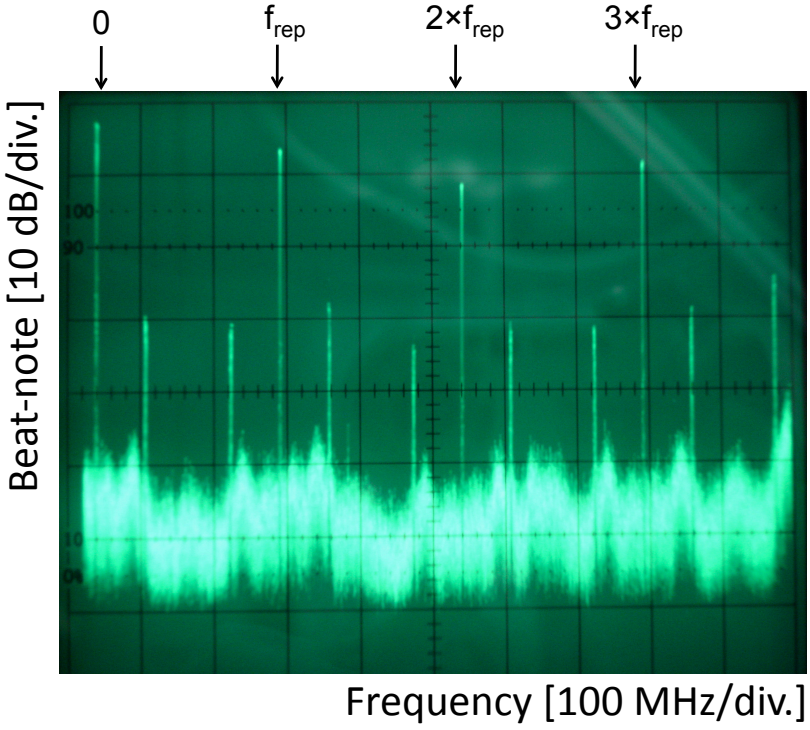

Fig. 5.14: The beat note spectrum between Ti:Sapphire laser light and the frequency comb light on a photodiode on a Hameg 1 GHz rf spectrum analyzer (HM5510).

5.4 Absolute Frequency Calibration of Molecular Reference Lines

The frequencies of the reference lines in molecular tellurium are calibrated by comparing the fundamental frequency at the Ti:Sapphire laser light with the frequency of laser radiation from an optical frequency comb. This is done simultaneously with the saturated absorption spectroscopy described in Section 5.3.1. A fraction of the IR light from the Ti:Sapphire laser is overlapped with light from the frequency comb on the pn junction of a InGaAs Photodiode (FGA04, 100 ps Rise Time, 800 - 1800 nm) from Thorlabs Inc., NJ, USA. The photodiode current contains frequency components at the difference frequency of the two lasers (beat note). The tellurium transition frequency, f_{Te} is then obtained through equation 5.7

$$f_{Te} = 2 \times (n f_{rep} + f_{CEO} + f_{BN}) + m_{AOM1} \times f_{AOM1} + m_{AOM2} \times \frac{f_{AOM2}}{2} \ , \quad (5.7)$$

Where f_{rep} and f_{CEO} are the repetition frequency and offset frequency of the frequency comb. The sign of f_{rep} and f_{CEO} may be negative as well as positive and needs to be determined. The integer n is mode number which can be determined by equation. 5.6 (see Fig. 5.6) and m_{AOM1} and n_{AOM2} are the order numbers of the sidebands from the two AOMs used in this measurement. f_{AOM1} and f_{AOM2} represents the operating frequencies of the two AOMs.

The saturated absorption lines shown in Fig. 5.7 and Fig. 5.8 were individually scanned and recorded. The repetition rate f_{rep} was chosen such that the beat note frequency f_{BN} at resonance was between 30 - 80 MHz. For the measurements temperature of the $^{130}Te_2$ oven was 804(1) K. The spectroscopy was performed with a total 3.5(5) mW blue power.

	Frequency [MHz]	Order number to tellurium setup
AOM1	328.500	0
AOM2	60.000	-1

TABLE 5.1: Frequencies and order numbers of the laser beams from the two AOMs used for tellurium spectroscopy.

A better indication of the vapor pressure in the tellurium cell at a given temperature is given by the linear absorption at a particular resonance. It has been

used previously [131,138–140] as a basis for determining the effective temperature of tellurium cell, and hence the vapor pressure. For a cell of length l, containing N molecules per unit volume, the linear absorption of a line is $A = 1 - exp(-N\sigma l)$, where effective absorption cross section σ in the range of the tellurium absorption spectrum is of the order of $10^{-22}\mathrm{m}^2$ [140]. In order to determine A as a function of temperature T, it is necessary to express N as a function of temperature. For

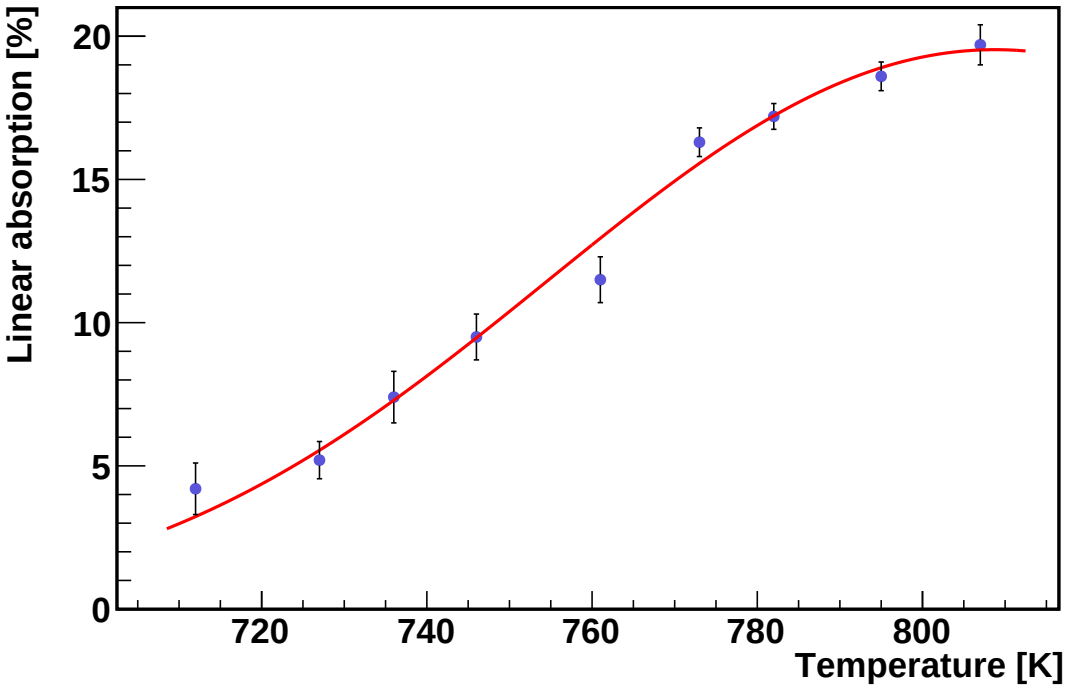

Fig. 5.15: Linear absorption as a function of temperature on a tellurium absorption line corresponding to the Te#3 line at 20715.59 cm^{-1}. The measured data is fitted with a least χ^2 function described in [141].

a gas at saturated vapor pressure P confined in a cell of volume V at absolute temperature T

$$N = \frac{PV}{k_B T} \ , \tag{5.8}$$

where k_B is the Boltzmann constant. Thus

$$\frac{N}{V} = \frac{P(T)}{k_B T} \ . \tag{5.9}$$

Linear absorption is measured as a function of cell temperature for a tellurium absorption line corresponding to the Te#3 saturated absorption line (Fig. 5.15).

A least χ^2 fit through the data points shows right behavior as observed in previous measurements [140, 141].

Under these conditions we calibrate the tellurium lines against the frequency comb. A subset of six of the lines is presented in Fig. 5.16. The line shape is in good agreement with a Lorentzian form. The linewidth of these transitions is between 11 and 28 MHz while the signal strength varies by a factor of 300 from line #0 (Fig. 5.7) to line #51 (Fig. 5.7).

Note that the strength of the saturated absorption signal is not proportional to the strength of the linear absorption or the number density of the molecules.

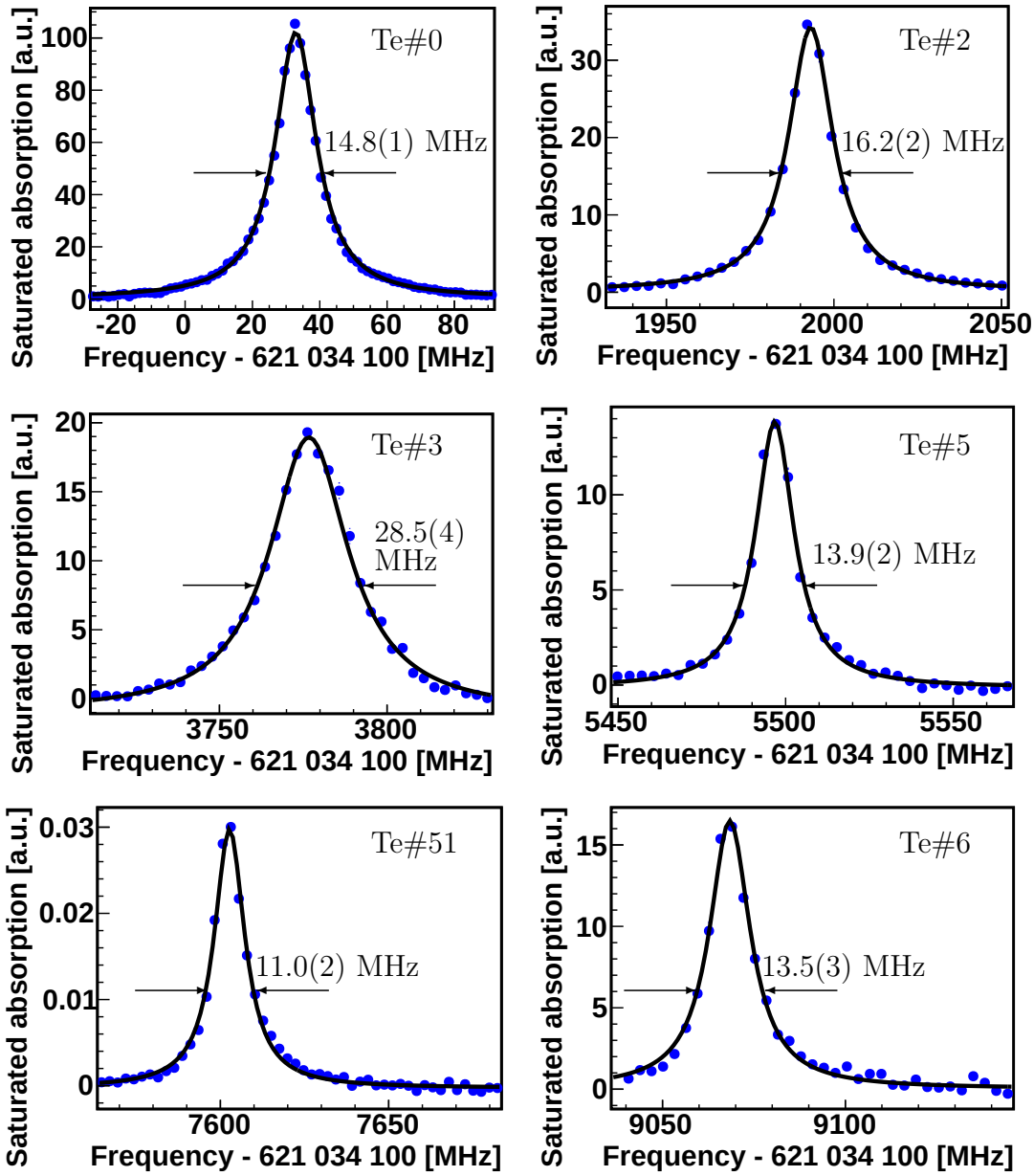

Fig. 5.16: Six individual saturated absorption lines in $^{130}Te_2$ as a function of absolute frequency. The full width at half maxima for all the lines is extracted by fitting the peaks with a Lorentzian fit function.

5.4.1 Estimate of Measurement Uncertainties

The Uncertainty of the frequency measurement arises from the statistical and systematic uncertainties. Statistical uncertainty arises due to finite signal to noise ratio of the data points. Systematic uncertainties arise from the drift of parameters in the experimental setup, e.g. density related shifts, ac Stark shift, second-order Doppler shift, and frequency standard and computer fitting . An estimate of the systematic uncertainties for the absolute frequency calibration of molecular tellurium is given below.

Collision Induced Shifts

Collisions induce pressure shifts of atomic and molecular transition frequencies [142]. These shifts are after referred to as pressure shifts. In case of an absolute accuracy to be better than 0.1 MHz is needed for a certain line, a critical investigation of pressure shift is necessary. In order to determine the pressure shift for tellurium lines, the vapor pressure of tellurium inside the cell needs to be stable and known on a level of 0.1 mbar or the cell temperature to 6 ^{o}C [143]. Assuming that the pressure shift is about 1 MHz/ mbar as observed for previously measured for some lines [138–140, 144] we estimate the uncertainty due to pressure shift in our measurement. During the data collection, the maximum observed fluctuation of the tellurium cell temperature is ± 1 ^{o}C, which limits the uncertainty on tellurium frequency due to pressure shift to ± 0.17 MHz.

ac Stark Shift

The ac Stark shift or light shift is the shift of energy levels of atoms and molecules due to presence of an external electromagnetic field (see e.g. [145]). The uncertainty in the intensity arises from the knowledge of the beam diameters in the overlapped region. We measured the ac Stark shift for the Te#0 line by variation of the intensity of light beam under the same beam focusing conditions. The lowest and highest intensities correspond to 190(50) mW/cm^2 and 570(160) mW/cm^2 respectively. The transition frequency changes by less than 1 MHz over this range of intensities. An ac Stark coefficient of 0.0016 MHz/(1 mW/cm^2) is obtained from the fit of the data points shown in Fig. 5.17.

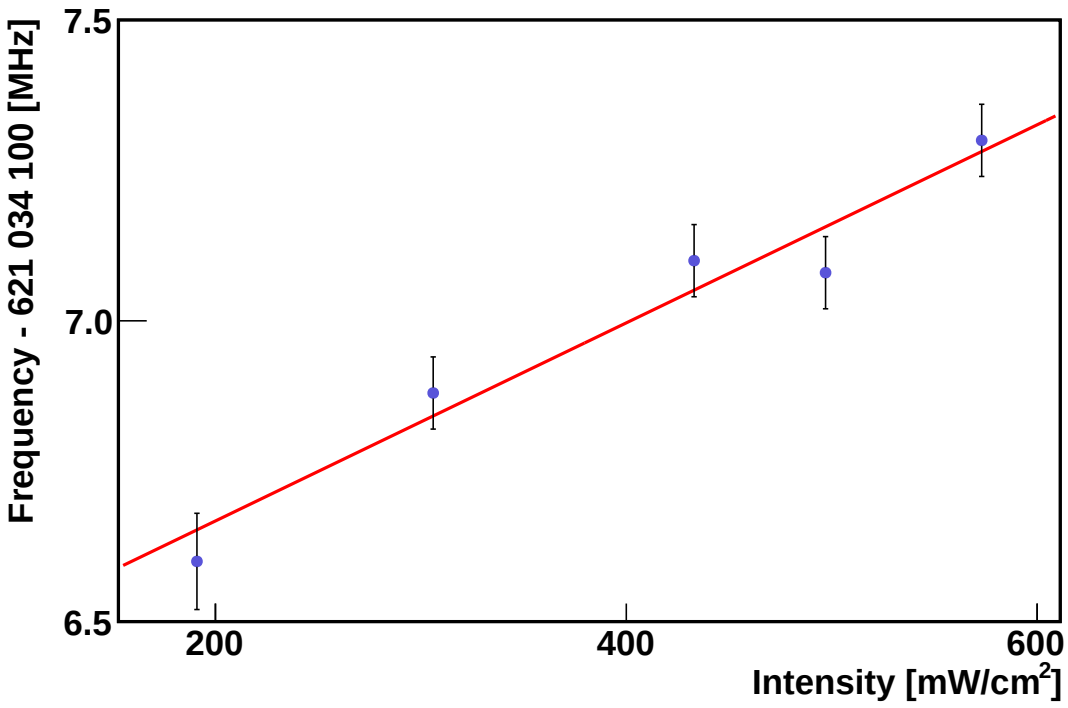

Fig. 5.17: The ac Stark shift is determined for the line Te#0 by measuring the transition frequency at different intensities.

Frequency Standard

The accuracy of our optical frequency comb is derived from a Global Positioning System stabilized Rb clock to be better than 10^{-11} [146]. The corresponding frequency uncertainty for the tellurium measurements is 0.006 MHz. To check the consistency of the frequency calibration by the frequency comb we measure the beatnote frequencies for the line #0 in molecular tellurium at three different repetition rates of the frequency comb as a function of the frequency difference between repetition rates. The slope of Fig. 5.18 provides the mode number of the comb-line with an uncertainty less than one mode. In this means the mode number can be determined if there is no frequency marker available at the order of the repetition rate of the comb.

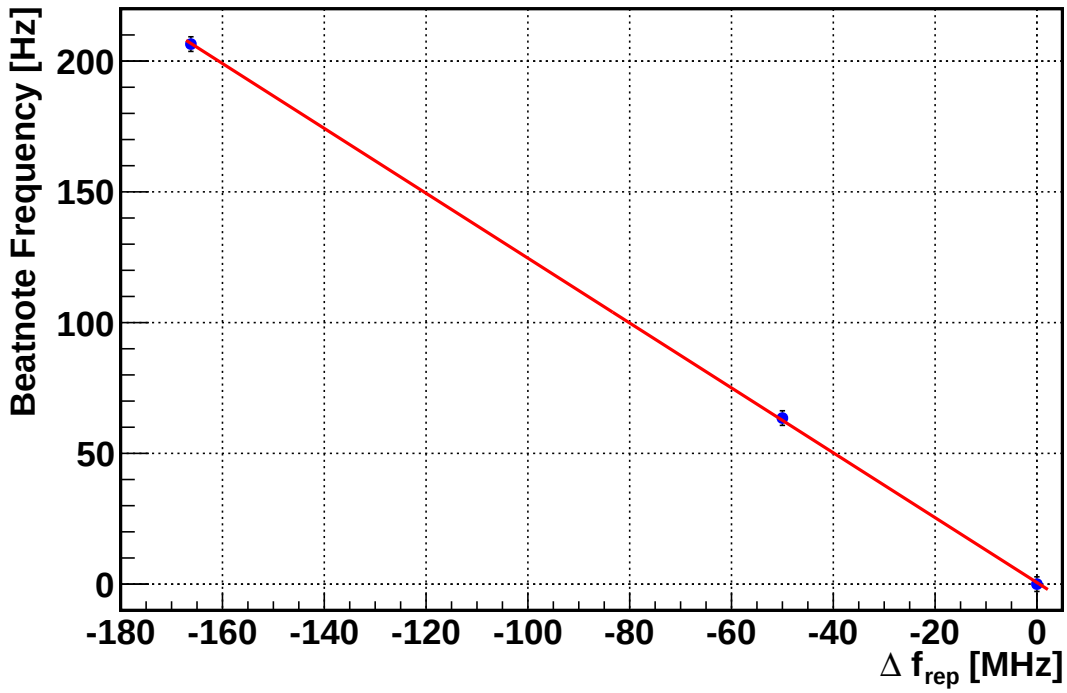

FIG. 5.18: The beatnote frequencies for the line #0 in molecular $^{130}Te_2$ at three different repetition rates of the frequency comb were measured. The vertical axis shows the frequency difference between repetition rates. The slope of this plot provides the mode number of the comb line with an uncertainty less than one mode. In this means the mode number can be determined if there is no frequency marker available at the order of the repetition rate of the comb.

Signal to Noise

In order to determine centre frequency of the measured saturated absorption peak, they are fitted by Lorentzian function

$$L(\omega) = \frac{1}{2\pi} \frac{\Gamma}{(\omega - \omega_0)^2 + \Gamma^2/4} \,, \tag{5.10}$$

where ω_0 is the center and Γ is the width of the profile. The accuracy of the fitted parameters depends on the signal to noise for the data points and the agreement of the line model with the measured data points. For all individual lines frequency uncertainty due to the fitting is 0.1 MHz.

The systematic uncertainties arising from various sources for the absolute frequency calibration of molecular $^{130}Te_2$ at 483 nm are listed in Table 5.2. Root mean square of all the uncertainties is 0.200 MHz. This uncertainty is smaller

Source of uncertainty	Uncertainties (MHz)
Pressure shift	0.170
ac Stark shift	0.048
Optical frequency comb	0.006
Signal to noise	0.100
Total (root mean square)	0.200

Table 5.2: Systematic uncertainties for the absolute frequency calibration of molecular tellurium.

than the statistical uncertainty in our measurement which arise from the contribution to the tellurium frequency from several measurements taken at identical conditions. Finally, serious consideration of frequency shift due to cell-to-cell variation is necessary for comparison of laser light frequencies stabilized to different tellurium cells. The cell-to-cell shift arises from the possible foreign gas contaminants in the cell. Previous measurement shows that this variation is less than MHz level [140] and therefore can be neglected to the laser spectroscopy experiments where an accuracy of $\leq$5 MHz is sufficient.

5.5 Conclusion

The laser spectroscopy tools for radium spectroscopy and laser cooling and trapping have been setup. This includes the light sources as well as the calibration and control of the optical frequencies of the laser light. Particularly we identified and calibrated reference lines in molecular $^{130}Te_2$ and $^{127}I_2$ by saturated absorption spectroscopy technique together with an optical frequency comb. These references permit the stabilization of the lasers for radium experiments.

Saturated absorption line	Absorption line marked in Te Atlas	Measured Wave number [cm^{-1}]	Measured Frequency [MHz]	Relative strength
-3		20715.22252	621026747.7(1.0)	23
-1		20715.44056	621033284.4(1.2)	37
0	# 2004	20715.46886	621034132.9(1.5)	100
1		20715.49432	621034896.2(1.6)	9
2		20715.53421	621036092.1(0.7)	34
3		20715.59374	621037876.7(1.6)	19
4		20715.60749	621038288.8(1.5)	9
5		20715.65112	621039596.9(1.6)	14
51		20715.72148	621041706.3(1.7)	0.03
6		20715.77029	621043169.4(1.5)	16
80	# 2008	20716.98905	621079707.1(0.3)	12
81		20717.08818	621082678.8(0.7)	21
82		20717.15013	621084536.0(0.8)	3
83		20717.34167	621090278.2(0.4)	6
90	# 2009	20717.43666	621093126.1(0.3)	15
91		20717.46039	621093837.3(0.4)	16

TABLE 5.3: Wave numbers, frequencies and relative strengths of saturated absorption and linear absorption lines in $^{130}Te_2$. The uncertainty of the wave number measurements is 0.00005 cm^{-1}. This corresponds to 1.5 MHz in the optical frequency measurement.

Chapter 6

Spectroscopy of Radium and Barium in Effusive Atomic Beam

Performing a search for *permanent Electric Dipole Moments* with radium isotopes requires not only precise knowledge of atomic states and nuclear properties, but also the practical implementation of the manipulation of the atomic states. In this chapter we report on the progress in laser spectroscopy of the main transition in radium for laser cooling and trapping. The strong singlet-singlet $^1S_0 - {}^1P_1$ transition is the only path to large optical slowing forces which are essential in reaching high capture efficiencies for a magneto optical trapp (see Section 3.3). In addition it is required for state selective population of the metastable ^3D-states in which large atomic enhancement factor for EDMs are present. The weaker intercombination line $^1S_0 - {}^3P_1$ is essential for second stage laser cooling since it give access to two orders of magnitude smaller Doppler temperature. There are two major aspects. Firstly the absolute calibration of these transitions with an uncertainty below the natural linewidth. This is required for stable operation of laser cooling and trapping. Secondly the stable realization of these optical frequencies is realized by stabilization of the lasers to secondary frequency standards in molecular transitions or directly by controlling the frequency with an optical frequency comb. The laser spectroscopic results were obtained by Doppler free fluorescence spectroscopy of the ^{225}Ra. Properties of the ^{225}Ra atomic beam is described in Section 4.2. The laser system and their frequency calibration is presented in Section 5.1, 5.2 and 5.3. The measurements presented here are required to test the atomic theory for upcoming experiments to search for an EDM in the radium atom.

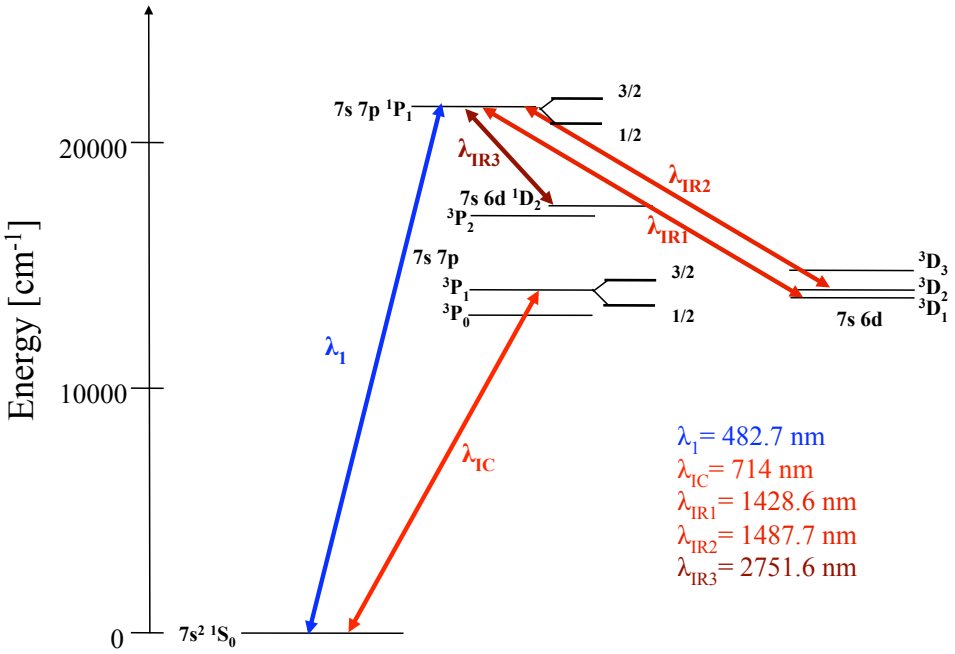

Fig. 6.1: Simplified energy level structure of atomic radium. The hyperfine states are shown only for $^1P_1$ and $^3P_1$ states. Wavelengths are taken from [67].

6.1 Laser Induced Fluorescence Spectroscopy

Laser spectroscopy of the two transitions from ground state in atomic radium is performed by laser induced Doppler free spectroscopy. As the flux of radium atoms in this experiment is about $10^5 - 10^6$ s^{-1} and the atoms are available for spectroscopy for a few hundred second, a good signal-to-noise ratio of the fluorescence spectroscopy is necessary. The Doppler free technique allows to simultaneously excite all the atoms in an atomic beam to a same frequency. This results in an enhanced signal-to-noise ratio for the fluorescence spectroscopy. The laser beam at λ_1 is overlapped with the atomic beam in a perpendicular direction (Fig. 6.2). This orthogonal geometry between the atomic beam and the laser beam eliminates the shifts in atomic transition frequencies due to first order Doppler effect. The laser power is measured after the laser-atom interaction region. The fluorescence count rate detected by a photomultiplier is normalized by laser power to eliminate unwanted noise in the fluorescence signal arising from fluctuation of the laser power.

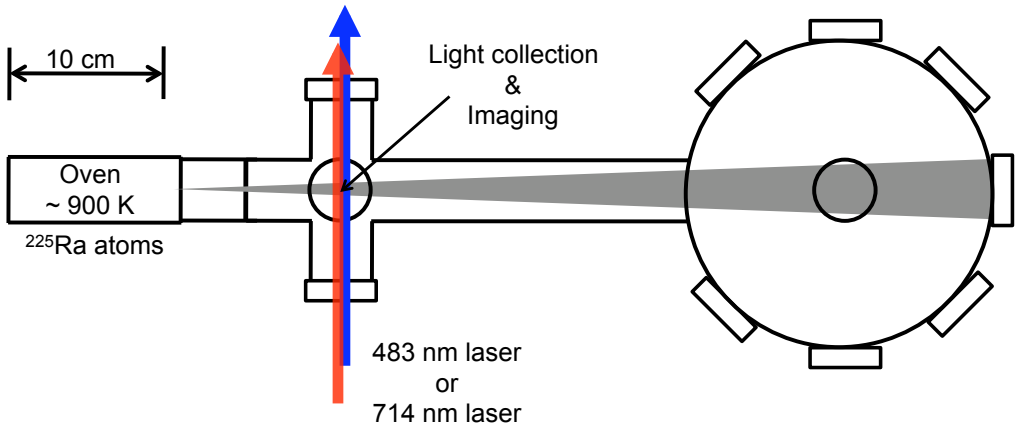

Fig. 6.2: Vacuum chamber for laser cooling and trapping of ^{225}Ra. Efficient trapping of atomic radium can be achieved by cooling on the $^1S_0 - {}^1P_1$ transition and trapping on the $^1S_0 - {}^3P_1$ transition. Doppler free fluorescence spectroscopy of these two transitions in ^{225}Ra is performed at an optical port 120(5) mm away from the oven orifice.

The atoms with an average velocity 300 ms^{-1} are probed at 120(5) mm away from the oven orifice. The atoms travel 3 mm in 10 μs at this velocity. A detail description of the flux and divergence of the ^{225}Ra atomic beam is given in Section 4.2.

The optical detection system for detecting fluorescence from atomic resonance consists of imaging system and photo multiplier tube (PMT) in photon counting mode. Schematic drawing of the optical detection system is shown in Fig. 6.4.

The fiducial volume of the imaging system is 10(2) mm. The system is designed to observe fluorescence from both wavelengths simultaneously. The fluorescence light at the different wavelength is separated by a dichroic mirror (50% transmission at 483 nm, 50% reflection at 714 nm) before the light is imaged onto a spatial filter. The light is collimated and transmitted through interference filters (FB480-10 and FB710-10) before it reaches the respective photomultipliers. The count rates from the PMTs are recorded together with other parameters (laser power, timing, laser frequencies, saturated absorption signals, control voltages and radium oven temperatures) by our DAQ system.

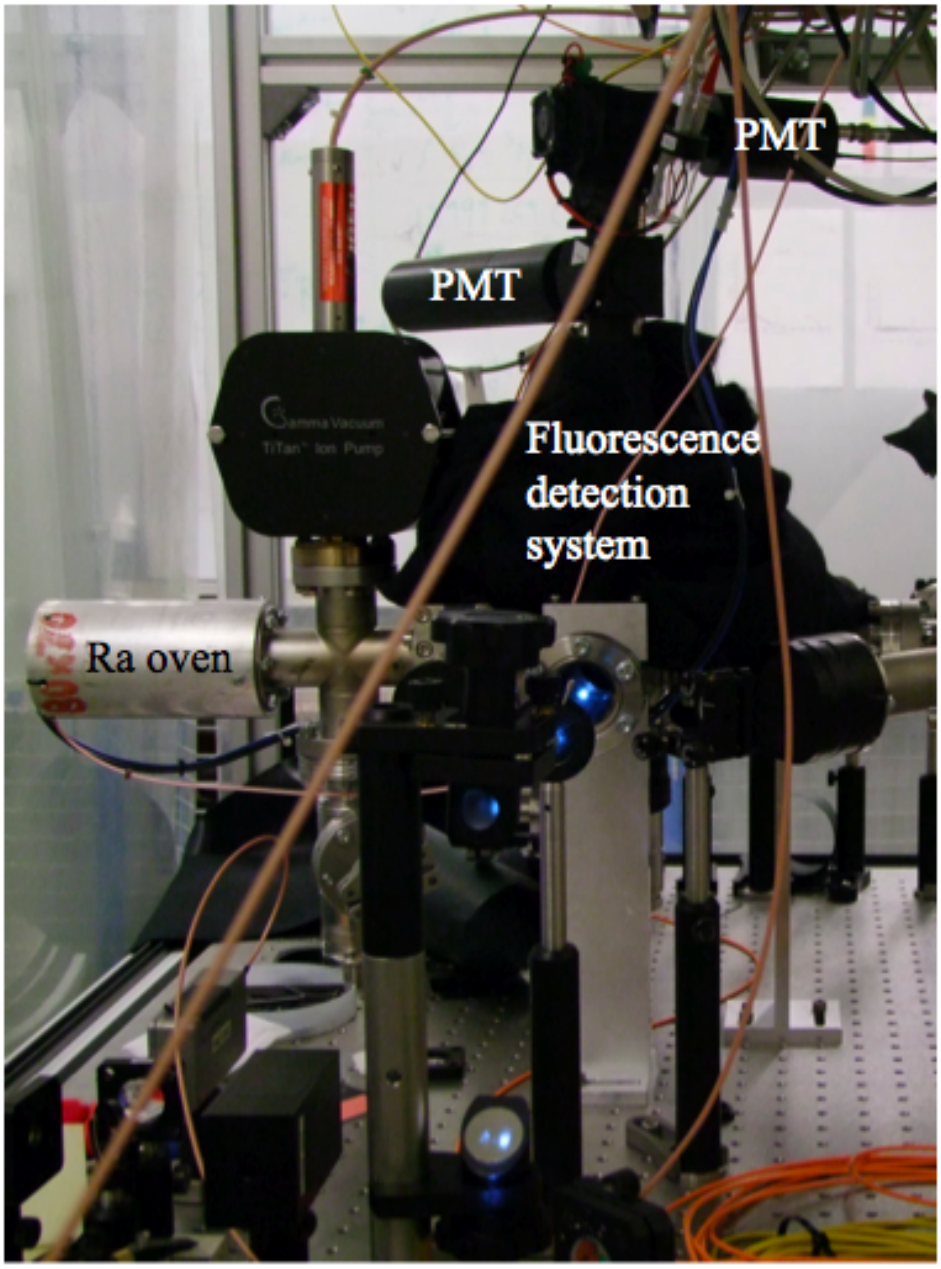

Fig. 6.3: Experimental setup for laser spectroscopy of ^{225}Ra at KVI. In this setup an effusive atomic beam of ^{225}Ra is produced at 900 K. ^{225}Ra is the product of α-decay of ^{229}Th inside a titanium crucible (Section 4.2). Laser light for excitation of the transitions enters the vacuum chamber perpendicular to the divergence of the atomic beam. Fluorescence from the excited atoms is collected by a lens assembly and imaged on two photomultiplier tubes, which are sensitive for the wavelength λ_1 and λ_{IC}.

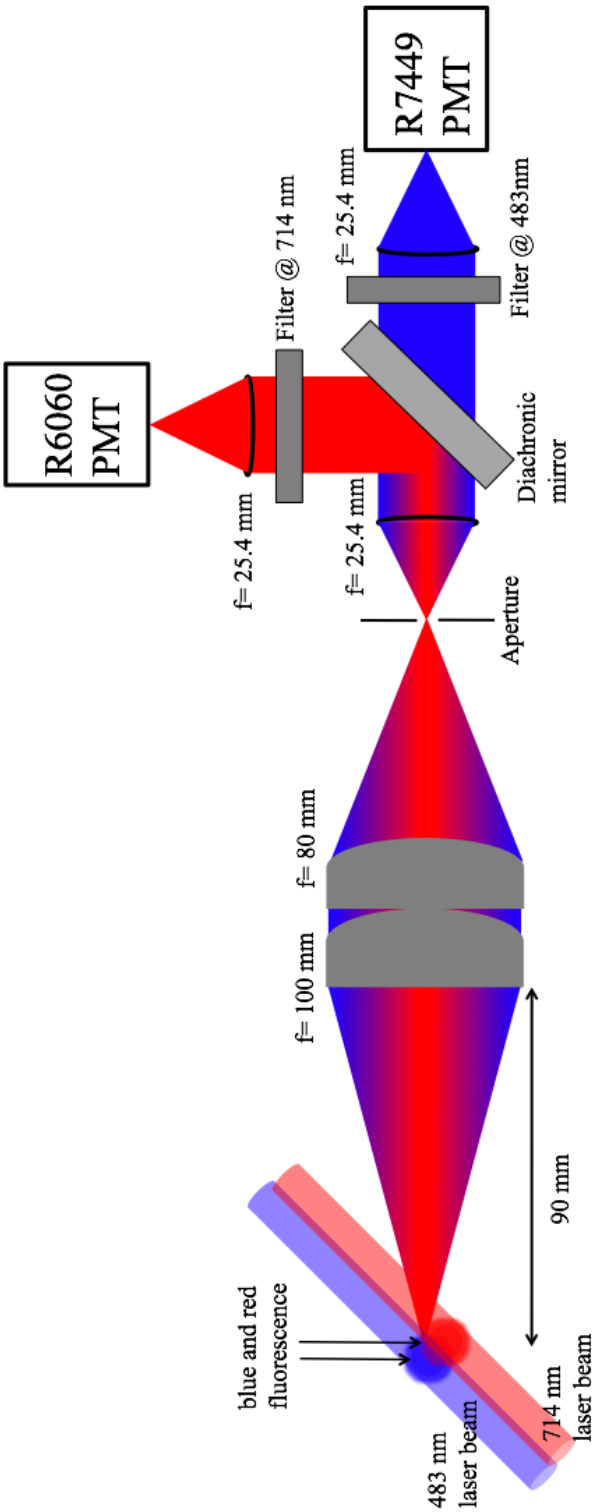

Fig. 6.4: Principle of the light collection and imaging system at wavelength λ_1 and at λ_{IC}.

The blue fluorescence is projected on to the photo cathode of a Hamamatsu R7449 PMT with head on type bialkali photocathode of an effective area of diameter 25 mm. The dark count rate of this PMT is ~ 100 s^{-1}. The quantum efficiency of this PMT at wavelength λ_1 is 18(1)% (Appendix C). A band pass filter (FB480-10) with center wavelength 480 nm, spectral width 10 nm and transmission 55 % (Appendix D) is placed in front of this PMT.

The red fluorescence is projected on a R6060-12 peltier cooled PMT with side on type multialkali photocathode of an effective area of 4×13 mm^2. The dark count rate of this PMT is < 10 s^{-1} when the cathode is cooled to 0 ^{o}C. The quantum efficiency of this PMT at wavelength λ_{IC} is 9(1)% (Appendix C). A band pass filter (FB710-10) with center wavelength 710 nm, spectral width 10 nm and transmission 55 % (Appendix D) is placed in front of this PMT.

The detection efficiency (ϵ_i) of a PMT for a wavelength depends on the solid angle (Ω) of light collection, the splitting factor of the dichroic mirror (ε_d), quantum efficiency (ε_i) of the PMT at that wave length, and the transmission efficiency (ε_f) of the filter

$$\epsilon_i = \Omega \cdot \varepsilon_d \cdot \varepsilon_i \cdot \varepsilon_f \quad . \tag{6.1}$$

The area A of the light-atom interaction section which is imaged on the PMT through a light collection system situated at a distance r from the image plane is defined by the solid angle of light collection Ω

$$\Omega = \iint_s \frac{\hat{n} dA}{r^2} \quad . \tag{6.2}$$

The light collection and imaging system consists of two achromatic doublet lenses of focal lengths $f_1 = 100$ mm and $f_2 = 80$ mm mounted next to the window of the vacuum chamber at a distance of 90(5) mm from the center of the vacuum chamber. The solid angle of light collection is 1×10^{-2} Sr. An aperture is placed at the focal plane of the combination of the achromatic doublet lenses. The object to image ratio for this system is 1:1. After the focal plane the image is collimated by another lens of focal length $f_3 = 25.4$ mm placed at a distance of 25.4 mm from the aperture. The collimated beam is split in blue and red components by using a dichroic mirror of splitting ratio 1:1. The detection efficiency for the blue fluorescence is $5(1) \cdot 10^{-4}$ and that for red is $3(1) \cdot 10^{-4}$.

6.2 The $7s^2\ ^1S_0 - 7s7p\ ^1P_1$ Transition in ^{225}Ra

The $7s^2\ ^1S_0$ - $7s7p\ ^1P_1$ transition at wavelength λ_1 is the strongest transition available in atomic radium from the ground state. The transition is crucial for an efficient slowing of radium atom from a thermal beam and as a sensitive probe for detecting metastable D-states, e.g. by two-photon Raman transition. The measurement employed radium atomic beam (Section 4.2), the laser system (Section 5.1) and the absolute frequency calibration in our experiment.

The setup for Doppler free fluorescence spectroscopy of the $^1S_0 - {}^1P_1$ transition in ^{225}Ra is shown in Fig. 6.2. The light at wavelength λ_1 which is produced by frequency doubling IR light from the Ti:Sapphire laser light is split for the saturated absorption spectroscopy of $^{130}Te_2$ and the radium fluorescence spectroscopy by AOM1. About 1 mW of light at wavelength λ_1 diffracted in the first order by AOM1 for the saturated absorption spectroscopy. A fraction of IR light is overlapped on a photodiode with the light from an optical frequency comb in order to create a beatnote. The absolute transition frequency of the reference $^{130}Te_2$ line and the ^{225}Ra transition is recorded simultaneously by the beatnote of IR laser with frequency comb light. A collimation lens is employed to produce a collimated laser beam at λ_1. Diameter of the beam at the interaction section is 6(1) mm. This correspond to an intensity of 26(2) mW/cm^2 which is about 80% of the saturation intensity of the transition. At the saturation intensity $I_s^{\lambda_1} = 31$ mW cm^{-2} scattering rate of this transition is $4.5{\cdot}10^7$ s^{-1}. Interaction time of the atoms with laser beam in the fiducial volume is about 20 μs. During the time of flight through the laser beam at λ_1 the radium atoms are re-excited for ~ 3000 times to collect fluorescence from the decay of radium atoms from the $7s7p\ ^1P_1$ state.

Absolute frequency calibration of the transition is performed against a reference saturated absorption line of $^{130}Te_2$ which is frequency calibrated by an optical frequency comb. AOM1 with an RF frequency, f_{rf1} of 450 MHZ (Section. 4.5.2; Fig. 4.26) splits the light beam at wavelength λ_1 for $^{130}Te_2$ and ^{225}Ra spectroscopy. 0^{th} order beam goes to $^{130}Te_2$ setup and -1^{st} order beam goes to ^{225}Ra experiment. Absolute frequency of the $^1S_0$(F=1/2) $- {}^1P_1$(F′=3/2) transition in ^{225}Ra is measured against the saturated absorption line #51 in $^{130}Te_2$. The radium transition frequency is obtained by

$$f_{Ra} - f_{Te} = n_{AOM1} \cdot f_{AOM1} - \frac{n_{AOM2} \cdot f_{AOM2}}{2} + \Delta f_{TeRa} \tag{6.3}$$

where Δf_{TeRa} is the observed frequency difference between the reference tel-

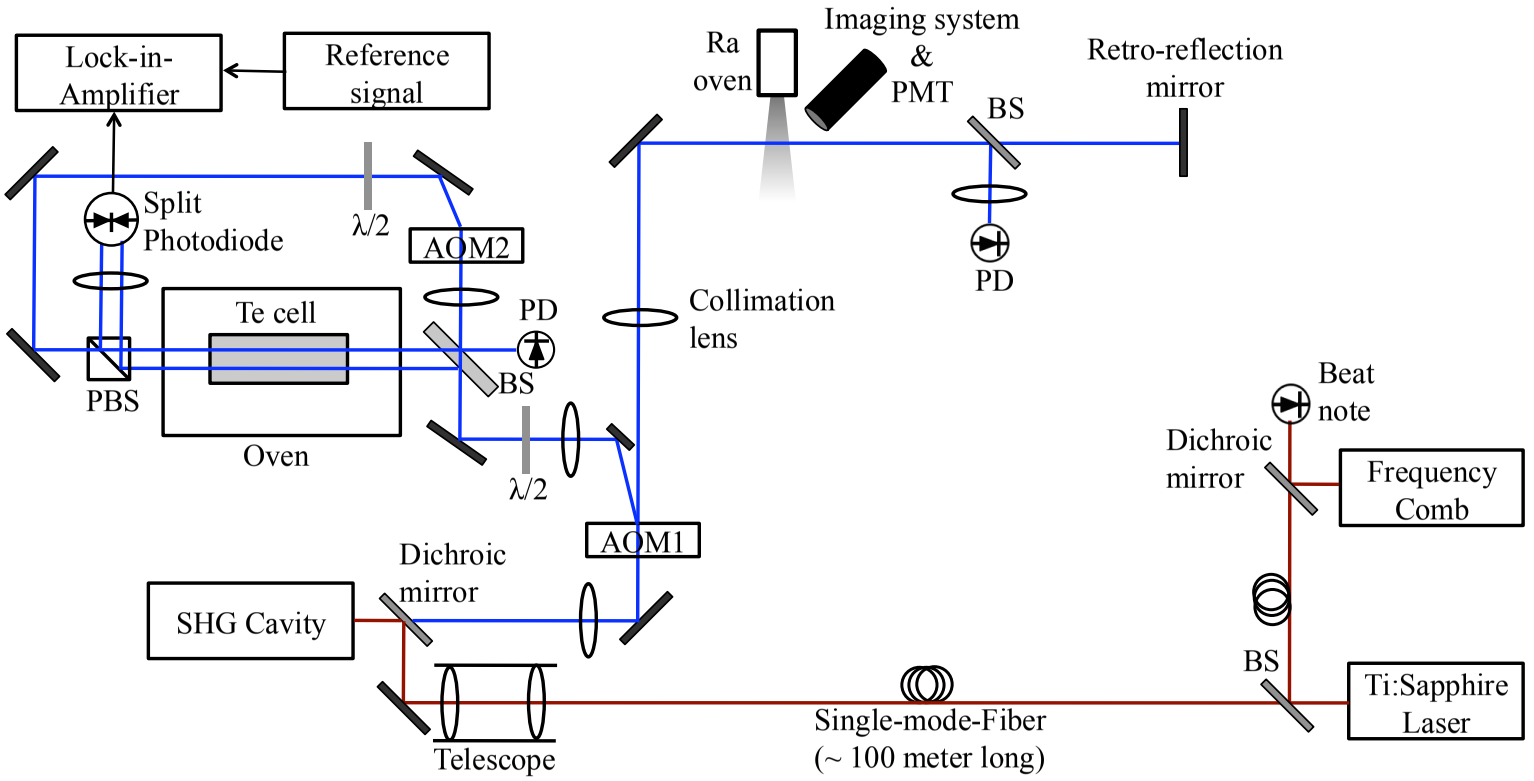

Fig. 6.5: For the measurement of the $7s^2\ ^1S_0 - 7s7p\ ^1P_1$ transition frequency the laser system (Section 5.1), the radium atomic beam (Section 4.2) and the absolute frequency measurement (with the combination of the frequency comb and the saturated absorption spectroscopy) are combined to work in one experiment. The light at wavelength λ_1 is produced by frequency doubling IR light from the Ti:Sapphire laser. The power of the laser beam is split by the acousto optical modulator AOM1 for the saturated absorption spectroscopy and the radium fluorescence spectroscopy. The beatnote together with the signals from the radium fluorescence and the $^{130}Te_2$ saturated absorption spectroscopy yield the transition frequency in radium. A fraction of IR light is overlapped on a photodiode with the light from an optical frequency comb. Absolute transition frequency of reference $^{130}Te_2$ line and ^{225}Ra transition is measured by measuring the beatnote of IR laser with frequency comb light.

lurium line and the radium line.

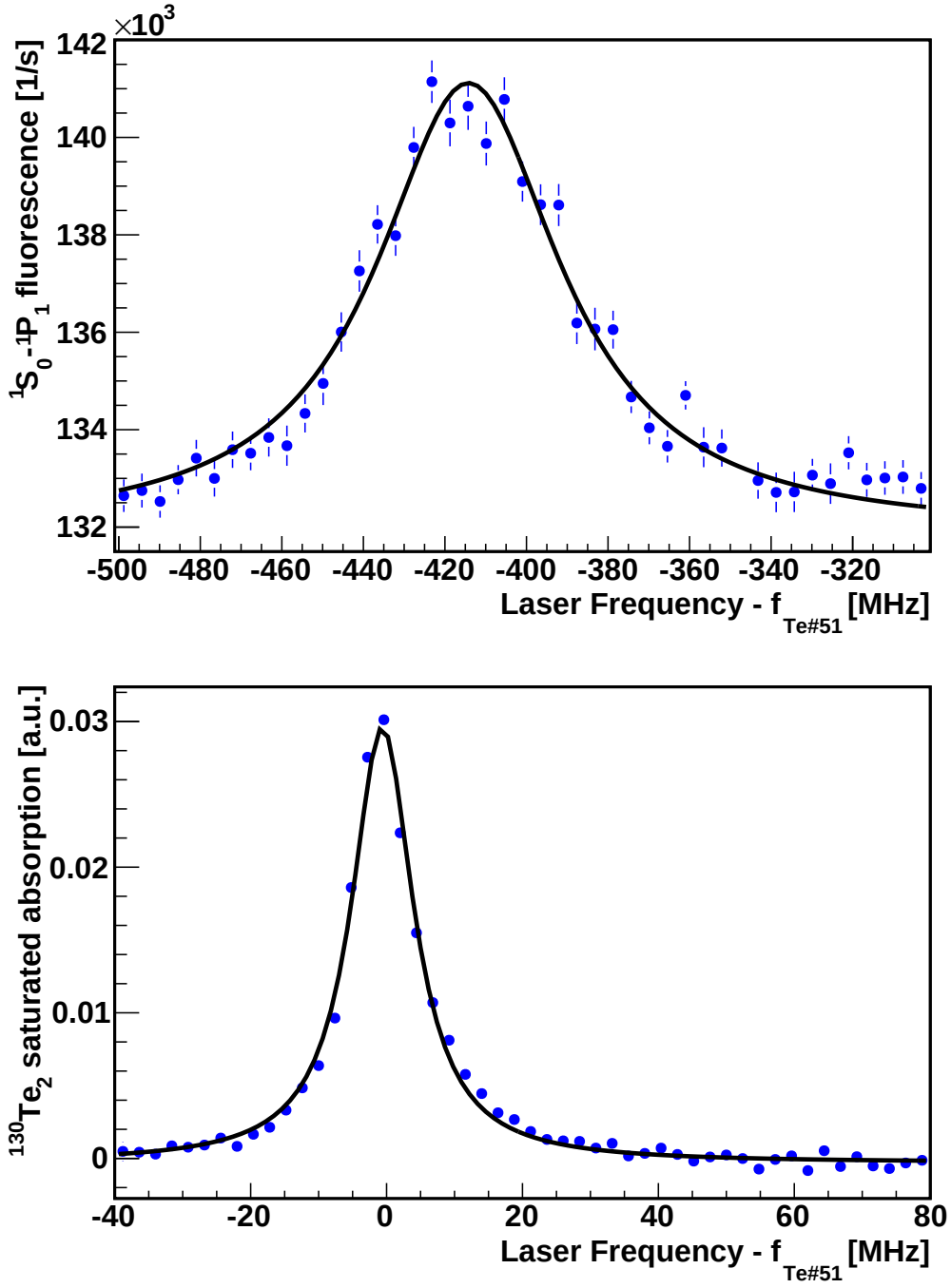

Fig. 6.6: (Top) Fluorescence from the $^1S_0$(F=1/2)-$^1P_1$(F=3/2) transition in ^{225}Ra. (Bottom) Saturated absorption line #51 in $^{130}Te_2$. The frequency of the transition in radium is 418(1) MHz lower than the reference line #51 (Section 5.4) in tellurium. The frequency axis is derived from the absolute frequency of the line #51 and the beatnote frequency f_{BN} with the frequency comb.

Isotope	Transition	Frequency [MHz]	Experiment by
^{225}Ra	$^1S_0^{F=1/2} - {}^1P_1^{F'=3/2}$	621042124 (2)	This work
^{226}Ra	$^1S_0 - {}^1P_1$	621038004 (180)	ANL [78]
^{226}Ra	$^1S_0 - {}^1P_1$	621041362 (1500)	Rasmussen [67]

Table 6.1: Wave numbers of the $^1S_0 - {}^1P_1$ transition in radium atom. The measurement in this work yield more than a factor of 100 improvement in uncertainty of the wave number or frequency of the strongest transition from ground state in atomic radium.

The radium transition is measured at 418(1) MHz lower in frequency relative to the reference tellurium line (Fig. 6.6). The measurement yields an absolute frequency for the radium transition to 621042124(2) MHz or 20715.73542(6) cm^{-1}. This is a factor of 100 improvement in uncertainty over other laser spectroscopic measurements [78] and three orders of magnitude better than Rasmussen [67].

Hyperfine Structure Interval of the 7s7p^{1}P$_1$ Level

The hyperfine structure of the 7s7p ^{1}P$_1$ level in ^{225}Ra atoms is observed in the same setup. The hyperfine structure is a sensitive probe of the atomic wave functions for short distances. It arises due to the interaction of the orbital angular moment L of electron with the nuclear spin I. The magnetic moment $\mu_{\mathbf{I}}$, of the nucleus acquires in a magnetic field $\mathbf{B}_e$ which is created by the orbital electrons of an interaction energy of

$$H_{HFS} = -\mu_{\mathbf{I}} \cdot \mathbf{B_e} \ . \tag{6.4}$$

The hyperfine structure interval energy is given by [147]

$$E_{HFS} = \frac{1}{2}CA + \frac{\frac{3}{4}C(C+1) - J(J+1)I(I+1)}{2J(2J-1)I(2I-1)}B \ , \tag{6.5}$$

where $C = F(F+1) - J(J+1) - I(I+1)$ and $F = |J+I|, |J+I-1|...|J-I|$ for nuclear spin I and total angular momentum quantum number J. A and B are the magnetic dipole interaction and electric quadrupole interaction constants.

Experimental setup (Fig. 6.5) for determining the hyperfine structure splitting of the 7s7p^{1}P$_1$ state in ^{225}Ra is same as for the Doppler free fluorescence

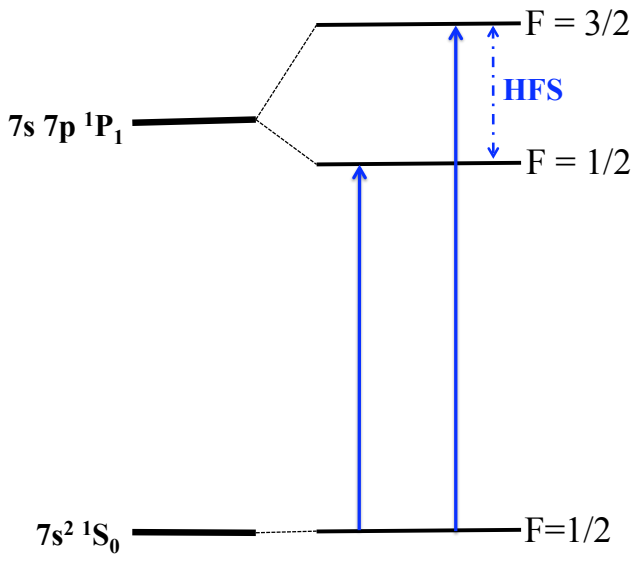

Fig. 6.7: Hyperfine splitting of the 7s7p $^1P_1$ state in ^{225}Ra (I=1/2).

spectroscopy except the order number of the beams taken for radium and tellurium from both AOMs. From AOM1 (rf = 450 MHz) 0^{th} order beam is taken for ^{225}Ra spectroscopy and $+1^{st}$ order beam is taken for tellurium spectroscopy. From AOM2 (rf = 60 MHz) $+1^{st}$ order beam is taken for the pump beam of the tellurium saturation absorption spectroscopy. Frequency difference between the tellurium saturated absorption line #3 and 6 (see Fig. 5.7) are taken for calibrating the frequency axis. In order to determine the hyperfine structure interval of the 7s7p^{1}P$_1$ state in ^{225}Ra atoms frequency of the light at λ_1 for driving the $^1S_0 - ^1P_1$ transition is scanned over both the hyperfine states (F=1/2 and F= 3/2) of the 7s7p$^1P_1$ level. Few such scans are averaged to obtain a better signal-to-noise ratio.

The hyperfine structure interval of the 7s7p^{1}P$_1$ level is determined to 4198(4) MHz. Our result is in good agreement with the previous measurement at ISOLDE, CERN [73]. These measurements provide valuable inputs for atomic theory to calculate wave functions of the low laying states in radium atom.

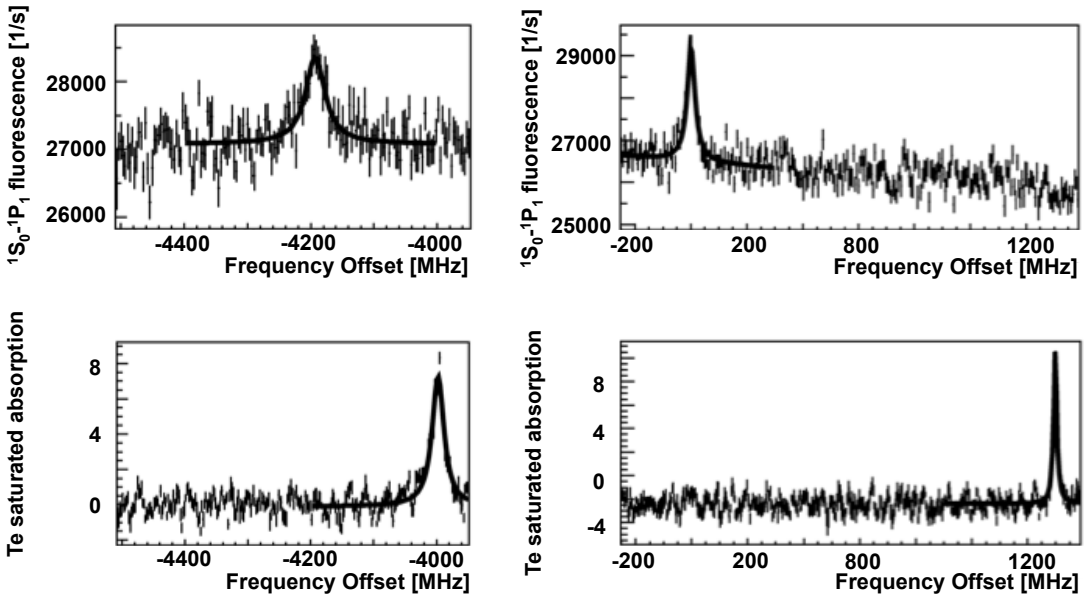

Fig. 6.8: (Top) Fluorescence signals from $^1S_0$(F=1/2)-$^1P_1$ (F= 1/2) transition (left) and $^1S_0$(F=1/2)-$^1P_1$ (F= 3/2) transition (right) in ^{225}Ra. (Bottom) $^{130}Te_2$ saturated absorption line #3 (left) and 6 (right).

6.3 Intercombination Transition in ^{225}Ra

Presence of the 7s7p $^3P_1$ level enhances the Electric Dipole Moment of radium in ^3D states (see section 3.4). Precise measurement of the energy of this level is of crucial importance towards measuring EDMs in radium atom in the ^3D states. The 7s7p $^3P_1$ level has a branching ratio to the 7s6d $^3D_1$ state of $4 \cdot 10^{-5}$, and a single repump laser tuned to the 7s6d $^3D_1$ - 7s7p $^1P_1$ transition is sufficient to bring the atoms back into the cooling cycle. The advantages of using this transition are the lower Doppler cooling limit and the simplicity of repumping. The intercombination transition is ideal for trapping and second stage cooling but not efficient for capturing atoms from a thermal beam.

We setup a laser system consists of two diode lasers at wavelength λ_{IC} to provide relative and absolute frequency reference for the intercombination transition in atomic radium. A schematic drawing of the laser system is shown in Fig. 6.9. First laser is locked to iodine (I_2) saturated absorption transition. Second laser is locked to the first laser by frequency offset locking. A fraction of light from first laser is mixed with the laser radiation from an optical frequency comb to produce beatnote. Another two diode lasers with same specifications at wavelength λ_{IC} are employed for spectroscopy of radium atoms.

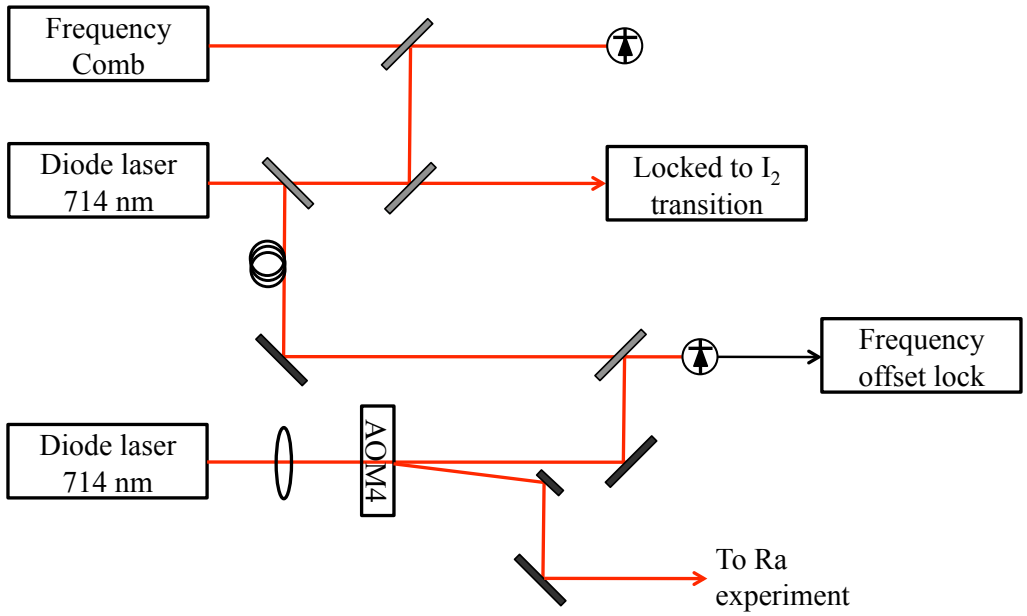

Fig. 6.9: Schematics of the laser system for providing light at 714 nm.

The $^1S_0 - {}^3P_1$ intercombination transition in atomic radium is investigated by means of laser induced fluorescence spectroscopy. Absolute transition frequency of the $^1S_0$(F=1/2) $-$ $^1P_1$(F=3/2) transition is measured with reference to secondary frequency standard molecular iodine. The iodine transitions are frequency stabilized to an optical frequency comb which is stabilized to a Rb clock. The Rb clock provides a relative precision to be better than 10^{-11}.

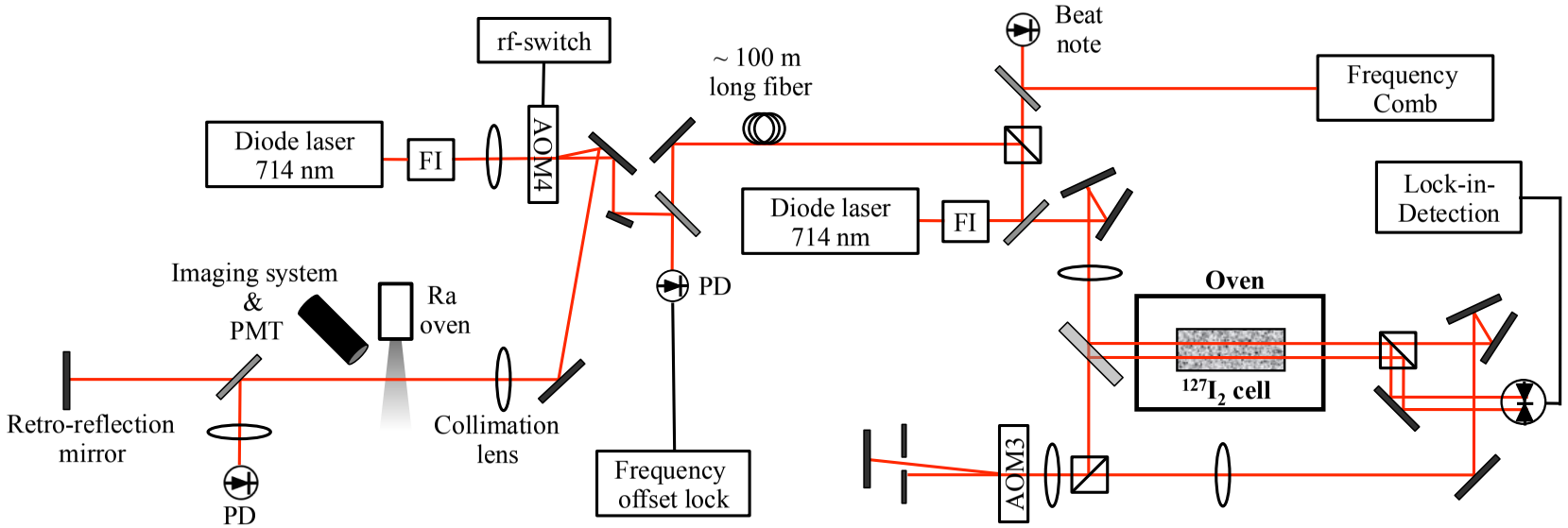

Fig. 6.10: Experimental setup for Doppler free fluorescence spectroscopy of the $^1P_1 - {}^3P_1$ intercombination transition in radium atom. Light at wavelength λ_{IC} is produced by a diode laser system. Saturated absorption spectroscopy of molecular iodine is employed for providing secondary frequency reference to the radium transition. Light from one of the diode lasers is split in two parts. One part is taken for iodine spectroscopy and beatnote with frequency comb. Other part is overlapped with the light from a second diode laser which was locked to the first diode laser by frequency offset lock. Light from the second diode laser is taken for radium spectroscopy. Absolute transition frequency of the intercombination transition in ^{225}Ra is determined by measuring the beatnote between the light from the first diode laser with the frequency comb and the frequency offset between two diode lasers.

Experimental setup for Doppler free fluorescence spectroscopy of the $^1P_1 - {}^3P_1$ intercombination transition in radium atom is shown in Fig. 6.10. Light at wavelength λ_{IC} is produced by a diode laser system. Saturated absorption spectroscopy of molecular iodine is employed for providing secondary frequency reference to the radium transition. Light from one of the diode lasers is split in two parts. One part is taken for iodine spectroscopy and beatnote with frequency comb. Other part is overlapped with the light from a second diode laser which was locked to the first diode laser by frequency offset lock. Stabilization and control of laser frequency for the intercombination transition is performed in two steps,

- The first diode laser at wavelength λ_{IC} (I_2-laser) is locked to the R(116) (2-9) a15 hyperfine component of $^{127}I_2$. The stability of locking is monitored by the beat note of this laser with the frequency comb.
- The second diode laser at wavelength λ_{IC} (Ra-laser) is locked to the I_2-laser by frequency offset lock [63]. The offset lock takes care of the stability of the Ra-laser as well as scanning of the Ra-laser light frequency at wavelength λ_{IC} over a suitable range for the experiment.

Light from the second diode laser is taken for radium spectroscopy. Absolute transition frequency of the intercombination transition in ^{225}Ra is determined by measuring the beatnote between the light from the first diode laser with the frequency comb and the frequency offset between between two diode lasers. Scattering rate of this transition is two orders of magnitude smaller compare to the strongest $^1S_0 - {}^1P_1$ transition. In order to achieve a good signal-to-noise in the fluorescence signal light at wavelength λ_{IC} to the radium experiment is chopped to 200 ns on and next 600 ns off by AOM4. The timing scheme is chosen based

f_{rf3} [MHz]	n_{AOM3}	f_{rf4} [MHz]	n_{AOM4}
78.9	+1	200	-1

Table 6.2: Frequencies and order numbers of the laser beams from the two AOMs employed for the spectroscopy of intercombination transition in ^{225}Ra.

on the lifetime of the 7s7p $^3P_1$ state [79]. The photomultiplier tube is gated to 400 ns off and 400 ns on. This excludes the background count occurring from scattered light. The synchronized timing scheme for the photomultiplier gate time and the laser on/off time is shown in Fig. 6.11. Diameter of the laser beam

at λ_{IC} at the interaction section is 6(1) mm. The power was 4.2(2) mW. This correspond to an intensity of 50(2) mW/cm^2. At the saturation intensity $I_s^{\lambda_{IC}}$ = 136 μW cm^{-2} scattering rate of this transition is about 2.4·10^6 s^{-1}. At these experimental parameters the the radium atoms can be reused for 30 times for collecting fluorescence at λ_{IC} transition.

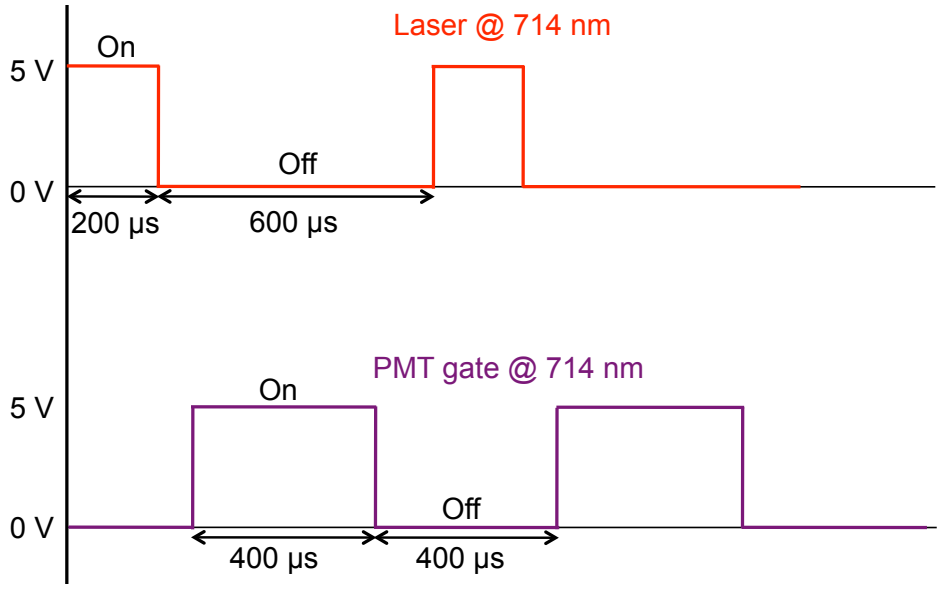

FIG. 6.11: TTL pulses for timing of the Ra-laser on/off (red) and for gate time of the photo multiplier tube (magenta) employed during the spectroscopy of 7s^2 ^{1}S$_0$(F=1/2) - 7s7p ^{3}P$_1$(F=3/2) transition in ^{225}Ra. Laser is on for 200 ns and off for next 600 ns. Photo multiplier count rate is gated for 400 ns on and next 400 ns off.

Absolute frequency of the ^{1}S$_0$ (F=1/2) − ^{3}P$_1$ (F=3/2) transition in ^{225}Ra is determined by

$$f_{Ra} - f_I = \Delta f_{IRa} - n_{AOM3} \times f_{rf3} + n_{AOM4} \times f_{rf4} \quad , \tag{6.6}$$

where, Δf_{IRa} represents relative frequency difference between the radium transition and the reference ^{127}I$_2$ line. Δf_{IRa} is determined to 1005(1) MHz. The parameters for AOM3 and AOM4 are provided in Table 6.2.

Frequency of the 7s^2 ^{1}S$_0$ (F=1/2) - 7s7p ^{3}P$_1$ (F=3/2) transition in ^{225}Ra is determined to 726(1) MHz high in relative to the frequency of the R(116) (2-9) a15 hyperfine component of ^{127}I$_2$. The measurement yield an absolute frequency of the 7s^2 ^{1}S$_0$ (F=1/2) - 7s7p ^{3}P$_1$ (F=3/2) transition to 13999.26932(13) cm^{-1} or 419687536(4) MHz.

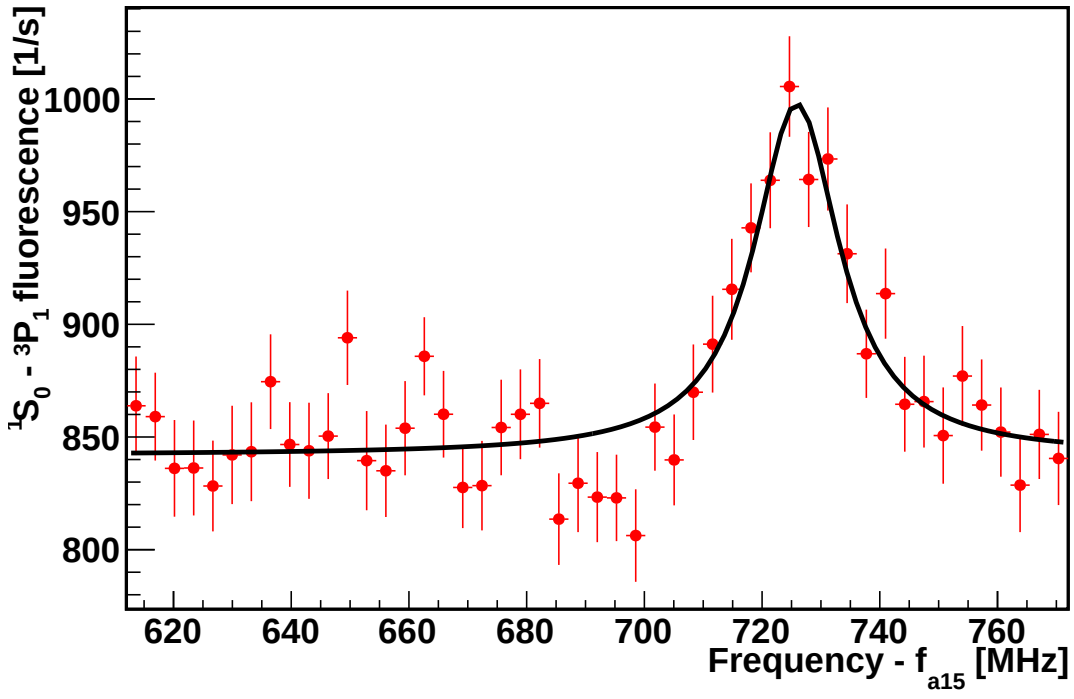

Fig. 6.12: The $7s^2\ ^1S_0$ (F=1/2) - 7s7p $^3P_1$ (F=3/2) transition in ^{225}Ra calibrated with an optical frequency comb to 419687536(4) MHz. The line through the data is a gaussian distribution due to residual Doppler shifts in the experiment.

Isotope	Transition	Frequency [MHz]	Experiment by
^{225}Ra	$^1S_0^{F=1/2} - {}^3P_1^{F'=3/2}$	419687536 (4)	This work
^{225}Ra	$^1S_0^{F=1/2} - {}^3P_1^{F'=3/2}$	419687526 (30)	ANL [79]
^{226}Ra	$^1S_0 - {}^3P_1$	419690854 (1500)	Rasmussen [67]

Table 6.3: Wave numbers of the $^1S_0 - {}^3P_1$ transition in radium atom. The measurement in this work yield more than a factor of 10 improvement in uncertainty of the wave number or frequency of this intercombination transition in atomic radium.

A list of measured absolute wave number of the $^1S_0 - {}^3P_1$ intercombination transition in radium atom till date is presented in Table 6.3. Our measurement improves the uncertainty by a factor of 10 over previous measurement [79].

6.4 Two Photon Transition in Atomic Barium

Laser spectroscopy of the transitions from the metastable D-states in heavy alkaline earth elements are indispensable for laser trapping because they provide significant losses from any laser cooling cycle. These losses are on the order $3{\cdot}10^{-3}$ (see Table 3.3). The strategies to overcome these losses have been investigated with atomic barium which provide a very similar atomic level scheme as radium [63,89,148]. The first infrared laser spectroscopy of these transitions from the D-states were performed in atomic beam spectroscopy [63, 134] and then the results were exploited in trapping of barium in a magneto optical trap [89, 148]. In these experiments a trapping efficiency from an effusive atomic beam of about 1% was achieved [148]. The efficiency was limited by the available laser power.

The strategy of the approach for barium needs to be transferred to radium trapping. Apart from the scarcity of radium isotopes the challenge in radium is that the respective transitions have not been observed yet directly. The approximate transition frequencies are extracted from calculated level energies (Section 3.3). A direct observation by laser driven transition would reduce the uncertainty on the transition frequencies. Furthermore, the energy gap between the 7s7p $^3P_1$ and 7s6d $^3D_2$ levels of 150 GHz is crucial for the size of the atomic enhancement of the EDM in these states (see Section 3.4).

Here we discuss a setup which exploits two photon Raman transitions in order to improve the signal-to-noise of laser induced fluorescence spectroscopy. First we will discuss the physics of coherent two photon transitions in a three level system. Then we describe the experimental setup for the three level system $\{^1S_0$, $^1P_1$, $^3D_2\}$ in atomic barium. The measurements on barium will then be discussed in term of signal-to-noise compared to laser induced fluorescence from a beam of metastable atoms which were employed in previous measurements [63, 134].

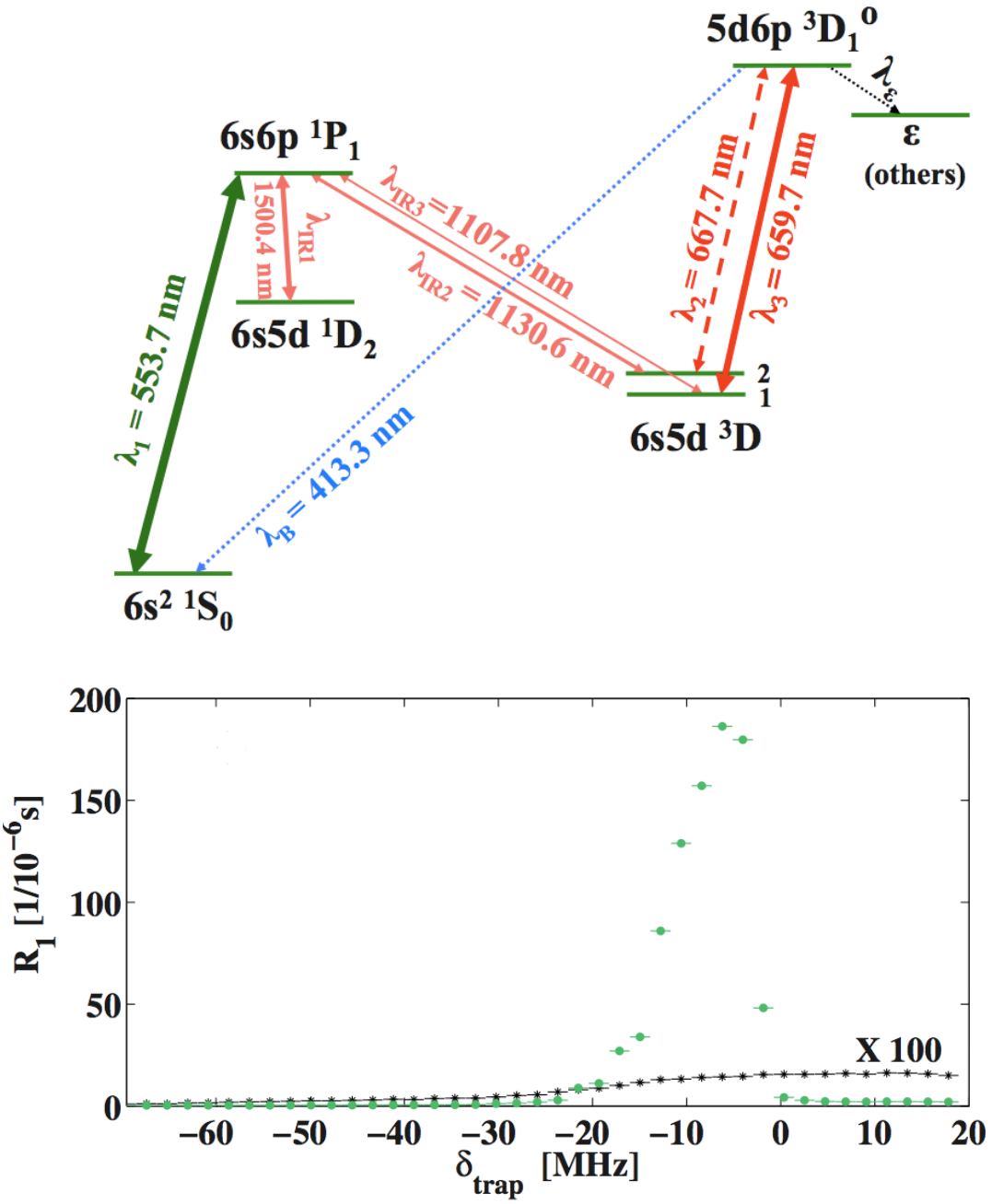

Fig. 6.13: Observation of magneto-optical trapping of barium (Top): Low-lying energy levels of atomic barium relevant for laser cooling. Full lines indicate laser-driven transitions and dashed lines show spontaneous decay channels. (Bottom): $^1S_0 - {}^1P_1$ fluorescence signal, R_1 from trapped atoms as a function of detuning, δ_{trap} of the trapping laser light at wavelength λ_1. The black points is the Doppler-free fluorescence signal arising from the MOT laser beam which is orthogonal to the atomic beam [148].

Two Photon Transition

A two-photon transition can be observed in a three level system, for example consisting of a ground state $|1\rangle$, an excited state $|2\rangle$, and a long lived state $|3\rangle$. A system simultaneously excited by two light fields at frequencies, f_1 and f_2, in

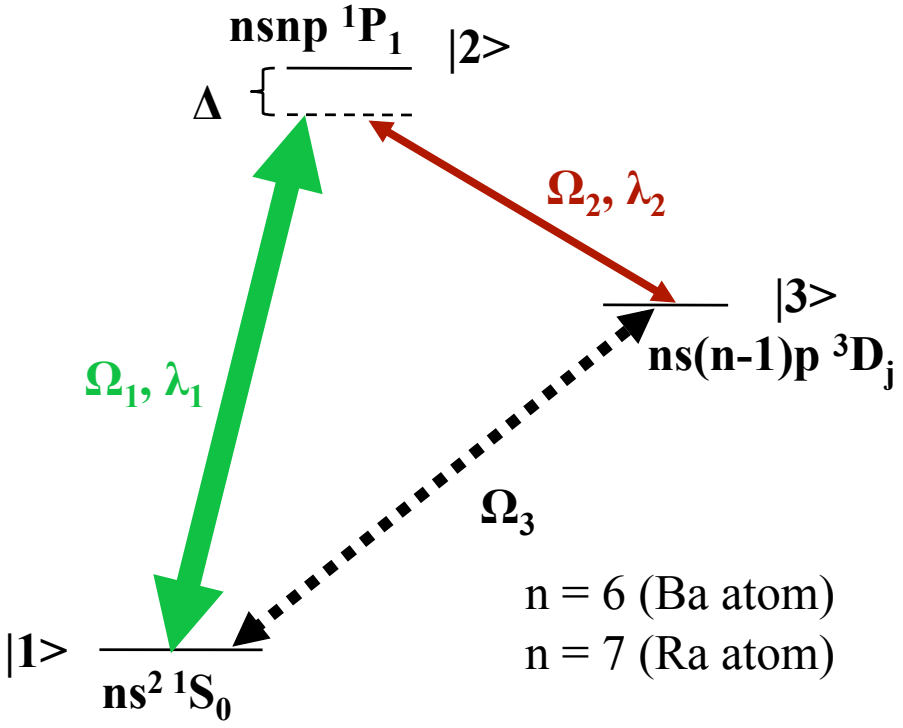

Fig. 6.14: Atomic level scheme for the observation of two-photon Raman transition in atomic barium (n = 6) and radium (n = 7). The $^1S_0$, $^1P_1$ and ^3D_j (j=1, 2) states forms three level Λ-system. They are referred to as $|1>$, $|2>$ and $|3>$. The interaction with the coherent light fields with the atomic levels are represented by the Rabi oscillation frequencies Ω_1 and Ω_2. Ω_3 represents the strength of coupling between the $^1S_0$ and the ^3D_j states by means of two-photon transition. Δ is the common detuning of the two lasers lights from their central frequencies at wavelengths λ_1 and λ_2.

such a way that the frequency difference (f_1 - f_2) matches the frequency difference between the ground state $|1\rangle$ and the $|3\rangle$ state results in a direct coupling of states $|1\rangle$ and $|3\rangle$ [149, 150]. The coupling is even present when the light fields f_1 and f_2 are detuned by a frequency Δ from the one-photon resonance condition (Fig. 6.14). The two-photon coupling yields a larger population in the state $|3\rangle$

than in the case of purely spontaneous decay. The population in $|3\rangle$ is removed from the fluorescence cycle $|1\rangle - |2\rangle$ and results in a reduction of the fluorescence from this transition. Hence, the fluorescence from the excited state can be efficiently exploited to monitor the coupling of the ground state and the metastable state.

The Raman coherence process between the ground state and the metastable state associated with a two-photon transition can lead to narrow linewidth of the dark resonance signal. Therefore, a two-photon process can be utilized as a proficient tool to probe the dipole-forbidden transitions in ions, atoms and molecules [151]. After the first experimental observation of dark resonance [152] it has been explored in many experiments. Such as high precision frequency measurements [153], single trapped ions [154, 155], optical lattice clocks [156], quantum information processing [157] and nuclear clocks [158].

A schematic overview of a three level system in atomic barium and radium is shown in Fig. 6.14. The population density at i^{th} (or j^{th}) level, is represented by the density matrix element ρ_{ij} (for $i = j$). Sum over all states fulfills

$$\sum_{i=1,2,3} \rho_{ii} = 1 \quad , \tag{6.7}$$

where i and j represents the initial and final states of the atom. For a detuning Δ of both the laser fields from the excited state the coupling strength Ω_1 and Ω_2 between the ground state and the metastable state represented by Rabi frequency can be written as

$$\Omega_3 = \frac{\Omega_1 \Omega_2}{2\Delta} \quad , \tag{6.8}$$

with the approximation $\Delta >> \Omega_1, \Omega_2$. A more detailed theoretical discussion of coherent dark resonance in three level Λ-system in atomic barium can be found in [63].

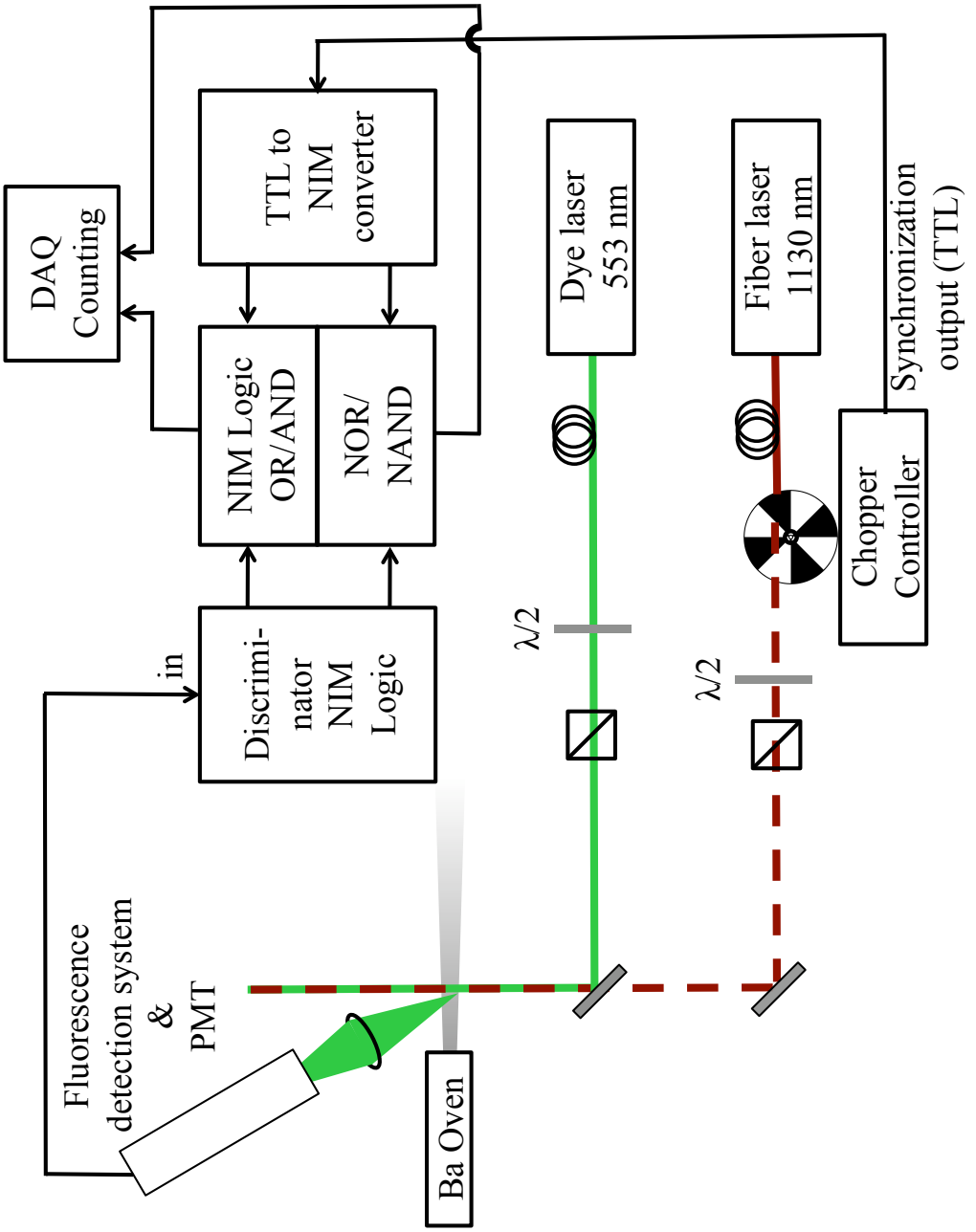

Fig. 6.15: Experimental setup for the two-photon Raman transition in ^{138}Ba. Light at wavelengths λ_1 and λ_2 are overlapped and taken to the atomic beam for two-photon spectroscopy. Light at wavelength λ_2 is chopped by a mechanical chopper. The reference signal from the chopper controller provides the timing information for the gated counting of the fluorescence at λ_1 from the atomic beam. This permits counting of the fluorescence of the one photon transition $|1\rangle - |2\rangle$ and the Raman transition at the same time. Fractional coupling of the barium atoms from the ground state to the D state is measured by taking a difference between these two signals.

Two-photon Raman transition is experimentally investigated in beam of the heavy alkaline earth atom barium. A schematic overview of the experimental setup is shown in Fig. 6.15. The $6s^2\ {}^1S_0$ ($|1\rangle$), $6s6p\ {}^1P_1$ ($|2\rangle$) and $6s5d\ {}^3D_2$ ($|3\rangle$) states in ^{138}Ba are coupled by the two laser fields at wavelengths λ_1 and λ_2 which are superimposed in copropagating direction. The laser beam direction is perpendicular to the direction of the atomic beam. Diameter of the superimposed beam is 3.0(2) mm, which defines the interaction time of 10 μs between the atoms and the laser beams. The relative polarization of the two laser beams is linear || linear. The dark resonance is monitored by observing the fluorescence from the $6s^2\ {}^1S_0$ - $6s6p\ {}^1P_1$ transition. The fluorescence is collected in a light collection system and subsequently imaged on a photomultiplier tube similar to the setup for the radium spectroscopy. The laser beam at wavelength λ_2 is chopped with a chopping frequency of 200 Hz by a mechanical chopper with 50% duty cycle. The reference output of the chopper controller is utilized to obtain gate signals from the photomultiplier. The gated signal S_{λ_1} contains information of one-photon $6s^2\ {}^1S_0$ - $6s6p\ {}^1P_1$ transition. The other signal $S_{\lambda_1\lambda_2}$ contains the count rate when the Raman transition is driven by both laser fields. The fractional depletion of the dark resonance signal S_{dark} can be written as

$$S_{dark} = \frac{S_{\lambda_1\lambda_2} - S_{\lambda_1}}{S_{\lambda_1\lambda_2} + S_{\lambda_1}} \ . \tag{6.9}$$

In Fig. 6.16 (top) green full circles represent the fluorescence signal S_{λ_1} with the presence of light at wavelength λ_1 only. The dark red open circles represent the fluorescence signal $S_{\lambda_1\lambda_2}$. Intensity of the light at wavelength λ_1 was 10(1) mW/cm^2 and the frequency of this light is scanned over the resonance. Intensity of the light at wavelength λ_2 was 90(6) mW/cm^2 and is fixed in frequency. The coupling between the ground state $|1\rangle$ and the metastable state $|3\rangle$ due to the two-photon excitation is strongest for zero detuningΔ which was chosen in this example. A maximum fractional depletion of the atoms to the metastable state represented by a dark resonance signal of 35(2) % of the total fluorescence is observed [Fig. 6.16 (bottom)].

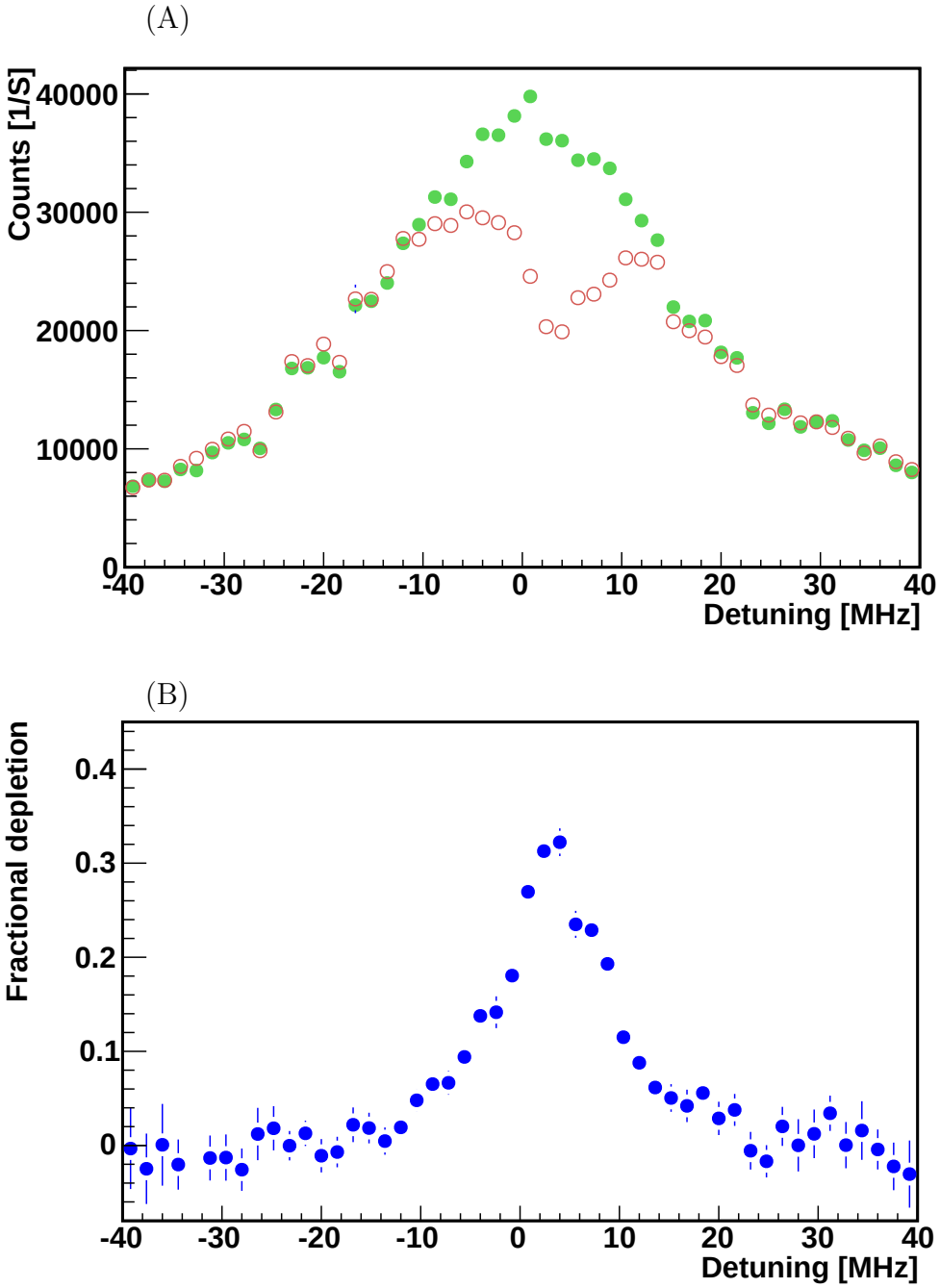

FIG. 6.16: (Top): $^1S_0 - {}^1P_1$ fluorescence signal as a function of common detuning Δ of the laser light wavelengths at λ_1 and λ_2 in ^{138}Ba atom. Green markers represent one-photon signal for laser light only at wavelength λ_1 interacting with barium atoms. Dark red markers represent two-photon signal for light at both wavelengths λ_1 and λ_2 interacting with barium atoms. (Bottom): Fractional depletion of the barium atoms from the $^1S_0$ ground state to the $^3D_2$ metastable by means of coherent Raman transition. The process causes a coherent dark resonance. The scatter in the count rates in A reflects the power fluctuation of the laser light at wavelength λ_1. This fluctuation is reduced in the differential measurement of the fractional depletion s_{dark} (B).

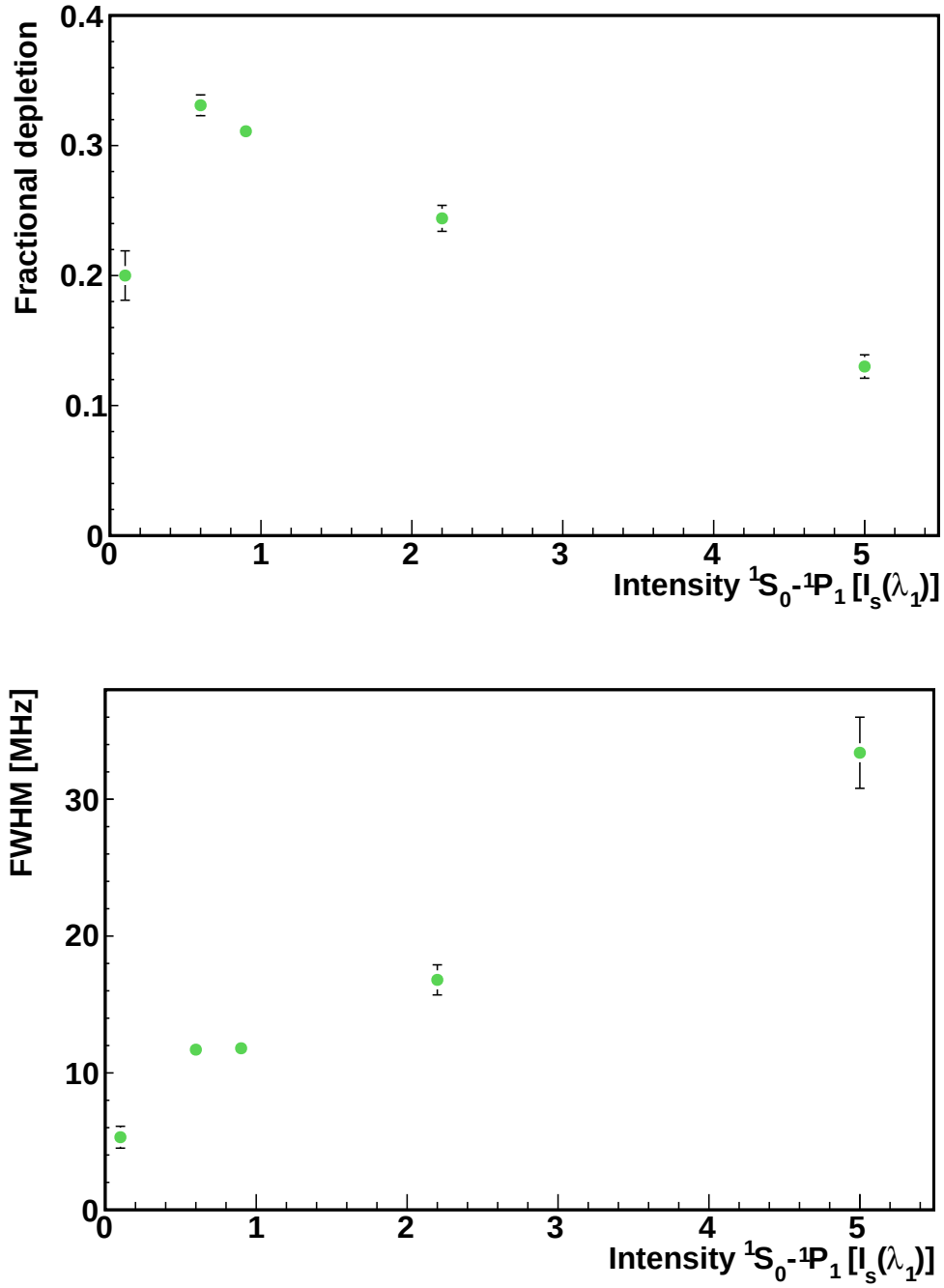

Fig. 6.17: (Top): Fractional depletion of the barium atoms from the $^1S_0$ ground state to the $^3D_2$ metastable state as a function of laser light intensity at wavelength λ_1. The depletion is maximum for an intensity which is very close to the saturation intensity of the transition at wavelength λ_1. (Bottom): FWHM of the coherent dark resonance signal as a function of the intensity of the laser light at wavelength λ_1. FWFM increases due to the power broadening as the light intensity increases.

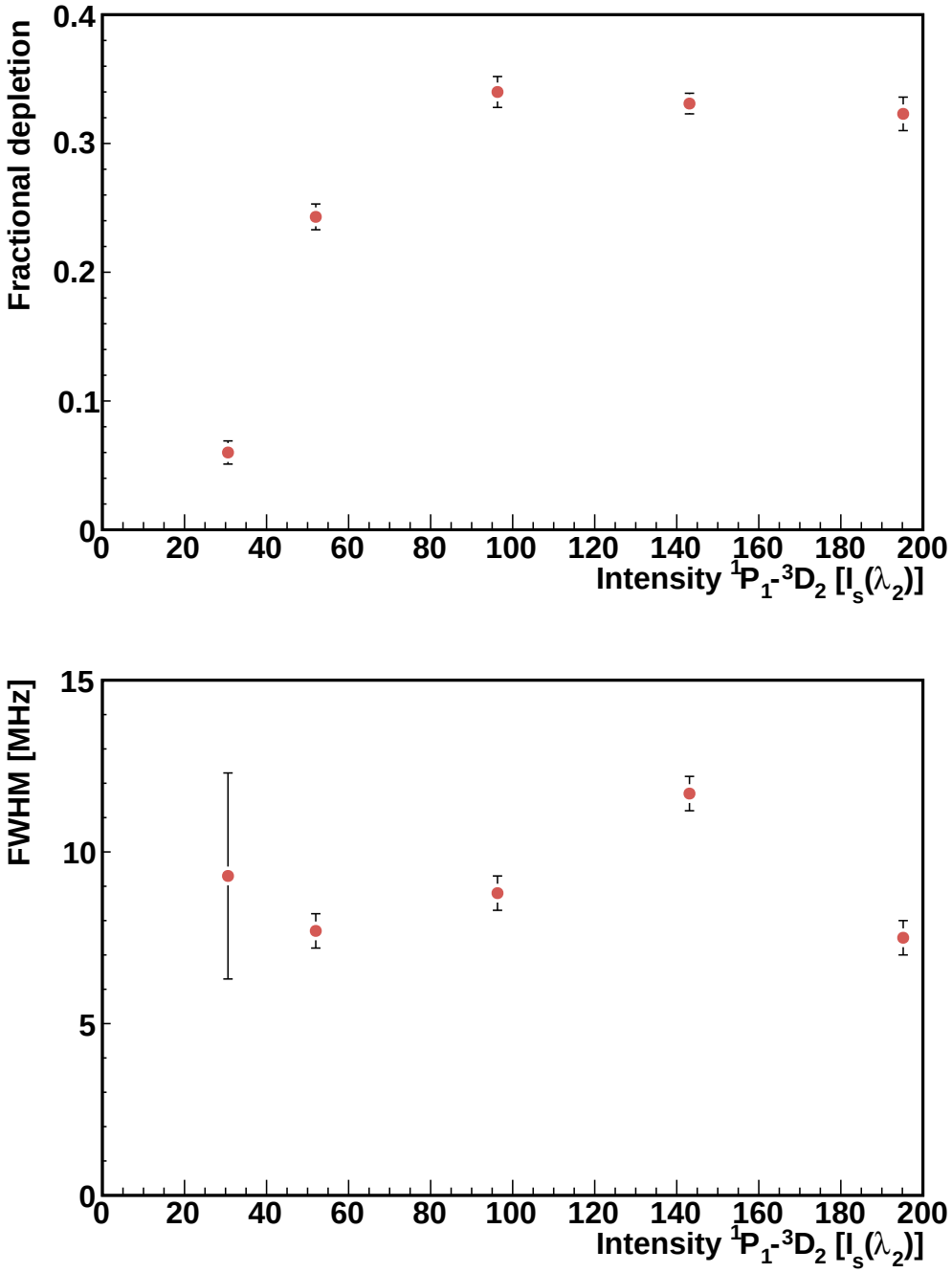

Fig. 6.18: (Top): Fractional depletion of the barium atoms from the $^1S_0$ ground state to the $^3D_2$ metastable state as a function of laser light intensity at wavelength λ_2. The depletion starts to occur at an threshold intensity which is above $20\times I_s(\lambda_2)$ and reaches a maximum at an intensity above $100\times I_s(\lambda_2)$. (Bottom): FWHM of the coherent dark resonance signal as a function of the intensity of the laser light at wavelength λ_2. FWFM does not change by a significant factor with the increase of light intensity at wavelength λ_2. This happens because the fluorescence signal collected at wavelength λ_1 is less affected due to the change of light intensity of light at wavelength λ_2.

Amplitude of fractional depletion (S_{dark}) and full width at half maximum (FWHM) of the dark resonance signal is characterized as a function of both of the laser light intensities involved in the two-photon process. One set of measurements for different intensities of the light at wavelength λ_1 while keeping the intensity of the light at wavelength λ_2 unchanged at 127(8) mW/cm^2 (Fig. 6.17) were recorded. Under this condition a maximum reduction of fluorescence is observed close to the saturation intensity $I_s^{\lambda_1}$ of the transition at wavelength λ_1. Increasing the intensity $I(\lambda_1)$ of the light at wavelength λ_1 leads to an expected increase of the width of the resonance, which is a measurement of the Rabi frequency Ω_3. Measurement is performed also for different intensities of the light at wavelength λ_2 (Fig. 6.18) while keeping the intensity of the light at wavelength λ_1 unchanged at 10(1) mW/cm^2. S_{dark} reaches maximum at an intensity $\sim 100 \times I_s(\lambda_2)$. No significant change in the FWHM is observed for the change of intensity $I(\lambda_2)$ of the light at wavelength λ_2.

Signal-to-noise of the dark resonance can be written as

$$\frac{S}{N} = \frac{S_{dark} \times FWHM \times \gamma_p(\lambda_1)}{\sqrt{FWHM \times \gamma_p(\lambda_1) + \left(\frac{I(\lambda_1)}{I_s^{\lambda_1}}\right) \times S_b}} , \tag{6.10}$$

where $\gamma_p(\lambda_1)$ is the scattering rate of the transition at wavelength λ_1. Best signal-to-noise is observed near the saturation intensity of the transition at wavelength λ_1 (Fig. 6.19).

Sensitivity of two-photon process for probing 7s6d $^3D_2$ state in Radium

Precise determination of the energy and lifetime of the 7s6d $^3D_2$ state in atomic radium is indispensable for efficient laser cooling of radium atoms. The knowledge also plays a crucial role for electric dipole moment measurements in radium atom [77, 82].

Detection of the metastable 7s6d $^3D_2$ state can be performed by two subsequent one-photon transitions. The detection scheme then consists of two steps

(i) Production of metastable atoms by exciting the atoms from the ground state to the 7s7p $^1P_1$ state. With the assumption that all the atoms in the excited state decay to the metastable state, about 20 % of the atoms populate the 7s6d $^3D_2$ state.

(ii) Exciting the metastable atoms from the 7s6d $^3D_2$ state to the 7s7p $^1P_1$ state. This excitation is followed by a photon burst from the 7s7p $^1P_1$ state

while the atoms decay to the ground state.

For this sequential detection the number of photons/atom in the signal are

$$S_{2\times one-photon} = B_r \times N_{photon} \ , \tag{6.11}$$

where, B_r represents the fraction of atoms which populates the metastable state and N_{photon} is the number of photon emitted per atom. For the 7s6d $^3D_2$ state in atomic radium the number of photons per atom in the sequential detection signal is 0.2 under the above assumptions.

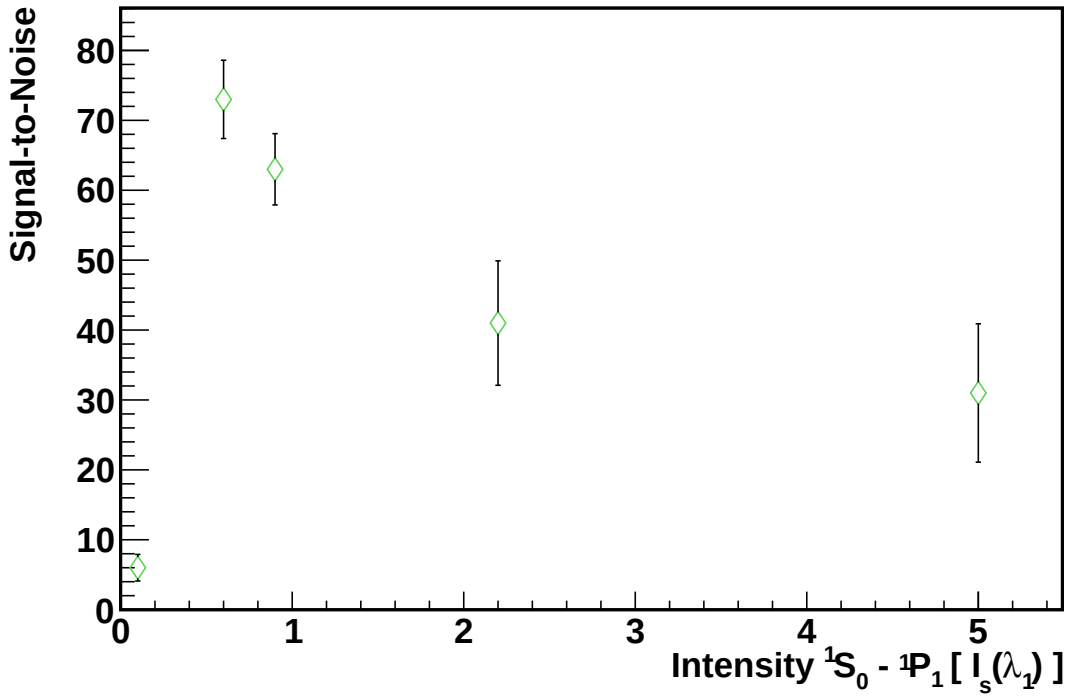

Fig. 6.19: Signal-to-noise of the coherent dark resonance for the three level system $\{^1S_0, {}^1P_1, {}^3D_2\}$ in ^{138}Ba atom as a function of intensity of light at wavelength λ_1. Intensity of the light at wavelength λ_2 is $145(3)\times I_s(\lambda_2)$. Best signal-to-noise is observed for an intensity of the light at wavelength λ_1 which is close to the saturation intensity of the transition at wavelength λ_1.

Another detection scheme for the metastable 7s6d $^3D_2$ state is performing two-photon excitation. The number of dark photons per atom for this detection scheme can be written as

$$S_{two-photon} = \gamma_p \times \Delta t \times S_{dark} \ , \tag{6.12}$$

where, γ_p represents the scattering rate of the atoms from the 7s7p $^1P_1$ excited state and Δt represents the time atoms spend in the superimposed laser beams for two photon excitation. At the saturation intensity of the $7s^2\ ^1S_0$ - 7s7p $^1P_1$ transition in radium γ_p is 3×10^7 s^{-1}. For a Δt of 10 μs and S_{dark} of 35 % the number of uncounted photons per atom in the signal is $S_{two-photon} = 105$. The number of uncounted photons in the two-photon signal is more than a factor of 500 more compare to the number of photons in the sequential detection of the 7s6d $^3D_2$ state by two one-photon spectroscopy.

6.5 conclusion

In this chapter we presented the results obtained with the effusive atomic beam of ^{225}Ra (Chapter 4) and the laser system and calibration (Chapter 5) on the laser spectroscopy of atomic radium. We obtained values for the transitions from the ground state ($7s^2\ ^1S_0$ - 7s7p $^1P_1$, $7s^2\ ^1S_0$ - 7s7p $^3P_1$) with an accuracy sufficient for laser cooling and manipulation of trapped radium atoms. Furthermore, we demonstrated a spectroscopy technique for the sensitive detection of weak transitions by employing Raman resonances. This technique is well suited for optical detection of the weak repump transitions from metastable D-states in radium. With this we have a complete set of building blocks to implement efficient laser cooling and trapping method for radium, which have been demonstrated with barium [148].

Chapter 7

Prospects for a Measurement of a Permanent Electric Dipole Moment in Radium Atoms

This thesis was written in the framework of the TRIμP group at KVI. The main interest of the group is in studies of fundamental interactions and symmetries. The search for permanent electric dipole moments, which violate parity (P) and charge conjugation (C) simultaneously has a strong leverage on model building beyond the Standard Model. Such searches, which exploit low energy precision measurements of properties of elementary particles, are complementary to the direct searches for new particles like the recent discovery of a new boson in the experiments ATLAS and CMS at LHC, CERN [7, 8]. Limits on EDMs of fundamental particles are providing the length scale of substructure of fundamental particles which is not accessible by direct searches.

Searches for *permanent Electric Dipole Moments* are conducted on many different objects, from elementary particles (μ, τ) to neutron, proton and deuteron and even complex systems like atoms and molecules. The systems are described to a very high degree by the known interactions. We have categorized the different experimental approaches in terms of their statistical sensitivity and sensitivity to new physics, which can be orders of magnitude larger due to intrinsic enhancement factors of the chosen systems. A measurement of a non-zero EDM in a single system does not provide a unique identification of the underlying process which generates the EDM. This is a consequence of the complex structure of the systems studied and the particular enhancement factors. Improvement of the sensitivity for some of the ongoing experiments, e.g. the neutron EDM, is only

possible by a larger total number of particles which is the product of the available rate and measurement time. Currently several collaborations worldwide are active in this field [53].

The sensitivity to fundamental physics can be increased by improving existing experimental strategies or by developing new experimental approaches. We followed the latter one. Here we were guided by selecting a system in which a large natural enhancement of EDMs is present. Apart from the enhancement which is proportional to the third power of the nuclear charge, some systems provide additional large factors due to molecular, atomic and nuclear structure. A careful analysis of the requirements for an EDM measurement in such a system is required and the experimental techniques need to be developed. Special care has to be taken in order to extract the small effect from the dominating atomic physics properties contributions. In addition, the availability of the respective atoms or molecules of interest can provide an additional challange for the development of a new EDM experiment.

Another major step towards new and sensitive EDM experiments is the exploration of new experimental strategies. We followed the strategy to employ ultracold atoms in a neutral atom trap which becomes attracive due to the advances in laser cooling and trapping methods in the two decades. A demonstration of the outmost sensitivity and control over external perturbation are neutral atom optical clocks in optical latices [146,159,160]. A first proposal for an EDM search with trapped atoms was presented for Yb [161]. The main advantages are possible long coherence times, very small volumes over which magnetic and electric fields have to be controlled and low velocities. Furthermore, there are experimental approaches for the electron EDM with Cs or Rb in optical lattices [162].

The described boundary conditions were the basic guidlines for this work. The identification of the promising candidate system with direct consequences for the availability of the material. Further, the implementation of the experimental strategies have to be developed. The main part of the thesis discusses these aspects in detail for EDM searches in atomic radium. It builds on work in the TRIμP group [63,89,134,148] and at Argonne National Lab [78–80].

Radium was selected because of its large enhancement factors for intrinsic EDMs, which are originating from the nuclear and atomic properties (Chapter 3). One additional aspect is that some states are sensitive to nuclear induced EDMs and others are sensitive to the electron EDM. The enhancement of the electron EDM in the 7s6d ^{3}D$_1$ is almost four orders of magnitude while the nuclear induced EDM is enhanced in the 7s6d ^{3}D$_2$ state by a factor of 10^5 over ^{199}Hg

EDM. In addition some octupole deformed radium nuclei lead to enhancements by a factor of 10^2 - 10^3 over ^{199}Hg EDM. The currently ongoing measurement campain on collectivity in these isotopes which can be related to the octupole induced enhancement factors at the ISOLDE facility at CERN in an attempt to lower the uncertainty of the nuclear enhancement [87]. The experiment was triggered by the interest in EDM searches.

The scarcity of radium isotopes with nuclear spin $I > 0$ will only allow sensitive experiments with confined atoms and long coherence times. The implementation of this experimental strategy to radium requires laser cooling of this heavy alkaline earth atom. The atomic structure of radium requires a complex approach to laser cooling because of the unavailability of a strong closed transition. Effcient laser cooling This was approached by the group at ANL with laser cooling on the weak intercombination line which leads to an inherent low trapping efficiency of 10^{-6} [80]. A way out of this is several additional lasers in the cooling process to avoid losses from the cooling cycle. Our group has demonstrated this successfully with the chemical homologue barium. In this case a significant increase in trapping efficiency of four orders of magnitude can be achieved [148]. The transfer of this cooling scheme in coupled to driving weak transitions which have not yet spectroscopically observed. The strategy for observing these weak transitions was developed in this thesis.

We discuss a setup for a sensitive measurement of weak metastable states, which was demonstrated with transitions in the chemical homologue barium (Chapter 5). The transitions from the metastable D states in atomic radium are essential repump transitions for effcient slowing of the atomic beam of radium. Furthermore, the energy gap between the $^3D_2$ and $^3P_1$ state determines the enhancement factor for the nuclear EDM. We have demonstrated a sensitive detection scheme for weak transition originating from metastable D-states with ^{138}Ba. The scheme comprises of twophoton Raman spectroscopy. An increase of more than two orders of magnitude in signal-to-noise compare to laser induced fluorescence spectroscopy has been achieved. This opens the path to observe weak transitions for scarce atomic species.

Source of Radium Iosotopes

A significant part of the work was devoted to sources of a set of radium isotopes and the subsequent conversion into an intense atomic beam (Chapter 4). Radium is available from online production at radioactive beam facilities. We have

executed experiments with beams at the TRIμP facility. Here, isotopes with live-times of a few seconds to minutes ($^{211-214}$Ra) are produced in fusion-evaporation reactions in inverse kinematics [94,97]. The production reaction is highly isotope specific and pure beams of radium can be produced. The available rates are 650 s^{-1} per particle nA [94] of lead beam with a maximum 2 μA Pb. The produced isotopes are also exploited. The results are for laser spectroscopy of trapped Ra^+ which aims at a measurement of atomic parity violation [95, 163, 164].

Some isotopes of radium near the valley of stability are available from radioactive sources. These are in particular ^{225}Ra from an alpha decay of ^{229}Th and ^{223}Ra from ^{227}Ac. We are interested in ^{225}Ra because of the nulcear spin I=1/2. One possibility is radiochemical extraction of radium from a thorium source, which is done at Oak Ridge National Laboratory for the radium experiment at Argonne National Laboratory [90]. The chemically extracted radium is then transfered to an oven crucible which is then place in a vacum system. The crucible is refilled after the radium has decayed or heated out of the oven.

Radium Atomic Beams

We have investigated various possibilities to build an atomic beam of radium and characterized two types of atomic beam of radium.

The first type is from a ^{229}Th source. This is a beam of ^{225}Ra atoms. This beam allows to perform spectroscopic measurement for 1000 s in each half-life of ^{225}Ra isotope. The second type of atomic beam characterized in this work is by converting ions to atoms at metal surface. Therefore the concept of the ion-to-atom converter is not isotope specific. It can be used for alkaline and alkaline earth elements at facilities where ion beams are available.

The Lasers for Spectroscopy of Radium

The laser and atomic physics system has been designed and setup at KVI.

We exploited the offline atomic beam of ^{225}Ra for Doppler-free laser induced spectroscopy of transition from the ground state where we achieved several results. We investigated the strong $7s^2\ ^1S_0$ - $7s7p\ ^1P_1$ transition which is the main transition for effcient slowing of atoms and capture range of a magneto optical trap. We have measured the absolute frequency of this transition with an optical frequency comb and relative against saturated absorption spectroscopy of $^{130}Te_2$. The measurements yield the absolute frequency of the $7s2\ ^1S_0$ - $7s7p\ ^1P_1$ transition in atomic radium with an uncertainty of 5 MHz, which is more than factor

of 30 better compare to previous measurements for same transition in ^{226}Ra. The hyperfine structure interval of the 7s7p $^1P_1$ in ^{225}Ra is in good agreement with an earlier measurement with a similar uncertainty. Furthermore, the weak intercombinations line 7s2 $^1S_0$ - 7s7p $^3P_1$ was is the most suitable transition for trapping radium atoms from a slow beam and keeping the trapped atoms in the cooling cycle for a longer time. The measurement yielded an absolute frequency of the 7s2 $^1S_0$ - 7s7p $^3P_1$ transition with an uncertainty < 5 MHz, which is factor of 6 improvement over previous measurement. The absolute frequencies and the reference lines in molecular tellurium and iodine are fundamental in a reliable and stable laser cooling and trapping setup for the radium atom.

The developed tools for intense radium atomic beams and the atomic physics tools together with the laser spectroscopy of radium are major ingreedients in a sensitive search for permanent electric dipole moments in radium isotopes. Intense radium sources are available a existing, i.e. ISOLDE [165], and future, i.e. ISOL@Myrrha [166], radioactive beam facilities which gives access not only to the long lived radium isotopes around ^{225}Ra, but also to the short lived ^{213}Ra.

Chapter 8

Summary

Discoveries in experimental endeavors and theories till date have provided ever deeper insights into the structure and behavior of the most fundamental building blocks of nature. The Standard Model (SM) summarizes the present understanding of particle physics in one coherent physical theory. This includes even the recent results from experiments at the Large Hadron Collider (LHC), CERN at Geneva, Switzerland. However, the SM does not provide answers to many yet open questions. For example, the origin of parity violation, the number of fundamental fermion generations and the dominance of matter over antimatter in the universe are not yet explained. The search for answers to such questions provides the driving force to performing precision experiments with highest possible sensitivity at low energies.

The SM knows the three discrete symmetries, charge conjugation (C), parity (P) and time reversal (T). The violations of these symmetries in some interactions produce major constrains for the underlying theory. The CP violation can be studied by searching for *permanent Electric Dipole Moments* (EDMs) in atomic physics experiments. Currently several experiments worldwide are underway in this field. Providing stringent experimental upper bound on an atomic EDM, e.g. the EDM of ^{199}Hg is $|d(^{199}\mathrm{Hg})| < 3.1 \times 10^{-29}$ e cm.

Radium provides the largest enhancement factors for intrinsic EDMs of any atomic system. They arise from the particular nuclear and atomic properties. One additional aspect is that some states are sensitive to nuclear induced EDMs and others are sensitive to the electron EDM. The enhancement of the electron EDM in the 7s6d $^3\mathrm{D}_1$ is almost four orders of magnitude while the nuclear induced EDM is enhanced in the 7s6d $^3\mathrm{D}_2$ state by a factor of 10^5 over ^{199}Hg EDM. In addition some octupole deformed radium nuclei lead to enhancements by a factor

of 10^2 - 10^3 over ^{199}Hg EDM. We have identified the most sensitive system, radium for our experiment. This thesis analyses possible EDM searches in radium and provides steps towards a measurement.

The scarcity of radium isotopes with nuclear spin $I > 0$ will only allow sensitive experiments with confined atoms and long coherence times. The implementation of this experimental strategy to radium requires laser cooling of this heavy alkaline earth atom. The atomic structure of radium requires a complex approach to laser cooling because of the unavailability of a strong closed transition. Our group has demonstrated this successfully with the chemical homologue barium. The transfer of this cooling scheme in radium is coupled to driving weak transitions which have not yet spectroscopically observed. The strategy for observing these week transitions was developed in this thesis.

We have investigated possibilities to create an atomic beam of radioactive radium isotopes and characterized two types of effusive thermal beams. One option is to collect radium from a radioactive source of thorium (^{229}Th) inside of the heated crucible of an oven. We successfully created the first thermal beam of atomic radium atoms with a flux of 10^6 atoms/(s cm^2) which enabled laser spectroscopic studies of the atomic structure of radium. Short lived isotopes of radium require a different approach since they are only available as ion beams at radioactive beam facilities. We have observed the neutralization of radium ions on a metallic surface (e.g. zirconium) and the subsequent release of neutral radium when the metal is heated. The release at temperature above 1300 K is first compared to the lifetime of the isotopes of interest and an ion-to-atom converter is designed which can be employed at radioactive beam facilities to create intense atomic beams.

We exploited the offline atomic beam of ^{225}Ra for Doppler-free laser induced spectroscopy of transition from the ground state where we achieved several results. We investigated the strong $7s^2\ ^1S_0$ - $7s7p\ ^1P_1$ transition which is the main transition for effcient slowing of atoms and capture range of a magneto optical trap. We have determined the absolute frequency of this transition with an optical frequency comb and relative against molecular reference transitions in $^{130}Te_2$. The absolute frequency accuracy of the $7s^2\ ^1S_0$ - $7s7p\ ^1P_1$ transition is improved by more than factor of 30 better compare to previous measurements and is now known with an uncertainty which is smaller than the natural linewidth of the transition. The hyperfine structure interval of the $7s7p\ ^1P_1$ in ^{225}Ra is in good agreement with an earlier measurement with a similar accuracy. Furthermore, the weak intercombinations line $7s^2\ ^1S_0$ - $7s7p\ ^3P_1$ is the most suitable transition for

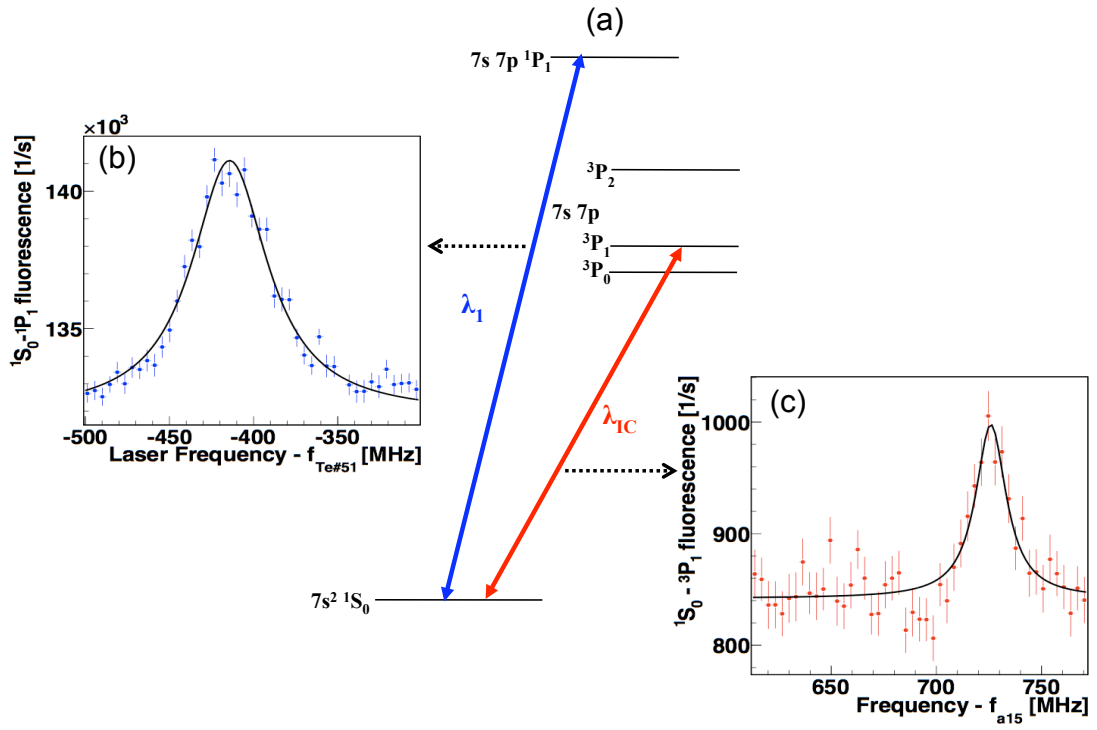

FIG. 8.1: (a) Energy level structure of atomic radium. Fluorescence signals from the (b) $^1S_0 - {}^1P_1$ transition at wavelength λ_1 and the (c) $^1S_0 - {}^3P_1$ transition at wavelength λ_{IC}, which permits the determination of the absolute transition frequencies.

trapping radium atoms from a slow beam and keeping the trapped atoms in the cooling cycle for a longer time. The measurement yielded an absolute frequency of the 7s2 $^1S_0$ - 7s7p $^3P_1$ transition with an accuracy better than the linewidth of the transition, which is factor of 6 improvement over previous measurement. The absolute frequencies and the reference lines in molecular tellurium and iodine are fundamental in a reliable and stable laser cooling and trapping setup for the radium atom.

The developed tools for intense radium atomic beams and the atomic physics tools together with the laser spectroscopy of radium are major ingredients in a sensitive search for *permanent Electric Dipole Moments* in radium isotopes.

Chapter 9

Samenvatting

Ontdekkingen in experimentele en theoretische natuurkunde hebben steeds dieper inzicht verschaft in de structuur en het gedrag van de meest fundamentele bouwstenen van de natuur. Het Standaard Model beschrijft ons huidige begrip van de elementaire deeltjesfysica in één coherente theorie, inclusief de recente resultaten van experimenten bij de Large Hadron Collider op CERN in het Zwitserse Geneve. Het Standaard Model heeft echter nog een aantal open vragen. Zo worden pariteitsschending, het aantal fundamentele fermion generaties en de overheersing van materie over antimaterie in het heelal niet verklaard. Het beantwoorden van zulke vragen is de drijvende kracht voor het uitvoeren van precisie-experimenten bij lage energie.

De drie discrete symmetrieën ladingconjugatie (C), pariteit (P) en tijdsomkeer (T) zijn onderdeel van het Standaard Model. Het behoud en de schending van deze symmetrieën leggen een enorme beperking op aan de theorie. De schending van CP kan bestudeerd worden door naar *permanente electrische dipoolmomenten* (EDMs) te zoeken in experimenten met atomen. Momenteel zijn er wereldwijd een aantal experimenten onderweg op dit gebied. Deze zetten stringente bovengrenzen aan atomaire EDMs, zoals bijvoorbeeld $|d(^{199}\mathrm{Hg})| < 3.1 \times 10^{-29}$ e cm.

Radium biedt door z'n atomaire structuur de grootste versterkingsfactoren voor intrinsieke EDMs. Sommige toestanden zijn gevoelig voor het EDM van de kern, terwijl anderen gevoelig zijn voor het elektron EDM. De versterking van het elektron EDM in de 7s6d $^3\mathrm{D}_1$ toestand is bijna vier ordes van grootte, terwijl de invloed van de kern EDM in de 7s6d $^3\mathrm{D}_2$ toestand versterkt is met een factor 10^5 ten opzichte van die van ^{199}Hg. Voor octupool-gedeformeerde kernen wordt de kern EDM zelfs nog verder versterkt met 10^2 - 10^3. In dit proefschrift worden de mogelijkheden voor een zoektocht naar een EDM in radium geanalyseerd en

worden een aantal stappen gezet.

De zeldzaamheid van radiumisotopen met kernspin I>0 maakt het alleen mogelijke om gevoelige experimenten te doen met ingevangen atomen en met lange coherentietijden. De implementatie van een experimentele strategie voor radium vereist laserkoeling van dit zware aard-alkali atoom. De atomaire structuur van radium, waarin een sterke gesloten overgang afwezig is, compliceert laserkoeling. Onze groep heeft laserkoeling van het chemisch homologe barium gedemonstreerd. Het ontwikkelde koel-schema voor radium bevat zwakke atomaire overgangen die nog niet spectroscopisch waargenomen zijn. In dit proefschrift is de ontwikkeling van een strategie voor het waarnemen van deze zwakke overgangen beschreven.

We hebben onderzocht welke mogelijkheden er zijn voor het maken van een atomaire bundel van radioactieve radiumisotopen en hebben twee soorten thermische bundels gekarakteriseerd. Eén mogelijkheid is het verzamelen van radium uit een thoriumbron (^{229}Th) in een oven. We zijn er in geslaagd om de eerste thermische bundel van atomair radium te maken met een flux van 10^6 atomen/(s cm^2). Dit maakt het mogelijk om laser-spectroscopisch onderzoek te doen naar de atoomstructuur van radium. Kortlevende radiumisotopen vergen een andere benadering want zij zijn alleen beschikbaar als ionenbundels bij radioactieve bundel faciliteiten. We hebben de neutralizatie van radiumionen waargenomen op metallische opervlakken (bijv. zirconium) en de daaropvolgende emissie als atoom als het metaal verwarmd word. De emissiesnelheid bij temperaturen boven 1300 K is vergelijkbaar met de levensduur van de gewenste isotopen. Op basis hier-van is een ion-naar-atoom omzetter ontwikkeld die gebruikt kan worden bij radioactieve bundel faciliteiten om intense atoombundels te maken.

We hebben de offline atomaire bundel van ^{225}Ra gebruikt om Doppler-vrije laser spectroscopie te doen aan de overgang vanuit de atomaire grondtoestand. We hebben de sterke 7s2 ^{1}S$_0$ - 7s7p ^{1}P$_1$ overgang bestudeerd. Deze overgang is de basis voor het efficient afremmen van atomen en het invangen in een magneto-optische val. We hebben de absolute frequentie van deze overgang bepaald ten opzichte van een optische frequentie-kam en relatief ten opzichte van moleculaire referentielijnen in ^{130}Te$_2$. De absolute nauwkeurigheid in de frequentie van deze overgang is met meer dan een factor 30 verbeterd ten opzichte van eerdere metingen en is nu bekend met een precisie beter dan de natuurlijke lijnbreedte. De gemeten hyperfijn-structuur van de 7s7p ^{1}P$_1$ toestand in ^{225}Ra komt goed overeen met eerdere metingen met een vergelijkbare precisie. De zwakke overgang 7s2 ^{1}S$_0$ - 7s7p ^{3}P$_1$ is het meest geschikt voor het invangen van langzame radium atomen en om ze vervolgens langere tijd in de koelcyclus te houden. De meting van

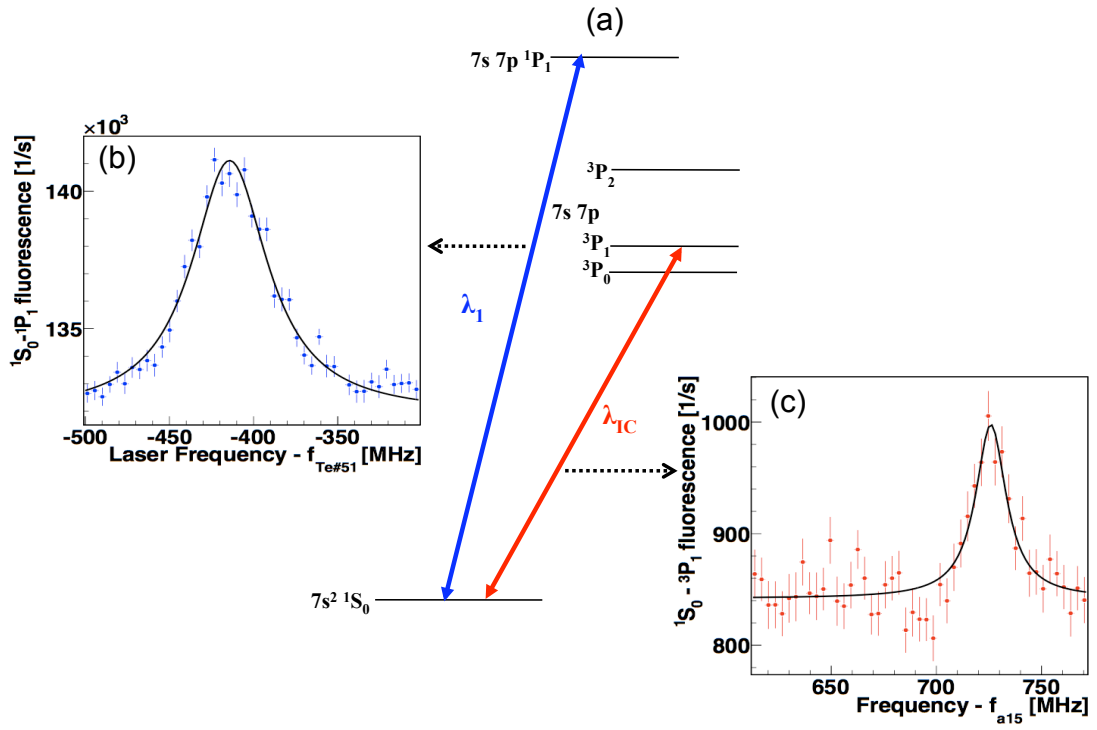

FIG. 9.1: (a) Energieniveaus van het radiumatoom. Waargenomen fluorescentiesignalen van de overgang (b) $^1S_0$ - $^1P_1$ bij golflengte λ_1 en (c) $^1S_0$ - $^3P_1$ bij golflengte λ_{IC}. Deze resultaten maken het mogelijk om de absolute frequenties van de overgangen te bepalen.

de absolute frequentie van deze overgang heeft een precisie die beter is dan de lijnbreedte en is zes keer beter dan eerdere metingen. De absolute frequenties en de referentielijnen in moleculair tellurium en iodium zijn de basis voor een betrouwbare en stabiele opstelling voor het laserkoelen en invangen van radium atomen.

De ontwikkelde mogelijkheden voor het maken van intense bundels van atomair radium en de bijbehoren apparatuur, samen met de laser spectroscopie van radium zijn de hoofdingredienten van een gevoelige zoektocht naar *permanente electric dipoolmomenten* in radium isotopen.

Appendix A

Experimental Setup for Laser Cooling and Trapping of ^{225}Ra

Efficient laser cooling and trapping of radium requires an extended cooling cycle consists of at least five levels which are $7s^2\ {}^1S_0$, $7s7p\ {}^1P_1$, $7s7p\ {}^3P_1$, $7s7p\ {}^1P_1$, $7s6d\ {}^3D_2$ and $7s6d\ {}^3D_1$. The complexity in cooling cycle arises because of leakage from the strongest optical transition to transitions connecting metastable states. In this appendix we describe an experimental setup for slowing radium atoms from a thermal atomic beam and a magneto optical trap (MOT) for capturing slowed radium atoms with high efficiency.

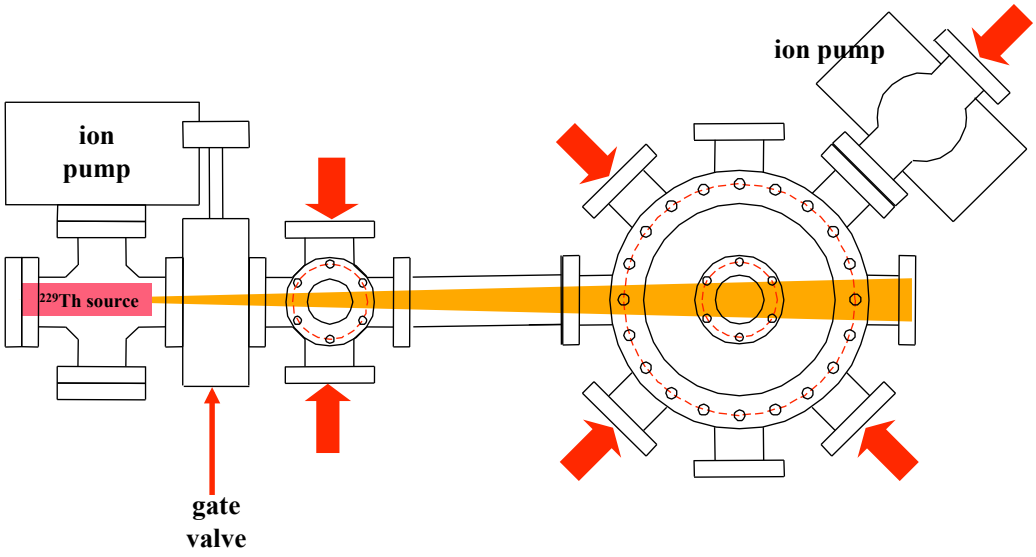

FIG. A.1: Vacuum chamber for laser cooling and trapping of ^{225}Ra.

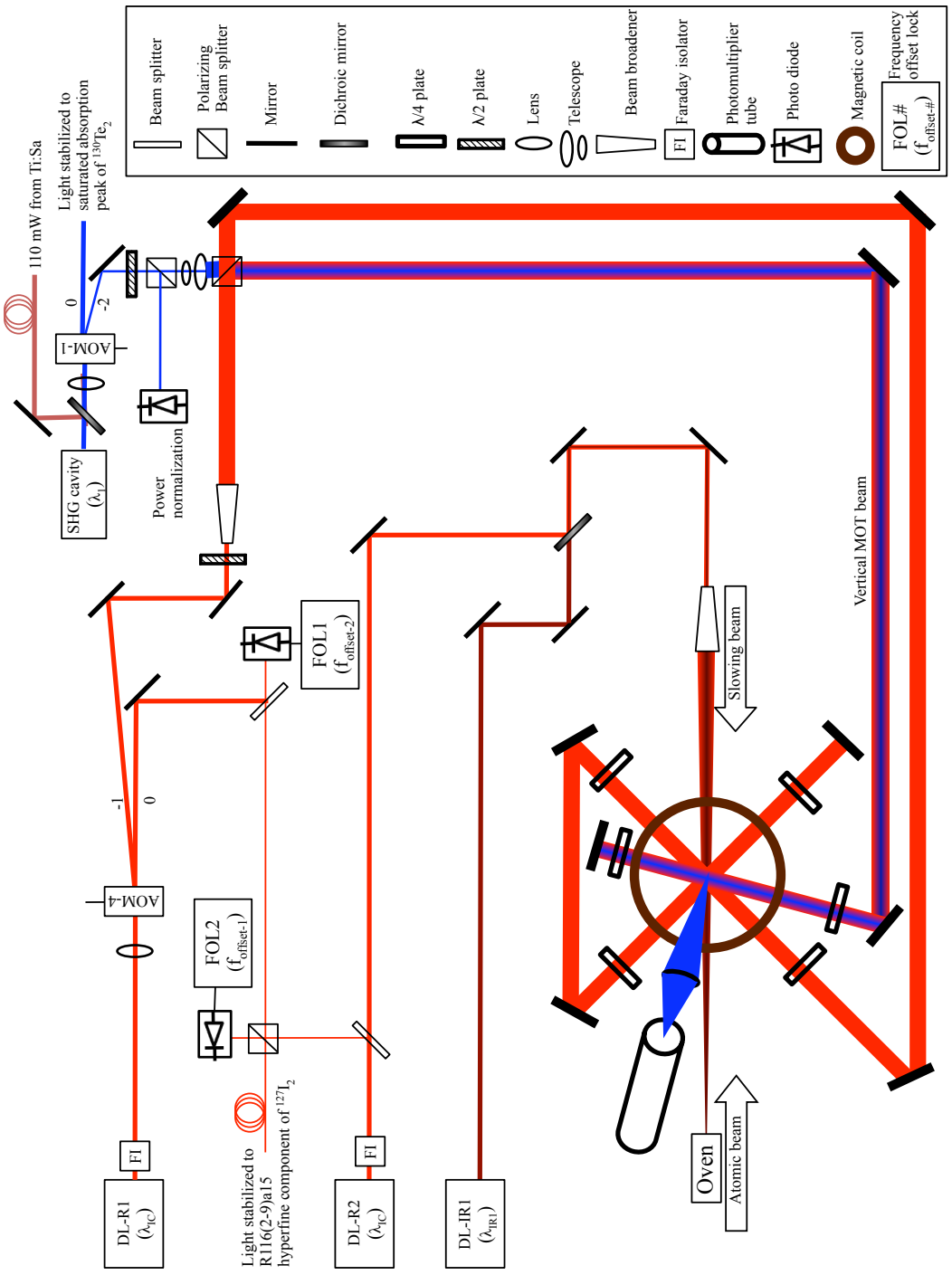

Fig. A.2: Optical layout of the experimental setup for laser cooling and trapping of ^{225}Ra.

The vacuum chamber for this experiment consists of a resistively heated effusive beam of ^{225}Ra atoms, an optical port for transverse laser cooling of the radium atomic beam and a chamber with sufficient optical access for the laser beams for slowing and magneto optical trapping (Fig. A.1). The detailed description of the ^{225}Ra atomic beam source is presented in Section 4.2. When the oven is operating, the pressure inside the vacuum chamber is maintained to 10^{-8} mbar by two ion pumps attached to the chamber.

Laser light at four wavelengths, λ_1, λ_{IC}, λ_{IR1} and λ_{IR2} (not shown in Fig. A.2) are employed in the setup. The generation of light at wavelength λ_1 by frequency doubling the output of a Ti:Sapphire laser (Section 5.1). The light at the other wavelengths is obtained from home build diode lasers (Section 5.2). The light at wavelength λ_1 is used for obtaining the strongest slowing forces to the radium atomic beam as well as detection of laser cooled atoms. Light at wavelengths λ_{IR1} and λ_{IR2} are overlapped with the slowing laser beam in order to provide repumping of atoms from metastable states. High signal-to-noise can be obtained by modulating the light intensity at wavelength λ_1 by an acousto optical modulator AOM1. Frequency offset locking is employed to provide suitable detuning for the trapping laser beam at wavelength λ_{IC}. A set of six $\lambda/4$ plates which works for both wavelengths λ_1 and λ_{IC} permit the control of the polarization of the six trapping laser beams in three orthogonal directions. A pair of magnetic coils electrically connected in anti-Helmholtz configuration provides the quadrupole magnetic field for holding the captured radium atoms in the MOT.

Appendix B

Data Acquisition System

The data acquisition system (DAQ) is utilized to control the components involved in the experiment and to acquire the data from the experiment. In order to provide an integrated data acquisition system a Control and Distributed Data-acquisition Integrated Environment (CADDIE) was developed at KVI.

The data stream from the experiment consists of analog, digital and wavelength-meter data. Analog and digital data are recorded using scalar module by a CADDIE installed in VME computer. Analog voltages are converted to frequencies by using voltage to frequency converter (VFC) before sending to scalar module. Data from each wavelength meter (WLM) is recorded by a CADDIE installed in the same computer for controlling the WLM. The data streams from different CADDIEs are combined by a master system called CatchCADDIE, which takes care of the storage and make the data available for online analysis.

In order to make the CADDIE data events available for online and offline analysis a programme, Bogey is developed. Bogey is an object oriented software based on analysis framework ROOT, which is a C++ based framework for large scale data analysis. Bogey interpret the CADDIE data format and makes it available in the form of ROOT classes.

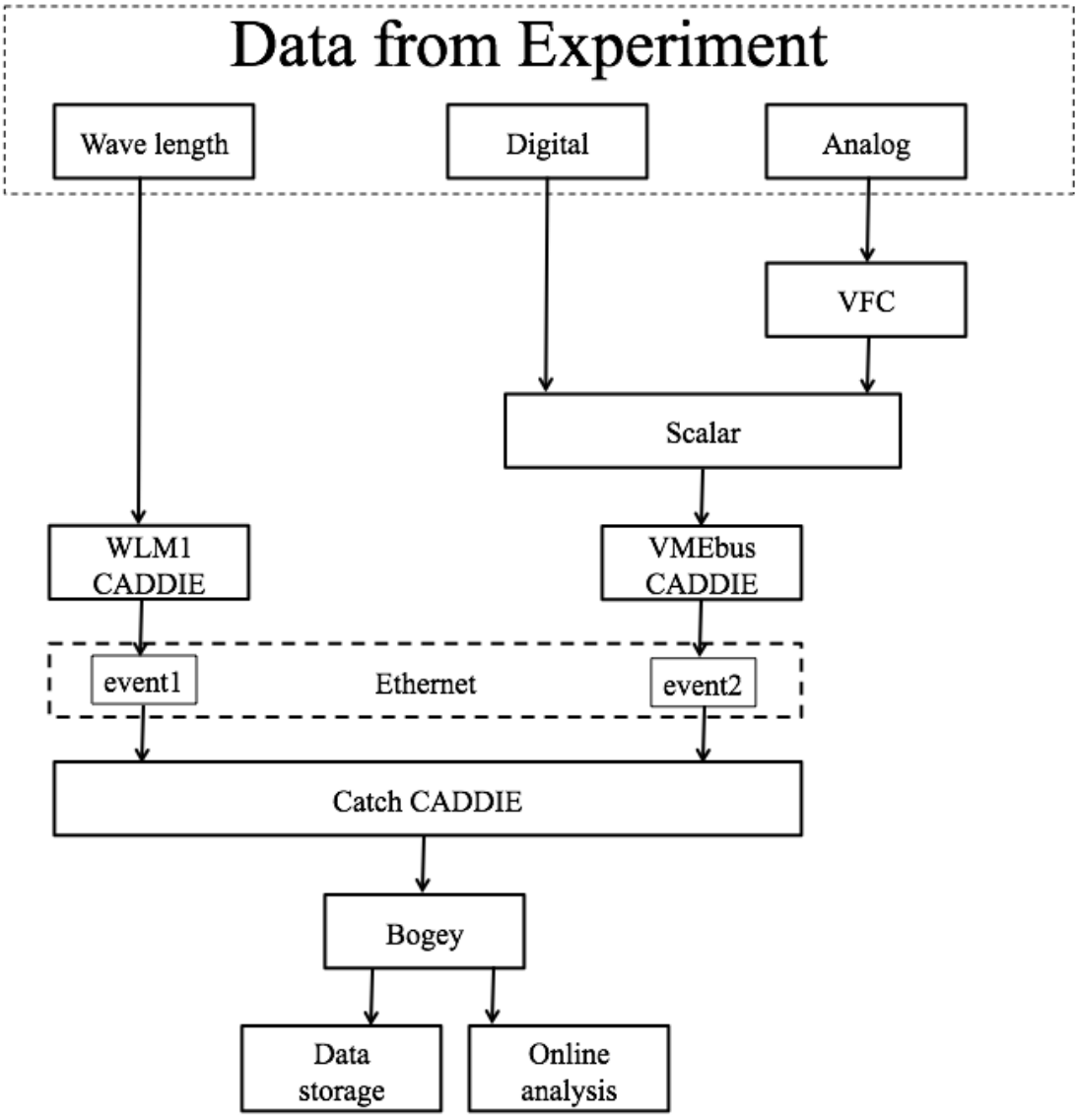

Fig. B.1: Principle of the data acquisition system in the Ra EDM experiment.

Appendix C

Photomultiplier Tubes

This appendix give the data-sheets for the photomultiplier tubes (PMT) which were used throughout this thesis. In order to collect fluorescence at wavelengths λ_1 and λ_{IC} the R7449 PMT and the R6060-12 PMT was employed. Both the PMTs were bought from Hamamatsu photonics, Japan.

C.1 Hamamatsu PMT R7449

28mm(1–1/8 Inch) Diameter, 11–stage, Bialkali Photocathode, Head–On Type, Low Dark Current, High Stability

GENERAL

Parameter		Description/Value	Unit
Spectral Response		185 to 650	nm
Wavelength of Maximum Response		420	nm
Photocathode	Material	Bialkali	–
	Minimum Effective Area	25	mm dia.
Window Material		UV glass	–
Dynode	Structure	Box and Line	–
	Number of Stages	11	–
Base		14–pin glass base	–
Suitable Socket		E678–14C (supplied)	–

MAXIMUM RATINGS (Absolute Maximum Values)

Parameter		Value	Unit
Supply Voltage	Between Anode and Cathode	1500	Vdc
	Between Anode and Last Dynode	250	Vdc
Average Anode Current		0.1	mA
Ambient Temperature		-80 to +50	°C

CHARACTERISTICS (at 25 °C)

Parameter		Min.	Typ.	Max.	Unit
Cathode Sensitivity	Luminous (2856K)	60	95	–	μA/lm
	Radiant at 420nm	–	88	–	mA/W
	Blue (CS–5–58 filter)	–	11	–	μA/lm-b
Anode Sensitivity	Luminous (2856K)	50	200	–	A/lm
	Radiant at 420nm	–	1.8×10^5	–	A/W
Gain		–	2.1×10^6	–	–
Anode Dark Current (after 30min. storage in darkness)		–	2	10	nA
Time Response	Anode Pulse Rise Time	–	4	–	ns
	Electron Transit Time	–	30	–	ns
	Transit Time Spread (FWHM)	–	3	–	ns

NOTE: Anode characteristics are measured with the voltage distribution ratio shown below.

Figure 1: Typical Spectral Response

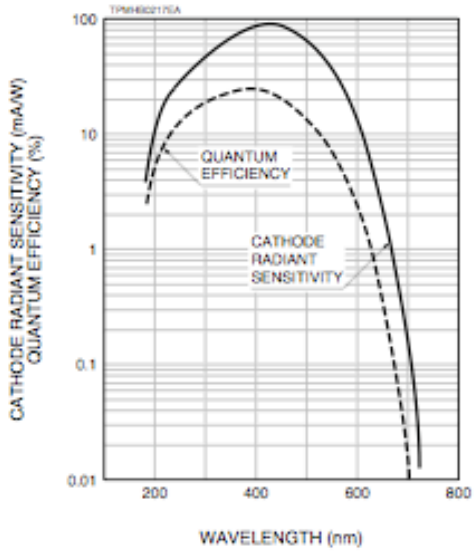

Figure 2: Typical Gain

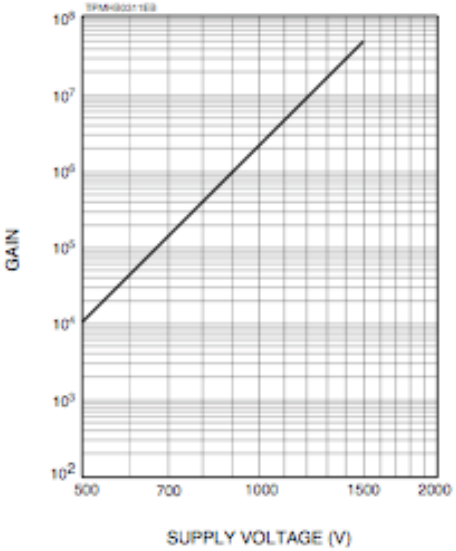

Figure 3: Dimensional Outline and Basing Diagram (Unit: mm)

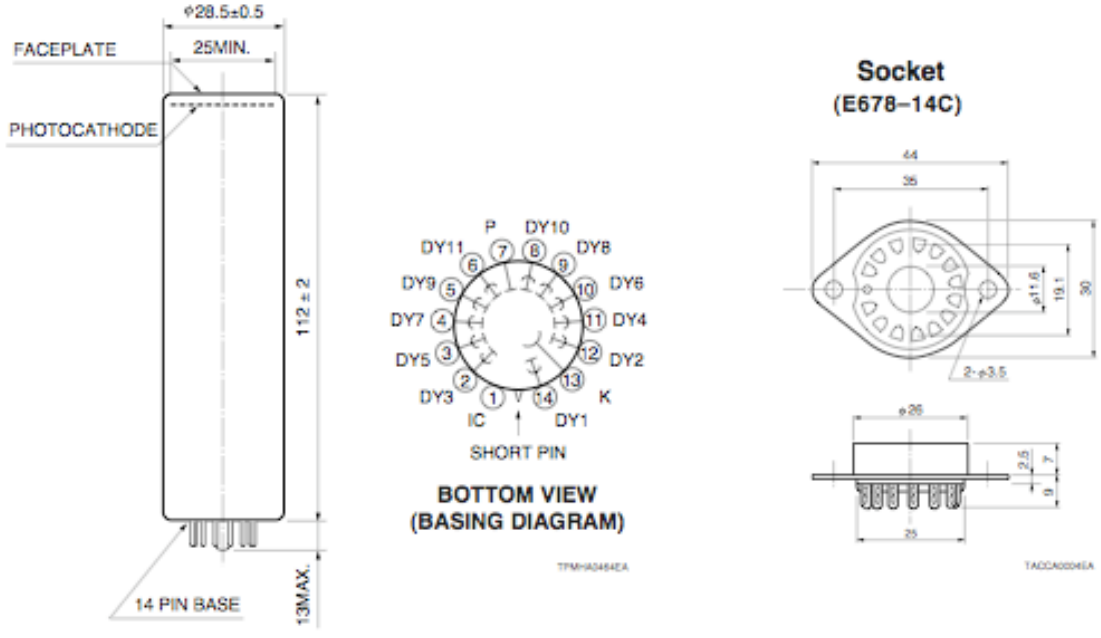

C.2 Hamamatsu PMT R6060-12

Photomultiplier Tube with Cooling Function
13mm (1/2 inch) Diameter, Side-on Type

FEATURES

- **Peltier Cooling**
  - Dark Current Decrease Capability 1/10
  - Cooling Capacity (ΔT*)
    - R6060-02 -15°C
    - R6060-12 -25°C

  *ΔT means temperature difference from an ambience.
  - Excelent ENI (Equivalent Noise Input *)
    - R6060-02 2.3×10^{-17} at 600 nm
    - R6060-12 1.7×10^{-16} at 800 nm

  *ENI : Equivalent to NEP at 1 Hz
- **Compact Cooling System with Peltier Cooler**
  - Fast Cooling Time 5 minutes (Typ.)
  - Power Consumption
    - R6060-02 1.6 W
    - R6060-12 9.2 W
- **High Sensitivity**
  - Spectral Response
    - R6060, -01, -02 185 to 850 nm
    - R6060-11, -12 185 to 900 nm
  - Photocathode Sensitivity
    - R6060, -01, -02 250 μA/lm (Typ.)
    - R6060-11, -12 450 μA/lm (Typ.)

APPLICATIONS

- ICP Emission Spectrophotometer
- Fluorescence Detector
- Chemiluminescence Detector
- Bioluminescence Detector
- Confocal Microscope
- NOx Detector

Figure 1 : ENI (Equivalent Noise Input)

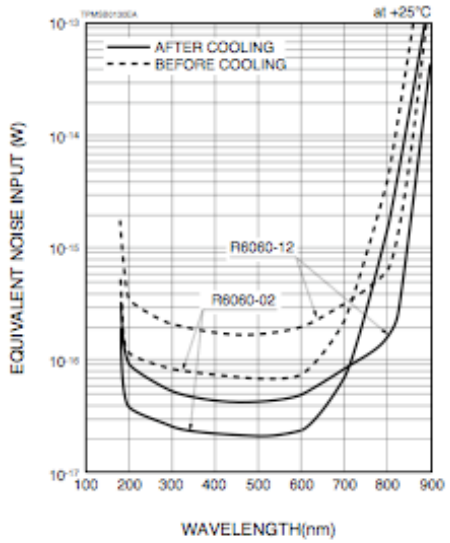

SELECTION GUIDE

Type No.	Notes
R6060	Photomultiplier tube only
R6060-01	Photomultiplier tube with Peltier Cooler
R6060-02	Photomultiplier tube with Peltier Cooler and Heatsink
R6060-11	Photomultiplier tube (High Sens.) with Peltier Cooler
R6060-12	Photomultiplier tube (High Sens.) with Peltier Cooler, Heatsink and Fan

Figure 2: Spectral Response Characteristics

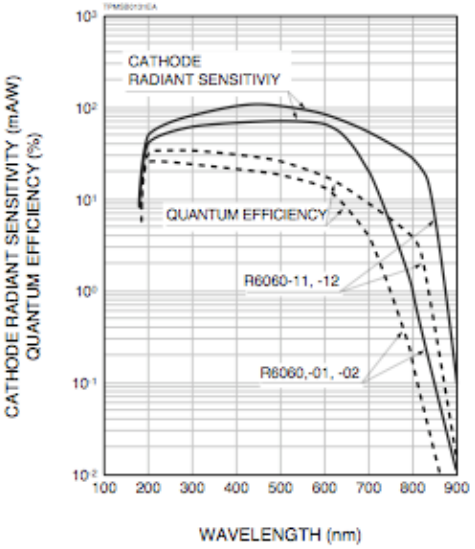

Figure 3: Anode Sensitivity and Gain

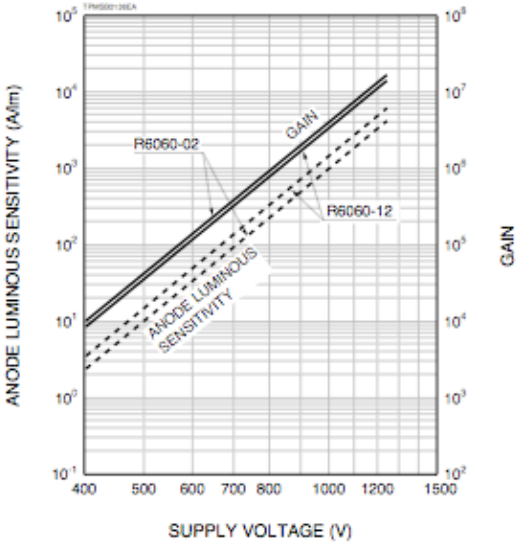

Appendix D

Bandpass Filters

This appendix provides the transmission of light as function of wavelength for the bandpass filters used in the laser spectroscopy in the frame work of this thesis. The filters we employed are from Thorlabs GmbH, Munich, Germany.

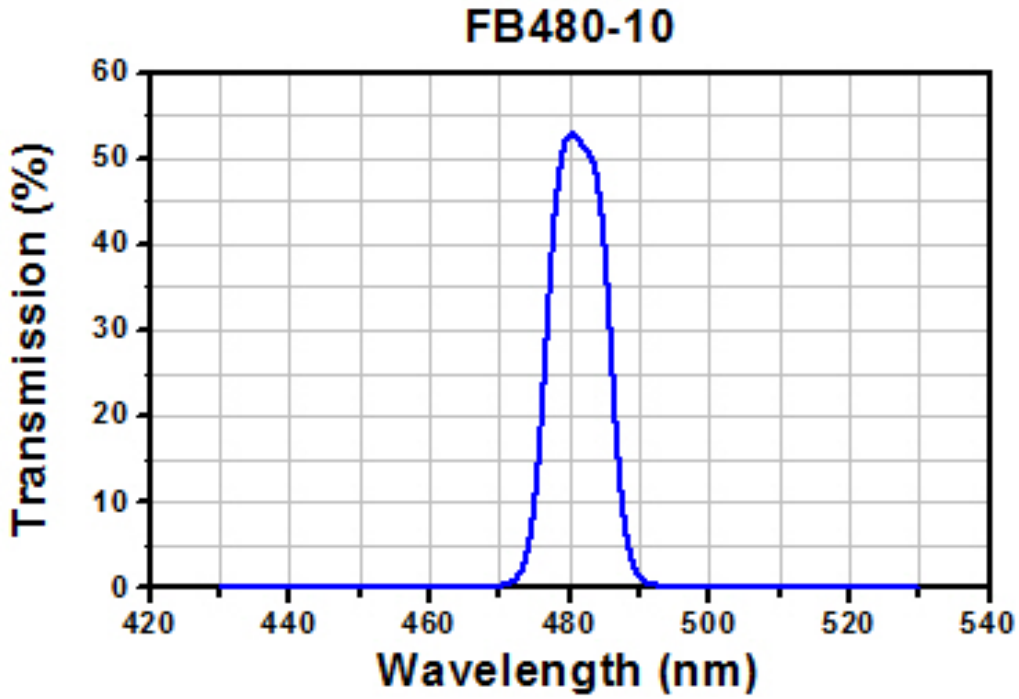

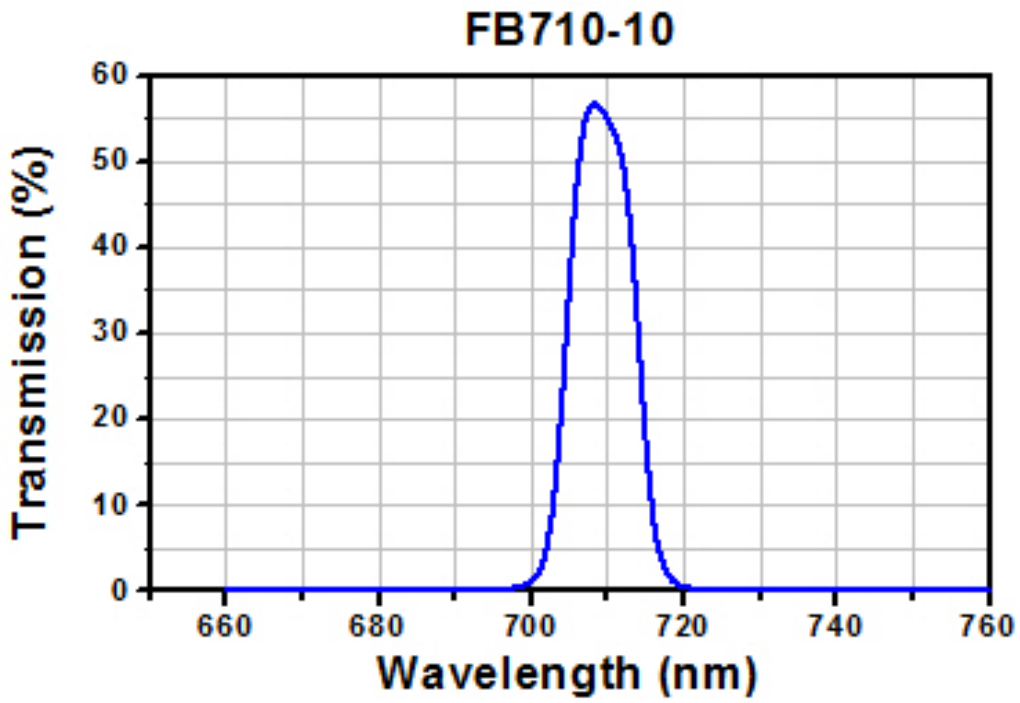
FB710-10
Transmission (%)
60
50
40
30
20
10
0
660
680
700
720
740
760
Wavelength (nm)

Bibliography

[1] W. C. Griffith, M. D. Swallows, T. H. Loftus, M. V. Romalis, B. R. Heckel, and E. N. Fortson. Improved limit on the permanent electric dipole moment of ^{199}Hg. *Phys. Rev. Lett.*, 102(10):101601, 2009.

[2] Sheldon L. Glashow. Partial-symmetries of weak interactions. *Nuclear Physics*, 22(4):579, 1961.

[3] Steven Weinberg. A model of leptons. *Phys. Rev. Lett.*, 19(21):1264, 1967.

[4] Abdus Salam. Gauge unification of fundamental forces. *Rev. Mod. Phys.*, 52(3):525, 1980.

[5] G. 't Hooft and M. Veltman. Regularization and renormalization of gauge fields. *Nuclear Physics B*, 44(1):189, 1972.

[6] Sheldon L. Glashow. Towards a unified theory - threads in a tapestry. *Nobel lecture*, 1979.

[7] CMS Collaboration. Observation of a new boson at a mass of 125 gev. *Phys. Lett. B*, 716(1):30, 2012.

[8] ATLAS Collaboration. Observation of a new particle in the search for the standard model higgs boson with the atlas detector at the lhc. *Phys. Lett. B*, 716(1):1, 2012.

[9] Fermi National Accelerator Laboratory. Batavia, IL, USA.

[10] LEP Collaboration. Search for the Standard Model Higgs boson at LEP. *Phys. Lett. B*, 565(0):61, 2003.

[11] J.A. Casas, J.R. Espinosa, and M. Quiros. Standard Model stability bounds for new physics within LHC reach. *Phys. Lett. B*, 382(4):374, 1996.

[12] Muon (g–2) Collaboration, G. W. Bennett, B. Bousquet, H. N. Brown, G. Bunce, R. M. Carey, P. Cushman, G. T. Danby, P. T. Debevec, M. Deile, H. Deng, S. K. Dhawan, V. P. Druzhinin, L. Duong, F. J. M. Farley, G. V. Fedotovich, F. E. Gray, D. Grigoriev, M. Grosse-Perdekamp, A. Grossmann, M. F. Hare, D. W. Hertzog, X. Huang, V. W. Hughes, M. Iwasaki, K. Jungmann, D. Kawall, B. I. Khazin, F. Krienen, I. Kronkvist, A. Lam, R. Larsen, Y. Y. Lee, I. Logashenko, R. McNabb, W. Meng, J. P. Miller, W. M. Morse, D. Nikas, C. J. G. Onderwater, Y. Orlov, C. S. ñzben, J. M. Paley, Q. Peng, C. C. Polly, J. Pretz, R. Prigl, G. zu Putlitz, T. Qian, S. I. Redin, O. Rind, B. L. Roberts, N. Ryskulov, Y. K. Semertzidis, P. Shagin, Yu. M. Shatunov, E. P. Sichtermann, E. Solodov, M. Sossong, L. R. Sulak, A. Trofimov, P. von Walter, and A. Yamamoto. Measurement of the negative muon anomalous magnetic moment to 0.7ppm. *Phys. Rev. Lett.*, 92(16):161802, 2004.

[13] Hans-Kristian Walter and Klaus Jungmann. Rare decays: Experiments. *Z. Phys. C*, 56(0):S135, 1992.

[14] Aaron E. Leanhardt. Precision measurement: A search for electrons that do the twist. *Nature*, 473(7348):459, 2011.

[15] Klaus Jungmann. Good fortune from a broken mirror. *Physics*, 2:68, 2009.

[16] T. D. Lee and C. N. Yang. Parity nonconservation and a two-component theory of the neutrino. *Phys. Rev.*, 105(5):1671, 1957.

[17] C. S. Wu, E. Ambler, R. W. Hayward, D. D. Hoppes, and R. P. Hudson. Experimental test of parity conservation in beta decay. *Phys. Rev.*, 105(4):1413, 1957.

[18] J. H. Christenson, J. W. Cronin, V. L. Fitch, and R. Turlay. Evidence for the 2 π decay of the K_2^0 meson. *Phys. Rev. Lett.*, 13(4):138, 1964.

[19] W Korsch. The hunt for permanent electric dipole moments. *J. Phys.: Conference Series*, 337(1), 2012.

[20] E. Noether. Invariante variationsprobleme. *Nachr. v. d. Ges. d. Wiss. zu Göttingen*, page 235, 1918.

[21] A. D. Sakharov. CP Symmetry Violation, C-Asymmetry and Baryonic Asymmetry of the Universe. *Pisma Zh. Eksp. Theor. Fiz.*, 5:32, 1967.

[22] K. Jungmann. Fundamental symmetries and interactions –some aspects. *Eur. Phys. J. A*, 25:677, 2005.

[23] Norval Fortson, Patrick Sandars, and Stephen Barr. The search for a permanent electric dipole moment. *Physics Today*, 56(6):33, 2003.

[24] Maxim Pospelov and Adam Ritz. Electric dipole moments as probes of new physics. *A. Phys.*, 318(1):119, 2005.

[25] Klaus Jungmann. Fundamental interactions. *Hyperfine Interactions*, 172:5, 2006.

[26] N. F. Ramsey. Breit Symposium, Yale. 1999.

[27] Varouzhan Baluni. CP-nonconserving effects in quantum chromodynamics. *Phys. Rev. D*, 19(7):2227, 1979.

[28] B. R. Martin. *Nuclear and Particle Physics an introduction.* John Wiley and Sons Ltd, 2nd edition, 2009.

[29] R. D. Peccei and Helen R. Quinn. CP conservation in the presence of pseudoparticles. *Phys. Rev. Lett.*, 38(25):1440, 1977.

[30] Muon (g–2) Collaboration, G. W. Bennett, B. Bousquet, H. N. Brown, G. Bunce, R. M. Carey, P. Cushman, G. T. Danby, P. T. Debevec, M. Deile, H. Deng, W. Deninger, S. K. Dhawan, V. P. Druzhinin, L. Duong, E. Efstathiadis, F. J. M. Farley, G. V. Fedotovich, S. Giron, F. E. Gray, D. Grigoriev, M. Grosse-Perdekamp, A. Grossmann, M. F. Hare, D. W. Hertzog, X. Huang, V. W. Hughes, M. Iwasaki, K. Jungmann, D. Kawall, M. Kawamura, B. I. Khazin, J. Kindem, F. Krienen, I. Kronkvist, A. Lam, R. Larsen, Y. Y. Lee, I. Logashenko, R. McNabb, W. Meng, J. Mi, J. P. Miller, Y. Mizumachi, W. M. Morse, D. Nikas, C. J. G. Onderwater, Y. Orlov, C. S. ñzben, J. M. Paley, Q. Peng, C. C. Polly, J. Pretz, R. Prigl, G. zu Putlitz, T. Qian, S. I. Redin, O. Rind, B. L. Roberts, N. Ryskulov, S. Sedykh, Y. K. Semertzidis, P. Shagin, Yu. M. Shatunov, E. P. Sichtermann, E. Solodov, M. Sossong, A. Steinmetz, L. R. Sulak, C. Timmermans, A. Trofimov, D. Urner, P. von Walter, D. Warburton, D. Winn, A. Yamamoto, and D. Zimmerman. Improved limit on the muon electric dipole moment. *Phys. Rev. D*, 80(5):052008, 2009.

[31] F. J. M. Farley, K. Jungmann, J. P. Miller, W. M. Morse, Y. F. Orlov, B. L. Roberts, Y. K. Semertzidis, A. Silenko, and E. J. Stephenson. New method of measuring electric dipole moments in storage rings. *Phys. Rev. Lett.*, 93(5):052001, 2004.

[32] C. A. Baker, D. D. Doyle, P. Geltenbort, K. Green, M. G. D. van der Grinten, P. G. Harris, P. Iaydjiev, S. N. Ivanov, D. J. R. May, J. M. Pendlebury, J. D. Richardson, D. Shiers, and K. F. Smith. Improved experimental limit on the electric dipole moment of the neutron. *Phys. Rev. Lett.*, 97(13):131801, 2006.

[33] I. B. Khriplovich. The quark electric dipole moment and the induced θ-term in the Kobayashi-Maskawa model. *Phys. Lett. B*, 173(2):193, 1986.

[34] J. J. Hudson, D. M. Kara, I. J. Smallman, B. E. Sauer, M. R. Tarbutt, and E. A. Hinds. Improved measurement of the shape of the electron. *Nature*, 473(7348):493, 2011.

[35] M. E. Pospelov and I. B. Khriplovich. Electric Dipole Moment of the W-Boson and the electron in the Kobayashi-Maskawa model. *Soviet J. Nucl. Phys.*, 53(4):638, 1991.

[36] M. A. Rosenberry and T. E. Chupp. Atomic electric dipole moment measurement using spin exchange pumped masers of ^{129}Xe and ^{3}He. *Phys. Rev. Lett.*, 86(1):22, 2001.

[37] M. J. Ramsey-Musolf and S. Su. Low-energy precision tests of supersymmetry. *Phys. Reports*, 456(1-2):1, 1 2008.

[38] B. C. Regan, Eugene D. Commins, Christian J. Schmidt, and David DeMille. New limit on the electron electric dipole moment. *Phys. Rev. Lett.*, 88(7):071805, 2002.

[39] V. V. Flambaum. Enhancement of parity and time invariance violation in the radium atom. *Phys. Rev. A*, 60(4):R2611, 1999.

[40] L. I. Schiff. Measurability of nuclear electric dipole moments. *Phys. Rev.*, 132(5):2194, 1963.

[41] P. G. H. Sandars. Electric dipole moments of charged particles. *Contemporary Physics*, 42(2):97, 2001.

[42] V. A. Dzuba, V. V. Flambaum, and J. S. M. Ginges. Calculation of parity and time invariance violation in the radium atom. *Phys. Rev. A*, 61(6):062509, 2000.

[43] V. V. Flambaum and I. B. Khriplovich. New bounds on the electric dipole moment of the electron and on t-odd electron- nucleon coupling. *Zh. Eksp. Teor. Fiz*, 89:1505, 1985.

[44] M. V. Romalis and L. Lin. Surface nuclear spin relaxation of ^{199}Hg. *J. Chem. Phys.*, 120(3):1511, 2004.

[45] M. A. Player and P. G. H. Sandars. An experiment to search for an electric dipole moment in the $^3P_2$ metastable state of xenon. *J. Ph. B: At. Mol. Opt. Phys.*, 3(12), 1970.

[46] T. E. Chupp, R. J. Hoare, R. L. Walsworth, and Bo Wu. Spin-exchange-pumped ^{3}He and ^{129}Xe Zeeman masers. *Phys. Rev. Lett.*, 72(15):2363, 1994.

[47] R. E. Stoner, M. A. Rosenberry, J. T. Wright, T. E. Chupp, E. R. Oteiza, and R. L. Walsworth. Demonstration of a two species noble gas maser. *Phys. Rev. Lett.*, 77(19):3971, 1996.

[48] Z. W. Liu and Hugh P. Kelly. Analysis of atomic electric dipole moment in thallium by all-order calculations in many-body perturbation theory. *Phys. Rev. A*, 45(7):R4210, 1992.

[49] Eugene D. Commins, Stephen B. Ross, David DeMille, and B. C. Regan. Improved experimental limit on the electric dipole moment of the electron. *Phys. Rev. A*, 50(4):2960, 1994.

[50] J. J. Hudson, B. E. Sauer, M. R. Tarbutt, and E. A. Hinds. Measurement of the electron electric dipole moment using YbF molecules. *Phys. Rev. Lett.*, 89(2):023003, 2002.

[51] Dhiren Kara. Toward an electron electric dipole moment measurement using ytterbium fluoride. *PhD thesis, Imperial College London*, 2010.

[52] P. G. Harris, C. A. Baker, K. Green, P. Iaydjiev, S. Ivanov, D. J. R. May, J. M. Pendlebury, D. Shiers, K. F. Smith, M. van der Grinten, and P. Geltenbort. New experimental limit on the electric dipole moment of the neutron. *Phys. Rev. Lett.*, 82(5):904, 1999.

[53] S. K. Lamoreaux and R. Golub. Experimental searches for the neutron electric dipole moment. *J. Phys. G*, 36(10), 2009.

[54] G. W. et. al. Bennett. Final report of the e821 muon anomalous magnetic moment measurement at bnl. *Phys. Rev. D*, 73(7):072003, 2006.

[55] J. de Vries, E. Mereghetti, R. G. E. Timmermans, and U. van Kolck. P and T violating form factors of the deuteron. *Phys. Rev. Lett.*, 107(9):091804, 2011.

[56] dEDM collaboration. Search for a permanent electric dipole moment of the deuteron nucleus at the $1e^{-29}$ e cm level. *AGS Proposal BNL*, 2008.

[57] J. Engel, M. Bender, J. Dobaczewski, J. H. de Jesus, and P. Olbratowski. Time-reversal violating schiff moment of ^{225}Ra. *Phys. Rev. C*, 68(2):025501, 2003.

[58] J. Dobaczewski and J. Engel. Nuclear time-reversal violation and the schiff moment of ^{225}Ra. *Phys. Rev. Lett.*, 94(23):232502, 2005.

[59] R. J. Holt, I. Ahmad, K. Bailey, B. Graner, J. P. Greene, W. Korsch, Z. T. Lu, P. Mueller, T. P. O'Connor, I. A. Sulai, and W. L. Trimble. Progress toward an edm measurement in ^{225}Ra. *Nucl. Phys. A*, 844(1-4):53c, 11 2010.

[60] Web page on the Naturally Occurring Radioactive Materials (NORM). Argonne National Laboratory. 2005.

[61] Mark Winter. The periodic table of elements on web. *The University of Sheffield*, 2012.

[62] The Handbook of Chemistry and Physics online. 2012.

[63] U. Dammalapati. Metastable D-State Spectroscopy and Laser Cooling of Barium. *PhD thesis, University of Groningen, NL*, 2006.

[64] S. Hoekstra. Atom trap trace analysis of calcium isotopes. *PhD thesis, University of Groningen, NL*, 2005.

[65] J. Beringer et. al. (Particle Data Group). Review of particle physics. *Phys. Rev. D*, 86(1):010001, 2012.

[66] Chart of Nuclides. National Nuclear Data Center. *Brookhaven National Laboratory*, 2012.

[67] Ebbe Rasmussen. Das Bogenspektrum des Radiums. *Z. Physik A Hadrons and Nuclei*, 87(9):607, 1933.

[68] Ebbe Rasmussen. Serien im Funkenspektrum des Radiums. Ra II. *Z. Phys. A Hadrons and Nuclei*, 86(1):24, 1933.

[69] Henry Norris Russell. The spectrum and ionization potential of radium. *Phys. Rev.*, 46(11):989, 1934.

[70] F. S. Tomkins and B. Ercoli. A modified King furnace for absorption spectroscopy of small samples. *Appl. Opt.*, 6(8):1299, 1967.

[71] J A Armstrong, J J Wynne, and F S Tomkins. Bound, 7snp $^1P_{1,0}$ series in Ra I: measurements and predictions. *J. Phy. B: At. Mol. Opt. Phys.*, 13(5):L133, 1980.

[72] S. A. Ahmad, W. Klempt, R. Neugart, E. W. Otten, K. Wendt, and C. Ekstrm. Determination of nuclear spins and moments in a series of radium isotopes. *Phys. Lett. B*, 133(1-2):47, 1983.

[73] K. Wendt, S. A. Ahmad, W. Klempt, R. Neugart, E. W. Otten, and H. H. Stroke. On the hyperfine structure and isotope shift of radium. *Z. Phys. D*, 4:227, 1987.

[74] E. Arnold, W. Borchers, M. Carre, H. T. Duong, P. Juncar, J. Lerme, S. Liberman, W. Neu, R. Neugart, E. W. Otten, M. Pellarin, J. Pinard, G. Ulm, J. L. Vialle, and K. Wendt. Direct measurement of nuclear magnetic moments of radium isotopes. *Phys. Rev. Lett.*, 59(7):771, 1987.

[75] J. Bieroń, P. Indelicato, and P. Jansson. Multiconfiguration dirac-hartree-fock calculations of transition rates and lifetimes of the eight lowest excited levels of radium. *Eur. Phys. J. Special Topics*, 144:75, 2007.

[76] V A Dzuba and V V Flambaum. Calculation of energy levels and transition amplitudes for barium and radium. *J. Phy. B: At. Mol. Opt. Phys.*, 40(1), 2007.

[77] V. A. Dzuba and J. S. M. Ginges. Calculations of energy levels and lifetimes of low-lying states of barium and radium. *Phys. Rev. A*, 73(3):032503, 2006.

[78] W. L. Trimble, I. A. Sulai, I. Ahmad, K. Bailey, B. Graner, J. P. Greene, R. J. Holt, W. Korsch, Z. T. Lu, P. Mueller, and T. P. O'Connor. Lifetime of the 7s6d $^1D_2$ atomic state of radium. *Phys. Rev. A*, 80(5):054501, 2009.

[79] N. D. Scielzo, J. R. Guest, E. C. Schulte, I. Ahmad, K. Bailey, D. L. Bowers, R. J. Holt, Z. T. Lu, T. P. O'Connor, and D. H. Potterveld. Measurement of the lifetimes of the lowest $^3P_1$ state of neutral Ba and Ra. *Phys. Rev. A*, 73(1):010501, 2006.

[80] J. R. Guest, N. D. Scielzo, I. Ahmad, K. Bailey, J. P. Greene, R. J. Holt, Z. T. Lu, T. P. O'Connor, and D. H. Potterveld. Laser trapping of ^{225}Ra and ^{226}Ra with repumping by room-temperature blackbody radiation. *Phys. Rev. Lett.*, 98(9):093001, 2007.

[81] K Jungmann, G P Berg, U Dammalapati, P Dendooven, O Dermois, M N Harakeh, R Hoekstra, R Morgenstern, A Rogachevskiy, M Sanchez-Vega, R Timmermans, E Traykov, L Willmann, and H W Wilscut. TRIμP - Trapped Radioactive Atoms - μicrolaboratories for Fundamental Physics. *Phys. Scripta*, 2003(T104), 2003.

[82] Jacek Bieroń, Charlotte Froese Fischer, Stephan Fritzsche, and Krzysztof Pachucki. Lifetime and hyperfine structure of the $^3D_2$ state of radium. *J. Phy. B: At. Mol. Opt. Phys.*, 37(17), 2004.

[83] Jacek Bieroń, Gediminas Gaigalas, Erikas Gaidamauskas, Stephan Fritzsche, Paul Indelicato, and Per Jnsson. Multiconfiguration dirac-hartree-fock calculations of the electric dipole moment of radium induced by the nuclear Schiff moment. *Phys. Rev. A*, 80(1):012513, 2009.

[84] W. C. Griffith, M. Swallows, and E. N. Fortson. *Lepton Dipole Moments*, volume 20 of *Advanced Series on Directions in High Energy Physics*. World Scientific Publishing Co. Pte. Ltd., 2010.

[85] J. Engel, J. L. Friar, and A. C. Hayes. Nuclear octupole correlations and the enhancement of atomic time-reversal violation. *Phys. Rev. C*, 61(3):035502, 2000.

[86] V. V. Flambaum and V. G. Zelevinsky. Enhancement of nuclear schiff moments and time-reversal violation in atoms due to soft nuclear octupole vibrations. *Phys. Rev. C*, 68(3):035502, 2003.

[87] P. Butler et al. Measurements of octupole collectivity in odd-mass Rn, Fr and Ra isotopes. *HIE-ISOLDE LOI*, 2010.

[88] K. Jungmann. (private communication).

[89] Subhadeep De. Laser Cooling and Trapping of Barium. *PhD thesis, University of Groningen, NL*, 2008.

[90] James Harvey et. al. Production of Actinium-225 via high energy proton induced spallation of Thorium-232. *Applications of High Intensity Proton Accelerators - Proceedings of the Workshop*, 2010.

[91] M. A. Hofstee et al. Progress towards high intensity heavy ion beams at the AGOR-facility. *Proceedings of CYCLOTRONS2010, Lanzhou, China*, 2010.

[92] E. Traykov, U. Dammalapati, S. De, O. C. Dermois, L. Huisman, K. Jungmann, W. Kruithof, A. J. Mol, C. J. G. Onderwater, A. Rogachevskiy, M. da Silva e Silva, M. Sohani, O. Versolato, L. Willmann, and H. W. Wilschut. Development of a thermal ionizer as ion catcher. *Nucl. Instrum. Methods B*, 266(19-20):4478, 2008.

[93] E. Traykov. Production of radioactive beams for atomic trapping. *PhD thesis, University of Groningen, NL*, 2006.

[94] P. D. Shidling, G. S. Giri, D. J. van der Hoek, K. Jungmann, W. Kruithof, C. J. G. Onderwater, M. Sohani, O. O. Versolato, L. Willmann, and H. W. Wilschut. Production of short lived radioactive beams of radium. *Nucl. Instrum. Methods A*, 606(3):305, 2009.

[95] O. O. Versolato, G. S. Giri, J. E. van den Berg, O. Boll, U. Dammalapati, D. J. van der Hoek, S. Hoekstra, K. Jungmann, W. L. Kruithof, S. Mueller, M. Nunez Portela, C. J. G. Onderwater, B. Santra, R. G. E. Timmermans, L. W. Wansbeek, L. Willmann, and H. W. Wilschut. Hyperfine structure of the level in trapped short-lived $^{211,209}Ra^{+}$ ions. *Phys. Lett. A*, 375(35):3130, 2011.

[96] G. P. A. Berg, O. C. Dermois, U. Dammalapati, P. Dendooven, M. N. Harakeh, K. Jungmann, C. J. G. Onderwater, A. Rogachevskiy, M. Sohani, E. Traykov, L. Willmann, and H. W. Wilschut. Dual magnetic separator for. *Nucl. Instrum. Methods A*, 560(2):169, 2006.

[97] P. D. Shidling, G. S. Giri, D. J. van der Hoek, K. Jungmann, W. L. Kruithof, C. J. G. Onderwater, B. Santra, M. Sohani, O. O. Versolato, L. Willmann, and H. W. Wilschut. Thermalization of different alkali and alkali-earth elements at the facility. *Nucl. Instrum. Methods A*, 622(1):11, 2010.

[98] Kaye G. W. C. and Laby T. H. *CRC Handbook of Chemistry and Physics*. CRC Press, 1995.

[99] J. P. Biersack and L. Haggmark. A Monte Carlo computer program for the transport of energetic ions in amorphous targets. *Nucl. Instr. and Meth.*, 174:257, 1980.

[100] G. J. Beyer, E. Hageb, A. F. Novgorodov, and H. L. Ravn. The role of diffusion in isol targets for the production of radioactive ion beams. *Nucl. Instrum. Methods B*, 204(0):225, 2003.

[101] Charles Kittel and Herbert Kroemer. Thermal physics. *W. H. Freenman and Company*, 1980.

[102] G. G. Kleiman and Uzi Landman. Theory of physisorption: He on metals. *Phys. Rev. B*, 8(12):5484, 1973.

[103] J. P. Hobson. Pumping at solid surfaces. *British Journal of Applied Physics*, 14(9), 1963.

[104] R. Mueller and H. W. Wassmuth. Desorption kinetics of alkaline earth adparticles on tungsten with variation of the oxygen surface coverage. *Surface Science*, 34(2):249, 1 1973.

[105] Yamamoto Shigehiko et al. Formation mechanism of a monoatomic order surface layer on a Sc-type impregnated cathode. *Jap. J. Appl. Phys.*, 28:490, 1989.

[106] R.H. Schumm, D.D. Wagman, S. Bailey, W.H. Evans, and V.B. Parker. *National Bureau of Standards (USA) Technical Notes*, 270, 1973.

[107] W. Kruithof. Laser trapping of sodium isotopes for a high-precision β-decay experiment. *PhD thesis, University of Groningen, NL*, 2012.

[108] D. Melconian, M. Trinczek, A. Gorelov, W. P. Alford, J. A. Behr, J. M. D'Auria, M. Dombsky, U. Giesen, K. P. Jackson, T. B. Swanson, and W. Wong. Release of ^{37}K from catcher foils. *Nuclear Instruments and*

Methods in Physics Research Section A: Accelerators, Spectrometers, Detectors and Associated Equipment, 538:93, 2 2005.

[109] Thorlabs GmbH, Munich, Germany.

[110] SIMION. Industry standard charged particle optics simulation software. *Scientific Instrument Services, Inc., NJ, USA*.

[111] A. Groot. Spectroscopy of neutral radium. *Masters thesis, University of Groningen, NL*, 2010.

[112] Dongfeng Xue and Siyuan Zhang. Comparison of non-linear optical susceptibilities of $KNbO_3$ and $LiNbO_3$. *J. Phys. Chem. of Solids*, 58(9):1399, 1997.

[113] P. A. Franken, A. E. Hill, C. W. Peters, and G. Weinreich. Generation of optical harmonics. *Phys. Rev. Lett.*, 7(4):118, 1961.

[114] Z. Y. Ou, S. F. Pereira, E. S. Polzik, and H. J. Kimble. 85% efficiency for cw frequency doubling from 1.08 to 0.54 ,m. *Opt. Lett.*, 17(9):640, 1992.

[115] R. Paschotta, P. Krz, R. Henking, S. Schiller, and J. Mlynek. 82% efficient continuous-wave frequency doubling of 1.06 m with a monolithic MgO:$LiNbO_3$ resonator. *Opt. Lett.*, 19(17):1325, 1994.

[116] Thomas Sudmeyer, Yutaka Imai, Hisashi Masuda, Naoya Eguchi, Masaki Saito, and Shigeo Kubota. Efficient 2nd and 4th harmonic generation of asingle-frequency, continuous-wave fiberamplifier. *Opt. Express*, 16(3):1546, 2008.

[117] Beat Zysset, Ivan Biaggio, and Peter Gunter. Refractive indices of orthorhombic $KNbO_3$. I. Dispersion and temperature dependence. *J. Opt. Soc. Am. B*, 9(3):380, 1992.

[118] D. A. Shaddock, M. B. Gray, and D. E. McClelland. Frequency locking a laser to an optical cavity by use of spatial mode interference. *Opt. Lett.*, 24(21):1499, 1999.

[119] Bruce G. Klappauf, Yannick Bidel, David Wilkowski, Thierry ChaneliEre, and Robin Kaiser. Detailed study of an efficient blue laser source by second-harmonic generation in a semimonolithic cavity for the cooling of strontium atoms. *Appl. Opt.*, 43(12):2510, 2004.

[120] FEE Gmbh. LASER Crystals and Nonlinear Optical Crystals. *Idar-Oberstein, Germany.*

[121] S. Arlee. SNLO software for modeling crystal nonlinear optics.

[122] Carl E. Wieman and Leo Hollberg. Using diode lasers for atomic physics. *Rev. Sci. Instrum.*, 62(1):1, 1991.

[123] H. Patrick and C. E. Wieman. Frequency stabilization of a diode laser using simultaneous optical feedback from a diffraction grating and a narrowband Fabry–Perot cavity. *Rev. Sci. Instrum.*, 62(11):2593, 1991.

[124] GaAIAs Infrared Emitting Diode. HL7001MG/02MG. *Opnext Japan Inc., Tokyo, Japan*, 2008.

[125] T. J. Pinkert, D. Z. Kandula, C. Gohle, I. Barmes, J. Morgenweg, and K. S. E. Eikema. Widely tunable extreme uv frequency comb generation. *Opt. Lett.*, 36(11):2026, 2011.

[126] Arman Cingoz, Dylan C. Yost, Thomas K. Allison, Axel Ruehl, Martin E. Fermann, Ingmar Hartl, and Jun Ye. Direct frequency comb spectroscopy in the extreme ultraviolet. *Nature*, 482(7383):68, 2012.

[127] P Maddaloni, P Malara, G Gagliardi, and P De Natale. Mid-infrared fibre-based optical comb. *New J. Physics*, 8(11), 2006.

[128] Christine Wang, Tobias Herr, Pascal Del'Haye, Albert Schliesser, Ronald Holzwarth, Theodor W. Haensch, Nathalie Picqué, and Tobias Kippenberg. Mid-infrared frequency combs based on microresonators. Optical Society of America, 2011.

[129] S. Gerstenkorn et. al. *Atlas du spectra d'Absortion de la Molecule d'Iode.* Laboratiry Aimr-Cotton, CERN, Orsay, France, 1993.

[130] J. Cariou and P. Luc. *Atlas du Spectre d'Absorption de la Molecule d'Tellure.* Laboratiry Aimr-Cotton, CERN, Orsay, France, 1980.

[131] M. G. Boshier, P. E. G. Baird, C. J. Foot, E. A. Hinds, M. D. Plimmer, D. N. Stacey, J. B. Swan, D. A. Tate, D. M. Warrington, and G. K. Woodgate. Laser spectroscopy of the 1s-2s transition in hydrogen and deuterium: Determination of the 1s lamb shift and the rydberg constant. *Phys. Rev. A*, 40(11):6169, 1989.

[132] J. D. Gillaspy and Craig J. Sansonetti. Absolute wavelength determinations in molecular tellurium: new reference lines for precision laser spectroscopy. *J. Opt. Soc. Am. B*, 8(12):2414, 1991.

[133] A A Optoelectronics Ltd. Ontario, Canada.

[134] U. Dammalapati, S. De, K. Jungmann, and L. Willmann. Isotope shifts of 6s5d 3D - 6s6p $^1P_1$ transitions in neutral barium. *E. Phys. D*, 53:1, 2009.

[135] H. Knnckel, B. Bodermann, and E. Tiemann. High precision description of the rovibronic structure of the I B-X spectrum. *Eur. Phys. J. D*, 28(2):199, 2004.

[136] Menlo Systems GmbH Germany. Optical Frequency Combs.

[137] Philip Russell. Photonic crystal fibers. *Science*, 299(5605):358, 01 2003.

[138] D. H. McIntyre and T. W. Haensch. Interferometric frequency measurement of a $^{130}Te_2$ reference line for muonium 1s-2s spectroscopy. *Phys. Rev. A*, 36(8):4115, 1987.

[139] D. H. McIntyre, Jr. Fairbank, W. M., S. A. Lee, T. W. Haensch, and E. Riis. Interferometric frequency measurement of $^{130}Te_2$ reference transitions at 486 nm. *Phys. Rev. A*, 41(9):4632, 1990.

[140] G. P. Barwood, W. R. C. Rowley, P. Gill, J. L. Flowers, and B. W. Petley. Interferometric measurements of $^{130}Te_2$ reference frequencies for 1s-2s transitions in hydrogenlike atoms. *Phys. Rev. A*, 43(9):4783, 1991.

[141] Robert E. Machol and Edgar F. Westrum. Vapor pressure of liquid tellurium. *J. Am. Chem. Soc.*, 80(12):2950, 1958.

[142] W. Demtroder. *Laser Spectroscopy: Basic Concepts and Instrumentation.* Spinger-Verlag, 2003.

[143] Robert F. Brebrick. Tellurium vapor pressure and optical density at 370-615.degree. *J. Phys. Chem.*, 72(3):1032, 1968.

[144] J. R. M. Barr, J. M. Girkin, A. I. Ferguson, G. P. Barwood, P. Gill, W. R. C. Rowley, and R. C. Thompson. Interferometric frequency measurements of $^{130}Te_2$ transitions at 486 nm. *Optics Communications*, 54(4):217, 6 1985.

[145] C. Cohen-Tannoudji and D. Guery-Odelin. *Advances in atomic physics*. World Scientific Publishing Co. Pte. Ltd., 2011.

[146] A. D. Ludlow, T. Zelevinsky, G. K. Campbell, S. Blatt, M. M. Boyd, M. H. G. de Miranda, M. J. Martin, J. W. Thomsen, S. M. Foreman, Jun Ye, T. M. Fortier, J. E. Stalnaker, S. A. Diddams, Y. Le Coq, Z. W. Barber, N. Poli, N. D. Lemke, K. M. Beck, and C. W. Oates. Sr lattice clock at 1×10^{-16} fractional uncertainty by remote optical evaluation with a Ca clock. *Science*, 319(5871):1805, 2008.

[147] C. J. Foot. *Atomic Physics (Oxford Master Series in Atomic, Optical and Laser Physics)*. Oxford University Press Inc., New York, 2005.

[148] S. De, U. Dammalapati, K. Jungmann, and L. Willmann. Magneto-optical trapping of barium. *Phys. Rev. A*, 79:041402, 2009.

[149] A. Nagel, S. Brandt, D. Meschede, and R. Wynands. Light shift of coherent population trapping resonances. *E. Phys. Lett.*, 48(4), 1999.

[150] E Arimondo. Coherent population trapping in laser spectroscopy. In *Progress in Optics, Vol 35*, volume 35 of *Progress in Optics*, page 257. Elsevier Science Publ. B V, 1996.

[151] Thomas Zanon-Willette, Emeric de Clercq, and Ennio Arimondo. Ultrahigh-resolution spectroscopy with atomic or molecular dark resonances: Exact steady-state line shapes and asymptotic profiles in the adiabatic pulsed regime. *Phys. Rev. A*, 84(6):062502, 2011.

[152] G. Alzetta, A. Gozzini, L. Moi, and G. Orriols. Experimental-method for observation of rf transitions and laser beat resonances in oriented na vapor. *Nuovo Cimento Della Soc. Italiana Di Fisica B*, 36(1):5, 1976.

[153] Vishal Shah, John Kitching, P. R. Berman E. Arimondo, and C. C. Lin. *Chapter 2 - Advances in Coherent Population Trapping for Atomic Clocks*, volume Volume 59, page 21. Academic Press, 2010.

[154] I. Siemers, M. Schubert, R. Blatt, W. Neuhauser, and P. E. Toschek. The trapped state of a trapped ion - line shifts and shape. *E. Phys. Lett.*, 18(2BIS):139, 1992.

[155] G. Janik, W. Nagourney, and H. Dehmelt. Doppler-free optical spectroscopy on the Ba^+ mono-ion oscillator. *J. Opt. Soc. Am. B*, 2(8):1251, 1985.

[156] Robin Santra, Ennio Arimondo, Tetsuya Ido, Chris H. Greene, and Jun Ye. High-accuracy optical clock via three-level coherence in neutral bosonic ^{88}Sr. *Phys. Rev. Lett.*, 94(17):173002, 2005.

[157] A. Greilich, R. Oulton, E. A. Zhukov, I. A. Yugova, D. R. Yakovlev, M. Bayer, A. Shabaev, Al. L. Efros, I. A. Merkulov, V. Stavarache, D. Reuter, and A. Wieck. Optical control of spin coherence in singly charged (In,Ga)As/GaAs quantum dots. *Phys. Rev. Lett.*, 96(22):227401, 2006.

[158] E. Peik and Chr. Tamm. Nuclear laser spectroscopy of the 3.5 eV transition in Th-229. *E. Phys. Lett.*, 61(2), 2003.

[159] Hidetoshi Katori. Optical lattice clocks and quantum metrology. *Nature Photonics*, 5(4):203, 2011.

[160] Masao Takamoto, Feng-Lei Hong, Ryoichi Higashi, and Hidetoshi Katori. An optical lattice clock. *Nature*, 435(7040):321, 2005.

[161] M. V. Romalis and E. N. Fortson. Zeeman frequency shifts in an optical dipole trap used to search for an electric-dipole moment. *Phys. Rev. A*, 59(6):4547, 1999.

[162] D. S. Weiss, F. Fang, and J. Chen. Measuring the electric dipole moment of Cs and Rb in an optical lattice. *Bull. Am. Phys. Soc.*, (APR03, J1.008), 2003.

[163] O. O. Versolato, G. S. Giri, L. W. Wansbeek, J. E. van den Berg, D. J. van der Hoek, K. Jungmann, W. L. Kruithof, C. J. G. Onderwater, B. K. Sahoo, B. Santra, P. D. Shidling, R. G. E. Timmermans, L. Willmann, and H. W. Wilschut. Laser spectroscopy of trapped short-lived Ra^+ ions. *Phys. Rev. A*, 82(1):010501, 2010.

[164] G. S. Giri, O. O. Versolato, J. E. van den Berg, O. Boll, U. Dammalapati, D. J. van der Hoek, K. Jungmann, W. L. Kruithof, S. Mueller, M. Nunez Portela, C. J. G. Onderwater, B. Santra, R. G. E. Timmermans, L. W. Wansbeek, L. Willmann, and H. W. Wilschut. Isotope shifts

of the 6d $^2D_{3/2}$-7p $^2P_{1/2}$ transition in trapped short-lived $^{209-214}Ra^+$. *Phys. Rev. A*, 84(2):020503, 2011.

[165] E. Kugler. The ISOLDE facility. *Hyperfine Interactions*, 129(1-4):23, 2000.

[166] H. A. Abderrahim et. al. MYRRHA, a multipurpose hybrid research reactor for high-end applications. *Nucl. Phys. News*, 20(1):24, 2010.

List of Publications

1. *Online production of thermal radium atoms at the TRIμP facility*,
   B. Santra, H. Bekker, J. E. van den Berg, O. Böll, U. Dammalapati, E. Dijck, K. Jungmann, S. Chirayath Mathavan, C. Meinema, A. Mohanty, S. Müller, M. Nuñez-Portela, C. J. G. Onderwater, A. van der Poel, M. Santin, L. Willmann, and H. W. Wilschut,
   (In preparation).

2. *Absolute frequency measurement of the* $^1S_0 - {}^3P_1$ *intercombination transition in neutral radium*,
   B. Santra, U. Dammalapati, K. Jungmann, and L. Willmann,
   (In preparation).

3. *Absolute frequency measurement of the* $^1S_0 - {}^1P_1$ *transition in neutral radium*,
   B. Santra, U. Dammalapati, A. Groot, K. Jungmann, and L. Willmann,
   (In preparation).

4. *New precise determination of the unperturbed* ^8B *neutrino spectrum*,
   T. Roger, J. Buscher, B. Bastin, O. S. Kirsebom, R. Raabe, M. Alcorta, J. Aysto, M. J. G. Borge, M. Carmona-Gallardo, T. E. Cocolios, J. Cruz, P. Dendooven, L.M. Fraile, H.O.U. Fynbo, D. Galaviz, L. R. Gasques, G. S. Giri, M. Huyse, S. Hyldegaard, K. Jungmann, W. L. Kruithof, M. Lantz, A. Perea, K. Riisager, A. Saastamoinen, **B. Santra**, P. D. Shidling, M. Sohani, A.J. Sorensen, O. Tengblad, E. Traykov, D. J. van der Hoek, P. Van Duppen, O. O. Versolato, and H. W. Wilschut,
   Phys. Rev. Lett. **108**, 162502 (2012).

5. *Light shifts and magic wavelengths for heavy alkaline earth elements: Ba and Ra*,
   U. Dammalapati, **B. Santra** and L. Willmann,
   J. Phys. B: At. Mol. Opt. Phys. **45**, 025001 (2012).

6. *Isotope shifts of $6d\,^2D_{3/2}$ - $7p\,^2P_{1/2}$ transition in trapped short-lived $^{209-214}Ra^+$*,
G.S. Giri, O.O. Versolato, J.E. van den Berg, O. Böll, U. Dammalapati, D.J. van der Hoek, K. Jungmann, W. Kruithof, S. Müller, M. Nuñez Portela, C.J.G. Onderwater, **B. Santra**, R.G.E. Timmermans, L.W. Wansbeek, L. Willmann, H.W. Wilschut,
Phys. Rev. A **84**, 020503(R) (2011).

7. *Hyperfine structure of the $6d\,^2D_{3/2}$ level in trapped short-lived $^{211,209}Ra^+$ ions*,
O.O. Versolato, G.S. Giri, J.E. van den Berg, O. Böll, U. Dammalapati, D.J. van der Hoek, S. Hoekstra, K. Jungmann, W. Kruithof, S. Müller, M. Nuñez Portela, C.J.G. Onderwater, **B. Santra**, R.G.E. Timmermans, L.W. Wansbeek, L. Willmann, H.W. Wilschut,
Phys. Lett. A **375**(35), 3130 (2011).

8. *Atomic parity violation in a single trapped radium ion*,
O.O. Versolato, L.W. Wansbeek, G.S. Giri, J.E. van den Berg, D.J. van der Hoek, K. Jungmann, W.L. Kruithof, C.J.G. Onderwater, B.K. Sahoo, **B. Santra**, P.D. Shidling, R.G.E. Timmermans, L. Willmann, and H.W. Wilschut,
Hyperfine Interact, **199**, 9 (2011).

9. *Precision spectroscopy of trapped radioactive radium ions*,
G.S. Giri, O.O. Versolato, L.W. Wansbeek, J.E. van den Berg, D.J. van der Hoek, K. Jungmann, W.L. Kruithof, C.J.G. Onderwater, B.K. Sahoo, **B. Santra**, P.D. Shidling, R.G.E. Timmermans, L. Willmann, and H.W. Wilschut,
Can. J. Phys. **89**(1), 69 (2011).

10. *Atomic parity violation in a single trapped radium ion*,
O.O. Versolato, L.W. Wansbeek, G.S. Giri, J.E. van den Berg, D.J. van der Hoek, K. Jungmann, W.L. Kruithof, C.J.G. Onderwater, B.K. Sahoo, **B. Santra**, P.D. Shidling, R.G.E. Timmermans, L. Willmann, and H.W. Wilschut,
Can. J. Phys. **89**(1), 65 (2011).

11. *Thermalization of different alkali and alkali-earth elements at the TRIμP facility*,
P.D. Shidling, G.S. Giri, D.J. van der Hoek, K. Jungmann, W. Kruithof, C.J.G. Onderwater, **B. Santra**, M. Sohani, O.O. Versolato, L. Willmann,

H.W. Wilschut,
Nucl. Instr. and Meth. A **622**, 11 (2010).

12. *Laser spectroscopy of trapped short-lived Ra^+ ions*,
O.O. Versolato, G.S. Giri, L.W. Wansbeek, J.E. van den Berg, D.J. van der Hoek, K. Jungmann, W.L. Kruithof, C.J.G. Onderwater, B.K. Sahoo, **B. Santra**, P.D. Shidling, R.G.E. Timmermans, L. Willmann, H.W. Wilschut, Phys. Rev. A **82**, 010501(R) (2010).

13. *β-Decay and the electric dipole moment: Searches for time-reversal violation in radioactive nuclei and atoms*,
H. W. Wilschut, D. J. van der Hoek, K. Jungmann, W. Kruithof, C. J. G. Onderwater, **B. Santra**, P. Shidling and L. Willmann,
Pramana **75** 163 (2010).

14. *β-Decay and the electric dipole moment: Searches for time-reversal violation in radioactive nuclei and atoms*,
H. W. Wilschut, U. Dammalapati, D. J. van der Hoek, K. Jungmann, W. Kruithof, C. J. G. Onderwater, **B. Santra**, P. Shidling and L. Willmann,
Nuclear Physics A **844** 143 (2010).

Acknowledgment

This PhD thesis is the tip of an iceberg, which has been grown up with the invaluable support in many aspects from all my direct and indirect well wishers.

I am proud to be a children of my parents who have shown me many first steps in my life. In particular my interest in physics has been grown by looking at the exciting pictures in the books of my first physics teacher, my father.

I would like to thank many of my teachers starting from primary school to the University. During my visit at Institute of Physics, Bhubaneswar, India as summer research student in 2006 Prof. Kalyan Kundu taught me how to learn physics and how to behave as a physicist. It will not be too much if I say that, it was a great motivation for me to aspire for becoming a successful physicist. From the day of my first meeting with Prof. Bhanu Pratap Das at Indian Institute of Astrophysics, Bangalore, India in December 2010, I have always received invaluable support and encouragement for pursuing successful research. I am grateful to Prof. V. Srinivas, Indian Institute of Technology Kharagpur (now at Madras) for his support whenever I needed.

I am thankful to my supervisors Prof. Klaus Jungmann and Dr. Lorenz Willmann for guiding me and critically evaluating my work that led to this thesis. At the beginning of my PhD work I did not know anything about experimental research. Both of you took the pain to prepare me as someone who can do something in a laboratory (I hope so). Lorenz taught me the concept of SMART (Specific, Measurable, Achievable, Realistic, Time bound) working, which I think I remember everyday at least once during my work. I have learnt from Klaus how to take a critical decision in economic time scale as well.

I thank the members of the reading committee Prof. W. Heil, Prof. Y. Blumenfeld, and Prof. P. Butler for the careful reading of this manuscript and

the constructive comments they provided.

I thank all my colleagues in the TRIμP group for their continuous support for the Ra EDM project. I would like to thank Hans Wilschut for his support on isotope production in a educational level and during the beam time. Many thanks to Gerco Onderwater for his enthusiastic help for smooth running of the data acquisition system. Otto Dermois and Leo Huisman were like GPS system whenever I needed to build something from the workshop or from drawing office. Enthusiastic support from Oliver Böll for setting up optics was adorable. I would like to give Umakanth Dammalapati my sincere thanks for his active support to the Ra EDM project and for the light shift paper. I thank Stefan Müller for his encouraging attitude which has helped me a lot during my PhD days.

I thank Bijaya Sahoo for his suggestion and support to me for professional and personal life. My sincere thanks to Subhadeep De, my long time senior for his valuable suggestions and support.

I will always remember Gouri for his constructive suggestion during my PhD days. I thank Steven Hoekstra, Oscar, Duurt, Mayerlin, Joost, Hendrik, Elwin, Amita, Sreekanth for their cooperation to run both offline and online Ra atom experiment. I also thank ex-TRIμP members Moslem, Praveen, Marléne, Alexandar and Sander. I was happy to get Wilbert, Jordy and Corine as my office mates.

I thank Gerco, Lorenz, Corine and Joost for translating the summary of my PhD thesis in Dutch language.

My sincere thanks to AGOR cyclotron group. I would like to thank all the personnels from IT department, drawing office, mechanical, electronic and vacuum workshops, administration, financial and personal offices for their potential support to complete my PhD work. I would like to give Hilde van der Meer a special thanks for taking care of all paper works throughout my PhD.

My sincere thanks to Ronnie Hoekstra and the atomic physics group for many useful discussions with them. A special thanks to Thomas, Erwin, Geert and Olmo for allowing me to borrow continuously many vacuum components.

I would like to give special thanks to Amit-da, Deepak-vai, Ayanangsha,

Sujata-di, Soumya and Dipayan for many wonderful evening. Discussion on many topics with Suresh and Ganesh was enjoyable. I thank Saurav Dhabal Deb for helping me to designing the cover of my thesis.

Finally I thank my parents and my sister for their never ending support. I thank Suranita for her love and support, and for willing to spend life with me. I am thankful to my parent and sister in laws for their support.

This research was supported by the Stichting voor Fundamenteel Onderzoek der Materie (FOM) under Program 114 (TRIμP), FOM and Nederlandse Organisatie voor Wetenschappelijk Onderzoek (NWO) and Ubbo Emmius PhD scholarship from the graduate school of science of the University of Groningen, The Netherlands.

Bodhaditya Santra